

**AUTONOMOUS STATE ESTIMATION AND ITS APPLICATION
TO THE AUTONOMOUS OPERATION OF THE DISTRIBUTION
SYSTEM WITH DISTRIBUTED GENERATIONS**

A Dissertation
Presented to
The Academic Faculty

by

Sungyun Choi

In Partial Fulfillment
of the Requirements for the Degree
Doctor of Philosophy in the
School of Electrical and Computer Engineering

Georgia Institute of Technology
December 2013

COPYRIGHT 2013 BY SUNGYUN CHOI

**AUTONOMOUS STATE ESTIMATION AND ITS APPLICATION
TO THE AUTONOMOUS OPERATION OF THE DISTRIBUTION
SYSTEM WITH DISTRIBUTED GENERATIONS**

Approved by:

Dr. A.P. Sakis Meliopoulos, Advisor
School of Electrical and Computer
Engineering
Georgia Institute of Technology

Dr. Ronald G. Harley
School of Electrical and Computer
Engineering
Georgia Institute of Technology

Dr. Magnus B. Egerstedt
School of Electrical and Computer
Engineering
Georgia Institute of Technology

Dr. Ying Zhang
School of Electrical and Computer
Engineering
Georgia Institute of Technology

Dr. Andy Sun
School of Industrial and Systems
Engineering
Georgia Institute of Technology

Date Approved: August 14, 2013

To my father Jung-Soo, to my mother Hee-Jae,
and to my sisters Tae-Eun and Tae-Sun.

ACKNOWLEDGEMENTS

I'm deeply indebted to all people who have supported and encouraged the completion of my dissertation during the long journey of my graduate studies at Georgia Tech.

First of all, I would like to express my deepest appreciation to my Ph.D. advisor, Professor A. P. Sakis Meliopoulos for his invaluable guidance, support, and inspiration. His extensive knowledge and professional experience have led me to complete this research work. Furthermore, since I first met him at Georgia Tech in August 2007, I have learned many things from his expertise in academia, considerate and generous personality, and infinite passion for research.

I would also like to extend my sincere gratitude to Professor Ronald G. Harley, Professor Magnus B. Egerstedt, Professor Ying Zhang, and Professor Andy Sun for serving as my dissertation committee and for their valuable time contribution in reviewing the drafts. Their insightful comments and suggestions have also made considerable contribution the completion of this work.

I am also grateful to Dr. George J. Cokkinides for his valuable support and practical contributions to complete my work. His professional expertise in theory and implementation was always excellent and admirable.

Moreover, I would like express my appreciation to Dr. Beungjin Kim of Hyundai Heavy Industries Co. for his constructive advice and practical support. It is within bounds to say that all this work started from a project on which I collaborated with him.

I must also thank to my undergraduate professors at Korea University. Especially, my graduate studies at Georgia Tech would not have begun at all without the recommendation and encouragement of Dr. Sunshin An, Dr. Chang-Sung Jeong, Dr. Tae-Woong Yoon, Dr. Lynn Choi, and Dr. Byongjun Lee. I also wish to thank to Dr. Gilsoo Jang and Dr. Sang Bin Lee for their practical suggestions and helpful advice.

Thanks should also go to my fellow colleagues in the Power System Control and Automation Laboratory. First of all, I would like to extend my sincere thanks to Dr. Salman Mohagheghi, Dr. Georgios K. Stefopoulos, and Dr. Q. Binh Dam, who welcomed me when I joined the lab. Their advice and guidance was valuable at the beginning of my graduate studies.

Above all, I also had great pleasure of working with Yonghee Lee, Aniemi Umana, and Rui Fan in various projects. They were instrumental in accomplishing the projects, and I had such a great collaboration with them.

Furthermore, I very much appreciate the opportunity to work and exchange ideas with Dr. Vangelis Farantatos, Dr. Curtis Roe, Renke Huang, Jongkook Park, and Dr. Ye Tao. Among them, I would like to thank to Dr. Vangelis Farantatos and Dr. Curtis Roe, with whom I joined the lab in 2007, for their unwavering support, insightful suggestions, and kind advice.

Additionally, I am also thankful to other lab mates for working and studying together: Dongbo Zhao, Evangelos Polymeneas, Zhenyu Tan, Liangyi Sun, Tharmer Alquithami, Semako Adovohekpe, Dr. Soohyoung Lee, and Sanghoon Choi. Moreover, I would also like to thank to other colleagues, who left the lab, for support and suggestions.

In specific, I would like to mention Kyle Howells, Anupama Keeli, Xubei Yu, Sandhya Madan, Stephanie M. Gossman, Dr. Sungsam Kim, and Dr. Sungyul Kim.

I cannot leave Georgia Tech without mentioning Dr. Yongnam Cho, who has provided technical advice, encouragement, and friendship throughout my graduate studies.

I would also like to acknowledge the assistance of Dr. Ratnesh K. Sharma of NEC Laboratories America, Inc. He provided me with encouragement and guidance throughout the duration of my summer internship in 2012.

In addition, I would like to recognize the help of the graduate students of the power group at Georgia Tech. Among them, special thanks to Dr. Sangtaek Han, Dr. Namhoon Cho, and Insoo Kim for friendship and advice.

Last but not least, I would also like to express my gratitude to the Alumni Association of Korea University at Georgia Tech for moral support, encouragement, and friendship. In particular, Joonhoi Hur played a decisive role in starting my graduate studies at Georgia Tech, and I have been always grateful to him for invaluable advice, ingenious suggestions, and true friendship.

Finally, the completion of my dissertation would not have been possible without the unwavering support, warm encouragement, and endless love of my family.

TABLE OF CONTENTS

ACKNOWLEDGEMENTS	iv
LIST OF FIGURES	xii
LIST OF TABLES	xviii
LIST OF ABBREVIATIONS	xix
SUMMARY	xxi
CHAPTER 1 INTRODUCTION AND OBJECTIVES OF RESEARCH	1
1.1 Problem Statement	1
1.2 Objectives of Research	2
1.3 Thesis Outline	3
CHAPTER 2 LITERATURE REVIEW AND BACKGROUND INFORMATION	5
2.1 Overview	5
2.2 Evolution of the Electric Distribution System	5
2.2.1 Protection Gaps in the Distribution System	8
2.2.2 Operation and Control of DGs	11
2.2.3 Need for Short-term Operational Planning	16
2.3 Real-time Monitoring System and Communication	19
2.4 State Estimation in Power Systems	22
2.5 Summary	26
CHAPTER 3 AUTONOMOUS STATE ESTIMATION	27
3.1 Overview	27
3.2 Motivation of the Autonomous State Estimation for the Distribution System	27
3.3 Requirements for the Autonomous State Estimation	29

3.3.1	Communication Infrastructure	29
3.3.2	Data-acquisition Units and UMPCUs	30
3.3.3	Three Types of Essential Data	34
3.4	Implementation of Autonomous State Estimation	37
3.4.1	Integration of Device Models	38
3.4.2	Definition of State Variable	39
3.4.3	Creation of the Measurement Model	39
3.4.4	State Estimation	42
3.4.5	Performance Metrics	45
3.4.6	Accuracy of Solution	47
3.4.7	Estimation Error of Measurements	48
3.4.8	Bad-data Detection, Identification, and Rejection	48
3.5	Process of Autonomous State Estimation	50
3.5.1	Step 1: Capture Streaming of All Available Data	52
3.5.2	Step 2: Update Device Models or Connectivity	52
3.5.3	Step 3: Form Measurement Models	53
3.5.4	Step 4: Contribution of Measurements	54
3.5.5	Step 5: Compute State Estimates	55
3.5.6	Step 6: Convergent Test	56
3.5.7	Step 7: Compute the Chi-square Critical Value, the Degrees of Freedom, and the Confidence Level	56
3.5.8	Step 8: Bad-data Detection, Identification, and Rejection	56
3.5.9	Step 9: Update the Past-history Values	56
3.5.10	Step 10: Proceed to the Next Time Step	57
3.6	Summary	57

CHAPTER 4 AUTONOMOUS OPERATION OF THE DISTRIBUTION SYSTEM WITH DISTRIBUTED GENERATIONS	59
4.1 Overview	59
4.2 Autonomous Operation of the Distribution System	59
4.3 Detailed Scheme of the Autonomous Operation	62
4.4 Setting-less Component Protection	65
4.4.1 Basic Concept of the Proposed Protection Scheme	66
4.4.2 Implementation of Setting-less Component Protection	69
4.4.3 Process of Dynamic State Estimation	72
4.4.4 Setting-less Component Protection and Autonomous State Estimation	79
4.5 Instant-by-instant Management (MPPT)	82
4.5.1 Operation and Control of the PV Generation System	82
4.5.2 Operation and Control of the Wind-turbine Generation System	84
4.6 Short-term Operational Planning	87
4.6.1 Application of Autonomous State Estimation	88
4.6.2 Multi-operational Mode	89
4.7 Summary	91
CHAPTER 5 LABORATORY DEMONSTRATIONS	94
5.1 Overview	94
5.2 Laboratory Test System 1	94
5.2.1 Electric Power Infrastructure	94
5.2.2 Data-communication Infrastructure	98
5.2.3 Experimental Test	101
5.3 Laboratory Test System 2	107
5.3.1 System Description	107

5.3.2	Test Scenarios	110
5.3.3	Experimental Test	112
5.4	Summary	124
CHAPTER 6 FEASIBILITY STUDY: SETTING-LESS COMPONENT PROTECTION OF THE THREE-PHASE TRANSFORMER		126
6.1	Overview	126
6.2	Hardware Requirements	126
6.3	Implementation of the Proposed Protection Scheme	129
6.3.1	Definition of States	129
6.3.2	Definition of Measurements	132
6.4	Feasibility Test with Numerical Experiments	137
6.4.1	Example Test System and Test Scenarios	138
6.4.2	Test Results	149
6.5	Summary	184
CHAPTER 7 CONCLUSIONS AND FUTURE RESEARCH DIRECTION		186
7.1	Conclusions	186
7.1.1	Design of Autonomous State Estimation	186
7.1.2	Autonomous Operation of the Distribution System with DGs	188
7.1.3	Laboratory Demonstration of Autonomous State Estimation	189
7.1.4	Feasibility Test of Setting-less Component Protection of the Transformer	190
7.1.5	Component Modeling	191
7.2	Contributions	191
7.3	Future Work Direction	192
APPENDIX A DEVICE MODELING TECHNIQUE		194
A.1	Overview	194

A.2 Quadratic Integration Method	194
A.3 Model Quadratzation	196
A.4 Summary	197
APPENDIX B PV-ARRAY MODEL	198
B.1 Overview	198
B.2 Component Model Description	198
B.3 ACF Model Description	201
B.4 State Variables	203
B.5 Summary	204
APPENDIX C THREE-PHASE-TRANSFORMER MODEL	205
C.1 Overview	205
C.2 Component Model Description of the Single-phase Transformer	205
C.3 Quadratzed Model Description of the Single-phase Transformer	207
C.4 AQCF Model Description of the Single-phase Transformer	208
C.5 AQCF Model Description of the Three-phase Transformer	212
C.6 State Variables	216
C.7 Summary	217
REFERENCES	218
VITA	227

LIST OF FIGURES

Figure 2.1:	Overcurrent relay scheme.	9
Figure 2.2:	Differential relay scheme.	10
Figure 2.3:	I-V characteristics of a PV cell.	13
Figure 2.4:	P-V characteristics of a PV cell.	13
Figure 2.5:	I-V curves from experimental data at different temperatures [33].	14
Figure 2.6:	I-V curves from experimental data at different irradiances [33].	14
Figure 2.7:	MPPT of the DFIG-based wind turbine [34].	15
Figure 3.1:	Overall concept of autonomous state estimation.	29
Figure 3.2:	Autonomous operation of the distribution system.	31
Figure 3.3:	Close-in view and functionality of the UMPCU.	32
Figure 3.4:	Close-in view and functionality of the data-acquisition unit.	33
Figure 3.5:	Basic concept of the device-model integration.	38
Figure 3.6:	Quality evaluation of state estimation based on the chi-square test.	47
Figure 3.7:	Overall process of autonomous state estimation.	51
Figure 4.1:	Illustration of the autonomous operation of the distribution system.	60
Figure 4.2:	Operational time frames of autonomous operations.	61
Figure 4.3:	Detailed scheme of the autonomous operation.	63
Figure 4.4:	Overall approach of the setting-less component protection scheme.	67
Figure 4.5:	Protection logic based on dynamic state estimation.	68
Figure 4.6:	Overall process of dynamic state estimation.	72
Figure 4.7:	Illustration of the use of samples for the setting-less component protection at the present time, t .	74
Figure 4.8:	Functionality of the UMPCU.	81

Figure 4.9:	Functionality of the data-acquisition unit.	81
Figure 4.10:	Instant-by-instant management of the PV generation system.	83
Figure 4.11:	Fundamental architecture of the DFIG.	84
Figure 4.12:	Instant-by-instant management of the wind-turbine generation system.	85
Figure 4.13:	Power coefficient for different pitch angles [79].	86
Figure 5.1:	Photograph of the laboratory setup in the PSCAL.	95
Figure 5.2:	Single-line diagram of the test laboratory system.	95
Figure 5.3:	Actual interconnections among components.	96
Figure 5.4:	Mechanical connection between the synchronous generator and the DC motor.	98
Figure 5.5:	Communication scheme between the relays and the autonomous state estimator.	100
Figure 5.6:	OPC manager.	101
Figure 5.7:	Estimated results of V_2 , the phase-A voltage measurement across <i>Main Bus</i> and <i>RGROUND</i> .	105
Figure 5.8:	Estimated results of I_2 , the phase-A current measurement from <i>Main Bus</i> to <i>XLINE-1</i> .	106
Figure 5.9:	Chi-square critical values.	106
Figure 5.10:	Confidence level.	107
Figure 5.11:	Average standard deviation of the error of the estimated states.	107
Figure 5.12:	Diagram of the smart grid energy system.	108
Figure 5.13:	Detailed circuit of the storage system.	109
Figure 5.14:	Daily load profile.	110
Figure 5.15:	On and off status of the inverter and the charger in the energy-storage system.	111
Figure 5.16:	Measured and estimated values of voltage measurements at the phases A and B.	113

Figure 5.17:	Measured and estimated values of voltage measurements at the phases A and B (zoomed in).	113
Figure 5.18:	Measured and estimated values of the active-power measurement.	114
Figure 5.19:	Measured and estimated values of the active-power measurement (zoomed in).	114
Figure 5.20:	Confidence level in the test with the data of the PV inverter.	115
Figure 5.21:	Measured and estimated values of voltage measurements at the phases A and B.	115
Figure 5.22:	Measured and estimated values of voltage measurements at the phases A and B (zoomed in).	116
Figure 5.23:	Measured and estimated values of the active-power measurement.	116
Figure 5.24:	Measured and estimated values of the active-power measurement (zoomed in).	117
Figure 5.25:	Confidence level in the test with the data of the load.	117
Figure 5.26:	Confidence level in the test with the data of the energy-storage system.	118
Figure 5.27:	Power input to the charger with the confidence level.	119
Figure 5.28:	Confidence level in the test with the data of the integrated model.	120
Figure 5.29:	Confidence level in the first test case.	121
Figure 5.30:	Confidence level in the second test case.	121
Figure 5.31:	Confidence level in the third test case.	122
Figure 5.32:	Confidence level in the fourth test case.	123
Figure 5.33:	Confidence level in the fifth test case.	123
Figure 5.34:	Confidence level in the sixth test case.	124
Figure 6.1:	Typical data-acquisition system.	127
Figure 6.2:	Recommended instrumentation and the data-acquisition system with cables.	128
Figure 6.3:	Secondary recommended instrumentation and the data-acquisition system with merging units and the process bus.	128

Figure 6.4:	Feasibility test scheme for verifying the proposed protection method.	138
Figure 6.5:	Test system for the proposed protection method.	139
Figure 6.6:	Settings of the three-phase transformer under protection.	140
Figure 6.7:	Measurements of the transformer (test A: the normal operating condition).	142
Figure 6.8:	Measurements of the transformer [test B: transformer energization (inrush current)].	143
Figure 6.9:	Measurements of the transformer (test C: transformer overexcitation).	144
Figure 6.10:	Fault location in the test system (test D: the through-fault condition).	145
Figure 6.11:	Measurements of the transformer (test D: the through-fault condition).	146
Figure 6.12:	Fault location in the test system (test E: the internal-fault condition).	147
Figure 6.13:	Measurements of the transformer (test E: the internal-fault condition).	148
Figure 6.14:	Confidence level (test A: the normal operating condition).	149
Figure 6.15:	Estimated and measured values of the current measurements with the confidence level (test A).	150
Figure 6.16:	Estimated and measured values of the voltage measurements with the confidence level (test A).	151
Figure 6.17:	Estimated value, measured value, residual, and normalized residual of the current measurement at the primary side (test A).	152
Figure 6.18:	Estimated value, measured value, residual, and normalized residual of the current measurement at the secondary side (test A).	153
Figure 6.19:	Estimated value, measured value, residual, and normalized residual of the voltage measurement at the primary side (test A).	154
Figure 6.20:	Estimated value, measured value, residual, and normalized residual of the voltage measurement at the secondary side (test A).	155
Figure 6.21:	Confidence level (test B: transformer energization).	156

Figure 6.22:	Estimated and measured values of the current measurements with the confidence level (test B).	157
Figure 6.23:	Estimated and measured values of the voltage measurements with the confidence level (test B).	158
Figure 6.24:	Estimated value, measured value, residual, and normalized residual of the current measurement at the primary side (test B).	159
Figure 6.25:	Estimated value, measured value, residual, and normalized residual of the current measurement at the secondary side (test B).	160
Figure 6.26:	Estimated value, measured value, residual, and normalized residual of the voltage measurement at the primary side (test B).	161
Figure 6.27:	Estimated value, measured value, residual, and normalized residual of the voltage measurement at the secondary side (test B).	162
Figure 6.28:	Confidence level (test C: transformer overexcitation).	163
Figure 6.29:	Estimated and measured values of the current measurements with the confidence level (test C).	164
Figure 6.30:	Estimated and measured values of the voltage measurements with the confidence level (test C).	165
Figure 6.31:	Estimated value, measured value, residual, and normalized residual of the current measurement at the primary side (test C).	166
Figure 6.32:	Estimated value, measured value, residual, and normalized residual of the current measurement at the secondary side (test C).	167
Figure 6.33:	Estimated value, measured value, residual, and normalized residual of the voltage measurement at the primary side (test C).	168
Figure 6.34:	Estimated value, measured value, residual, and normalized residual of the voltage measurement at the secondary side (test C).	169
Figure 6.35:	Confidence level (test D: the through-fault condition).	170
Figure 6.36:	Estimated and measured values of the current measurements with the confidence level (test D).	171
Figure 6.37:	Estimated and measured values of the voltage measurements with the confidence level (test D).	172
Figure 6.38:	Estimated value, measured value, residual, and normalized residual of the current measurement at the primary side (test D).	173

Figure 6.39:	Estimated value, measured value, residual, and normalized residual of the current measurement at the secondary side (test D).	174
Figure 6.40:	Estimated value, measured value, residual, and normalized residual of the voltage measurement at the primary side (test D).	175
Figure 6.41:	Estimated value, measured value, residual, and normalized residual of the voltage measurement at the secondary side (test D).	176
Figure 6.42:	Confidence level (test E: the internal-fault condition).	178
Figure 6.43:	Estimated and measured values of the current measurements with the confidence level (test E).	178
Figure 6.44:	Estimated and measured values of the voltage measurements with the confidence level (test E).	179
Figure 6.45:	Estimated value, measured value, residual, and normalized residual of the current measurement at the primary side (test E).	180
Figure 6.46:	Estimated value, measured value, residual, and normalized residual of the current measurement at the secondary side (test E).	181
Figure 6.47:	Estimated value, measured value, residual, and normalized residual of the voltage measurement at the primary side (test E).	182
Figure 6.48:	Estimated value, measured value, residual, and normalized residual of the voltage measurement at the secondary side (test E).	183
Figure A.1:	Quadratic integration method.	195
Figure B.1:	Equivalent circuit of the ideal PV cell.	199
Figure B.2:	Equivalent circuit of the practical PV array.	200
Figure B.3:	Definition of the external and internal states of the PV-array model.	201
Figure C.1:	Single-phase-transformer model.	206
Figure C.2:	Delta-wye connection of three single-phase transformers.	212
Figure C.3:	Indices of the AQCFs of the single-phase transformer and the three-phase delta-wye-connected transformer.	213

LIST OF TABLES

Table 5.1:	Definition of system states.	103
Table 5.2:	Definition of measurement data.	103
Table 5.3:	Performance test in terms of time latency.	104
Table 5.4:	Initial settings for the real-time operation of autonomous state estimation.	104
Table 5.5:	Test cases.	112
Table 6.1:	All state variables for the three-phase, delta-wye-connected transformer when n is five.	129
Table 6.2:	Actual across measurements for the three-phase transformer.	133
Table 6.3:	Actual through measurements for the three-phase transformer.	134
Table 6.4:	Virtual measurements for the three-phase transformer.	135
Table 6.5:	Pseudo measurements for the three-phase transformer.	137
Table 6.6:	Transformer parameters.	141
Table C.1:	Pointer mapping between the AQCF of the single-phase transformer and that of the AQCF of the three-phase transformer.	213

LIST OF ABBREVIATIONS

AC	Alternative current
ACF	Algebraic companion form
AMI	Advanced metering infrastructure
AQCF	Algebraic quadratic companion form
COMTRADE	Common format for transient data exchange
CT	Current transformer
DBMS	Database management system
DC	Direct current
DER	Distributed energy resource
DFIG	Doubly-fed induction generator
DG	Distributed generator
DMS	Distribution management system
EMS	Energy management system
EPRI	Electric power research institute
GPS	Global positioning system
IED	Intelligent electronic device
IEEE	Institute of electrical and electronics engineers
IPMS	Intelligent power management system
IP	Internet protocol
IT	Information technology
LAN	Local area network
LN	Logical node

MPPT	Maximum power point tracking
ODBC	Open database connectivity
OPC	Object linking and embedding for process control
PHEV	Plug-in hybrid electrical vehicle
PMU	Phasor measurement unit
PSCAL	Power system control and automation laboratory
PT	Potential transformer
PV	Photovoltaic
RTU	Remote terminal unit
SCADA	Supervisory control and data acquisition
UMPCU	Universal monitoring protection control unit
WAMS	Wide-area monitoring system
WAN	Wide area network

SUMMARY

The objective of this thesis is to propose guidelines for advanced operation, control, and protection of the restructured distribution system by designing the architecture and functionality for autonomous operation of the distribution system with DGs. The proposed architecture consists of (1) autonomous state estimation and (2) applications that enable autonomous operation; in particular, three applications are discussed: setting-less component protection, instant-by-instant management, and short-term operational planning. Key elements of the proposed approach have been verified: (1) the proposed autonomous state estimation has been experimentally tested using laboratory test systems and (2) the feasibility of the setting-less component protection has been tested with numerical simulations.

The recent trends in distribution systems are increasing penetration of DGs most of which are based on renewable energy resources such as the solar or wind energy, and introduction of power-electronics-interfaced devices to the grid. These trends will eventually restructure the distribution system. In the restructured distribution system, new grid problems have emerged in terms of (1) protection gaps, (2) operation and control of DGs, and (3) need for short-term operational planning. Traditional protection schemes may lead to misoperation and difficulty in coordinating the protection of an active distribution system with inverter-interfaced DGs. The operational characteristics of DGs are controlled by renewable energy resources and change moment by moment as weather conditions change. Moreover, these systems are non-dispatchable DGs and are based on intermittent energy resources. It is difficult to forecast and schedule the operation of these

resources in the long term, so short-term operational planning is more suitable for the restructured distribution system.

The most efficient way to solve these new grid problems is by autonomous and decentralized operation. In fact, the autonomous operation is primarily based on the real-time operating conditions, which are typically computed by state estimation. However, traditional state estimation, which is based on balanced operation, symmetric system structure, and relatively fixed system topology, is not applicable to the restructured distribution system, which is dynamic and unpredictable. Therefore, this thesis proposes an autonomous state estimation that can compute accurate and real-time operating conditions of the dynamically changing system, eventually providing the capability to detect the continuous changing of system topology and achieve the concept of plug-and-play. The proposed implementation of the autonomous state estimation requires the three types of data: (1) connectivity, (2) device models, and (3) measurements. The connectivity indicates buses/nodes where the device is connected, and the device model is mathematical equations that represent physical characteristics of a device. Measurements are numeric values obtained by meters; the three sets of data can be collected and sent to the local DMS by UMPCUs or various data-acquisition units through the data-communication system. The state estimation needs only these three types of data to compute the best estimate of state variables and the best estimate of each device model; collecting all validated real-time models yields the entire system model of the distribution system. It is important to note that the autonomous state estimation is based on the well-known weighted-least-squares method. The data and models are validated by computing the confidence level, which quantifies the goodness of fit of

models to measurements. If the confidence level is low, then it can be concluded that there exist any bad data. In this case, bad-data-identification methods are applied to identify the bad data and remove them from the measurement set.

The proposed autonomous state estimation enables autonomous operations of the distribution system for three different operational time frames: (1) setting-less component protection, (2) instant-by-instant management, and (3) short-term operational planning. The setting-less component protection, the instant-by-instant management, and the short-term operational planning should be operated every few cycles, every few seconds, and every few minutes, respectively. First, the setting-less component protection is an innovative protection method that is based on dynamic state estimation, which uses real-time measurements and the component dynamic model. The dynamic state estimation provides the confidence level that an internal fault has occurred or not. Second, the validated model and measurements from the autonomous state estimation can be used for the instant-by-instant management of DGs; for example, DGs can be controlled to pull out maximum available power from renewable energy resources (e.g., the solar or wind energy) under variable environmental conditions (e.g., solar irradiation, temperature, wind speed, and wind direction). Last but not least, the proposed autonomous state estimation can facilitate the short-term operational planning by providing the real-time operating conditions of non-dispatchable DGs that are changing with environmental conditions, which is followed by solving various optimization problems (e.g., economic or environmental dispatch) that determine the reference operating points of dispatchable DGs.

Finally, this thesis describes experimental tests to verify the feasibility of the proposed autonomous state estimation with two laboratory setups: (1) the scaled-down power system in the PSCAL at the Georgia Institute of Technology, and (2) the smart grid energy system in NEC Laboratories America, Inc. In addition, the proposed setting-less component protection has been validated with numerical experiments performed on three-phase, two-winding, variable-tap, and saturable-core transformers. The results of the laboratory tests and the numerical experiments are described in this thesis.

CHAPTER 1

INTRODUCTION AND OBJECTIVES OF RESEARCH

1.1 Problem Statement

New technologies aiming to create a smarter power grid have naturally resulted in more sensors, communications, management tools, and controls. This trend naturally focuses among others on distribution systems and integration of renewable energy resources, possible storages, and various architectures. For example, anticipated eco-friendly and highly efficient PHEVs are expected to have substantial impact on the distribution system as they represent additional loads to the system and possibility of serving as distributed resources to the system. Charging of PHEVs can result in overloading of distribution transformers, which eventually decreases the expected life of the transformer [1], and PHEVs can also operate as reactive power sources or as real power sources in case of need.

Therefore, the distribution system with new technologies and DGs requires an advanced operation and control scheme that can solve various grid problems in an efficient, economic, reliable, stable, and secure way. For example, in a situation where power supply from DGs and power demands of PHEVs are changing every moment, economic dispatch, which finds least-cost dispatch of available generation resources, can be solved more efficiently and rapidly by an autonomous local distribution system than by a centralized control center because the local system has low time latency taken in data communication and computation. Then, the local distribution system can make their own decisions according to properly designed strategies and operational goals.

Indeed, the distributed and autonomous operation of the distribution system is fundamentally based on the real-time operating conditions of the system, which can be

obtained by processing measurement data from field sensors. Such computational process is referred to as state estimation. However, conventional centralized state estimation is not suitable for the restructured distribution system because of uncertainties that result from the intermittent operation of DGs and from irregular scheduling of PHEVs or batteries. Accordingly, it is recommended to implement state estimation in an autonomous manner. In other words, the local distribution system collects all available information from all electric components in the local territory and then extracts local operating conditions. This estimation process is referred to as autonomous state estimation. Finally, the local distribution system can use these computed operating conditions for its autonomous operation, eventually solving various grid problems.

1.2 Objectives of Research

The objective of this research work is to design the architecture and functionality for autonomous operation of distribution systems with DGs, which consists of (1) autonomous state estimation and (2) applications that enables autonomous operation from the three points of view: setting-less component protection, instant-by-instant management, and short-term operational planning. The next step is to verify the proposed approach; (1) experimental tests of the proposed autonomous state estimation using laboratory test systems and (2) feasibility study of the setting-less component protection with numerical simulation.

The proposed autonomous state estimation can obtain real-time operating conditions in the changeable and unpredictable distribution system. The autonomous state estimation is a method that automatically identifies network topology of the distribution system, and it can extract operating conditions of the system in real time while system topology, resources, and loads may be continuously changing. Accordingly, this method is capable of providing the infrastructure for plug-and-play capability, which enables hundreds of smart devices to easily connect to and interact with grid; the DMS would

automatically detect the newly plugged-in smart devices and incorporate them into the real-time model of the system.

The implementation of proposed autonomous state estimation requires that each monitoring device streams three sets of data to the DMS: (1) connectivity, (2) the device model, and (3) measurements. First and foremost, connectivity data refer to buses/nodes to which a device is connected. Next, device model data represent the mathematical model of a device. Finally, measurement data are numerical values of physical quantities, such as voltages, currents, flux, and speed as appropriate for a specific device. Indeed, typical IEDs can be programmed to provide these three sets of data. In particular, this research work proposes a specific architecture of an IED that is named a UMPCU. The UMPCU is similar to the merging unit with the additional capability to provide connectivity data and model data, executing control commands received from the DMS. As a result, UMPCUs should be connected to high-speed communication infrastructure that supports interoperability among multi-vendor devices.

Based on real-time operating conditions computed from autonomous state estimation, this research work proposes autonomous operation, control, and protection of the restructured distribution system. First, an adaptive component protection scheme is proposed, for high penetration of DGs can cause bi-directional power flow and small fault currents, which may lead to misoperation in traditional protection coordination. Second, the local DMS should be able to control non-dispatchable DGs, which are based on the renewable energy resources such as solar or wind energy, to operate at maximum available power in any conditions. Finally, while these non-dispatchable generation units produce maximum power, short-term operational planning can provide optimum operating points for dispatchable DGs.

1.3 Thesis Outline

The remaining of the document is organized as follows:

Chapter 2 presents the literature review and background relevant to the origin and history of the topic. This chapter describes the history of the restructured distribution system and newly emerging grid problems, the real-time monitoring system and communication, and state estimation in power systems.

Chapter 3 presents basic concept of autonomous state estimation and its fundamental requirements. The detailed algorithm of the autonomous state estimation is also presented.

Chapter 4 describes how to apply autonomous state estimation to autonomous operation of the distribution system with DGs. This chapter explains three approaches of the autonomous operation: (1) setting-less component protection, (2) instant-by-instant management, and (3) short-term operational planning.

Chapter 5 presents laboratory demonstrations of the proposed autonomous state estimation with actual test systems. For this purpose, two laboratory setups are tested: (1) the scaled-down power system in the PSCAL at the Georgia Institute of Technology and (2) the smart grid energy system in NEC Laboratories America, Inc.

Chapter 6 presents the feasibility study of the setting-less component protection scheme with three-phase, two-winding, variable-tap, and saturable-core transformers.

Finally, Chapter 7 concludes this research work and presents remaining tasks to be completed in future.

There are three appendices at the end of this dissertation.

Appendix A presents two innovative methods for deriving the device model: (1) the quadratic integration method and (2) model quadratization.

Appendix B describes how to model the PV array in the standard form of device models.

Appendix C presents the component dynamic model of the three-phase, two-winding, variable-tap, and saturable-core transformer, which is used for the setting-less component protection scheme.

CHAPTER 2

LITERATURE REVIEW AND BACKGROUND INFORMATION

2.1 Overview

The ultimate goal of this work is to design architecture and functionality for autonomous operation of the distribution system with DGs by introducing a new concept of state estimation. Therefore, this research work is fundamentally based on the following background:

- The restructured distribution system and newly emerging grid problems,
- The real-time monitoring system and communication,
- State estimation in power systems.

This chapter presents the origin and history of the above topics based on literature survey.

2.2 Evolution of the Electric Distribution System

Since the first centralized power generation and its distribution system were implemented in Edison's historic Pearl Street Station in New York City, the electric power system had evolved in terms of their size and hierarchical structure, and the design of the modern power system was established in the 1950s; the three-phase AC system, the high-voltage power delivery system, and the radial network topology of the distribution system [2], [3]. This hierarchical and passive system architecture has predominated in electric power industries until today during almost 50 years.

In the last decade, however, the traditional power system has been restructured by new end-use devices, availability of renewable energy resources, emerging technology such as IT and power-electronics-interfaced technology, and service requirements in terms of reliability and power quality. This restructuring trend has been focused initially

on the distribution system near the customer side, and thus, various research groups have created new concepts for the restructured distribution system; (1) the intelligrid, (2) the microgrid, and (3) Smart Grid.

- Intelligrid: the intelligrid, which was initiated by the EPRI affiliates, refers to technical architecture that integrates the electric industry with the communication system and computer control [4-7]. The ultimate goal of the intelligrid is to develop advanced applications, automated systems, and integrated systems, which eventually help to manage the power grid in a more efficient and reliable fashion. In fact, for the interface between power systems and customers through communication infrastructure, the intelligrid initiative proposes the Consumer Portal [8], [9], which provides more advanced services to customers including demand response, real-time pricing, theft detection, energy management, outage detection, the DER interface and control, and remote disconnect.
- Microgrid: in an attempt to meet the increasing need for the use of renewable energy resources (e.g., the wind or solar energy), which increases energy efficiency and reduces pollution and green gas emissions, the installation of DGs has been recommended inside or near the distribution system [10]. For the purpose of the full utilization of DGs, the microgrid concept, which combines a cluster of loads and DGs to form a single controllable system, has been introduced [11-13]. One of the most important functions of the microgrid is the islanding mode, which isolates the microgrid from the main grid during disturbance to secure the microgrid from power outage or damage. Indeed, for the purpose of fast response to transients that come from islanding or re-connecting, DGs should be controlled without data communication between the DMS and the DGs. With respect to energy efficiency, however, the microgrid also requires the data communication [14-16]; for example, centralized control based on data

communications can discriminate critical and non-critical loads to perform automated load shedding.

- Smart Grid: in the modern distribution system, highly interconnected and aging power grids are too sensitive to small changes, and thus, various grid problems occur in aspects of stability, reliability, and efficiency. For example, in case of the 2003 blackout of the northeastern United States and the southeastern Canada, the localized disturbance caused the cascade failures of the entire power grid, making 50 million people out of power and costing 6 billion dollars [17]. In an attempt to provide solution to the modern grid problems, the academia, industry, and government pay attention to the concept of Smart Grid [17-20], which aims for the self-healing, economical, and cleaner grid by means of digital technology, IT, and communication systems. Therefore, Smart Grid can fully utilize the information data of the grid, thereby making it possible to perform various applications such as demand response, real-time pricing, peak-load reduction, volt/var control, automation, power quality, and cyber security. Furthermore, all these applications of Smart Grid, including existing and emerging technologies, can be integrated to make significant synergy effects in solving present grid problems.

The common and main interests of the intelligrid, the microgrid, and Smart Grid lie in the distribution system, and they encourage customer-side participation in grid operation and control using real-time operational data through the communication network. Moreover, in the new grid concepts, DGs based on renewable energy resources are recommended to be located near the distribution system to enhance network stability and reliability, grid efficiency, and power quality. The main reason for increasing concern about the distribution system is that in situations where the demand is increasing continuously and where distribution assets (e.g., electric lines, distribution transformers, and protective equipment) are aging, the solution approach from the distribution side is

more achievable and effective than that from the centralized generation or the transmission side.

Ironically, the new approaches (e.g., the intelligrid, the microgrid, and Smart Grid) to solve grid problems make the distribution system more complex and unpredictable. Indeed, the use of DGs and residential power generations enables customers to generate electric power and then to deliver it back to the grid. Thus, the operation and control of this bidirectional power flow requires the two-way metering system, rewarding policies, and new contracts. Moreover, according to the vehicle-to-grid concept, the clusters of PHEVs can act not only as power demands but as supply-side resources [21-23], and therefore, grid operators or electric utilities need to establish deliberate operating strategies and policies.

The following sub-sections deal with three grid problems that are newly emerging in the restructured distribution system: (1) protection gaps in the distribution system, (2) operation and control of DGs, and (3) need for short-term operational planning.

2.2.1 Protection Gaps in the Distribution System

In the electric power industry, power system protection is one of the most important areas because faults in the power system not only cause power outages that make millions of people out of power service but damage power components by flowing huge fault currents [24]. As the scale of the power system become massive, cascading outages occur over the wide area of the system, causing significant economical loss.

For example, the transformer is one of the most essential components in the power system, for it increases the efficiency of power transmission by stepping up or down the voltage level. However, once a transformer breaks down, high fault current that is generated from the transformer can overwhelm the entire power system, seriously damaging other devices. Therefore, from the perspective of power system protection,

system operators should detect any internal fault of the transformer and isolate it from other parts of the system within few milliseconds.

Among various transformer protection methods, the overcurrent relay and the differential relay have been widely used. As depicted in Figure 2.1, the overcurrent relay monitors three-phase winding currents through CTs and trips breakers if the monitored currents exceed a certain threshold.

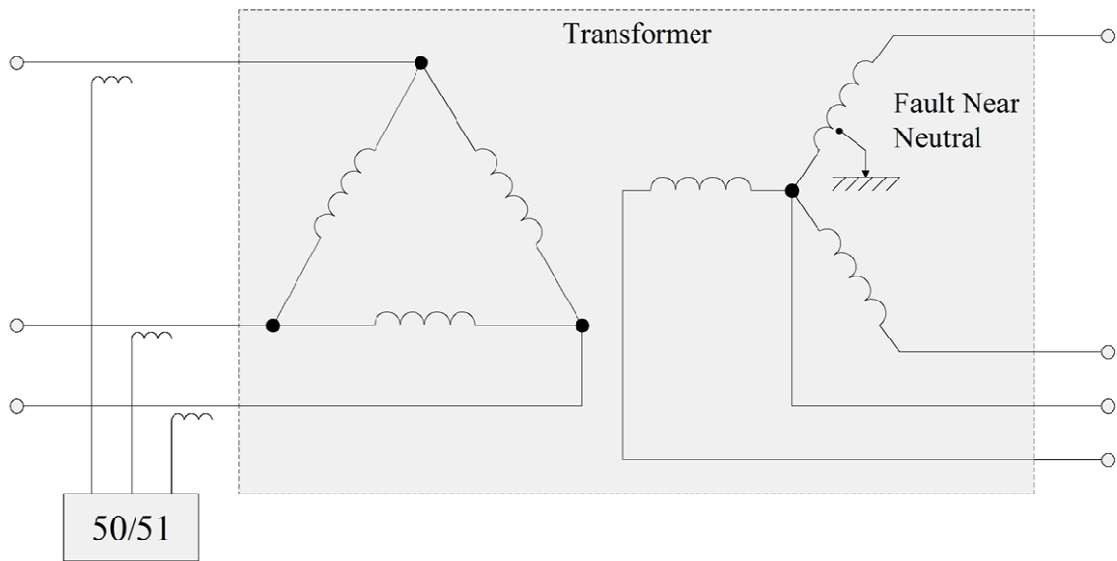


Figure 2.1: Overcurrent relay scheme.

In addition, Figure 2.2 illustrates the differential relay scheme and its configuration with CTs; the letters *R* and *O* represent the restraint coil and the operating coil, respectively. Similar to the overcurrent relay, the differential relay monitors the currents of both sides of the transformer and trips breakers if the ratio of the operating current to the restraint current exceeds a specific quantity.

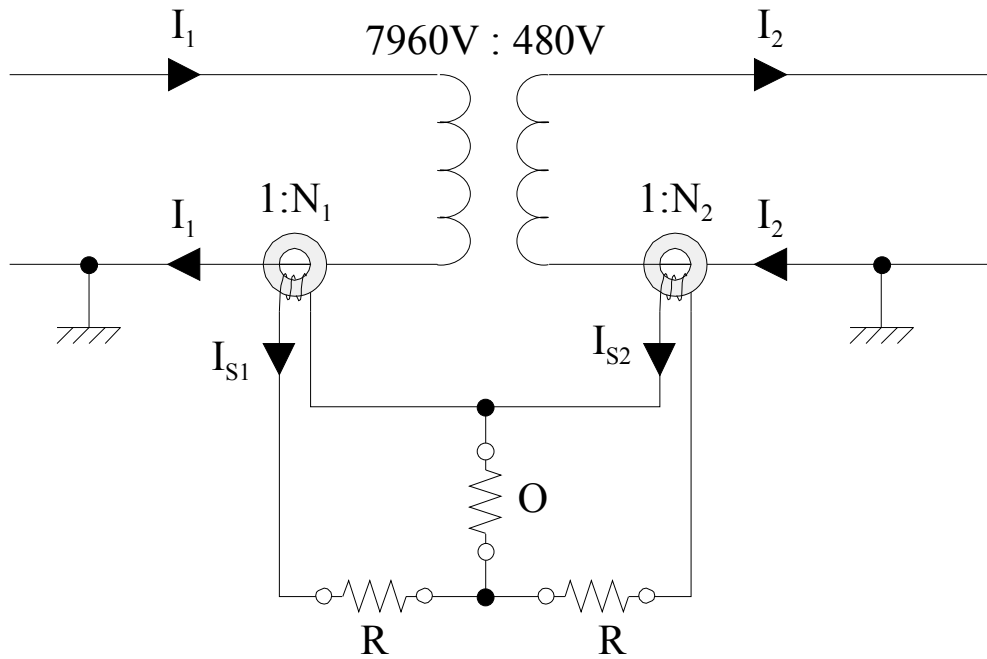


Figure 2.2: Differential relay scheme.

Like the overcurrent relay and the differential relay aforementioned, the traditional schemes of transformer protection have been based on monitoring a specific quantity or quantities (currents and voltages) and acting when the quantity or quantities enter a specific area. However, this approach has limitations because a specific quantity or quantities do not always represent the condition (i.e., health) of the component under protection. For example, when a transformer is energized, the inrush current can flow through windings. Although such flow is the normal operation of the transformers, the overcurrent relay can mistake the high inrush current for the fault current [25]. This kind of relay misoperation can also occur in the differential relay because of the high inrush current that appears on the operating coil.

False relay operations have been major challenges in transformer protection, and thus, many protection algorithms [25-27] that increase security have been developed; examples of such algorithms are time-delay settings in the differential relay, the desensitization of relays during the inrush condition, the consideration of voltages, the harmonic-restraint method, waveform-shape identification, and the dwell-time method.

Nevertheless, these algorithms are insecure because they sometimes fail to identify the inrush current because of improper relay settings. Moreover, the algorithms sometimes compromise dependability or speed according to relay settings.

Moreover, traditional protection methods based on large fault currents could be more severe in the restructured distribution system with a number of inverter-interfaced DGs. Unlike conventional rotating generation units, which generate extremely high fault currents when short circuit occurs, inverter fault currents are typically limited by silicon devices, thus generating about twice rated currents [28-32]. Especially, this relatively low fault current of inverters could be critical when the distribution system operates in the islanded mode because the traditional overcurrent relay may not operate even in the event of short circuit. Therefore, this protection gap requires a new protection scheme that can detect the low fault current. There were several researches to solve this protection gap [30], [32], but they require relay settings and coordination between relays. In addition, when it comes to dynamically changing network topology, the settings and coordination is no longer applicable. In conclusion, new philosophy of protection that is more adaptive than traditional protection methods is required.

2.2.2 Operation and Control of DGs

With increasing concerns about energy consumption and sustainable energy, DGs such as PV arrays, wind farms, fuel cells, and micro-turbines have drawn global interest. Typically, the small-scale DGs are interconnected with main power grid at lower voltages in the distribution system, bringing many advantages:

- High energy efficiency: in general, DGs based on renewable energy resources can be located close to demands, thus minimizing power loss in the transmission system. Additionally, combined heat and power can increase energy efficiency by using heat emitted by the power plant.

- Reduced emissions: unlike traditional fossil fuels, renewable energy resources can reduce the emission of green house gas such as carbon dioxide, sulfur dioxide, and nitrogen oxides.
- Uninterruptible power supply: high penetration of DGs to the grid enables the islanding operation, where the DGs can autonomously support the local power demands, ensuring reliable power supply to critical loads, where interruptible service is unacceptable (e.g., hospitals or traffic signals).
- Reduced investment: demand-side installation can save the investment for building the transmission and distribution system.

Although DGs have numerous advantages as previously mentioned, their operations are not always optimized. In fact, the amount of daily energy production from DGs varies with several environmental conditions such as the intensity and duration of insolation; the wind's speed, direction, and duration; and temperature. Furthermore, grid disturbances such as voltage drops or faults can severely affect the operation of DGs. For example, DFIG-based wind turbines can experience overcurrents in the rotor windings because of the voltage dip in the grid. Accordingly, the well-designed and effective scheme for the operation, control, and protection of the grid is required to maximize the utilization of DGs. Such operation and control scheme should be able to pull out maximum power from distributed energy resources even during the constant variation of environmental conditions. Moreover, the protection scheme should guarantee reliable operation of DGs by minimizing the effect of the grid disturbance on the DGs.

It is necessary to note that the operation, control, and protection scheme depends on plant-specific characteristics (i.e., the type of energy resources). For instance, the PV cell has nonlinear characteristics between the operating voltage and current as shown in Figure 2.3, and there is a maximum power point that generates maximum available power from the solar energy as depicted in Figure 2.4. Note that in Figure 2.3 and Figure 2.4,

the subscript mp, sc, and oc represent maximum power, short circuit, and open circuit, respectively.

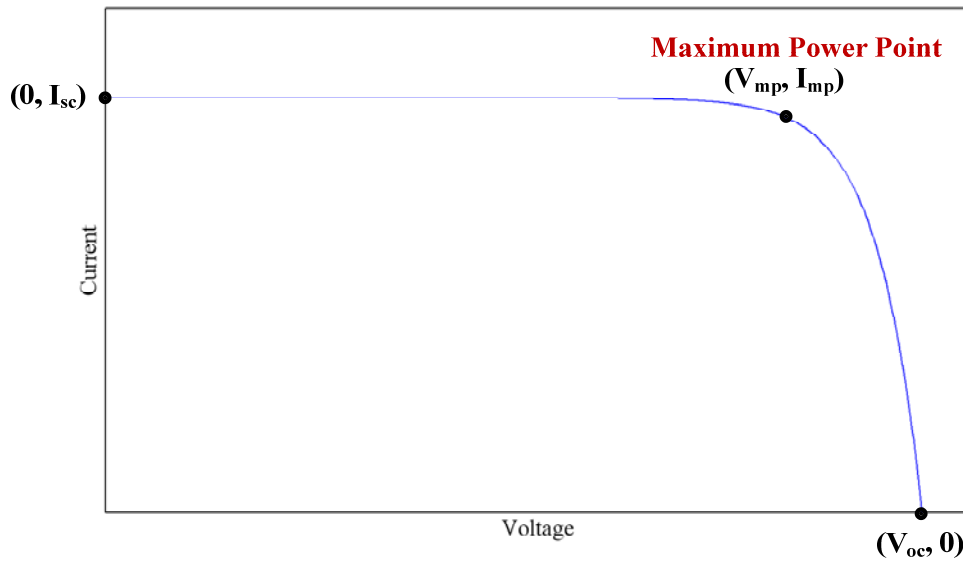


Figure 2.3: I-V characteristics of a PV cell.

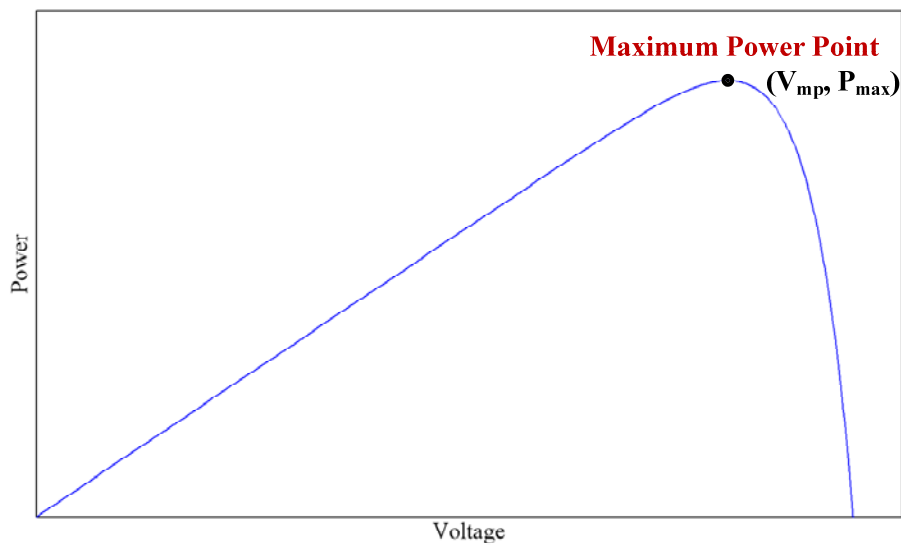


Figure 2.4: P-V characteristics of a PV cell.

The nonlinear I-V curve, however, is severely affected not only by the temperature of PV cells but also by solar irradiation. This behavior can be explained by experimental data shown in Figure 2.5 and Figure 2.6. Therefore, to pull out the maximum power from the PV generation, the control system should be able to track the

maximum power point every moment and control the PV system to operate at the maximum power point.

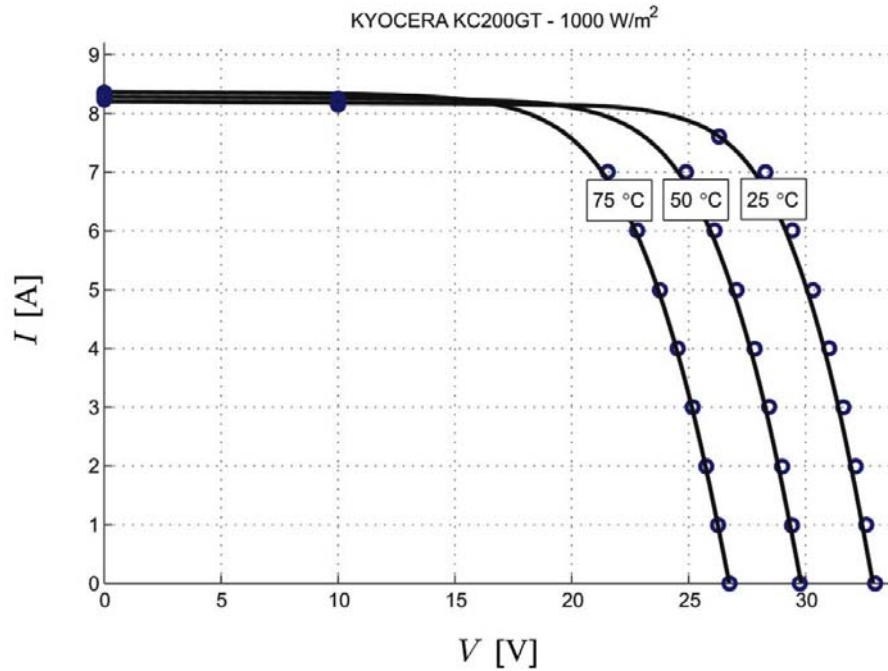


Figure 2.5: I-V curves from experimental data at different temperatures [33].

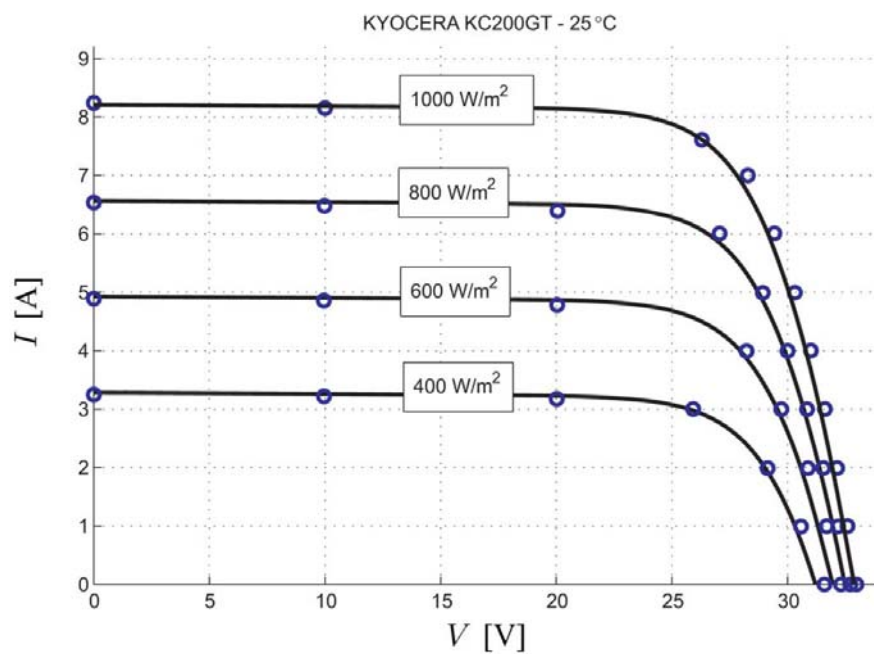


Figure 2.6: I-V curves from experimental data at different irradiances [33].

As another example, the wind turbine generator also has its own specific characteristics. As illustrated in Figure 2.7, the optimal mechanical speed (i.e., generator speed) that pulls out the maximum available power from the wind energy depends primarily on the wind speed. For example, DFIG-based wind turbine can track the optimal speed by controlling the generator speed within its speed limit, which is shown in Figure 2.7 with a red line.

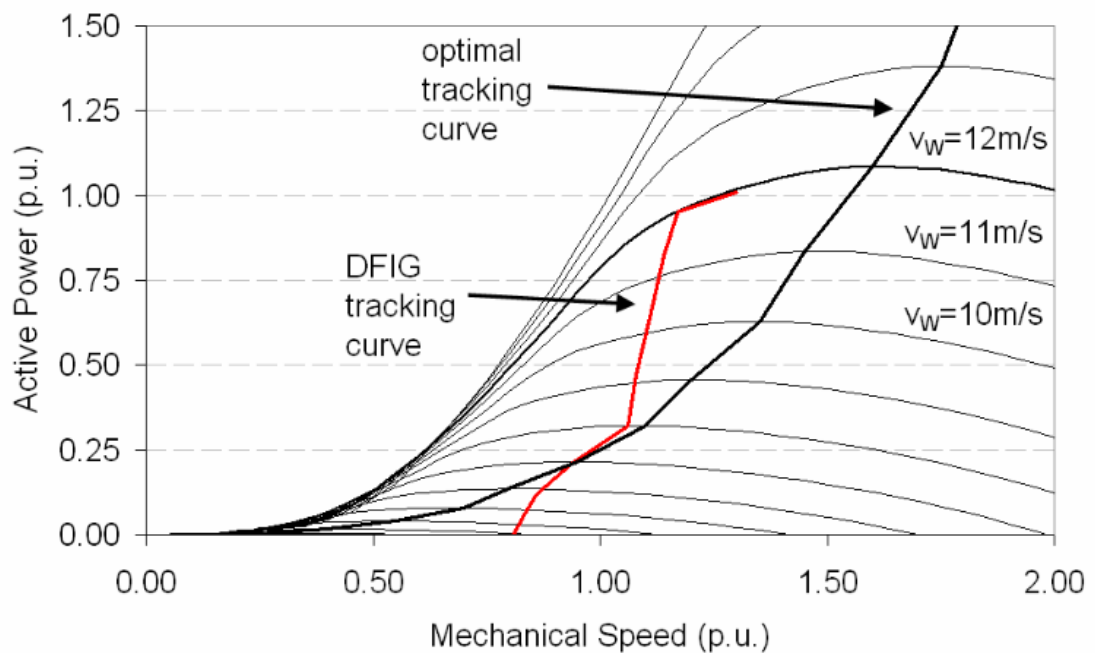


Figure 2.7: MPPT of the DFIG-based wind turbine [34].

As discussed so far, each DG requires its own optimized scheme of management (i.e., operation, control, and protection) that takes into account the plant-specific characteristics of distributed energy resources. With the increasing penetration of DGs in distribution systems, the most efficient and economic way to manage the DGs is by distributed and autonomous operation and control because it is almost impossible for the central control center to manage all DGs, which are dispersed over the wide area. In other words, local entities (i.e., local distribution systems) have the right and duty to manage their local DGs based on local information. As a result, operation, control, and protection

scheme of DGs can be determined inside the local boundary without knowing the entire system.

2.2.3 Need for Short-term Operational Planning

Operational planning, one of the most essential and complex processes in the electric power system, aims at energy balance between electricity supply and demand at any moment of time, and therefore, it requires deliberate scheduling and adequate dispatch. While the scheduling is a process that determines the amount of power that will be produced by each generation unit in future to meet forecasted power demand, the dispatch is a mechanism that calibrates balance between power supply and demand every second based on the reference values of active and reactive power determined by the scheduling. Actually, with the advent of the deregulated energy market, in which utility customers such as grid operators can choose whether to buy power from existing utilities or to use DGs inside the grid, utilities bid and sell their output power to grid operators, and thus, operators require an optimization that minimizes the total operating cost from the economic point of view. This optimization eventually determines the scheduling of the hourly energy production of each generation unit and the amount of power that is imported from or exported to the main grid.

In general, operational planning can be divided into three parts: short-, medium-, and long-term based on the time period that the scheduling takes into account in anticipating power supply and demand. Normally, while long-term planning deals with from one year to one month, short-term planning does from one week to one day. When it comes to the distribution system with high penetration of DGs, the time scope of short-term operational planning is becoming shorter and shorter (e.g., 15 minutes). This near-real-time span is due to time-variant characteristics of DGs. For example, the instant variance of environmental conditions (e.g., solar irradiation, the wind speed, and the wind direction) affects maximum power availability by changing operating points of DGs.

Moreover, the need for the shorter time scope of operational planning arises from the increased uncertainty of power demand such as the intermittent charging of multiple PHEVs.

In the end, to achieve such short-term (i.e., near-real-time) operational planning, operation should be localized and autonomous because autonomous planning in the localized distribution system is more rapid, efficient, and economic than the centralized one, which covers operation of the entire system. Indeed, grid operators in the local distribution system may pay attention to the scheduling and dispatch inside their own local territories. In other words, based on the energy price that utilities bid, autonomous operational planning determines the hourly energy production of each generation unit that resides inside the local distribution system and the amount of power that will be imported from or exported to the main grid; this transaction between the local distribution system and the main grid can save the operating cost of the local system, guaranteeing reliable operation of the system.

The following sub-sections describe the general operating cost of generation units and formulation of the economic-dispatch problem.

2.2.3.1 Operating Cost of the Generation Unit

Given a set of generating units and the electric load, economic dispatch calculates schedules of the generation units that will minimize the overall operating cost while satisfying the power balance among electric loads, losses, power that is exported to or imported from the main grid, and power generated by DGs. The total operating cost can be computed by summing the operating costs (i.e., generating costs) of all the units as follows:

$$C = \sum_{i=1}^n f_i(P_{gi}), \quad (2.1)$$

where P_{gi} is the real power output of the unit i , $f_i(P_{gi})$ is the production cost of unit i operating at power P_{gi} , and n is the number of units committed for production. Note that ultimate goal of economic dispatch is to minimize the total operating cost, C .

For example, in case of a thermal power plant, the operating cost of a unit, $f_i(P_{gi})$, is represented approximately by a quadratic function in terms of P_{gi} as follows:

$$f_i(P_{gi}) = a_i + b_i P_{gi} + c_i P_{gi}^2 \quad (\$/hr), \quad (2.2)$$

where a_i , b_i , and c_i are the coefficients and can be estimated from measurements of real power outputs.

2.2.3.2 Optimization Problem of Economic Dispatch

The generation scheduling problem for economic dispatch is formulated as an optimization problem that is stated as minimization of the total operating cost while meeting constraints. To formulate mathematical equations, typically, the optimal power flow method is used. In this method, variables in the power flow equations are divided into control variables, u , and state variables, x . The solution of an optimization problem determines the control variables, which are, then, provided to each DG controller as optimal reference of power generation. Mathematically, the optimization problem can be stated as follows [35]:

$$\min J = F(u) = \sum_{i=1}^n (a_i + b_i P_{gi} + c_i P_{gi}^2), \quad (2.3)$$

subject to

$$g(x, u) = 0 \quad (2.4)$$

$$h(x, u) \leq 0 \quad (2.5)$$

$$u_{i,\min} \leq u_i \leq u_{i,\max} \quad (i = 1, 2, \dots, n) \quad (2.6)$$

where

$$u = [P_{g1}, P_{g2}, \dots, P_{gn}]^T, \quad (2.7)$$

u is the vector of the output powers of generating units that are controllable; $F(u)$ is the function of total operating cost; x is the vector of system states; $u_{i,min}$ is the minimum available power of the i -th generation unit; $u_{i,max}$ is the maximum available power of the i -th generation unit; n is the number of generation units; equation (2.4) is the equality constraints such as power flow equations; and equation (2.5) is the inequality constraints such as voltage constraints, circuit flow constraints, and network constraints.

In a restructured distribution system that has multi-operational models such as normal operation or islanded one, the objective function and constraints are varying with its mode. In fact, some operational modes such as the islanded or grid-assistant mode happen accidentally, and thus, the objective function and constraints should be updated in accordance with change of the operation mode [36]. In this sense, short-term operational planning is more recommendable than medium- or long-term one in the restructured distribution system with multi-operational modes.

2.3 Real-time Monitoring System and Communication

Operation, control, and protection of the highly interconnected power system primarily depend on the real-time monitoring system that can generate real-time operating conditions of the system. For example, independent system operators keep monitoring operating conditions such as power flow over the generation and transmission system to balance electricity supply and demand. Additionally, in the substation, protective relays continuously monitor voltages and currents at a high sampling rate to detect fault currents and operate protective devices (e.g., circuit breakers) as soon as possible. Moreover, the real-time monitoring system can be useful in terms of asset management, for the asset management system can estimate loss of life of assets such as transformers or circuit breakers based on real-time measurement data.

In fact, the data communication system plays an essential role in facilitating the real-time monitoring system. High-speed and reliable data transmission enables rapid

collection of a large amount of data, contributing to timely decision making. However, the monitoring system at the early stage used low-speed communication media such as RS-232 standard, thus suffering from high time latency taken in data collection and process. Moreover, communication standards that were initially used in the electric power industry were non-unified and vendor-specific, and therefore, the additional cost was incurred for the monitoring system to communicate through various standards. In addition, performance of old-fashioned computers was too poor to be utilized in analysis of the highly interconnected and complex power system.

In an attempt to improve the real-time monitoring system, various high technologies have been adapted, and new standards have been established. First of all, development of high-performance micro-processors and a large-size memory drastically reduces the time to compute the solution regardless of complexity and size of the system, enabling a single device to perform multi-functions including monitoring, protection, and control. In addition to high-performance micro-processors, the IP network protocol, the Ethernet standard, and the LAN technology, which have been mostly used in the area of computer networks, have brought tremendous benefits to data communication in the electric power industry [37], [38]; faster data integration, fewer communication lines, and the WAN technology. Recently, unified communication standards such as IEC61850 [39] and IEEE C37.118 [40] provide interoperability between multi-vendor devices, minimizing or eliminating the use of protocol converters.

With the advent of cutting-edge technologies, the real-time monitoring system begins to be applied to the electric power industry. For example, the SCADA system [41-43] is a centralized management system that can monitor and control the power system. The SCADA system consists of a master station and a number of RTUs, which are usually located in the substation, communicating with the master station in the control center. In general, the RTUs collect measurement data of the substation using sensors (e.g., ammeters, voltmeters, speedometers, and flow meter) and send them to the master

station at a high refreshing rate so that the master station can monitor the overall power system on a real-time basis. As a result, the master station can keep aware of operating conditions of power systems under monitoring, which can be displayed graphically via the human machine interface. The final stage of SCADA system is the centralized control scheme; the master station sends command signals to RTUs to control power equipment such as circuit breakers, switches, tap changers, valves, motors, and actuators.

In the meantime, advances in the communication system inspire development of the WAMS for situational awareness of the interconnected power system over the wide areas. The WAMS has been successfully implemented in the western interconnection of the power system of North America over three decades, and then, the 2003 blackout in the eastern interconnection of North America highlights the urgent need for the deployment of the WAMS [44]. The main advantages of the WAMS are the synchronized phase measurement using the GPS and phasor-data concentration through phasor data concentrators, which can provide accurate measurements based on time synchronism. Moreover, while the measurement interval of SCADA is between 1s and 10s, that of the WAMS is less than 200ms, and therefore, the WAMS is more suitable for the real-time control system. Finally, the WAMS provides numerous benefits for reliable power system operation; voltage and frequency stability, power oscillation, and temperature monitoring of transmission lines [45].

Unlike the substation and the widely interconnected power system, structure of the traditional distribution system was simply radial, passive, and hierarchical. Therefore, the data communication system and the DMS are still in their infancy. For example, only passive protective devices such as reclosers, sectionalizers, and fuses, which can operate without communication in case of fault conditions, are installed. However, with emerging grid concepts such as the intelligrid, the microgrid, and Smart Grid, the new power-electronics-interfaced devices (e.g., PHEVs and DGs) and various smart meters begin to be introduced in the distribution system, which, as a result, becomes more meshed, active,

and bidirectional than before. Thus, development of the data-acquisition and control system has become urgent issues for reliable and efficient operation of the distribution system.

For example, Smart Grid proposes to extend the use of smart meters down to the distribution transformers (e.g., pole- or pad-mounted transformers) and even to the customer side, eventually constructing the AMI [46], [47]. By means of these meters, which support two-way communication among the DMS and customers, the DMS can collect real-time data available to be utilized for real-time pricing, load profiles, and asset management. Such real-time prices, which are provided to customers, can affect their pattern to use electricity. Furthermore, data communication through the AMI can be the cornerstone of distribution automation; a sufficient amount of grid data can be integrated in an instant, and then, control commands are sent to the corresponding components in the distribution system without any manual operation.

In conclusion, the real-time monitoring system based on the communication infrastructure is a key component of operation, control, and protection of the power system, and therefore, it has developed in substations and wide-area power systems that are highly interconnected to one another. Now, the real-time monitoring system needs to be applied to the distribution system because power-electronics-interfaced devices and smart devices, which have recently been introduced, make the distribution system more complicated and dynamic.

2.4 State Estimation in Power Systems

The most basic information for many electric power system applications such as optimal power flow, security assessment, and load forecasting is current operating conditions of the system. Traditionally, operating conditions of the power system are normally defined with complex voltage phasors at all buses or nodes [48]. Occasionally, the system frequency, the magnetic flux linkage, the magnetizing current, and the rotor

speed can be used to define operating conditions. All these numeric values that form the operating conditions are referred to as state variables. Largely, there are two types of state variables: external state variables and internal ones. While voltages of buses or nodes are external states, variables that are confined in one device are internal states.

The state variables are primarily based on measuring units or sensors in the field. In the substation, RTUs collect measurements through PTs or CTs and then send them to the central control center. Recently, IEDs have been introduced to facilitate acquisition of measurements. Finally, the raw measurement data in the central control center are processed to generate operating conditions of system (i.e., state variables). However, some measurements may be corrupted with the measurement error, communication noise, and data loss, and therefore, the measurement data may not always be trustable. These inaccurate data can lead to misoperation of power systems.

In the context of data confidence, application of state estimation to the power system was first proposed by Fred Schweppe et al. in 1960's [49-51]. The idea is to extract, from redundant measurements, optimal state variables that best approximate to the mathematical model of the system. More specifically, the goal of state estimation to obtain the best estimate of state variables base on measured quantities, and for this purpose, maximum likelihood estimation, which is based on the statistical approach, has been used [52]. This approach assumed that measurement errors are distributed within a well-known distribution such as Gaussian distribution, and then, the likelihood function can be constructed by the joint probability density function for all measurements. Eventually, optimal state variables can be obtained by making the likelihood function be maximized, and this objective function can be converted to the minimization problem of the sum of normalized residuals squared, which are differences between measurements and expected values.

Initially, Fred Schweppe et al. addressed static state estimation in which all state variables consist of voltage phasors with an assumption that the power system operates in

the steady state, so all voltage and current waveforms are purely sinusoidal with the constant frequency. Another assumption of conventional static state estimation is that all power circuits are balanced and three-phase, and all series or shunt devices are symmetric in three phases. Such balanced operation and symmetric system enables to simplify the three-phase power system to the single-phase positive-sequence equivalent circuit, thereby reducing the computational burden when state estimation is performed over the large power system.

However, the real world is much different from these balanced and symmetric conditions. The actual power system operates not in perfectly balanced conditions but in slightly unbalanced conditions. Furthermore, it is impossible for components of the electric power system (e.g., transmission lines and customer-side loads) to be symmetric since impedances of any phases cannot be same as those of other phases. As a result of unbalanced operation and asymmetric system structure, state estimation based on the single-phase positive-sequence equivalent circuit produces biased results [53-55], which deteriorates the accuracy and convergence performance of state estimation. Indeed, the negative effect of biased results increases with the system size [53]. In other words, the more buses and power injections (e.g., generators and loads) the power system has, the more errors the results of state estimation contain.

Another sources for the biased state estimation is measurement errors [53], [55]. In fact, the sensor with a totally different scale can generate the error. Moreover, instrument transformers such as PTs and CTs never have unity frequency response to the phasor magnitude and the phase angle, and thus, harmonic frequencies can make measurements incorrect. In addition, the error can originate from phasor data that are extracted from the analog signal; even tiny frequency deviation from nominal frequency causes incorrect phasor computation. The other source that causes measurement errors is long cables that connect between the instrument transformer and the sensor because the

long distance can attenuate signal intensity. Time non-synchronism (i.e., time skewness among measurements) can be the source of the measurement error.

With an attempt to eliminate the impact of biased state estimation, new algorithms and technologies have been introduced; the three-phase state estimation, time synchronism, and merging units. The three-phase state estimation, which is based on three-phase measurements and the exact model of three-phase circuits, can achieve a great improvement in terms of the accuracy and performance of state estimation [56-59]. The accuracy of the phase angle can be enhanced by GPS synchronization [60-62], which minimizes time skewness among measurements in different locations. It should be noted that time synchronism is more stressed in the WAMS. The merging unit, an analog-to-digital converter that is detached from the relay, is usually located near the instrument transformer of the substation and send digitized data to relays through data communication, thereby reducing the attenuation of signals, which is induced from long cables [63].

Finally, state estimation in the power system was usually used in the transmission system. In contrast, the distribution system were not monitored nor controlled because of the structural simplicity of the distribution network and the cost of installing sensors, so state estimation was not required in the distribution. However, with the advent of DGs, PHEVs, and various smart meters, need for monitoring and controlling the distribution system is increasing. As a result, development of state estimation for the distribution system has become one of important issues in operation, control, and protection of the distribution system. Undoubtedly, the distribution electric network is more unbalanced and asymmetric than the transmission system, and therefore, three-phase state estimation needs to be implemented [64].

2.5 Summary

This chapter summarizes the origin and history of the proposed research work in terms of (1) the restructured distribution system and new grid problems, (2) real-time monitoring system and communication, and (3) state estimation in power systems. As the distribution system is restructuring with new introduction of DGs, power-electronics-interfaced devices, and new technologies, the new grid problems has been emerging with respect to protection gaps, high penetration of DGs, and need for short-term operational planning. Therefore, to solve these grid problems in the restructured distribution system, new philosophy of operation, control, and protection is required based on the real-time monitoring system, the communication system, and accurate operating conditions that state estimation provides in real time.

In an attempt to provide the guideline for advanced operation, control, and protection of the restructured distribution system, this research work designs the architecture and functionality for autonomous operation of the distribution system with DGs, which consists of (1) autonomous state estimation and (2) applications that enables autonomous operation from three points of view: setting-less component protection, instant-by-instant management, and short-term operational planning. The next step is to verify the proposed approach in two ways: (1) experimental tests of the proposed autonomous state estimation using laboratory test systems and (2) feasibility study of the setting-less component protection with numerical simulation.

CHAPTER 3

AUTONOMOUS STATE ESTIMATION

3.1 Overview

This chapter, first, introduces the motivation and concept of autonomous state estimation and then explains fundamental requirements with respect to data collection and data types. Finally, the detailed algorithm of the autonomous state estimation is presented.

3.2 Motivation of the Autonomous State Estimation for the Distribution System

Introduction of renewable energy resources, electrical vehicles, and storage has restructured the distribution system, transforming the passive and radial system into an active and dynamic one. For instance, the operational characteristics of a PV or wind-turbine generation system depends on environmental conditions (e.g., the intensity of insolation, the wind's speed, or temperature), which change every second or minute. In a microgrid that consists of dispatchable DGs (e.g., gas-turbine generators and batteries), non-dispatchable DGs (e.g., PV panels and wind-turbine generators), and PHEVs, the operational planning should be implemented in a short term due to increased uncertainty from variable renewable energy and the intermittent charging of PHEVs. Moreover, the microgrid has multi-operational modes (e.g., the grid-connected, islanded, and assistant mode), and each mode has its own operation and control scheme. In general, the mode switches according to the conditions of the main grid or the microgrid.

In fact, the operation and control of this restructured distribution system, which is dynamic and unpredictable, must be driven by the real-time operating conditions within the system. For this reason, the need for state estimation to extract the real-time operating condition of the system arises. State estimation has not been applied to these systems

before for a variety of technical reasons. This research work proposes an approach that enables fast execution of the state estimation process, and it is executed autonomously without the need for human operators. This new approach for state estimation is named as autonomous state estimation [65]. The new method has two major advantages: (1) it provides the validated model for each device in the system (as opposed to the traditional state estimator that provides the bus voltages and works with transmission lines and transformers only), and (2) the autonomous state estimator executes very fast – several times per second. The new method is described next.

The autonomous state estimation can provide real-time operating conditions in an autonomous fashion using high-speed data communication. The basic concept is to collect all information from all available devices inside the distribution system under management and then use the integrated data for general state estimation. This research work presents three types of data acquired from devices for the autonomous state estimation: (1) connectivity, (2) device models, and (3) measurements. The connectivity data indicate the location of devices so that their connection to or disconnection from the grid can be detected and identified by the local DMS. The device model data are mathematical equations that represent the equivalent circuit of electric devices, and the measurement data refer to numeric quantities measured by sensors.

Based on connectivity and device models, autonomous state estimation identifies state variables and then integrates all device models, forming a model for the entire system. Using the integrated device model and the measurements streaming into the autonomous state estimator, general state estimation is performed. A series of these processes should be repeated whenever real-time streaming data comes in, which, in turn, produces real-time operating conditions of the local distribution system. This frequent repetition also makes it possible to detect grid reconfiguration caused by smart devices plugged-in or unplugged. The overall concept of autonomous state estimation is summarized in Figure 3.1.

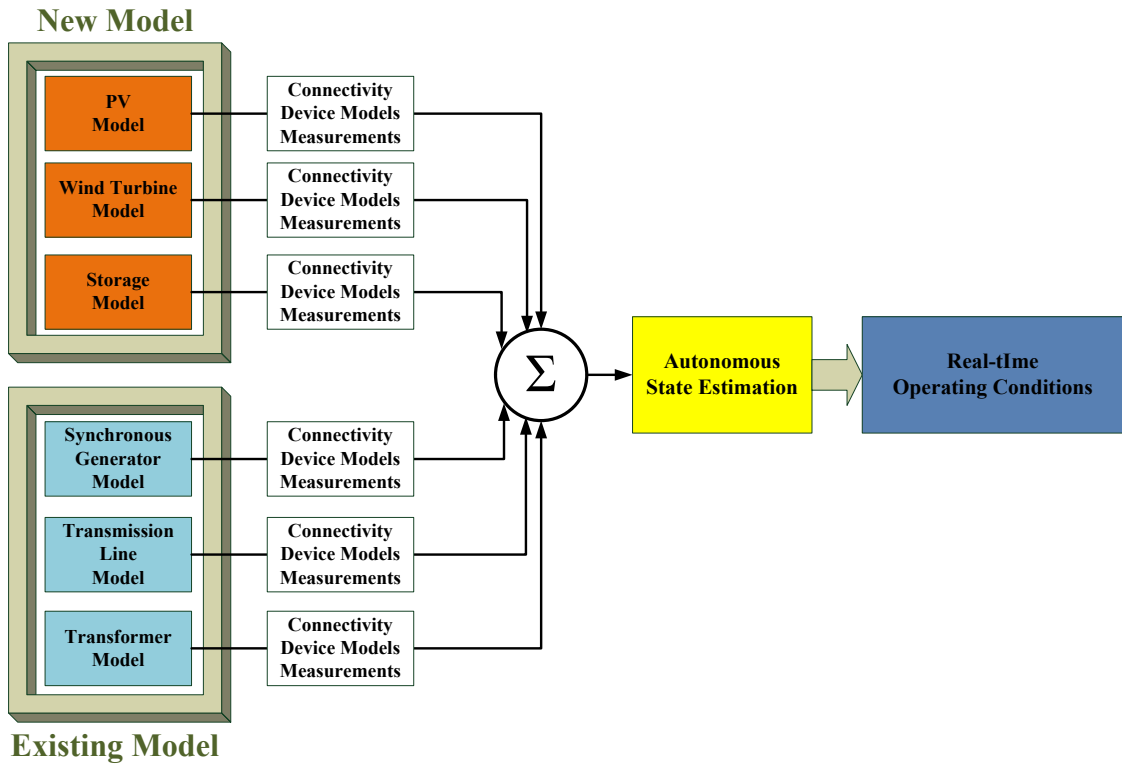


Figure 3.1: Overall concept of autonomous state estimation.

3.3 Requirements for the Autonomous State Estimation

The following sub-sections describe three requirements to implement autonomous state estimation: (1) communication infrastructure, (2) data-acquisition units and UMPCUs, and (3) the three types of essential data.

3.3.1 Communication Infrastructure

An essential prerequisite for autonomous state estimation is the high-speed data-communication infrastructure, which enables the fast collection of information including measurement data (e.g., voltages, currents, active powers, and reactive powers) and device-model data. Based on the information collected, the autonomous state estimation can provide real-time operating conditions. As a matter of fact, the faster the data communication, the faster situational awareness over the local distribution system the DMS can achieve.

In fact, the fast situational awareness enables the plug-and-play capability in the grid operation. For instance, when a PHEV is newly plugged into the local distribution system, if PHEV-model data are immediately sent to the local DMS while real-time measurement data start streaming to the DMS, the DMS can recognize the newly-plugged PHEV and perform timely actions for the operation and control of the PHEV. In addition, whenever the operational mode of a device (e.g., the charging or discharging mode) is changed, the model data of the device should be updated immediately through data communication. Otherwise, autonomous state estimation would be based on the wrong model data, thereby generating bad operating states.

All in all, autonomous state estimation based on the high-speed data communication increases situational awareness over the distribution system, providing the plug-and-play capability, which eventually facilitates the distributed and autonomous operation of the distribution system.

3.3.2 Data-acquisition Units and UMPCUs

The autonomous operation of the distribution system, fundamentally, requires the data-acquisition and communication system that enables to monitor the operating conditions of the grid. Therefore, this research work proposes to place any data-acquisition units (e.g., meters, relays, recorders) or UMPCUs near most of electric devices in the entire area of the grid for the purpose of data collection and control as illustrated in Figure 3.2; note that the UMPCU is a device that is capable of monitoring, protecting, controlling a device under supervision. These data-acquisition devices or UMPCUs generate various data (e.g., measurement data and the operational status of devices under supervision) and send them to the local DMS. Then, based on the data collected from all available UMPCUs, the DMS determines how to operate, control, and protect the distribution system and then takes proper actions by sending control signals to UMPCUs or controllers.

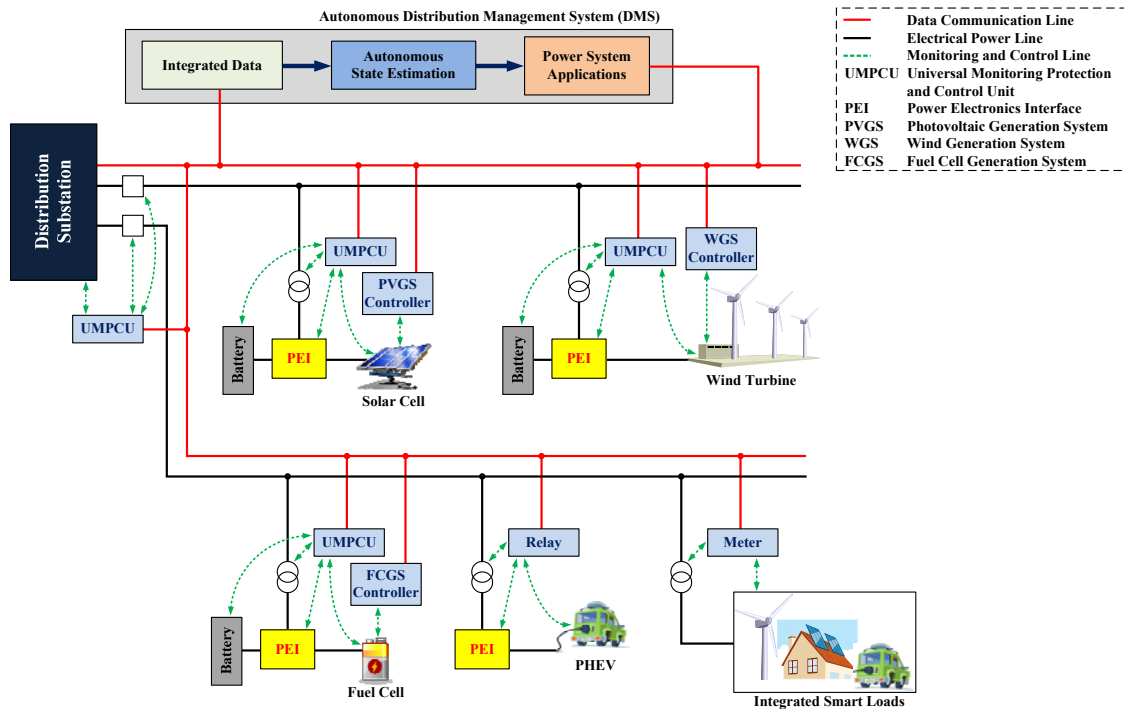


Figure 3.2: Autonomous operation of the distribution system.

As shown in Figure 3.2, any data-acquisition units or UMPCUs are normally deployed at every device in the distribution system and continuously communicate with the DMS through the communication infrastructure. As an illustration, when a new DG (e.g., a solar panel or a wind turbine generator) is connected to the local grid, data-acquisition units or UMPCUs first notify to the local DMS the newly-connected DG along with the connectivity information of the DG. Then, the devices measure the various quantities of the DG in real time and also provide the explicit device model of the DG.

In more details, as described in Figure 3.3, the UMPCU not only collects typical measurement data (e.g., voltages, currents, breaker status, or model measurements) but also senses the changes of models or connectivity on a real-time basis. Based on connectivity, device models, and measurements, the UMPCU can perform a component protection scheme that includes the process of dynamic state estimation, chi-square test, and protection logic. From the estimated dynamic states, which is calculated from the dynamic state estimation, quasi-static states can be extracted using phasor computation

and then sent to the autonomous DMS. Note that measurements are tagged with GPS time signals from a GPS antenna for the purpose of time synchronism. In principle, any IEDs can be programmed to provide the same functionality as the UMPCU.

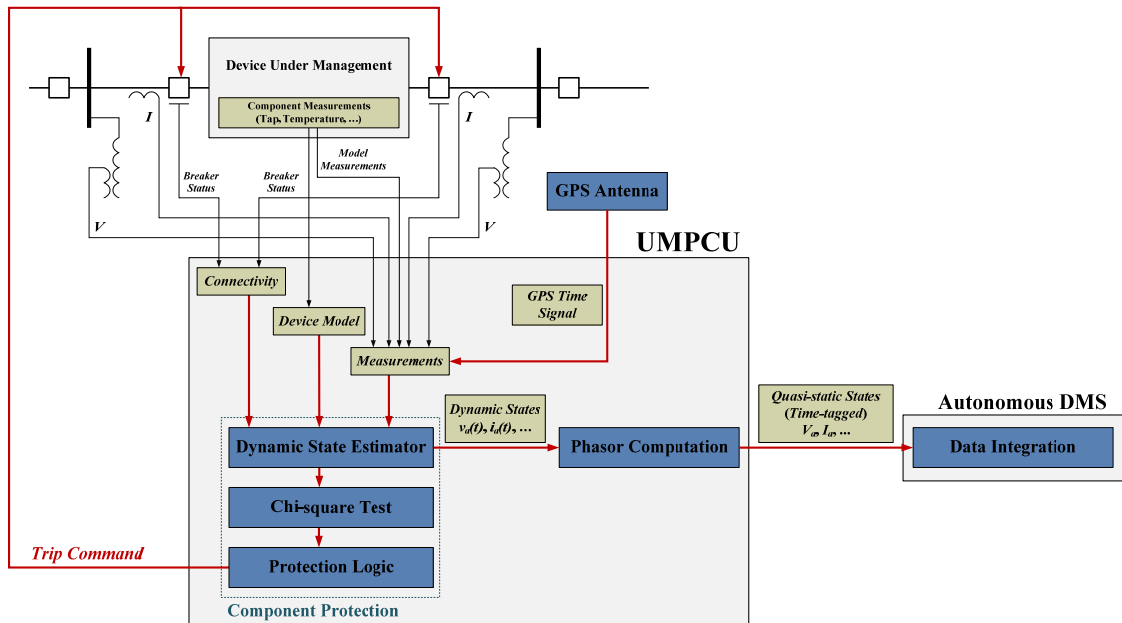


Figure 3.3: Close-in view and functionality of the UMPCU.

In contrast to the UMPCU, normal data-acquisition units (e.g., meters, relays, or recorders) do not typically support the component protection function but have the capability to send the three types of essential information (e.g., connectivity, device models, and measurements) to the autonomous DMS, which is followed by autonomous state estimation and power system applications. The close-in view and functions of the data-acquisition units are described in Figure 3.4.

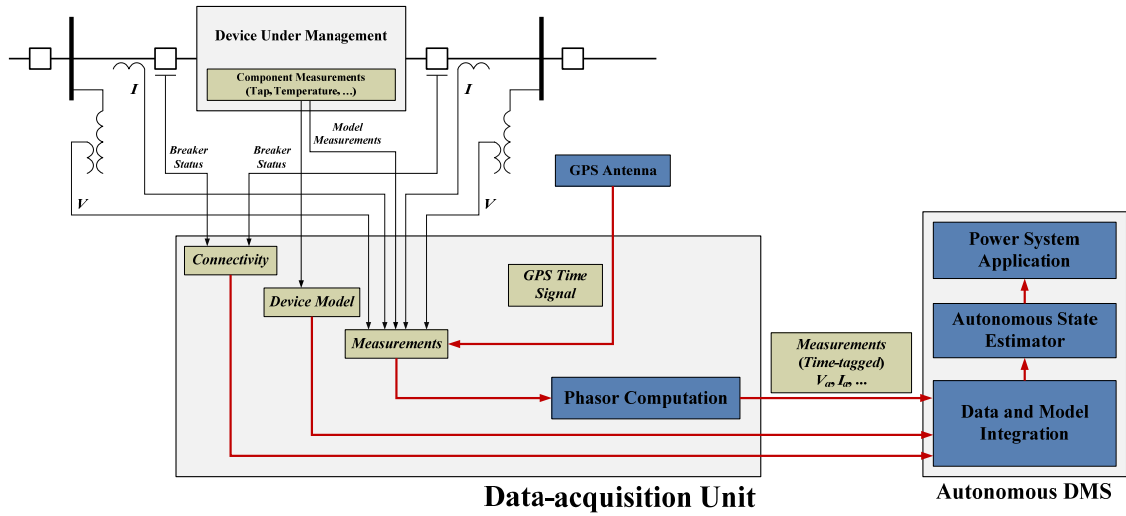


Figure 3.4: Close-in view and functionality of the data-acquisition unit.

Based on data from UMPCUs and other data-acquisition units, the local DMS extracts the real-time model of the system via autonomous state estimation. Having the real-time model, a number of applications can be performed related to optimization and management of the system. As an example, the real-time model can be used to determine optimal allocation of reactive power resources so as to levelize the voltage profile for the present operating conditions. Similarly, one can compute the optimal policy for using storage devices, scheduling the charging of PHEVs, or controlling the use of non-critical appliance. The applications of the real-time model of the distribution system can be numerous, depending on the specific characteristics of the system.

In summary, UMPCUs or data-acquisition units play a pivotal role in supplying essential data (e.g., connectivity, device models, and measurements) required for autonomous state estimation, which produces the real-time operating conditions of the grid. Furthermore, UMPCUs not only control grid operation but protect it from unwanted fault situations, and such control and protection can finally achieve the autonomy of the distribution system.

3.3.3 Three Types of Essential Data

To implement autonomous state estimation, the three types of data are proposed: (1) connectivity, (2) device models, and (3) measurements. Each data-acquisition unit or UMPCU has its own three sets of data from electric devices under supervision and provide them to the local DMS.

3.3.3.1 Connectivity

Connectivity data are related to points (e.g., buses or nodes) where devices are connected to the grid. The names of these points should be unique; the naming convention may include the company name, the asset name, or the UMPCU name. Connectivity data are utilized for the local DMS to autonomously identify the locations of electric devices in the distribution system. Therefore, when a new device is initially plugged into the distribution system, a data-acquisition unit or a UMPCU sends the connectivity data of the device to the DMS by exception. Whenever the connecting buses or nodes change, connectivity data should be sent to the DMS again.

3.3.3.2 Device Models

Device (i.e., component) model data are the mathematical models of devices that express the relationship among voltage, current, and other quantities that are required to describe the states of the devices. For interoperability, the mathematical model should be expressed in a standard form. In other words, the standard form can be used to facilitate the autonomous creation of the measurement model, which describes the relationship among measured values and state variables and finally used for state estimation.

The proposed autonomous state estimation uses the quasi-static model, which neglects electrical transients but captures other dynamics. Indeed, the frequency of the system may change as generators oscillate, but over the period of the measurement (e.g., two cycles), voltages and currents can be expressed as phasors. As a result, the device

model can be represented by a set of complex equations and differential equations as expressed in equations (3.1) and (3.2), respectively:

$$0 = g(\tilde{I}, \tilde{V}, y), \quad (3.1)$$

$$\frac{dy(t)}{dt} = f(\tilde{I}, \tilde{V}, y(t), t), \quad (3.2)$$

where \tilde{I} is the vector of current phasors, and \tilde{V} is the vector of voltage phasors, $y(t)$ is the internal states including mechanical or magnetic variables, and t is the current time. These equations can be transformed into a set of complex and real algebraic equations, which can be linear or quadratic, using a numerical integration method. The proposed approach uses the quadratic integration method, for this method has no numerical oscillation compared to the trapezoidal integration method [66]. Moreover, in case of the nonlinear device, the device model may be defined by high-order polynomial equations and differential equations. In this case, model quadratization can be applied [67], [68], generating the model whose order is no more than two.

Conceptually, the standard form of device models can be derived as follows: first, complex and differential equations that describes the device behavior needs to be developed. Then, the equations are quadratized based on model quadratization; in case of nonlinearities of higher order, additional state variables are introduced to reduce the nonlinearities to order not higher than two. Subsequently, the quadratized equations are integrated using the quadratic integration method, finally providing a standard ACF that consists of complex and real algebraic equations. Equation (3.3) represents the standard form of device models:

$$\begin{bmatrix} \tilde{I} \\ 0 \\ 0 \end{bmatrix} = \begin{bmatrix} K_1 \\ K_2 \\ K_3 \end{bmatrix} + \begin{bmatrix} L_{11} & L_{12} & L_{13} \\ L_{21} & L_{22} & L_{23} \\ L_{31} & L_{32} & L_{33} \end{bmatrix} \begin{bmatrix} \tilde{V} \\ y(t) \\ y(t_m) \end{bmatrix} - \begin{bmatrix} N_{11} & N_{12} \\ N_{21} & N_{22} \\ N_{31} & N_{32} \end{bmatrix} \begin{bmatrix} 0 \\ y(t-h) \end{bmatrix} + \begin{bmatrix} f_1(t) \\ f_2(t) \\ f_2(t_m) \end{bmatrix}, \quad (3.3)$$

$$f(t) = \begin{bmatrix} f_1(t) \\ f_2(t) \\ f_2(t_m) \end{bmatrix} = \begin{bmatrix} \vdots \\ \tilde{V}^T & y(t)^T & y(t_m)^T \\ \vdots \end{bmatrix} Q_i \begin{bmatrix} \tilde{V} \\ y(t) \\ y(t_m) \end{bmatrix}, \quad (3.4)$$

$$K = \begin{bmatrix} K_1 \\ K_2 \\ K_3 \end{bmatrix}, \quad (3.5)$$

$$L = \begin{bmatrix} L_{11} & L_{12} & L_{13} \\ L_{21} & L_{22} & L_{23} \\ L_{31} & L_{32} & L_{33} \end{bmatrix}, \quad (3.6)$$

$$N = \begin{bmatrix} N_{11} & N_{12} \\ N_{21} & N_{22} \\ N_{31} & N_{32} \end{bmatrix}, \quad (3.7)$$

where K is the constant vector; L and M are the device-model matrices; h is the integration time step; t_m is the intermediate time (i.e., the half point in the interval, $[t$ to $t-h]$); $f(t)$ is the vector of the quadratic nonlinear terms; and Q_i are the quadratization matrices. It is also important to note that the complex equations in equation (3.3) are converted into real equations by substituting all complex variables with their real and imaginary parts and then separating the real and imaginary parts of the resulting equations.

To derive the device model, this research work proposes two innovative methods: (1) the quadratic integration method and (2) model quadratization. The quadratic integration method converts differential equations to the standard form of device models, which is equation (3.3), and the model quadratization reduces the nonlinearity. Further explanation of these two methods is provided in APPENDIX A, and an example of deriving the device model from the PV array is represented in APPENDIX B.

It is important to note that the device model does not change with time unless the device experiences structural changes such as the tap changes of transformers. Thus, the device model is sent to the DMS whenever a device is newly plugged into the distribution system or whenever device models change.

3.3.3.3 Measurements

One of roles of UMPCUs and IEDs is to measure physical quantities such as voltage, current, and temperature with high sampling rate, typically more than 2.4ks/s (i.e., kilo samples/second). The sampled values are utilized to extract other information, such as the frequency, the rate of change of the frequency, and the phasor. More specifically, actual measurements in the field are categorized into two types: the across measurement and the through measurement. Examples of across measurements and through measurements are the voltage measurement and the current measurement, respectively.

3.4 Implementation of Autonomous State Estimation

It is necessary to note that autonomous operation in the distribution system should be based on highly trustable data to prevent false control actions. Therefore, state estimation, which can extract accurate operating conditions from measurements and device models, is required. To meet the requirements of the autonomous operation of the distribution system, this research work proposes autonomous state estimation, which evolves from conventional state estimation. Based on the real-time communication system, raw data are collected to the DMS, where the autonomous state estimator is installed. Once the DMS receives the three sets of data (i.e., connectivity, device models, and measurements) from all available UMPCUs or data-acquisition units, the autonomous state estimator in the DMS refines the collected data to useful data.

In fact, autonomous state estimation is the combination of state estimation and a robotic process: (1) the role of state estimation is to produce highly accurate operating conditions, and (2) the robotic process is to automatically create system states and build the measurement model for state estimation. Therefore, the local DMS can autonomously integrate device models of local electric devices, forming the measurement model based on device models and measurements. Finally, state estimation uses the measurement model to produce the accurate, operating conditions of the system. The overall approach will be described next.

3.4.1 Integration of Device Models

The key concept of autonomous state estimation is to integrate all available device models of components in the local distribution system, yielding the entire system model. As described in Figure 3.5, the device-model integration is basically based on common points that connect different devices. By sharing the common points, the device models are merged into a system. In general, the local DMS integrates all available device models that are collected from UMPCUs or data-acquisition units through communication infrastructure.

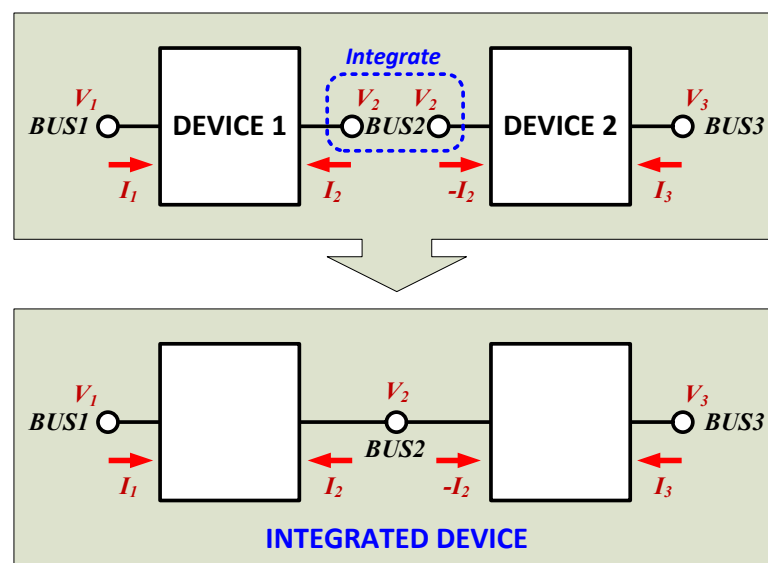


Figure 3.5: Basic concept of the device-model integration.

3.4.2 Definition of State Variable

States refer to a set of variables that completely define the operating conditions of the power system. This research work proposes two types of states: external and internal. While external states are voltage phasors at buses or nodes, internal states are variables that depend on a specific device; examples of internal states are the magnetic flux linkage, the rotor speed, and mechanical power. Unlike external states, internal states can be phasors or real variables. Note that all phasors can be converted into real variables by dividing the phasor (i.e., the complex number) into the real and imaginary part. Typically, external and internal state variables can be defined based on the entire device model integrated from each device model.

3.4.3 Creation of the Measurement Model

This section describes the creation of the mathematical models of measurements (i.e., measurement models). The measurement model is a formula that expresses the relationship among the measured value and state variables. In this research work, four types of measurements are proposed: (1) across measurements, (2) through measurements, (3) virtual measurements, and (4) pseudo measurements. It is important to point out that any measurement can be expressed as functions of state variables and measurement errors, forming the following the measurement model:

$$z = h(x) + \eta , \quad (3.8)$$

where

$$z = [z_1, z_2, \dots, z_r, \dots, z_m]^T , \quad (3.9)$$

$$h(x) = [h_1(x), h_2(x), \dots, h_r(x), \dots, h_m(x)]^T , \quad (3.10)$$

$$\eta = [\eta_1, \eta_2, \dots, \eta_r, \dots, \eta_m]^T , \quad (3.11)$$

z is the vector of measured values, $h(x)$ is the vector of the functions of state variables, η is the vector of measurement errors, x is the vector of state variables, r is the index of a

measurement, and m is the total number of measurements. Note that a measurement can be expressed by state variables via a known function [i.e., one of $h(x)$], so the function is named as the measurement model or the system model.

For the purpose of the automatic process of formulating measurement models, any measurement can be expressed in the following standard format:

$$z_r = h_r(x) + \eta_r, \quad (3.12)$$

$$h_r(x) = c + \sum_i a_i x_i + \sum_j \sum_k b_{jk} x_j x_k, \quad (3.13)$$

where $h_r(x)$ is the function of state variables for the r -th measurement; c is the constant term; a_i are the linear coefficient terms; b_{jk} are the nonlinear coefficient terms (i.e., quadratic terms); x_i , x_j , and x_k are the state variables; and i , j , and k are the indices of summation. Note that the standard form is composed of a measured quantity, a constant term, the linear combination of state variables, the combination of nonlinear terms whose order is no greater than two, and a measurement error.

Generally, the measurement model of across and pseudo measurements can be expressed with simple equations that make a measured quantity equal to the corresponding states or to the linear combinations of two states that correspond to measured buses/nodes. In comparison, the measurement model of through measurements can be extracted from the device model, which is expressed as equation (3.3). The following sub-sections describe how to formulate the measurement model according to the measurement type.

3.4.3.1 Formulation of the Across Measurement Model

The voltage measurement, which is a typical across measurement, measures voltages across two buses/nodes, thus forming the following measurement model:

$$z_r = h_r(x) + \eta_r = x_a - x_b + \eta_r, \quad (3.14)$$

where x_a and x_b are state variables that correspond to two measured points.

3.4.3.2 Formulation of the Through Measurement Model

The current measurement, which is a typical through measurements, is the measured quantity of an electric current with direction. The measurement model of a current measurement can be derived from the device model, which follows the standard form as expressed in equation (3.3), and therefore, the current measurement model is one of the rows of the following ACF, which is part of the standard form:

$$\tilde{I} = K_1 + L_{11}\tilde{V} + L_{12}y(t) + L_{13}y(t_m) + N_{12}y(t-h) + f_1(t). \quad (3.15)$$

Finally, the current measurement model of the r -th measurement can be expressed as follows:

$$z_r = h_r(x) + \eta_r = \tilde{I}^{(k)} + \eta_r, \quad (3.16)$$

where k indicates the k -th row of the vector, \tilde{I} .

3.4.3.3 Formulation of the Virtual Measurement Model

Meter-based actual measurements such as the across or through measurement are not enough for the complete observability of the system, and therefore, virtual measurements, which are intrinsic characteristics of a specific device, should be introduced for making the system observable and providing redundancy.

Similar to the current measurement model, the virtual measurement model can be induced from the device model, equation (3.3). In detail, the following ACFs, which are parts of the standard form of device models, can become the virtual measurement model:

$$0 = K_2 + L_{21}\tilde{V} + L_{22}y(t) + L_{23}y(t_m) + N_{22}y(t-h) + f_2(t), \quad (3.17)$$

$$0 = K_3 + L_{31}\tilde{V} + L_{32}y(t) + L_{33}y(t_m) + N_{32}y(t-h) + f_3(t). \quad (3.18)$$

Finally, all rows in equations (3.17) and (3.18) can be used to formulate the virtual measurement model with the following format:

$$0 = z_r = h_r(x) + \eta_r = Equ(k) + \eta_r, \quad (3.19)$$

where $Equ(k)$ indicates the k -th row of the equation (3.17) or (3.18).

3.4.3.4 Formulation of the Pseudo Measurement Model

The pseudo measurement is not meter-based actual measurement, but it can be created based on theoretically known values. For example, the pseudo measurement is based on the network topology such as Kirchhoff's current law, the individual phase voltage, the neutral/shield wire current, or the neutral-to-ground voltage [69]. Since the pseudo measurement is not a directly measured value, so they are treated as measurements with relatively large standard deviation. In case of a pseudo measurement model that refers to a neutral voltage can be expressed as follows:

$$0 = z_r = h_r(x) + \eta_r = x_k + \eta_r, \quad (3.20)$$

where x_k refers to a state variable that corresponds to the neutral voltage.

3.4.4 **State Estimation**

In general, the number of measurements (i.e., m) is larger than the number of state variables (i.e., n). In other words, the measurement model, equation (3.8), is over-determined set of nonlinear equations, so there is a unique solution for x only if the system model, $h(x)$, is exact and the measurements, z , are thoroughly precise. Nevertheless, this condition is impossible in a real system, so typically, equation (3.8) does not have a solution for x . However, state estimation enables to compute the most likelihood solution by obtaining the best estimates of states that minimize measurement errors [i.e., residuals between system models, $h(x)$, and measurements, z]. The measurement errors can be rearranged as follows:

$$\eta = h(x) - z. \quad (3.21)$$

For simplification, it is assumed that the measurement errors are unbiased and distributed based on the Gaussian distribution with a known standard deviation (i.e., σ). Moreover, the expected mean value of a measurement error is zero, and the measurement

error is uncorrelated with the error of any other measurement. These conditions can be expressed as the following equations:

$$E[\eta_i] = 0, \quad (3.22)$$

$$E[\eta_i^2] = \sigma^2, \quad (3.23)$$

$$E[\eta_i \eta_j] = 0, \quad i \neq j, \quad (3.24)$$

where i and j are the indices of measurements.

Autonomous state estimation is based on the generally used state estimation, the weighted-least-squares method, which minimizes the sum of the weighted squares of residuals as follows:

$$\min \quad J = \eta^T W \eta = [h(x) - z]^T W [h(x) - z], \quad (3.25)$$

where J is the objective function, and W is the weight matrix, which is a diagonal matrix.

The diagonal entries of the weight matrix consist of the inverse of the squared standard deviations of measurement errors:

$$W = \text{diag} \left\{ \frac{1}{\sigma_1^2}, \frac{1}{\sigma_2^2}, \dots, \frac{1}{\sigma_r^2}, \dots, \frac{1}{\sigma_m^2} \right\}, \quad (3.26)$$

where σ_r is the standard deviation of the r -th measurement. The normalized measurement error can be defined as follows:

$$s_r = \frac{\eta_r}{\sigma_r}, \quad (3.27)$$

where s_r is the normalized measurement error of r -th measurement. Then, the weighted-least-squares problem can be re-formulated by an objective function that minimizes the sum of the squares of normalized measurement errors. This objective function can be stated as follows:

$$\min \quad J = \eta^T W \eta = \sum_{i=1}^m \left(\frac{h_i(x) - z_i}{\sigma_i} \right)^2 = \sum_{i=1}^m s_i^2. \quad (3.28)$$

The vector of unknown state variables, x , can be obtained by solving the objective function via a necessary condition that is expressed as follows:

$$\frac{dJ}{dx} = 0. \quad (3.29)$$

As defined in the standard format of measurement models, equations (3.12) and (3.13), the system model, $h(x)$, consists of nonlinear equations. Hence, a solution that satisfies the necessary condition, equation (3.29), is obtained using Gauss-Newton iterative method with an initial guess of state variables (i.e., x^0); note that initial values can be set as state variables that are estimated in the previous time step.

The nonlinear equations of measurement errors (i.e., η) are linearized near the point x^0 as follows:

$$\eta = h(x^0) + \left. \frac{\partial h(x)}{\partial x} \right|_{x=x^0} (x - x^0) + h.o.t - z, \quad (3.30)$$

where *h.o.t* denotes higher order terms. As the vector x^0 is much close to the solution, the higher order terms becomes negligibly small, so terms can be omitted, producing the following equation:

$$\eta = \left. \frac{\partial h(x)}{\partial x} \right|_{x=x^0} (x - x^0) + h(x^0) - z, \quad (3.31)$$

where the Jacobian matrix (i.e., the matrix of all first-order partial derivatives) of the system model is denoted by H :

$$\left. \frac{\partial h(x)}{\partial x} \right|_{x=x^0} = H. \quad (3.32)$$

Moreover, the vector b can be defined as follows:

$$b = Hx^0 - h(x^0) + z. \quad (3.33)$$

Now, equation (3.31) can be expressed as follows:

$$\eta = Hx - b. \quad (3.34)$$

Then, the solution for the vector x can be obtained by solving the necessary condition, equation (3.29):

$$\frac{dJ}{dx} = \frac{d}{dx} \eta^T W \eta = \frac{d}{dx} [(Hx - b)^T W (Hx - b)] = 2H^T W (Hx - b) = 0. \quad (3.35)$$

Thus, the solution can be computed as follows:

$$x = (H^T W H)^{-1} H^T W (Hx^0 - h(x^0) + z) = x^0 - (H^T W H)^{-1} H^T W (h(x^0) - z). \quad (3.36)$$

Eventually, the last equation can be generalized into the following iterative equation:

$$x^{v+1} = x^v - (H^T W H)^{-1} H^T W (h(x^v) - z), \quad (3.37)$$

where v means the v -th iteration, H is the Jacobian matrix of $h(x)$ that is calculated at $x = x^v$, and $(H^T W H)^{-1}$ is the information matrix. All in all, the solution of the state estimation problem can be computed using the iterative method, equation (3.37).

3.4.5 Performance Metrics

The performance of the state estimator is evaluated by the goodness of fit of the model to the measurement data. Indeed, the goodness of fit can be quantified by the confidence level, which is the probability of the fit between measurements and the model. The confidence level can be calculated from the degrees of freedom, ν , and chi-square critical value, ζ . The degrees of freedom can be computed as follows:

$$\nu = m - n, \quad (3.38)$$

where ν is the degrees of freedom, m is the number of measurements, and n is the number of unknown state variables.

Practically, the measurement of a physical quantity of the electric power system is obtained via the instrumentation channel, which can be complex, and thus, the measurement process could contain some error. For simplicity, we introduced a normalized error for a measurement, assuming that the normalized error is a random variable with Gaussian distribution, which has a standard deviation of 1.0 and a cross

correlation of zero. Finally, the chi-square critical value, ζ , can be computed by summing all the squares of the normalized errors of measurements as follows:

$$\zeta = \sum_{i=1}^m \left(\frac{h_i(\hat{x}) - z_i}{k\sigma_i} \right)^2, \quad (3.39)$$

where ζ is the chi-square critical value, \hat{x} is the best estimate of states, and k is the normalization constant. Finally, the confidence level can be obtained as follows:

$$\Pr[\chi^2 \geq \zeta] = 1.0 - \Pr[\chi^2 \leq \zeta] = 1.0 - \Pr(\zeta, \nu). \quad (3.40)$$

The goodness of fit is defined as the probability that the distribution of measurement errors are within expected bounds. The chi-square test is utilized to provide the probability that the expected error of estimated state values will be within a specific range. However, there are many data-acquisition units in any substation with different accuracy, and therefore, the normalization constant, k , needs to be introduced. The variable k can be defined as follows: if k is 1.0, then the standard deviation of each measurement is equal to the accuracy of the meter with which this measurement was obtained. If k is different from 1.0, then the standard deviation of each measurement error equals to the accuracy of the meter times k . The introduction of the variable k allows us to characterize the accuracy of the estimated states with only one variable, which is equivalent of providing an expected error that equals to the variable k times the standard deviation of the measurement error. Figure 3.6 illustrates a k -factor curve that is the parameter k versus the confidence level.

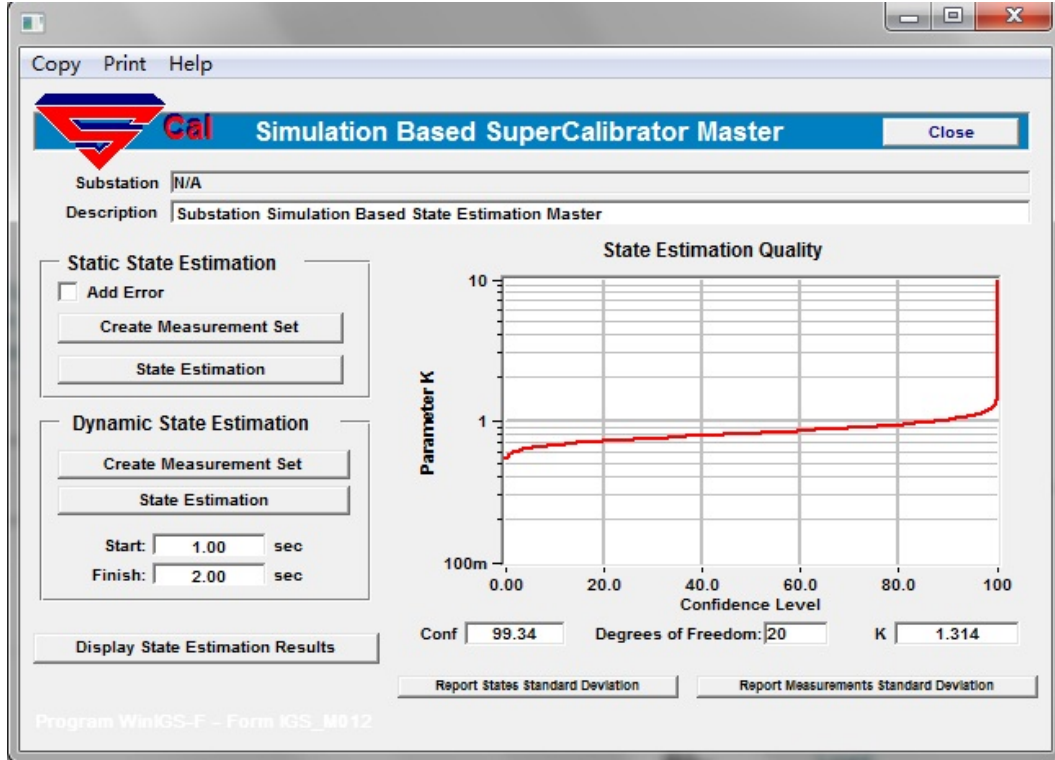


Figure 3.6: Quality evaluation of state estimation based on the chi-square test.

3.4.6 Accuracy of Solution

The accuracy of estimated states is provided by the covariance matrix (i.e., the information matrix), which is expressed as follows:

$$C_x = E[(\hat{x} - \bar{x})(\hat{x} - \bar{x})^T] = (H^T W H)^{-1}, \quad (3.41)$$

where \hat{x} is the estimated states, and \bar{x} is the true but unknown state values. Specifically, the standard deviation of each estimated state is computed as follows:

$$\sigma_{x_i} = \sqrt{C_x(i,i)}, \quad (3.42)$$

where $C_x(i,i)$ is the i -th diagonal entry of C_x . The covariance matrix is also known as the information matrix, for it provides useful information on the expected error of the computed state variables. The information matrix is symbolized with I .

$$I = (H^T W H)^{-1}. \quad (3.43)$$

In summary, the quality of state estimation can be quantified by expressing the validity of measurement data with the confidence level, which is obtained from the chi-square test. In addition, the accuracy of estimated state variables can be expressed by the diagonal entries of the information matrix, which expresses the variance of the state estimates.

3.4.7 Estimation Error of Measurements

The estimated value of measurements can be calculated as follows:

$$\hat{b} = h(\hat{x}). \quad (3.44)$$

Moreover, the statistics of the estimation \hat{b} are computed as follows:

$$E(\hat{b}) = h(\bar{x}), \quad (3.45)$$

$$\text{Cov}(\hat{b}) = E[(\hat{b} - \bar{b})(\hat{b} - \bar{b})^T], \quad (3.46)$$

where \bar{b} is the true values of measurements. The covariance matrix can be substituted using the following equation:

$$\hat{b} - \bar{b} = h(\hat{x}) - h(\bar{x}) = H(\bar{x})(\hat{x} - \bar{x}) \cong H(\hat{x})(\hat{x} - \bar{x}). \quad (3.47)$$

As a result, the covariance matrix can be expressed as follows:

$$\text{Cov}(\hat{b}) = E[H(\hat{x} - \bar{x})(\hat{x} - \bar{x})^T H^T] = H(H^T W H)^{-1} H^T. \quad (3.48)$$

Finally, the standard deviation of measurements can be obtained as follows:

$$\text{Cov}(\hat{b} - b) = W^{-1} - H(H^T W H)^{-1} H^T. \quad (3.49)$$

3.4.8 Bad-data Detection, Identification, and Rejection

In the actual power system, it is possible to have failed meters or relays, generating bad data. Autonomous state estimation, which is based on the concept of the SuperCalibrator [70], detects the presence of bad data, identifies the bad data, rejects the bad data, and issues alarms for the purpose of fixing the problem.

The algorithm of the SuperCalibrator follows the weighted-least-squares method, which minimizes the sum of normalized residuals squared. Furthermore, the performance of the estimator is assessed using the chi-square test, which provides the confidence level, as well as using the computation of the information matrix, which provides the expected accuracy of states. If the results are not acceptable, the process of bad-data identification and rejection is initiated. The SuperCalibrator is based on the detailed model of the power system (e.g., three-phase and breaker-oriented model, instrumentation-channel-inclusive model, data-acquisition-inclusive model), and thus, the bad data identification procedure is much easier and less demanding computationally than the traditional state estimation [61], [62], [69], [71].

In details, detection of the existence of bad data can be achieved with the chi-square test, which computes the confidence level. If the measurements are free of bad data, the confidence level will be high. On the other hand, in the presence of one or more bad data, the confidence level will decrease.

Note that the chi-square test does not indicate which datum or data are bad, and therefore, the identification of bad data can be achieved with other methods to be described next. Bad data can be classified into the following types:

- Bad measurement data: the measurement may contain a very huge error when compared with its actual value,
- Bad status/topology data: the bad data is related with the open/close status of the breaker or switch (i.e., the topology of the system).

The methodology of the identification of bad data normally consists of two steps. In the first step, bad data may be identified by inspection or simple consistency rules. This step identifies the obviously bad data, depending on the system. For example, in the state estimation of the power system, measurements of voltages or power flows are known to have specific ranges. If a measurement is out of this range, it will be classified as a bad measurement or at least as a measurement suspected of being bad (i.e., a suspect

measurement). In the second step, bad data are identified with statistical analysis of the residuals and its effects on confidence level. This analysis depends on the selected method for the solution of the estimation problem. In the case of the weighted-least-squares method, the possible bad data are identified with their large residuals. However, it is known that there are two possibilities: (1) a measurement with a large residual may not be always a bad measurement and (2) a bad measurement may have a very small residual. A rather secure but computationally demanding way to identify a bad datum is by means of hypothesis testing. Specifically, it is assumed that a measurement (or a group of measurements) has been identified as suspect; this characterization may be due to a large normalized residual or because of failure to pass a consistency check. For this purpose, a suspected datum is removed. In other words, the corresponding measurement model (i.e., $z_r = h_r(x) + \eta_r$) is removed from a set of measurement models. Then, the weighted-least-squares solution is computed again, subsequently computing the confidence level. A drastic improvement in the confidence level indicates that the data under consideration is actually bad.

3.5 Process of Autonomous State Estimation

This section describes the procedure of autonomous state estimation. The overall process is summarized in Figure 3.7.

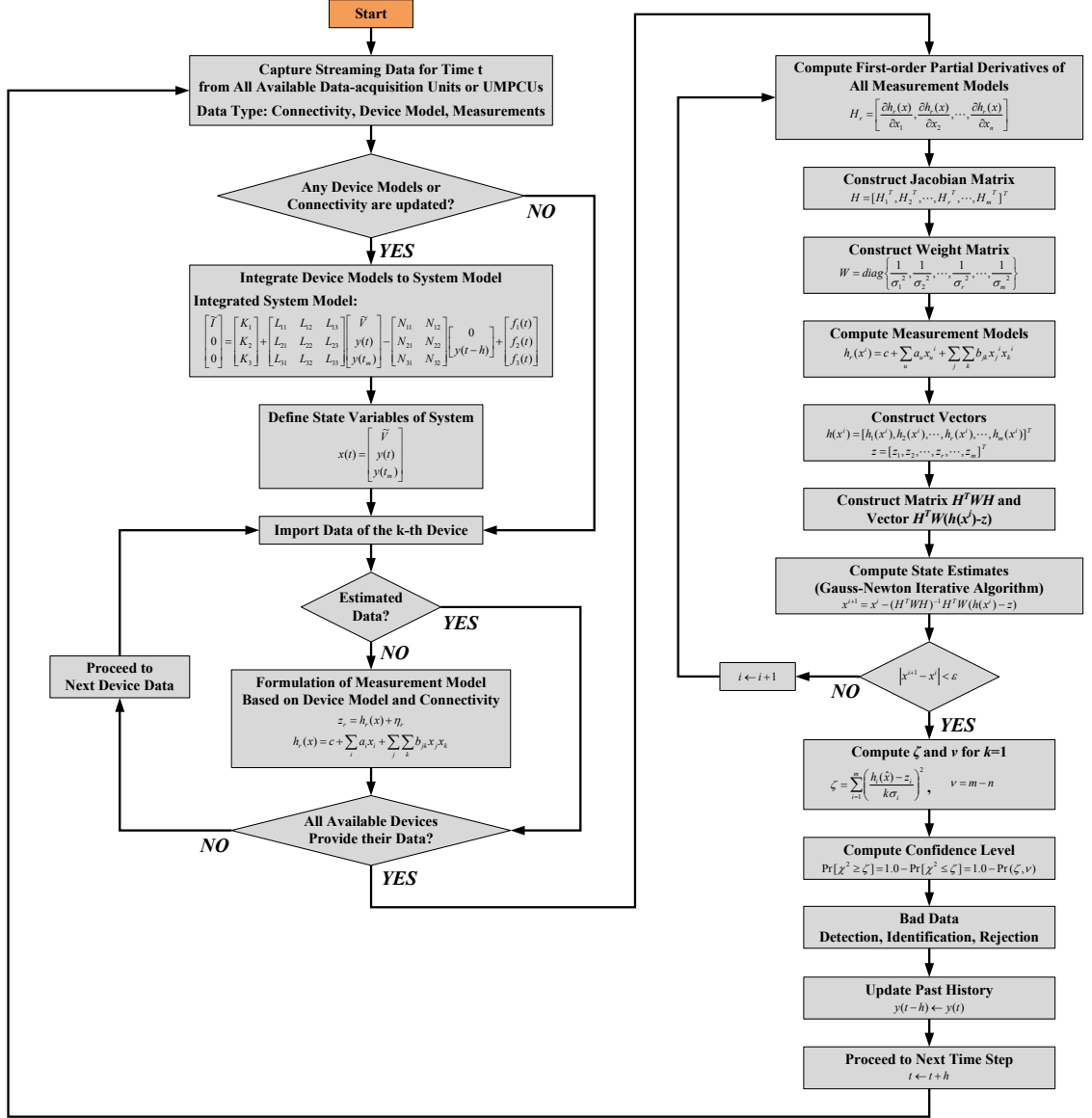


Figure 3.7: Overall process of autonomous state estimation.

As initialization, all state variables are set to zero as follows:

$$\begin{bmatrix} \tilde{V} \\ y(t) \\ y(t_m) \end{bmatrix} = \begin{bmatrix} 0 \\ 0 \\ 0 \end{bmatrix}. \quad (3.50)$$

3.5.1 Step 1: Capture Streaming of All Available Data

Autonomous state estimation is initiated once streaming data (e.g., connectivity, device models, and measurements) from all available data-acquisition units or UMPCUs for a specific instant of time have been completed, and data for the next time interval start streaming in, thereby requiring a buffer system that separates the sets of data at specific intervals. The process of autonomous state estimation at time t is applied on the set of data for a specific time interval, from $t-h$ to t .

3.5.2 Step 2: Update Device Models or Connectivity

Whenever devices are newly connected to the distribution system, or whenever devices change their operational modes, the device models or connectivity of the corresponding devices should be updated. After updating device models or connectivity, the updated device models and other device models need to be integrated again, formulating the integrated system model that is now newly updated. Then, based on the new integrated system model, state variables should be defined. It is necessary to point out that unless any device model or connectivity is updated, there is no need to reintegrate device models and to redefine state variables. The following sub-sections describe the integration of device models and the definition of state variables.

3.5.2.1 Integration of Device Models

All available device models in the DMS at the current processing time, t , are integrated based on the device-model-integration approach, forming a device model that represents the entire model of the distribution system under management. The integrated device model follows the standard form of device models, equation (3.3).

3.5.2.2 Definition of State Variables

In the restructured distribution system, the operational modes of devices or the system topology is continuously changing, and therefore, state variables to be estimated

should be automatically identified before performing state estimation algorithm. Based on the three sets of data (i.e., connectivity, device models, and measurements), relevant state variables are created and named with the connectivity data (in case of external states) or with the device name (in case of internal states). For example, in case of the device model of the PV array described in APPENDIX B, a total of 12 state variables are created as described in equation (B.34).

It is necessary to note that by construction, the overall setup of autonomous state estimation results in an observable state estimator. If there are devices that are not instrumented with any data-acquisition unit or UMPCU, these devices will not provide device information (i.e., connectivity, device models, and measurements), which will not be part of the state-estimation process. This means that the autonomous state estimator has the property of being operational even in case that some devices may not participate in the state-estimation process.

Finally, the automatically created state variables can be defined as follows:

$$x(t) = \begin{bmatrix} \tilde{v} \\ y(t) \\ y(t_m) \end{bmatrix}. \quad (3.51)$$

where \tilde{v} is the vector of all external states (e.g., voltages) of the integrated system, $y(t)$ is the vector of all internal states of the integrated system, t is the current time, and t_m is the intermediate time between one time step, $[t-h \text{ to } t]$.

3.5.3 Step 3: Form Measurement Models

For autonomous state estimation, there are four types of measurements: across, through, virtual, and pseudo measurements. Each measurement can be involved in the process of autonomous state estimation by formulating its own measurement model, which follows the standard format, equations (3.12) and (3.13); note that if a measurement has already been used for any state estimation (e.g., dynamic state

estimation), then there is no need to formulate the measurement model of the measurement as long as autonomous state estimation utilizes state variables computed by the prior state estimation, which is based on the measurement. The formulation of measurement models for autonomous state estimation depends on the measurement type, which is explained in Section 3.4.3.

3.5.4 Step 4: Contribution of Measurements

For the state-estimation process, all measurements, which are across, through, virtual, and pseudo measurements, are formulated into the standard form of the measurement model as described in equations (3.12) and (3.13). Then, all the measurement models are contributed to generate the matrix H^TWH and the vector $H^TW(h(x^i)-z)$, which is described in the following sub-sections.

3.5.4.1 Compute the First-order Partial Derivatives of Measurement Models

The Jacobian matrix, H , consists of the first-order partial derivatives of each measurement model, which is represented as follows:

$$H_r = \left[\frac{\partial h_r(x)}{\partial x_1}, \frac{\partial h_r(x)}{\partial x_2}, \dots, \frac{\partial h_r(x)}{\partial x_n} \right], \quad (3.52)$$

where H_r is the first-order partial derivatives of the r -th measurement model, and n is the number of state variables.

3.5.4.2 Construct the Jacobian Matrix

The Jacobian matrix can be formed with the partial derivatives of all measurements as follows:

$$H = [H_1^T, H_2^T, \dots, H_r^T, \dots, H_m^T]^T, \quad (3.53)$$

where m is the number of measurements.

3.5.4.3 Construct the Weight Matrix

The diagonal entries of the weight matrix, W , consists of the inverse of squared standard deviation of measurements.

$$W = \text{diag} \left\{ \frac{1}{\sigma_1^2}, \frac{1}{\sigma_2^2}, \dots, \frac{1}{\sigma_r^2}, \dots, \frac{1}{\sigma_m^2} \right\}, \quad (3.54)$$

where σ_r is the standard deviation of the r -th measurement.

3.5.4.4 Compute the Measurement Models

With state variables estimated at the i -th iteration (i.e., x^i) the measurement model of the r -th measurement can be computed as follows:

$$h_r(x^i) = c + \sum_u a_u x_u^i + \sum_j \sum_k b_{jk} x_j^i x_k^i. \quad (3.55)$$

3.5.4.5 Construct Vectors $h(x^i)$ and z

The vectors $h(x^i)$ and z can be constructed as follows:

$$h(x^i) = [h_1(x^i), h_2(x^i), \dots, h_r(x^i), \dots, h_m(x^i)]^T, \quad (3.56)$$

$$z = [z_1, z_2, \dots, z_r, \dots, z_m]^T. \quad (3.57)$$

3.5.4.6 Construct the Matrix and the Vector for State Estimation

Based on the Jacobian matrix (i.e., H), the weight matrix (i.e., W), and vectors (i.e., $h(x^i)$ and z), the matrix $H^T W H$ and the vector $H^T W (h(x^i) - z)$ are constructed.

3.5.5 Step 5: Compute State Estimates

The state variables at $(i+1)$ -th iteration can be obtained by the following Gauss-Newton iterative algorithm:

$$x^{i+1} = x^i - (H^T W H)^{-1} H^T W (h(x^i) - z). \quad (3.58)$$

3.5.6 Step 6: Convergent Test

A condition for testing the convergence of the iterative method is as follows:

$$|x^{i+1} - x^i| < \varepsilon. \quad (3.59)$$

In other words, only if all absolute differences between state variables estimated at the $(i+1)$ -th iteration (i.e., x^{i+1}) and those estimated at the i -th iteration (i.e., x^i) are less than a threshold ε , then the iterative method is converged, indicating state variables at the time t are obtained. Therefore, proceed to the next step. However, any differences between state variables at the $(i+1)$ -th iteration (i.e., x^{i+1}) and those at the i -th iteration (i.e., x^i) are larger than the threshold ε , return to step 4 with the following update:

$$i \leftarrow i + 1. \quad (3.60)$$

3.5.7 Step 7: Compute the Chi-square Critical Value, the Degrees of Freedom, and the Confidence Level

State variables estimated are used to check the goodness of fit of the device model to measurements, which can be quantified by the confidence level based on the chi-square test using the degrees of freedom, ν , and the chi-square critical value, ζ .

3.5.8 Step 8: Bad-data Detection, Identification, and Rejection

If the confidence level is high, the estimated state variables are trustable data, so they can be used for the operation and control of the power system. On the other hand, if the confidence level is low, then it is assumed that there are any bad data, thus issuing the identification and rejection process of the bad data.

3.5.9 Step 9: Update the Past-history Values

Before proceeding to the next time step, the past-history value, $y(t-h)$, should be updated with estimated state variables as follows:

$$y(t-h) \leftarrow y(t). \quad (3.61)$$

3.5.10 Step 10: Proceed to the Next Time Step

Proceed to the next time step with the following update:

$$t \leftarrow t + h. \quad (3.62)$$

Then, return to the step 1.

3.6 Summary

This chapter introduces the motivation, requirements, and detailed algorithm of autonomous state estimation. As the distribution system is becoming dynamic and unpredictable with the high penetration of DGs and inverter-based devices, the distribution system is required to be operated and controlled in an autonomous way by the local DMS. For this operation and control, autonomous state estimation can provide real-time operating conditions by means of communication infrastructure, where UMPCUs or data-acquisition units continuously send the local DMS the three types of essential data (i.e., connectivity, device model, and measurements).

The main concept of autonomous state estimation is the integration of the device models of all available devices in the local distribution system, providing the integrated device model, which is then used to formulate measurement models. Based on these measurement models, the weighted-least-squares state estimation, which is a general state estimation algorithm, extracts the accurate operating conditions of the distribution system. With the results estimated, the chi-square test can be performed, thus yielding the confidence level, which is the probability that the normalized residuals are distributed within the expected boundary. If the confidence level is low, then the process of detecting, identifying, and rejecting bad data is applied.

In conclusion, a series of steps that consist of the collection of data, the integration of device models, the automatic formulation of measurement models, state estimation, and performance evaluation is repeated on a continuous basis, eventually providing real-time operating conditions of the dynamic and unpredictable distribution

system, which are ultimately utilized for the autonomous operation and control of the system.

CHAPTER 4

AUTONOMOUS OPERATION OF THE DISTRIBUTION SYSTEM WITH DISTRIBUTED GENERATIONS

4.1 Overview

This chapter describes how to apply autonomous state estimation to the autonomous operation of the distribution system from the three points of view: (1) setting-less component protection, (2) instant-by-instant management, and (3) short-term operational planning.

4.2 Autonomous Operation of the Distribution System

Recently, with the increasing penetration of DGs and power-electronics-interfaced devices, the distribution system requires new management schemes for its autonomous operation, control, and protection. For this purpose, UMPCUs or data-acquisition units (e.g., relays, meters, or recorders) are installed in the local distribution system, continuously monitoring the components of the system and generating the essential data (i.e., connectivity, device model, and measurement). The utilization of these data can facilitate the autonomous operation in two ways: (1) decentralized operation and (2) centralized operation. As described in Figure 4.1, while the decentralized operation can be achieved directly by UMPCUs or generation system controllers, the centralized operation requires the high-speed communication system as well as the local autonomous DMS to which all available UMPCUs or data-acquisition units transmit their own data. In the DMS, the integrated data are filtered by autonomous state estimation, yielding the real-time operational conditions of the local distribution system, which are then used for power system applications such as various optimizations. The optimized results are sent

back to UMPCUs or controllers, which control the distribution system to operate at the optimum points.

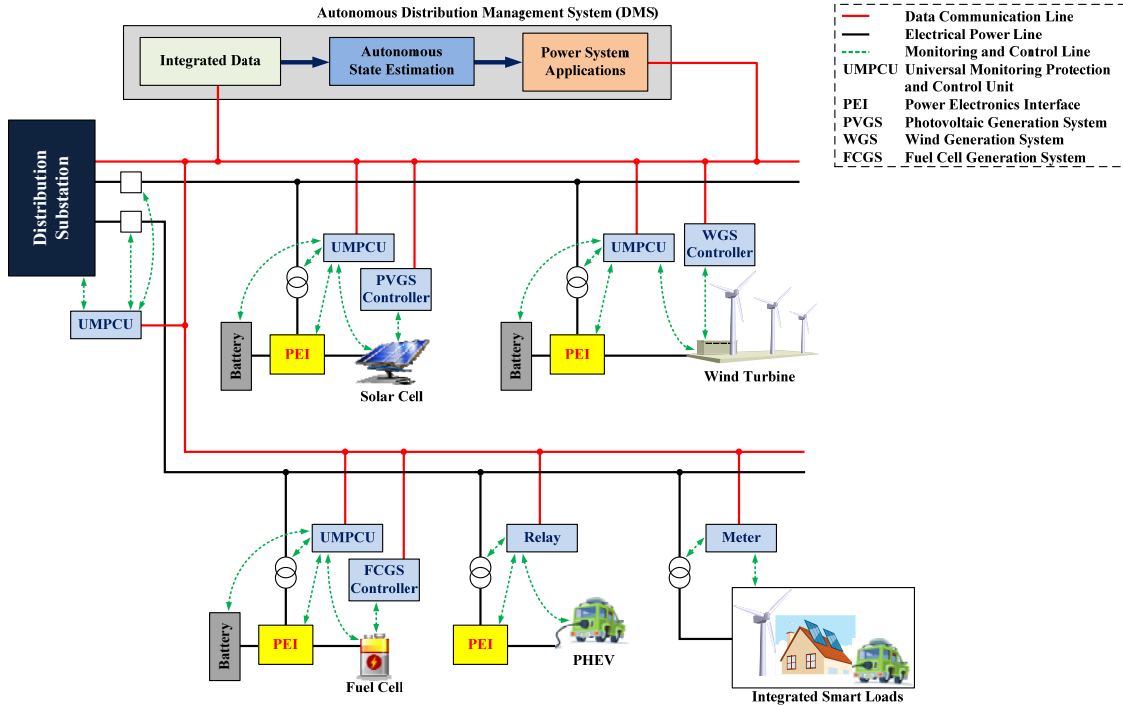


Figure 4.1: Illustration of the autonomous operation of the distribution system.

In general, decentralized operation is based on fast response, so the time interval for this operation is very short (e.g., in several cycles or seconds). In contrast, centralized operation requires data collection from UMPCUs or data-acquisition units through data-communication systems. Hence, the time interval for the centralized operation is relatively longer than that for the decentralized operation.

This research work presents three autonomous operations of the distribution system in terms of the operational time frame: (1) setting-less component protection, (2) instant-by-instant management, and (3) short-term operational planning. As illustrated in Figure 4.2, the function of the setting-less component protection should be performed every few cycles, and the instant-by-instant management is implemented every few seconds. The time intervals for both operations are too short to be taken into account for exchanging data with other components through communication systems, and therefore,

the setting-less component protection and the instant-by-instant management are suited to decentralized operations. In the meantime, the short-term operational planning is performed every few minutes and need to know the overall operating conditions of the local distribution system in advance. As a result, the short-term operational planning should be implemented in the local DMS on a centralized basis.

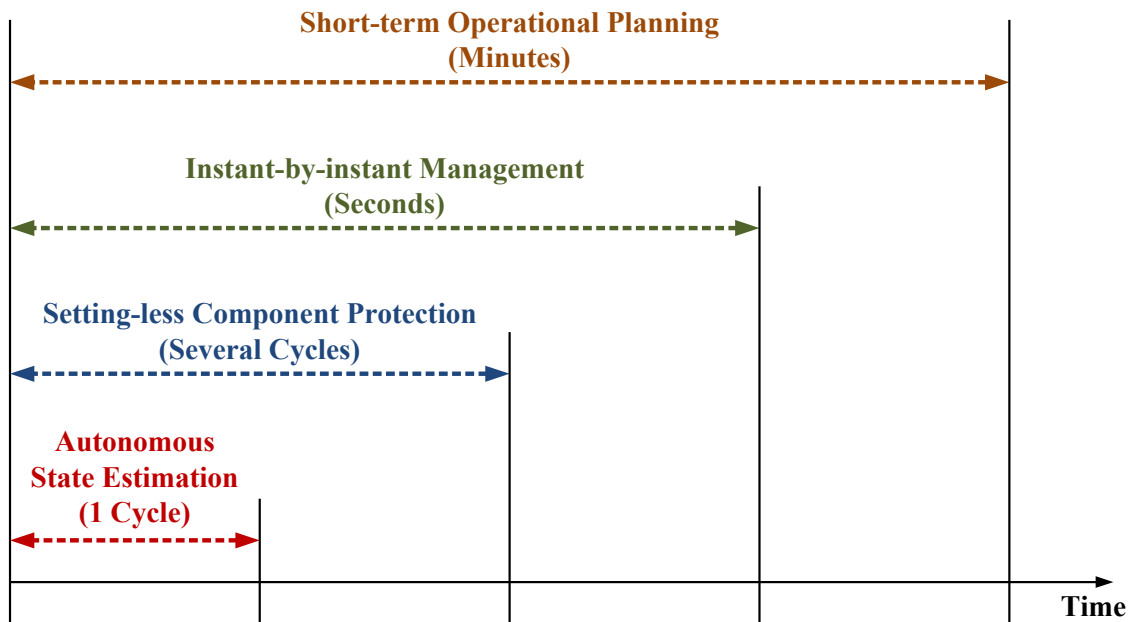


Figure 4.2: Operational time frames of autonomous operations.

In specific, the purpose of setting-less component protection is to protect devices from internal faults of the devices. In contrast to traditional protection methods, which have been based on the complicated coordination of many protection functions, the setting-less component protection scheme uses an adaptive protection method that is based on time-based dynamic state estimation and its performance metrics such as the confidence level, which is the probability that indicates the goodness of fit of component (i.e., device) models to measurement data. Therefore, the setting-less component protection can detect any kinds of internal faults of devices, for the faults certainly change the physical characteristics of the devices. For example, when short circuit occurs inside a device, the equivalent circuit of the device is changed. Such change makes

discrepancy between post-fault measurements and pre-fault component models, which results in the low confidence level.

Meanwhile, DGs or inverter-based devices, which have recently emerged in the distribution system, requires the instant-by-instant management in a decentralized way so as to operate autonomously with fast response to various grid situations. As an example of the instant-by-instant management, the MPPT algorithm can be implemented to enable DGs to operate at maximum available power under ever-changing weather conditions in such a way that the generation system controller regulates the power-electronic interface (e.g., inverters that interface between DGs and the grid). It should be noted that the centralized operation through the DMS is not suitable for the MPPT in two reasons: the first reason is that the MPPT has no need to recognize the operation of the entire grid, and the second one is that the centralized approach increases time latency in data communication between the DMS and UMPCUs.

Finally, the short-term operational planning of the distribution system should be based on centralized operation by means of data exchange through the communication system. Based on the integrated data, autonomous state estimation computes the real-time operational conditions, which are then processed by the optimizer that solves various optimization problems with specific short-term operational purposes such as economic dispatch, reliable operation, and environmental dispatch. Among them, this research work deals with economic dispatch that aims to minimize overall operating cost by properly scheduling dispatchable DGs under the condition that the local distribution system has non-dispatchable DGs (e.g., PV panels or wind turbines), which are, in general, recommended to generate maximum available power using the MPPT control.

4.3 Detailed Scheme of the Autonomous Operation

The detailed scheme of the autonomous operation of the distribution system is described in Figure 4.3. In this figure, all devices including a PV generation system, a

wind-turbine generation system, a gas-turbine generation system, and a transformer are monitored, protected, and controlled by their own UMPCU or generation system controller. Initially, a UMPCU or a data-acquisition unit is monitoring a device under supervision, generating the three sets of data (i.e., connectivity, device models, and measurements) of the device. While the UMPCU have multiple operating capabilities such as monitoring, controlling, and protecting a device, the data-acquisition unit basically provides monitoring functions (e.g., creating the three sets of data and sending them to the local DMS).

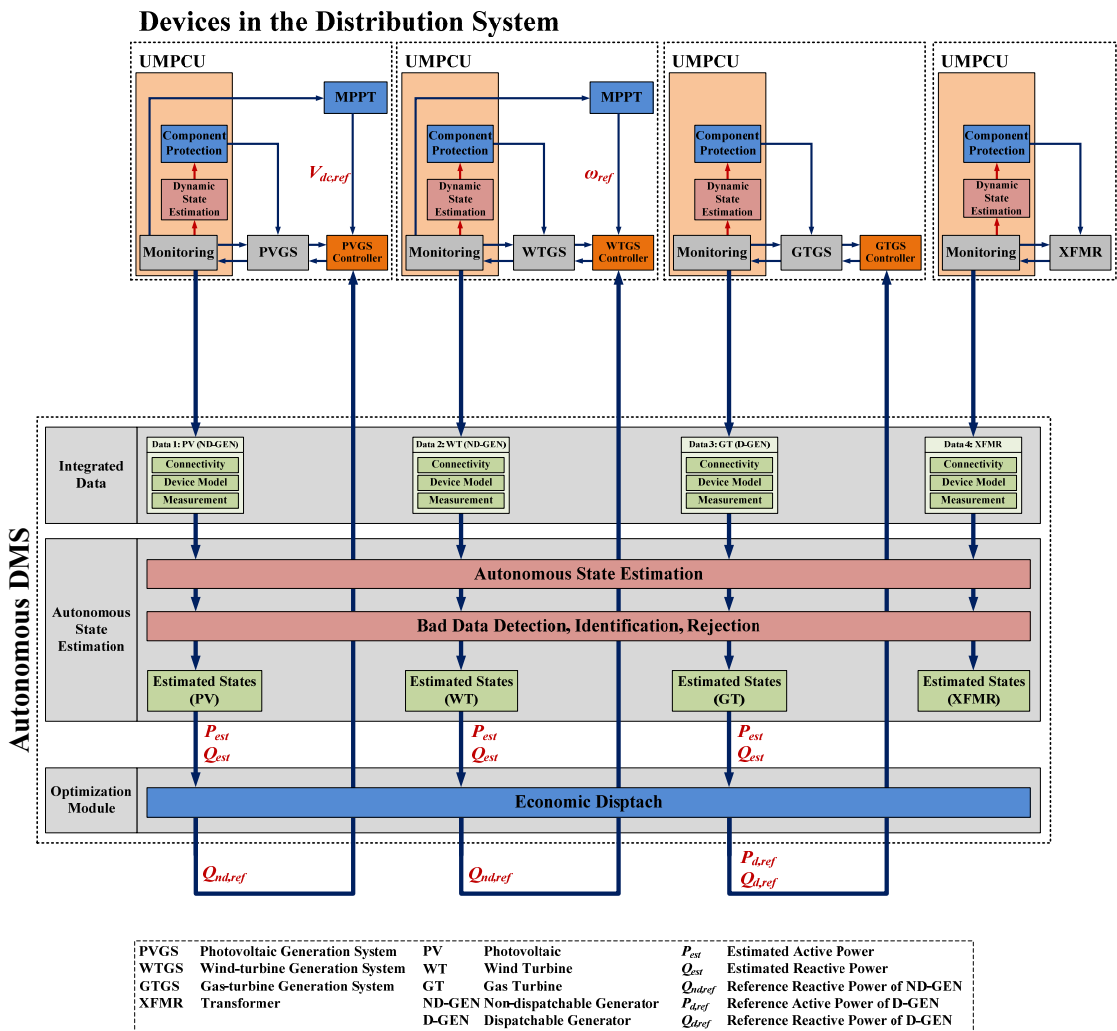


Figure 4.3: Detailed scheme of the autonomous operation.

First, the three sets of data monitored by UMPCUs or data-acquisition units are, first, used for the decentralized operation and control including (1) setting-less component protection and (2) instant-by-instant management. The setting-less component protection module in a UMPCU is autonomously protecting a device that is managed by the UMPCU, based on performance metrics (e.g., the confidence level) that results from time-based dynamic state estimation. In fact, the low confidence level indicates the existence of internal faults inside the device, thus taking proper actions such as tripping circuit breakers or switches. In addition to the component protection, the MPPT method, which is an instant-by-instant management, uses the three sets of data to provide reference operating points capable of pulling out maximum available power from non-dispatchable renewable generation resources (e.g., PV arrays or wind turbines). For instance, the MPPT algorithm for the PV generation system computes the reference value of the dc voltage (i.e., $V_{dc,ref}$) that enables the PV system to generate maximum power, finally providing the reference value to the PV generation system controller. Likewise, the MPPT algorithm for the wind-turbine generation system provides the reference value of the rotor angular speed (i.e., ω_{ref}) to the controller of wind-turbine generation system.

Whereas the MPPT control and the setting-less component protection is implemented in a decentralized fashion, short-term operational planning such as economic dispatch requires centralized approach through the autonomous DMS. As described in Figure 4.3, all available UMPCUs or data-acquisition units send the three sets of data (i.e., connectivity, device models, and measurements) to the autonomous DMS, and the integrated data are tied in a bundle; note that each bundle refers to the corresponding device. Then, autonomous state estimation in the autonomous DMS processes the integrated data, extracting the real-time operating conditions of the distribution system, which are then evaluated by bad-data detection/identification/rejection. As a result, the accurate operating conditions (i.e., estimated state variables) are

obtained, and these state variables are used by the optimization module designed for various operational purposes.

The optimization module in the autonomous DMS should be able to solve the optimization problem that minimizes overall operating cost while meeting power balance within the grid. For this purpose, the active and reactive power (i.e., P_{est} and Q_{est}) of all generation units should be known, and these values can be provided by autonomous state estimation. Finally, economic dispatch can determine the optimal active- and reactive-power reference of dispatchable generation resources (i.e., $P_{d,ref}$ and $Q_{d,ref}$), but it has no need to decide the active-power reference of non-dispatchable generators because they normally operate at their maximum power. However, if the reactive power flow of a non-dispatchable generator is controllable, then economic dispatch may provide the optimal reactive-power reference (i.e., $Q_{nd,ref}$). Finally, all optimal reference values of active or reactive powers are sent to each generation system controller. Then, to drive target values to the reference values, the controller regulates the inverter (in case of PV arrays or wind turbines) or the steam valve (in case of gas turbines).

The following sub-sections will explain autonomous operation, control, and protection based on autonomous state estimation in more details:

- Setting-less component protection,
- Instant-by-instant management (MPPT),
- Short-term operational planning.

4.4 Setting-less Component Protection

The traditional protection scheme and coordination requires any settings of relays, but the settings are not reliable and sometimes compromise the security; in other words, the relay may generate false trips in spite of normal operating conditions. Furthermore, in the distribution system with a number of DGs, the traditional overcurrent relay could not detect small fault currents that are generated by inverter-based DGs. In this sense, a new

protection scheme that is autonomous, setting-less, and adaptive is required, so this research work proposes a novel protection method for a single component or a cluster of components using dynamic state estimation based on the dynamic model of the components [72], [73].

4.4.1 Basic Concept of the Proposed Protection Scheme

The basic idea of the proposed protection scheme is based on traditional differential protection, which does not need to be coordinated with other protection functions. While differential protection is based on Kirchhoff's current law, the proposed method extends the concept of differential protection to investigating all physical laws of a component such as Kirchhoff's voltage law or Faraday's law. These physical laws can be expressed with the dynamic model of a component under protection, which can be provided by dynamic state estimation [74], [75]. Finally, any violation of the physical laws can be detected by dynamic state estimation, which uses the device model and real-time measurement data.

The overall approach of the proposed setting-less component protection scheme is described in Figure 4.4. In this approach, a numerical relay or a UMPCU is continuously monitoring a component under protection, measuring terminal data (e.g., the voltage magnitude, the voltage angle, the frequency, or the rate of frequency change), internal component values (e.g., the temperature or the speed), and status data (e.g., the tap setting or the breaker status). With these real-time measurement data and the device model of the component, dynamic state estimation computes the real-time dynamic operating conditions of the component. Then, the well-known chi-square test evaluates the goodness of fit of measurements to the device model by computing the probability that measurement errors are distributed within expected bounds, assuming that the measurement errors are distributed according to the chi-square distribution.

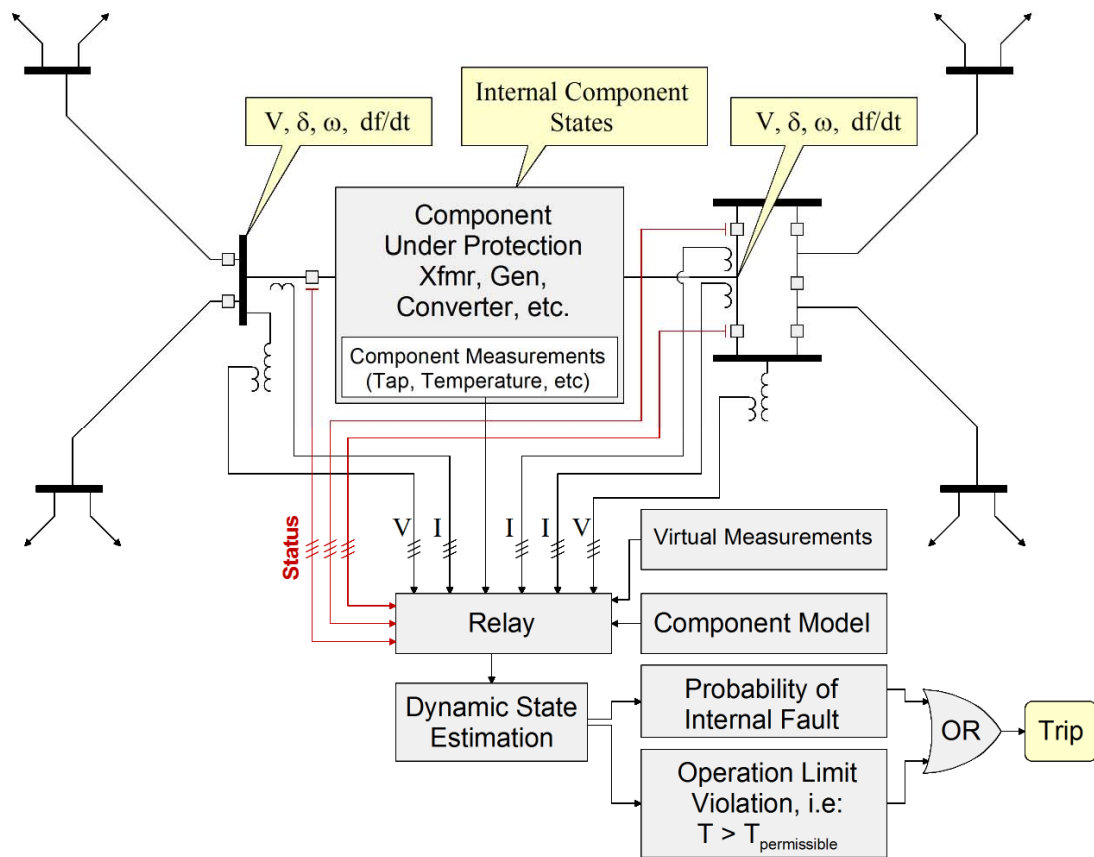


Figure 4.4: Overall approach of the setting-less component protection scheme.

The goodness of fit of the model to measurements can be used as the confidence level. In other words, if the confidence is high, then the model is consistent with the measurements, which implies that there is no internal fault. On the other hand, if the confidence level is low, it indicates the poor fit between the model and measurements, which implies any internal faults in the component under protection. When detecting any internal faults, relays or UMPCUs trip breakers or switches immediately. Note that the trip operation can also be issued when operating conditions violate their limits as described in Figure 4.4.

It should be pointed out that the approach of setting-less component protection is primarily based on the component (i.e., device) model and real-time measurements, so it does not require any settings (e.g., pick-up currents or restraining quantities) or any

coordination with other protection functions. The detailed protection logic of the proposed setting-less component protection is described in Figure 4.5.

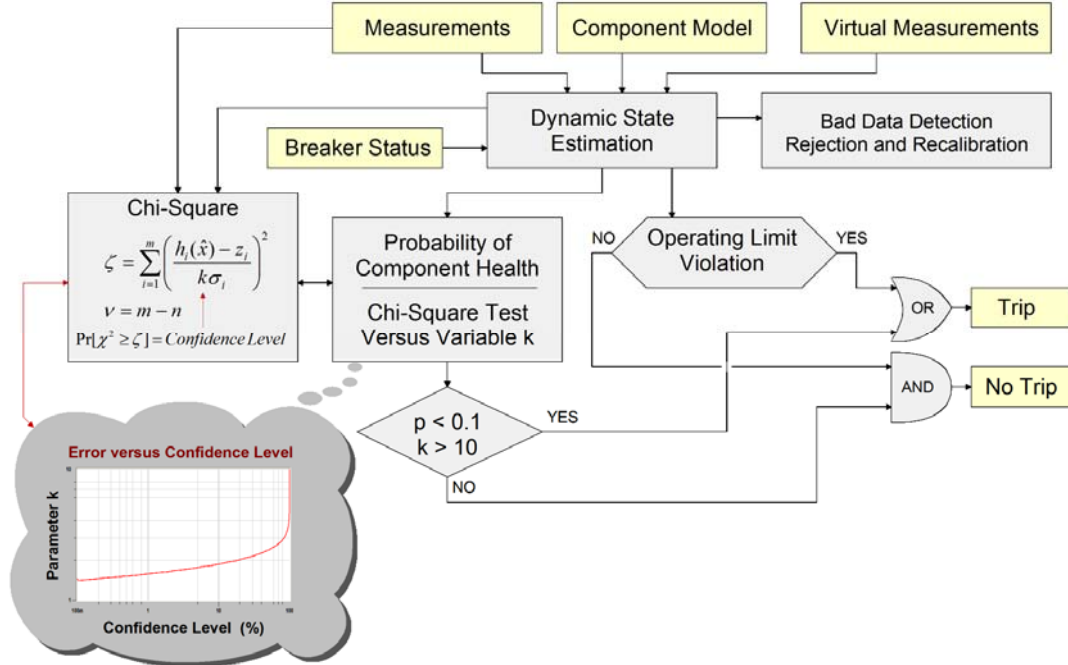


Figure 4.5: Protection logic based on dynamic state estimation.

For example, in case of transformer protection, dynamic state estimation can extract the dynamic operating conditions of a transformer that reflects the nonlinear magnetism characteristics of the transformer core, providing capability to adaptively differentiate transformer internal faults from inrush currents or overexcited currents, which are normal operating conditions of transformers. Moreover, the setting-less component protection can be applied to detect the high impedance fault in distribution systems. The traditional overcurrent protective relay is hard to detect the high impedance fault because the fault current is not huge enough to be detected. In contrast, the proposed method is capable of detecting the high impedance fault because the high impedance fault is the case of the internal fault of distribution lines, which eventually make dynamic state estimation and the chi-square test yield the low confidence level.

4.4.2 Implementation of Setting-less Component Protection

The implementation of the setting-less component protection consists of four steps: (1) the component (or protection-zone) dynamic model, (2) measurement-model formulation, (3) dynamic state estimation, and (4) protection logic.

4.4.2.1 Component Dynamic Model

Dynamic state estimation extends the concept of static state estimation by using the dynamic states and models of power system components (i.e., devices). In this approach, state estimation is implemented based on a time-domain formulation, and as a result, both electrical and other dynamics are taken into consideration. Therefore, the component dynamic model is described by a set of algebraic and differential equations that is expressed as follows:

$$0 = g(i(t), x(t), t), \quad (4.1)$$

$$\frac{dx(t)}{dt} = f(i(t), x(t), t), \quad (4.2)$$

$$x(t) = [\nu(t) \quad \gamma(t)]^T, \quad (4.3)$$

where $x(t)$ is the state variables, $i(t)$ is the currents, $\nu(t)$ is the voltages, $\gamma(t)$ is the internal states, and t is the current time.

To implement dynamic state estimation, the component dynamic model, which is expressed as equations (4.1) and (4.2), should be converted into a set of linear and quadratic algebraic equations (i.e., AQCF) using two innovative methods: (1) the quadratic integration method and (2) model quadratization. The quadratic integration method is a numerical integration method that is applied for the quadratic model, assuming that functions vary quadratically over the integration time step, and model quadratization reduces model nonlinearity to have at most quadratic terms by introducing additional state variables. Both methods are described in APPENDIX A. Finally, the component dynamic model can be expressed in the following AQCF:

$$\begin{bmatrix} i(t) \\ 0 \\ i(t_m) \\ 0 \end{bmatrix} = \begin{bmatrix} K_1 \\ K_2 \\ K_3 \\ K_4 \end{bmatrix} + \begin{bmatrix} L_{11} & L_{12} & L_{13} & L_{14} \\ L_{21} & L_{22} & L_{23} & L_{24} \\ L_{31} & L_{32} & L_{33} & L_{34} \\ L_{41} & L_{42} & L_{43} & L_{44} \end{bmatrix} \begin{bmatrix} v(t) \\ y(t) \\ v(t_m) \\ y(t_m) \end{bmatrix} + \begin{bmatrix} f_1(t) \\ f_2(t) \\ f_1(t_m) \\ f_2(t_m) \end{bmatrix} - \begin{bmatrix} b_1(t-h) \\ b_2(t-h) \\ b_3(t-h) \\ b_4(t-h) \end{bmatrix}, \quad (4.4)$$

$$f(t) = \begin{bmatrix} f_1(t) \\ f_2(t) \\ f_1(t_m) \\ f_2(t_m) \end{bmatrix} = \begin{bmatrix} \vdots & & & \\ \left[v(t)^T & y(t)^T & v(t_m)^T & y(t_m)^T \right] Q_i & \begin{bmatrix} v(t) \\ y(t) \\ v(t_m) \\ y(t_m) \end{bmatrix} \\ \vdots & & & \end{bmatrix}, \quad (4.5)$$

$$b(t-h) = \begin{bmatrix} b_1(t-h) \\ b_2(t-h) \\ b_3(t-h) \\ b_4(t-h) \end{bmatrix} = \begin{bmatrix} M_{11} & M_{12} \\ M_{21} & M_{22} \\ M_{31} & M_{32} \\ M_{41} & M_{42} \end{bmatrix} \begin{bmatrix} i(t-h) \\ 0 \end{bmatrix} + \begin{bmatrix} N_{11} & N_{12} \\ N_{21} & N_{22} \\ N_{31} & N_{32} \\ N_{41} & N_{42} \end{bmatrix} \begin{bmatrix} v(t-h) \\ y(t-h) \end{bmatrix}, \quad (4.6)$$

$$K = \begin{bmatrix} K_1 \\ K_2 \\ K_3 \\ K_4 \end{bmatrix}, \quad (4.7)$$

$$L = \begin{bmatrix} L_{11} & L_{12} & L_{13} & L_{14} \\ L_{21} & L_{22} & L_{23} & L_{24} \\ L_{31} & L_{32} & L_{33} & L_{34} \\ L_{41} & L_{42} & L_{43} & L_{44} \end{bmatrix}, \quad (4.8)$$

$$M = \begin{bmatrix} M_{11} & M_{12} \\ M_{21} & M_{22} \\ M_{31} & M_{32} \\ M_{41} & M_{42} \end{bmatrix}, \quad (4.9)$$

$$N = \begin{bmatrix} N_{11} & N_{12} \\ N_{21} & N_{22} \\ N_{31} & N_{32} \\ N_{41} & N_{42} \end{bmatrix}, \quad (4.10)$$

where K is the constant vector; L , M , and N are the device-model matrices; h is the integration time step; t_m is the intermediate time (i.e., the half point in the interval $[t$ to $t-h]$); $f(t)$ is the quadratic nonlinear terms; and Q_i are the quadratization matrices. An example of deriving the component dynamic model from the three-phase, two-winding, variable-tap, and saturable-core transformer is represented in APPENDIX C.

4.4.2.2 Dynamic State Estimation

Dynamic state estimation, which setting-less component protection uses, is based on the well-known weighted-least-squares method, which is explained in Section 3.4.4 of CHAPTER 3. It is necessary to note that dynamic state estimation requires real-time measurements, component dynamic models, and the definition of component state variables.

4.4.2.3 Protection Logic

The entire protection logic is based on measurements obtained from hardware (e.g., PMUs, relays, CTs, and PTs) and the dynamic state estimator. When receiving measurements from both sides of a component under protection, the dynamic state estimator runs with the component dynamic model. Then, the chi-square of all the measurements is calculated to investigate the goodness of fit of measurements to the model, determining whether the component is in healthy status. If the confidence level drops to a low value for several cycles, then the measurements do not fit the model, and thus, the dynamic model of the component is incorrect, indicating that any internal faults happen. As a result, a relay or a UMPCU would trip breakers immediately. In the meantime, during the state-estimation process, the operating limit is being monitored so that the component under protection will be tripped once the operating conditions of the component violate the operating limit.

4.4.3 Process of Dynamic State Estimation

This section describes the process of dynamic state estimation. The overall dynamic-state-estimation process for the proposed setting-less component protection scheme is summarized and illustrated in Figure 4.6.

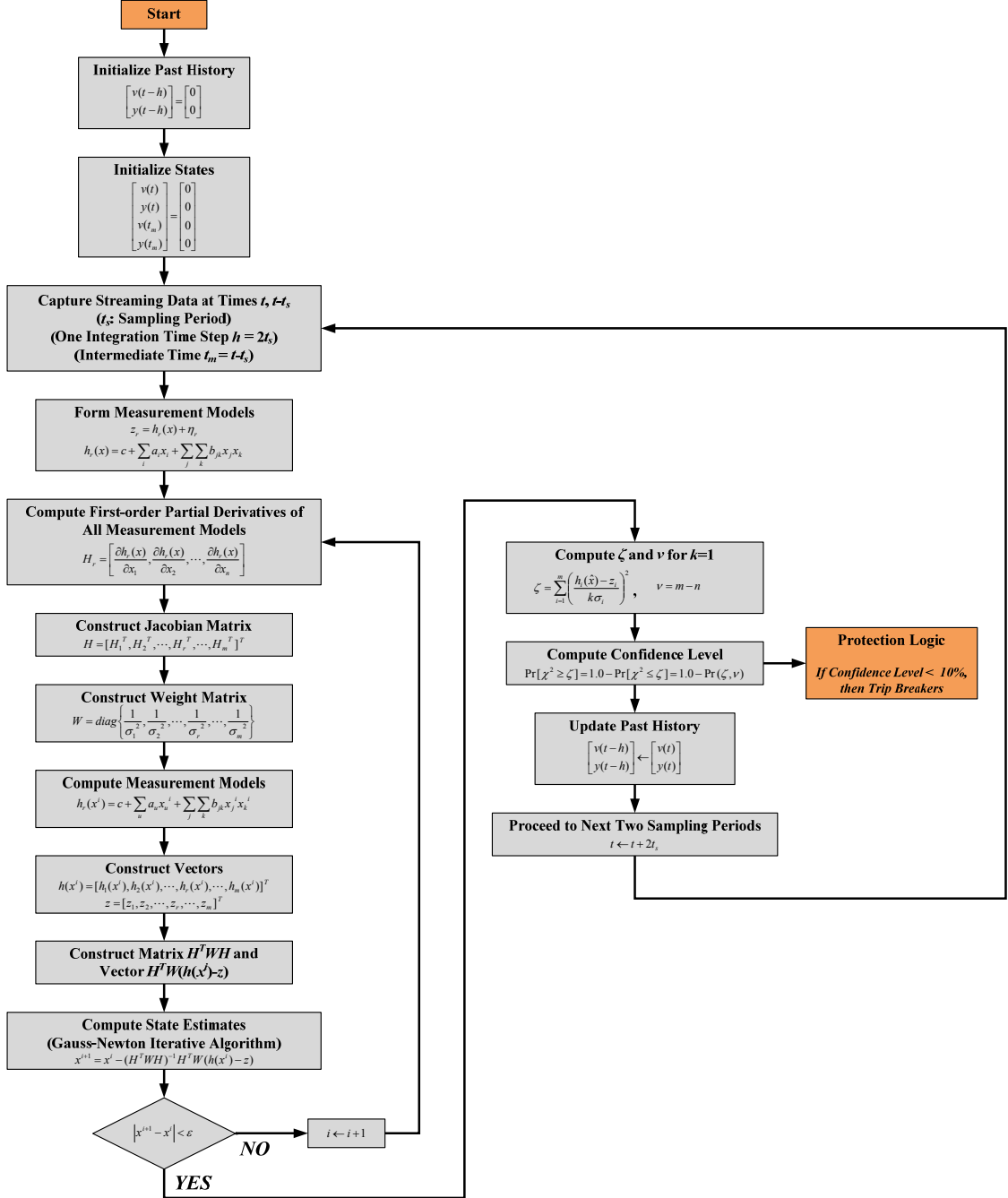


Figure 4.6: Overall process of dynamic state estimation.

First, the state variables of a component under protection are defined as follows:

$$\begin{bmatrix} v(t) \\ y(t) \\ v(t_m) \\ y(t_m) \end{bmatrix}, \quad (4.11)$$

where $v(t)$ is the voltages (i.e., the external states), $y(t)$ is the internal states, t is the current time, t_m is the intermediate time (i.e., the half point in the interval $[t$ to $t-h]$), and h is the integration time step.

Before applying the setting-less component protection method, past-history values, $v(t-h)$ and $y(t-h)$, are initialized to zero as follows:

$$\begin{bmatrix} v(t-h) \\ y(t-h) \end{bmatrix} = \begin{bmatrix} 0 \\ 0 \end{bmatrix}. \quad (4.12)$$

Then, all state variables are initialized to zero:

$$\begin{bmatrix} v(t) \\ y(t) \\ v(t_m) \\ y(t_m) \end{bmatrix} = \begin{bmatrix} 0 \\ 0 \\ 0 \\ 0 \end{bmatrix}. \quad (4.13)$$

4.4.3.1 Step 1: Capture Streaming Data at Two Consecutive Time Instances

The state estimation is initiated once the streaming of measurements for a specific instant of time, t , has been completed while measurement data for the next time interval start streaming in; for this purpose, a buffer system that separates the sets of data at the time interval needs to be implemented. Finally, the state-estimation process at time t is applied on the set of data for the time interval, from $t-h$ to t .

In the meantime, the AQCF model of a component under protection is expressed with various measurements at two consecutive time instances (i.e., two consecutive samples) and past-history values, indicating that the setting-less component protection operates on the samples of two consecutive time instances. As described in Figure 4.7, for

the present processing time, t , dynamic state estimation uses two samples (i.e., measurements) at consecutive time instances, t and $t-t_s$; note that t_s is defined as the sampling period, and one integration time step, h , is twice the sampling period t_s . Therefore, when a sample at the time t is used as the present-time measurement, $z(t)$, the sample at the time $t-t_s$ is used as the intermediate-time measurement, $z(t_m)$.

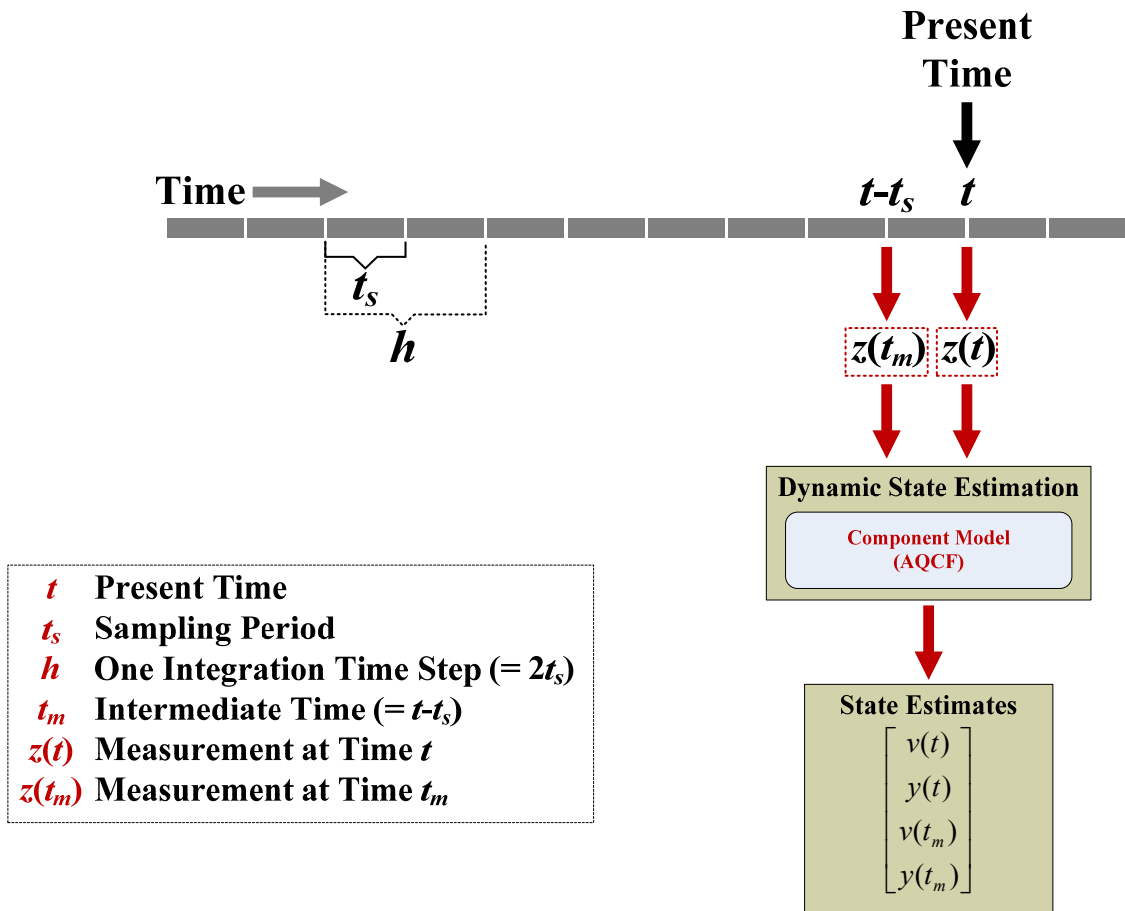


Figure 4.7: Illustration of the use of samples for the setting-less component protection at the present time, t .

4.4.3.2 Step 2: Form Measurement Models

The formulation of measurement models for dynamic state estimation is similar to the case of autonomous state estimation, which is presented in Section 3.4.3 of CHAPTER 3. For dynamic state estimation, there are four types of measurements (i.e., across measurements, through measurements, virtual measurements, and pseudo

measurements), and each measurement model is expressed as equations (3.12) and (3.13). The following sub-sections describe how to formulate the measurement model for dynamic state estimation according to the measurement type.

4.4.3.2.1 Formulation of the Across Measurement Model

The voltage measurement, which is a typical across measurement, measures voltages across two buses/nodes, thus forming the following measurement model:

$$z_r = h_r(x) + \eta_r = x_i - x_j + \eta_r, \quad (4.14)$$

where x_i and x_j refer to state variables that correspond to two measured points.

4.4.3.2.2 Formulation of the Through Measurement Model

The current measurement, which is a typical through measurement, is the measured quantity of an electric current with direction. The measurement model of a current measurement can be derived from the component dynamic model, as expressed in equation (4.4), and therefore, the current measurement model at time t is one of the rows of the following AQCF, which is part of the component dynamic model:

$$i(t) = K_1 + L_{11}v(t) + L_{12}y(t) + L_{13}v(t_m) + L_{14}y(t_m) + f_1(t) - b_1(t - h). \quad (4.15)$$

In fact, the current measurement model for the time t can be expressed as follows:

$$z_r = h_r(x) + \eta_r = i(t)^{(k)} + \eta_r, \quad (4.16)$$

where k indicates the k -th row of the vector, $i(t)$.

Likewise, the current measurement model at the intermediate time (i.e., t_m) is based on one of the rows of the following AQCF:

$$i(t_m) = K_3 + L_{31}v(t) + L_{32}y(t) + L_{33}v(t_m) + L_{34}y(t_m) + f_1(t_m) - b_3(t - h). \quad (4.17)$$

The current measurement model for the time t_m can be expressed as follows:

$$z_r = h_r(x) + \eta_r = i(t_m)^{(k)} + \eta_r, \quad (4.18)$$

where k indicates the k -th row of the vector, $i(t_m)$.

4.4.3.2.3 Formulation of the Virtual Measurement Model

Similar to the current measurement model, the virtual measurement model can be induced from the component dynamic model, equation (4.4). In detail, the following AQCFs, which are parts of the component dynamic models, can become the measurement model:

$$0 = K_2 + L_{21}v(t) + L_{22}y(t) + L_{23}v(t_m) + L_{24}y(t_m) + f_2(t) - b_2(t-h), \quad (4.19)$$

$$0 = K_4 + L_{41}v(t) + L_{42}y(t) + L_{43}v(t_m) + L_{44}y(t_m) + f_2(t_m) - b_4(t-h). \quad (4.20)$$

Finally, all rows in equations (4.19) and (4.20) can be used to formulate the virtual measurement model with the following format:

$$0 = z_r = h_r(x) + \eta_r = Equ(k) + \eta_r, \quad (4.21)$$

where $Equ(k)$ indicates the k -th row of the equation (4.19) or (4.20).

4.4.3.2.4 Formulation of the Pseudo Measurement Model

For example, in case of a pseudo measurement model that refers to a neutral voltage at the time t or t_m can be expressed as follows:

$$0 = z_r = h_r(x) + \eta_r = x_i + \eta_r, \quad (4.22)$$

where x_i refers to a state variable that corresponds to the neutral voltage at the time t or t_m .

4.4.3.3 Step 3: Contribution of Measurements

For the state-estimation process, all measurements, which include across, through, virtual, and pseudo measurements, are formulated into the standard form of the measurement model as described in equations (3.12) and (3.13). Then, all the measurement models are contributed to generate the matrix H^TWH and the vector $H^TW(h(x^i)-z)$, which is described in the following sub-sections.

4.4.3.3.1 Compute the First-order Partial Derivatives of Measurement Models

The Jacobian matrix, H , requires the first-order partial derivatives of each measurement model, which is represented as follows:

$$H_r = \left[\frac{\partial h_r(x)}{\partial x_1}, \frac{\partial h_r(x)}{\partial x_2}, \dots, \frac{\partial h_r(x)}{\partial x_n} \right], \quad (4.23)$$

where H_r is the first-order partial derivatives of the r -th measurement model, and n is the number of state variables.

4.4.3.3.2 Construct the Jacobian Matrix

The Jacobian matrix can be formed with the partial derivatives of all measurements as follows:

$$H = [H_1^T, H_2^T, \dots, H_r^T, \dots, H_m^T]^T, \quad (4.24)$$

where m is the number of measurements.

4.4.3.3.3 Construct the Weight Matrix

The diagonal entries of the weight matrix, W , consists of the inverse of squared standard deviation of measurements.

$$W = \text{diag} \left\{ \frac{1}{\sigma_1^2}, \frac{1}{\sigma_2^2}, \dots, \frac{1}{\sigma_r^2}, \dots, \frac{1}{\sigma_m^2} \right\}, \quad (4.25)$$

where σ_r is the standard deviation of the r -th measurement.

4.4.3.3.4 Compute the Measurement Models

With state variables estimated at the i -th iteration (i.e., x^i), the measurement model of the r -th measurement can be computed as follows:

$$h_r(x^i) = c + \sum_u a_u x_u^i + \sum_j \sum_k b_{jk} x_j^i x_k^i. \quad (4.26)$$

4.4.3.3.5 Construct Vectors $h(x^i)$ and z

The vectors $h(x^i)$ and z can be constructed as follows:

$$h(x^i) = [h_1(x^i), h_2(x^i), \dots, h_r(x^i), \dots, h_m(x^i)]^T, \quad (4.27)$$

$$z = [z_1, z_2, \dots, z_r, \dots, z_m]^T. \quad (4.28)$$

4.4.3.3.6 Construct the Matrix and the Vector for State Estimation

Based on the Jacobian matrix (i.e., H), the weight matrix (i.e., W), and vectors (i.e., $h(x^i)$ and z), the matrix H^TWH and the vector $H^TW(h(x^i)-z)$ are constructed.

4.4.3.4 Step 4: Compute State Estimates

The state variables at $(i+1)$ -th iteration can be obtained by the following Gauss-Newton iterative algorithm:

$$x^{i+1} = x^i - (H^TWH)^{-1} H^TW(h(x^i) - z). \quad (4.29)$$

4.4.3.5 Step 5: Convergence Test

A condition for testing the convergence of the iterative method is as follows:

$$|x^{i+1} - x^i| < \varepsilon. \quad (4.30)$$

In other words, only if all absolute differences between state variables estimated at the $(i+1)$ -th iteration (i.e., x^{i+1}) and those estimated at the i -th iteration (i.e., x^i) are less than a threshold ε , then the iterative method is converged, indicating state variables at the time t are obtained. Therefore, proceed to the next step. However, any differences between state variables at the $(i+1)$ -th iteration (i.e., x^{i+1}) and those at the i -th iteration (i.e., x^i) are larger than the threshold ε , return to step 3 with the following update:

$$i \leftarrow i + 1. \quad (4.31)$$

4.4.3.6 Step 6: Compute the Chi-square Critical Value, the Degrees of Freedom, and the Confidence Level

State variables estimated are used to compute the goodness of fit of the component dynamic model to measurements, which can be quantified by the confidence level based on the chi-square test using the degrees of freedom, ν , and the chi-square critical value, ζ . Then, based on the confidence level calculated, the protection logic determines if the goodness of fit of the model to measurements is good or poor. In fact, this decision is based on a threshold value (e.g., 10%); if the confidence level is higher than the threshold, then it can be concluded that no internal fault has occurred. Otherwise, the device under protection has any internal fault, thus requiring protecting actions such as tripping breakers.

4.4.3.7 Step 7: Update Past-history Values

Before proceeding to the next time step, the past-history values, $\nu(t-h)$ and $y(t-h)$, should be updated with state variables estimated:

$$\begin{bmatrix} \nu(t-h) \\ y(t-h) \end{bmatrix} \leftarrow \begin{bmatrix} \nu(t) \\ y(t) \end{bmatrix}. \quad (4.32)$$

4.4.3.8 Step 8: Proceed to the Next Two Sampling Periods

Proceed to the next two sampling periods as follows:

$$t \leftarrow t + 2t_s. \quad (4.33)$$

Then, return to the step 1.

4.4.4 **Setting-less Component Protection and Autonomous State Estimation**

The setting-less component protection can be implemented by a UMPCU or a relay that is monitoring a component under protection. As described in Figure 4.8, a UMPCU performs dynamic state estimation based on three sets of data such as

connectivity, device models (i.e., component dynamic models), and measurements, yielding time-based dynamic states. As a matter of fact, these dynamic states can be converted to quasi-static states by the phasor computation unit in the UMPCU, and then, these quasi-static states are delivered to the autonomous DMS with connectivity and/or with frequency-domain device models that are converted from time-domain device models. As described in Figure 4.8, the quasi-static states are tagged with the GPS-time signal from the GPS antenna so that the autonomous DMS can integrate quasi-static states with the same time frame from different UMPCUs, providing the real-time operating conditions of the distribution system. Note that autonomous state estimation in the autonomous DMS does not need to estimate quasi-static states that are converted from dynamic states because the dynamic states have already been filtered by the dynamic state estimator in the UMPCU. In other words, autonomous state estimation applies only on the data from data-acquisition units (as described in Figure 4.9) or from UMPCUs that do not perform the function of dynamic state estimation.

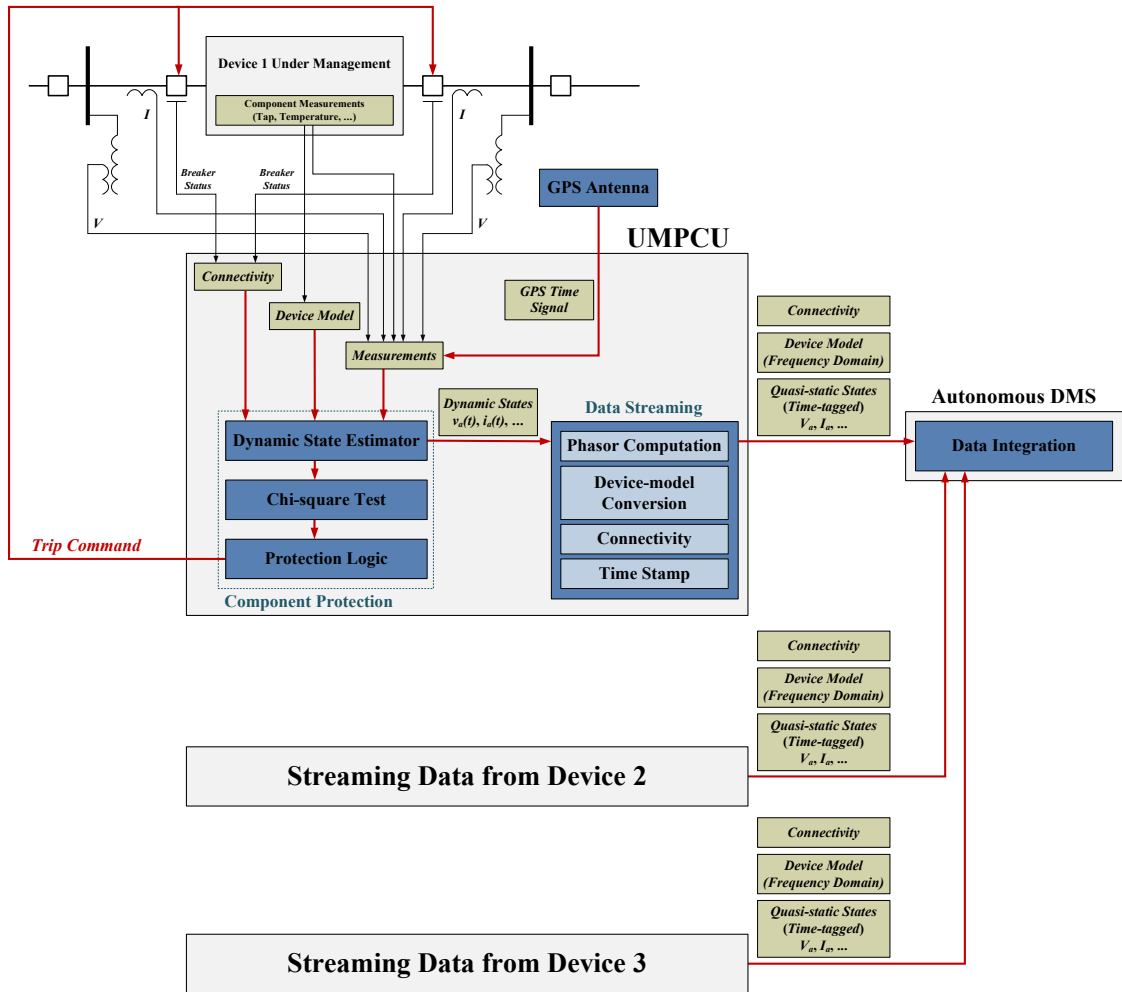


Figure 4.8: Functionality of the UMPCU.

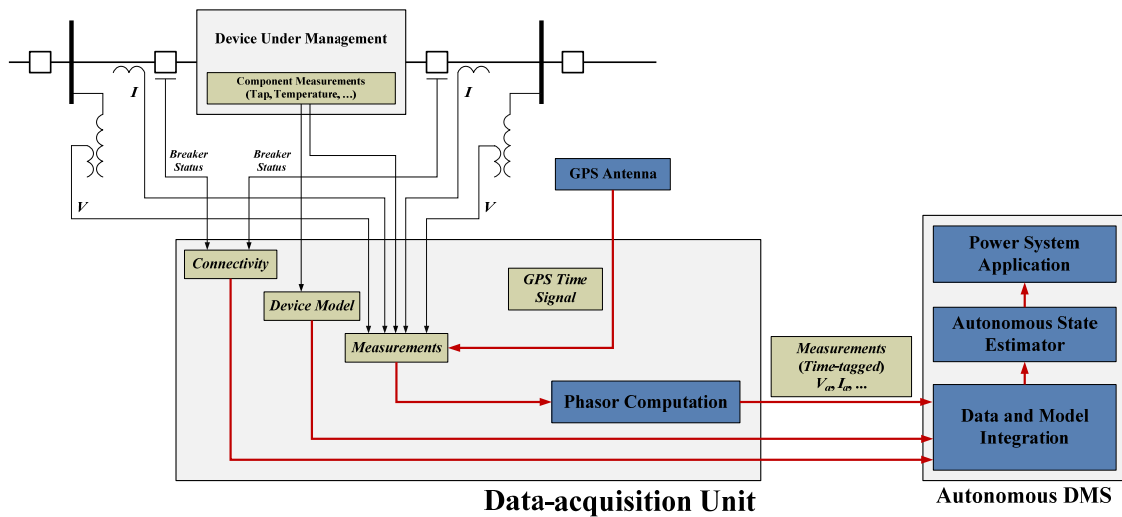


Figure 4.9: Functionality of the data-acquisition unit.

4.5 Instant-by-instant Management (MPPT)

The characteristics of DGs such as maximum available power and an I-V curve are continuously varying with time, weather, season, and geographic locations. Therefore, to maximize power generated by DGs, the generation system controller should be able to control the operation of DGs every moment (i.e., instant by instant). Indeed, such instant-by-instant management can be accomplished more effectively by a decentralized entity (e.g., the generation system controller) in an autonomous fashion. This is due to the fact that a centralized control may suffer from high time latency in data communication and decision making. Therefore, the instant-by-instant management requires the autonomous control, which utilizes the local data such as connectivity, device models, and measurements of the device. In the following sub-sections, the operation and control scheme of the PV and wind-turbine generation system.

4.5.1 Operation and Control of the PV Generation System

As shown in Figure 4.10, the PV generation system typically consists of PV arrays, an inverter, and a transformer. Each component is monitored by a UMPCU in such a way that the UMPCU collect three essential data (i.e., connectivity, device models, and measurements), which are used for the instant-by-instant management (e.g., MPPT). The MPPT algorithm can compute the optimal operating values (e.g., dc voltages), and then, the controller controls the inverter to make the PV generation system to operate at the optimum values.

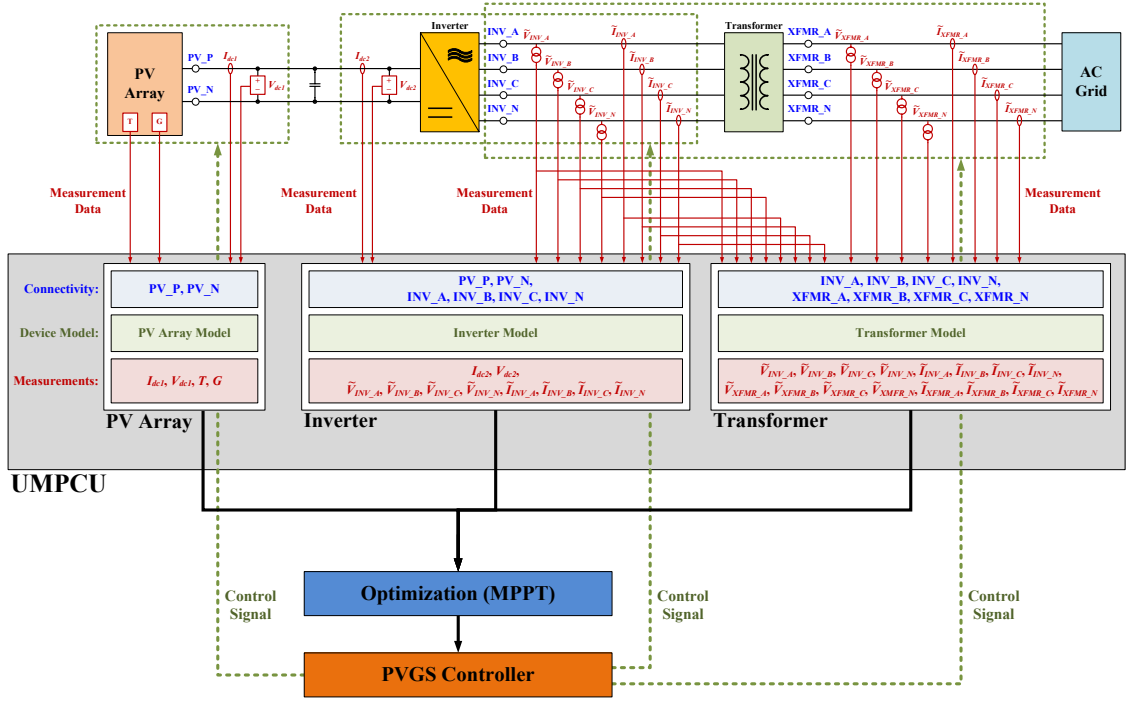


Figure 4.10: Instant-by-instant management of the PV generation system.

In fact, various MPPT techniques, including perturbation and observation (P&O), incremental conductance, fractional open-circuit voltage, fractional short-circuit current, fuzzy logic control, and a computational method [76], [77], have been developed. Among them, this research work uses a computational method that is based on the device model of the PV array, which is developed in APPENDIX B. Such computational method formulates the optimization problem for obtaining the maximum power point (i.e., $v_{1,opt}$) as follows:

$$\begin{aligned} \text{maximize } P &= -v_1 \times i_1 \\ &= -v_1 \times [K_1 + L_{11}\tilde{V} + L_{12}y(t) + L_{13}y(t_m) - N_{12}y(t-h) + f_1(t)]^{(1)}, \end{aligned} \quad (4.34)$$

subject to

$$0 \leq v_1 \leq V_{oc}, \quad (4.35)$$

$$-I_{sc} \leq i_1 \leq 0, \quad (4.36)$$

where V_{oc} is the open-circuit voltage, I_{sc} is the short-circuit current, v_1 is the terminal voltage of the PV array, i_1 is the terminal current of the PV array, and (1) means the first row of the PV device model, equation (B.32).

4.5.2 Operation and Control of the Wind-turbine Generation System

Today, the wind-turbine generation system that has been mostly used is the DFIG with variable generator speed. The basic architecture of DFIG is illustrated in Figure 4.11, and it is necessary to note that the DFIG has two converters, a rotor-side converter and a grid-side converter. These two converters draw the rotor field current from the main grid and control the active- and reactive-power output of the wind-turbine generation system. Additionally, the DFIG has many features to enhance the performance of the wind turbine; for example, the grid-side converter can maintain the voltage profile especially during the voltage dip by providing reactive power from the DC-link to the grid. Moreover, the main advantage of the DFIG is that the rotor-side converter can control the rotor speed to the optimal operating point, where the wind turbine can draw maximum available power from the wind energy within the speed limits of the DFIG.

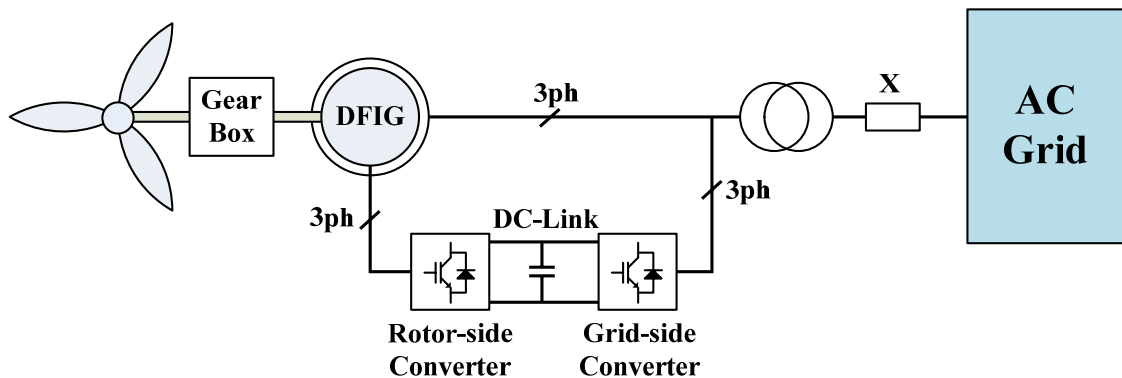


Figure 4.11: Fundamental architecture of the DFIG.

In Figure 4.12, a UMPCU is monitoring the components of the wind-turbine generation system, which consists of a DFIG, a rotor-side converter, a grid-side converter, and a transformer, generating the three-sets of essential data (i.e., connectivity, device models, and measurements). These data are utilized for the MPPT algorithm to compute

the optimum rotor speed, where the DFIG can draw the available maximum power from the wind energy at any instant in any wind conditions. Finally, the controller of the wind-turbine generation system drives the actual rotor speed to track the optimum rotor speed by controlling the electrical torque of the rotor.

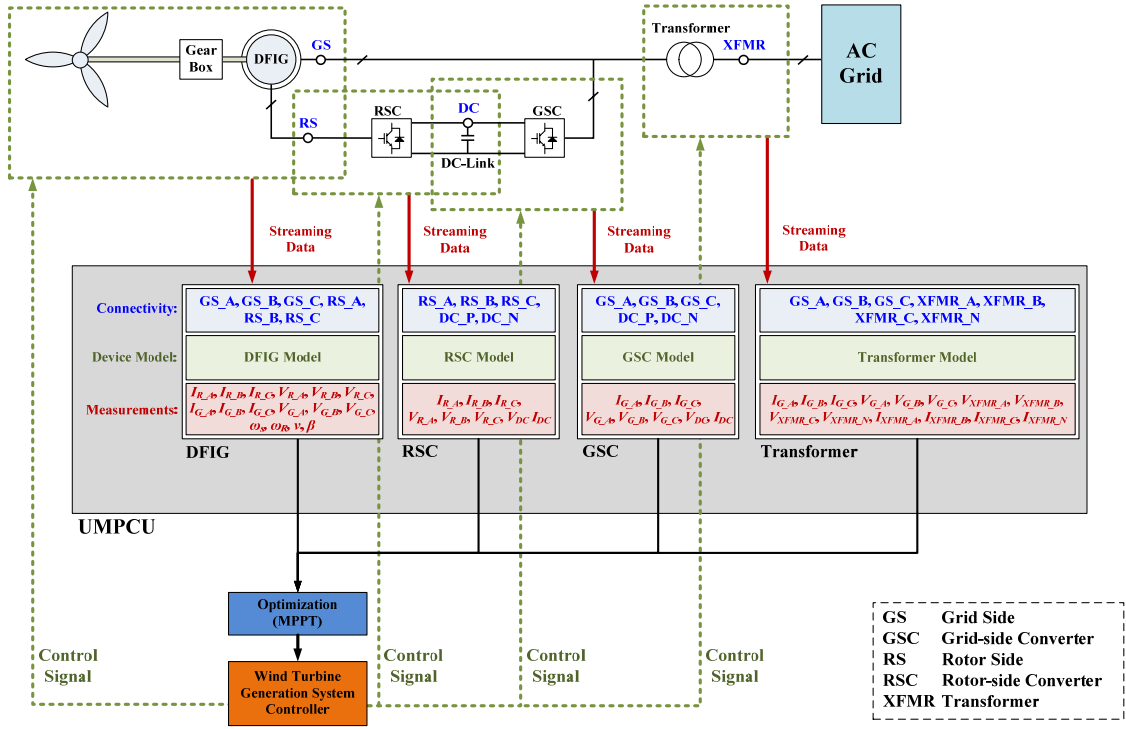


Figure 4.12: Instant-by-instant management of the wind-turbine generation system.

If the DFIG-based wind-turbine generation system can adjust the rotor speed, then the next step for the MPPT is to find the maximum power point (i.e., the optimum rotor angular speed, ω_{opt}) in spite of the various wind speed. Among many ways to find the MPPT (e.g., perturbation and observation, the wind-speed measurement, and power signal feedback [78]), this research work is based on the wind-speed-measurement method because the rotor speed can be estimated using the device model of the DFIG and real-time measurements from the field.

In general, the output power of the DFIG can be expressed as follows [78]:

$$P = \frac{1}{2} C_p(\lambda, \beta) \rho A v^3, \quad (4.37)$$

where $C_p(\lambda, \beta)$ is the power coefficient of the DFIG, λ is the tip-speed ratio, β is the pitch angle, ρ is the air density, A is the swept area of the rotor blade, and v is the wind velocity. The optimization problem for the MPPT of the DFIG can be formulated by maximizing the power coefficient, $C_p(\lambda, \beta)$, which is the function of λ and β [78].

$$\text{maximize } C_p(\lambda, \beta) = 0.5176 \left(\frac{116}{\lambda_i} - 0.4(\beta - 5)e^{\frac{-21}{\lambda_i}} + 0.0068\lambda \right), \quad (4.38)$$

where

$$\frac{1}{\lambda_i} = \frac{1}{\lambda + 0.08\beta} - \frac{0.035}{\beta^3 + 1}. \quad (4.39)$$

The power coefficient for different pitch angles is illustrated in Figure 4.13, indicating that given a specific pitch angle, the maximum power coefficient depends on the tip-speed ratio, λ . Therefore, if the pitch angle is known, an optimum tip-speed ratio (i.e., λ_{opt}) that maximizes the power coefficient (i.e., C_p) can be obtained using equations (4.38) and (4.39).

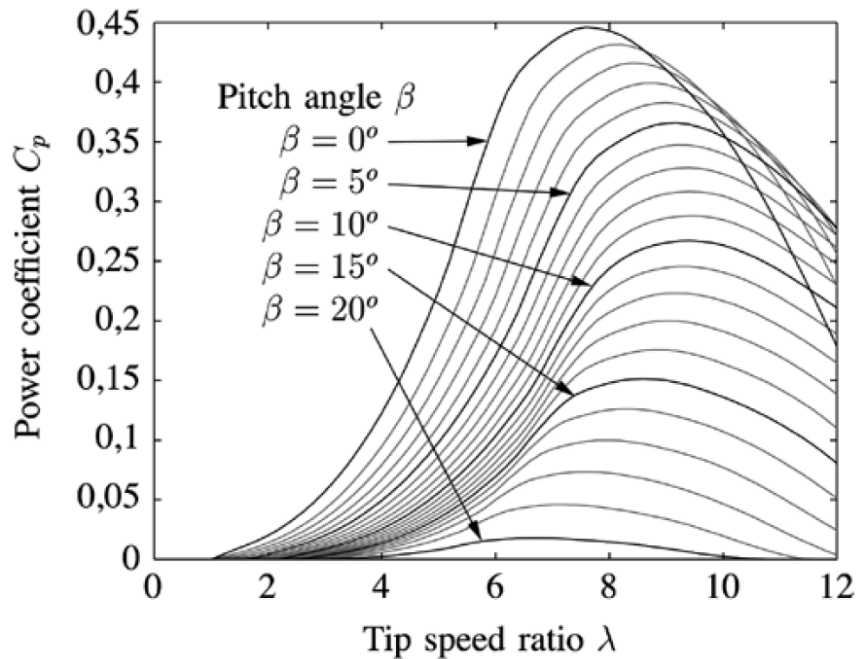


Figure 4.13: Power coefficient for different pitch angles [79].

Indeed, the tip-speed ratio, λ , which is the ratio between the rotational speed of the tip of the blade and the wind velocity, is represented as follows:

$$\lambda = \frac{\omega R}{v}, \quad (4.40)$$

where ω is the rotor angular speed and R is the rotor radius. Therefore, with the optimum tip-speed ratio (i.e., λ_{opt}) and the measured wind speed (i.e., v), the optimum rotor angular speed (i.e., ω_{opt}) can be computed using equation (4.40), and this optimum speed becomes the reference value of the rotor angular speed (i.e., ω_{ref}). Finally, the wind-turbine generation system controller adjusts the electromagnetic torque so as to drive the actual rotor speed to the reference value (i.e., ω_{ref}).

4.6 Short-term Operational Planning

Short-term operational planning relies on the real-time model and the estimated parameters of various generation resources to provide controls to achieve specific operational objectives. The operational objectives will vary depending upon the status of the system. For example, under normal conditions, the operating objectives may be as simple as economic or environmental dispatch (e.g., the minimization of pollutants and carbon dioxide). In case of islanding operation, the objective will be to maximize loads supported by the island.

Under normal operating conditions, the control problem can be partitioned into two problems: (1) the control of non-dispatchable resources and (2) the control of remaining resources. The control of non-dispatchable resources can be separated from the remaining control problem for a simple reason that the optimal operation will require that the non-dispatchable resources be operated at their maximum capability. For example, the PV system or the wind-turbine system should be operated at its maximum power point for prevailing conditions. Then, for the operating points of non-dispatchable resources, the remaining of the system is optimized. There may be instances that this operating

strategy may be changed (e.g., the case of emergency conditions in the main grid or the case of requests from the main grid to operate in the assistance mode).

4.6.1 Application of Autonomous State Estimation

The economic purpose has been accomplished in the planning stage with forecasted electric loads and generation scheduling. In actual operation, however, the operational characteristics of non-dispatchable DGs are changing with environmental conditions (e.g., solar irradiation, wind speed, and wind direction), and the system loading conditions and available generation units may be quite different from those assumed at the planning stage. Therefore, the DMS in the local grid should be able to autonomously optimize economic operation in real time.

In fact, the maximum available power of the non-dispatchable DG is determined by present operating conditions and environmental conditions that are changing in real time. For instance, the intensity of solar irradiation or the temperature of solar cells changes the I - V characteristics. Therefore, available maximum power point is also changed by time, so the capability to update the device model of DGs on a real-time basis is important for short-term operating planning. This capability can be achieved by autonomous state estimation as well as the high-speed communication infrastructure in the local distribution system.

Autonomous state estimation facilitates such autonomous optimization in such a way that the autonomous state estimation produces the real-time model (i.e., operating conditions) of the local grid. The real-time model can determine maximum available power that is generated from non-dispatchable DGs such as PV systems or wind-turbine generators, thus reducing power that should be generated from dispatchable DGs, which, in turn, minimizes operating cost. As a result, only the dispatchable DGs are involved in the optimization problem for economic dispatch. Note that the real-time model, which results from autonomous state estimation, reflects the instantaneous change of network

topology and environmental conditions for DGs, and therefore, real-time economic scheduling can be achieved. Finally, economic dispatch determines the desired output power (i.e., P_{ref}) of all dispatchable units participating in production, and then, the automatic generation control scheme uses these reference power values (i.e., P_{ref}) to control the generation units.

4.6.2 Multi-operational Mode

The real-time model, which autonomous state estimation extracts from the three sets of essential data (i.e., connectivity, device models, and measurements) is utilized to operate and control the distribution system under a variety of operating conditions. In general, the distribution system has three operating modes depending on the status of the interconnection to the main power grid: (1) the grid-connected mode, (2) the islanded mode, and (3) the assistant mode. Each mode has a different operational purpose, so the local DMS should be able to provide proper control actions. The following sub-sections explain the three operational modes and how to formulate the objective function and constraints.

4.6.2.1 Grid-connected Mode

The traditional operational purpose in the power system is to minimize the operating costs of generating units. However, with increasing concerns about the environmental issues, the reduction of the emission of greenhouse gases has recently been taken into account. Therefore, when the distribution system operates at the grid-connected mode, the objectives of the operation and control are to minimize operational cost while minimizing the production of air pollutants, which becomes the multi-objective dispatch problem as follows [80], [81]:

$$\min J = \lambda_1 F_1(x, u) + \lambda_2 F_2(x, u), \quad (4.41)$$

subject to

$$\lambda_1 + \lambda_2 = 1, \quad (4.42)$$

$$g(x, u) = 0, \quad (4.43)$$

$$h(x, u) \leq 0, \quad (4.44)$$

$$u_{i,\min} \leq u_i \leq u_{i,\max} \quad (i = 1, 2, \dots, n), \quad (4.45)$$

where

$$F_1(x, u) = \sum_{i=1}^N [f_{g,i}(x, u) + f_{OM,i}(x, u)] + f_{BUY}(x, u) - f_{SELL}(x, u), \quad (4.46)$$

$$F_2(x, u) = \sum_{i=1}^N [f_{CO_2,i}(x, u) + f_{SO_2,i}(x, u) + f_{NO_x,i}(x, u)], \quad (4.47)$$

$$u = [P_{g1}, P_{g2}, \dots, P_{gn}]^T, \quad (4.48)$$

x is the vector of state variables of the distribution system; u is the vector of the controllable output power of dispatchable generation units; $F_1(x, u)$ is the function of total production cost; $F_2(x, u)$ is the function of total emission cost; λ_1 and λ_2 are the weight coefficients; $u_{i,\min}$ is the minimum available power of the i -th dispatchable generation unit; $u_{i,\max}$ is the maximum available power of the i -th dispatchable generation unit; n is the number of dispatchable generation units; $f_{g,i}(x, u)$ is the cost function of the i -th dispatchable unit; $f_{OM,i}(x, u)$ is the operation and maintenance cost function of the i -th dispatchable unit; $f_{BUY}(x, u)$ is the cost function of buying power from the main grid; $f_{SELL}(x, u)$ is the cost function of selling power to the main grid; $f_{CO_2,i}(x, u)$ is the emission cost function of the carbon dioxide of the i -th dispatchable unit; $f_{SO_2,i}(x, u)$ is the emission cost function of the sulfur dioxide of the i -th dispatchable unit; $f_{NO_x,i}(x, u)$ is the emission cost function of the nitrogen oxides of the i -th dispatchable unit; and P_{gi} is the output power of the i -th dispatchable generation unit. Additionally, equation (4.43) is the equality constraints such as power flow equations, and equation (4.44) represents the inequality constraints.

It is necessary to note that Kirchhoff's current law can be equality constraints, which is presented in equation (4.43). Therefore, device models, which are collected from UMPCUs or data-acquisition units, can be used as equality constraints. Meanwhile, in the grid-connected mode, several constraints (e.g., the heat balance, the limitation of the gas emissions of DGs, spinning-reserve capacity, and the node-voltage magnitude) can be considered.

4.6.2.2 Islanded Mode

In emergency conditions when the distribution system is disconnected from the main grid, the control strategy is aiming for ensuring grid reliability by maximizing power supply to local loads or by load-shedding. The objective function and constraints for this mode is same as those of grid-connected mode except that there is no power transaction between the local distribution system and the main grid. If locally generated power is insufficient to sustain local loads, then some of loads in the consumer side need to be shed based on their priorities.

4.6.2.3 Assistant Mode

Given the request of power support from the main grid, the local distribution system needs to keep providing extra power to the main grid within the permissible limit. The objective function and constraints for this mode is same as those of grid-connected mode except that the local distribution system should provide a certain amount of power to the main grid. If local power is enough to support the main grid but insufficient to sustain local loads, then it is required to shed loads or to reduce the amount of power that should be provided to the main grid.

4.7 Summary

This chapter deals with conceptual methodology for the autonomous operation of the distribution system based on autonomous state estimation. The increasing penetration

of DGs in the distribution system requires new approaches to solve various grid problems in an autonomous fashion. Three approaches are introduced: (1) setting-less component protection, (2) instant-by-instant management, and (3) short-term operational planning.

The setting-less component protection method is presented in this chapter to accomplish autonomous, setting-less, and adaptive protection in the distribution system with DGs. The setting-less component protection relies on the dynamic model of a component under protection that dynamic state estimation can extract from real-time measurements and component dynamic models. In other words, after performing dynamic state estimation, the chi-square test computes the goodness of fit of measurements to component dynamic models, which is referred to as the confidence level. Finally, the occurrence of internal faults is determined by the confidence level. Moreover, states that are estimated by dynamic state estimation can be integrated in the autonomous DMS by means of time synchronism and phasor computation.

Instant-by-instant management is useful for operating and controlling DGs, whose characteristics vary with environmental conditions such as time, weather, season, and geographic locations. This chapter explains how to obtain maximum power points from DGs (e.g., PV panels or wind turbines) based on the three sets of essential data (i.e., connectivity, device models, and measurements). Based on optimum references, which are computed from the MPPT algorithm, the generation controller regulates the generation system to operate at the maximum power point.

Finally, short-term operational planning should depend on the real-time model of various generation resources to achieve specific operational objectives. While autonomous state estimation can provide the real-time operating conditions of non-dispatchable DGs that utilize renewable energy resources, the optimization problem can be formulated to determine the reference operating points of dispatchable generation units that meet various operational purposes. This chapter describes the three operational

modes (i.e., the grid-connected mode, the islanded mode, and the assistant mode) and how to formulate the objective function and constraints.

CHAPTER 5

LABORATORY DEMONSTRATIONS

5.1 Overview

The research of the electric power system usually relies on computer simulation because it is hard to test with the actual system in the field without interrupting the operation of the system. However, although the results of computer simulation are acknowledged, many unexpected situations can happen, and therefore, the validation by laboratory experiments is definitely required before testing in the actual field.

This chapter presents the laboratory demonstrations of the proposed autonomous state estimation with actual test systems. For this purpose, two laboratory setups are tested: (1) the scaled-down power system in the PSCAL at the Georgia Institute of Technology, and (2) the smart grid energy system in NEC Laboratories America, Inc.

5.2 Laboratory Test System 1

In the PSCAL at the Georgia Institute of Technology, there have been efforts to build a laboratory setup for the experimental test-bed of power system monitoring, protection, and control [82-85]. The setup is a scaled-down power-system model that consists of three substations, and the construction method is unique. The proposed autonomous state estimation is implemented and tested with this laboratory setup [65].

5.2.1 Electric Power Infrastructure

All components such as transmission lines, a step-up transformer, and a generator are realistically modeled. Figure 5.1 shows a photograph of the actual laboratory setup, and Figure 5.2 illustrates the simplified diagram of the laboratory test system. In specific, the acronyms *SYNC-GEN*, *XFMR*, and *XLIN*E represent the three-phase synchronous

generator, the delta-wye-connected transformer, the three-phase transmission line, respectively.

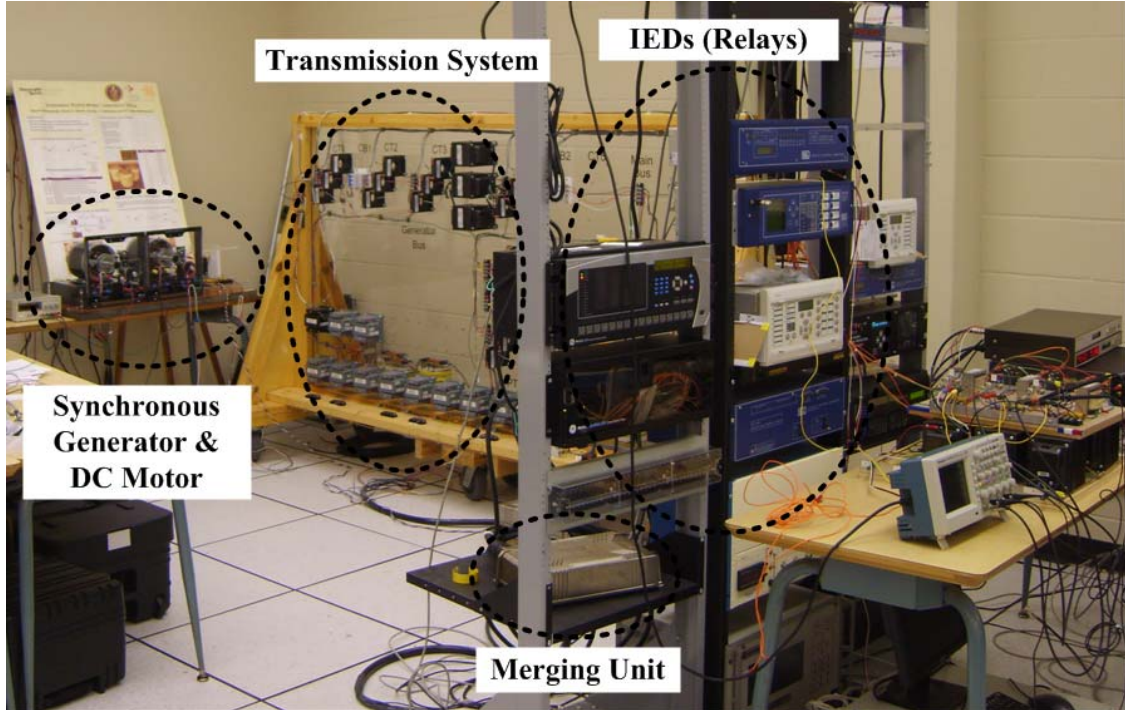


Figure 5.1: Photograph of the laboratory setup in the PSCAL.

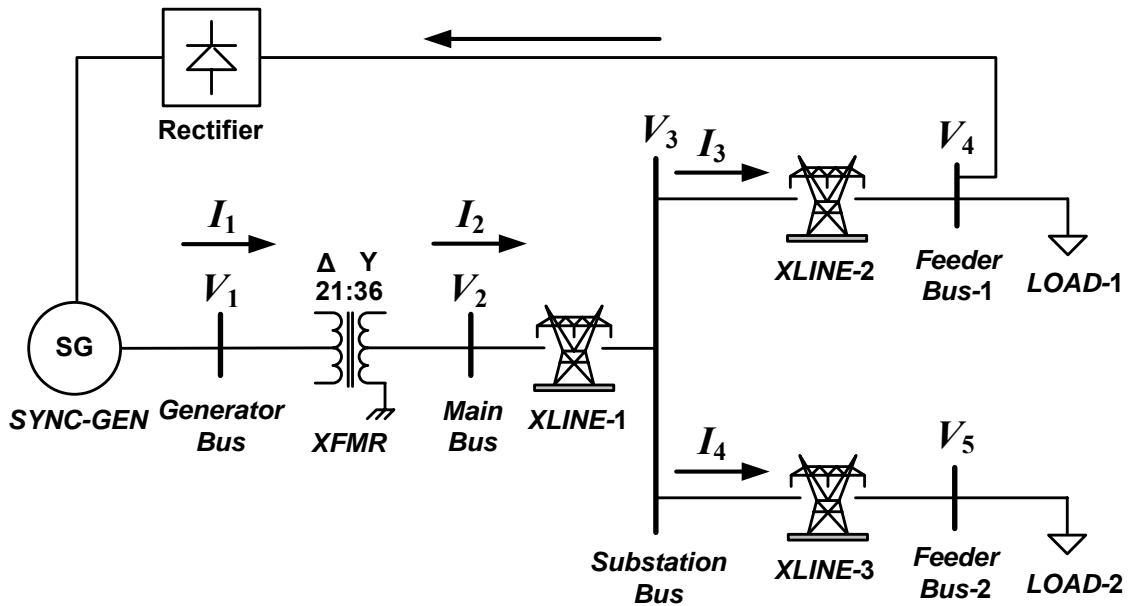


Figure 5.2: Single-line diagram of the test laboratory system.

The laboratory setup was initially designed to implement various applications of the power system such as autonomous state estimation, alarming processing, testing protective relays, testing PMUs, testing interoperability among multi-vendor devices, and implementing the IEC61850-based communication system. For this purpose, instrument transformers like PTs and CTs are installed at every node and line, enabling relays to measure voltages and currents. Furthermore, numerical relays send measurement data to an autonomous state estimator through the communication system. Note that all relays receive time signals from the GPS clock, and therefore, all the measurements can be time-tagged and time-synchronized. Figure 5.3 illustrates connections among the generation system, the transmission system, the data-acquisition system (i.e., relays, PTs, and CTs), and the autonomous state estimator.

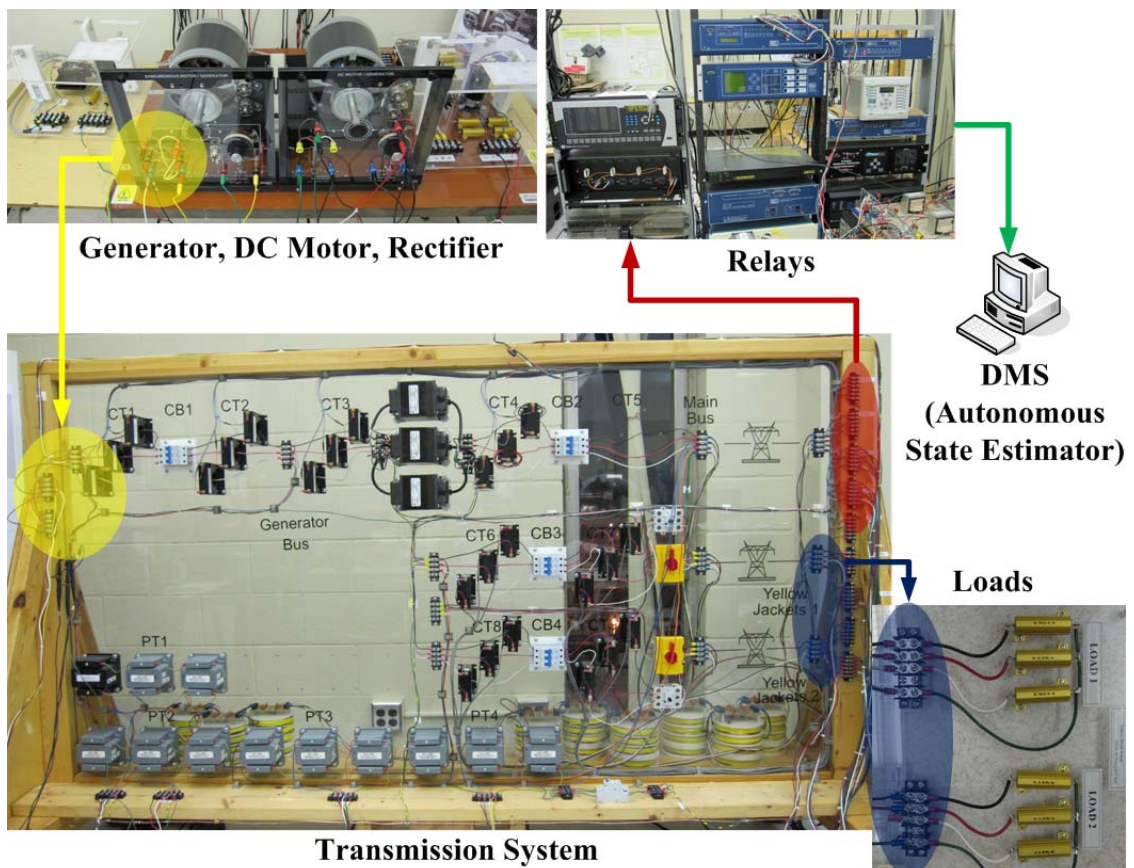


Figure 5.3: Actual interconnections among components.

The following sub-sections present detailed descriptions about several components such as transmission lines; instrumentation channels and relays; and a synchronous generator and a DC motor.

5.2.1.1 Transmission Lines

The transmission lines are designed based on a 2-mile section of three-phase actual lines with neutral conductors. Self and mutual inductances among four conductors and shunt capacitances are taken into account in designing the transmission lines. In more details, a 150 turns of a magnet wire per phase in a dielectric core generates the mutual inductances, and the capacitances of the lines are modeled using a printed circuit board with capacitors. The impedances are slightly different from each phase, so asymmetries are included in these transmission lines.

5.2.1.2 Instrumentation Channels and Relays

PTs and CTs are located in this scaled-model for relays to measure voltages and currents at various points. These relays send the measured data to an IEC61850 client in an autonomous state estimator. For interoperability, multi-vendor relays (e.g., GE-N60, GE-G60, SEL-421, and Arbiter 1133A) with the PMU capability are installed; most of relays can support time synchronism that uses the GPS signal. Especially, GE-G60 uses the GE Hard Fiber system, which is a merging unit that uses point-to-point fiber-optic cables to connect between relays and instrumentation channels. The Hard Fiber system can ultimately obsolete the use of copper lines and control cables.

5.2.1.3 Synchronous Generator and DC Motor

The test system includes a synchronous generator that provides three-phase power at 60Hz. Its prime mover is a DC motor that is connected to the synchronous-generator shaft through a belt. The generated voltage is elevated by a step-up transformer and supplied to the transmission system as illustrated in Figure 5.2. The power for the DC

motor is normally fed from building electricity through a rectifier, but it can be fed from *Feeder Bus-1*, thereby creating circulating power. Since the synchronous generator and the DC motor are connected to each other via the timing belt, the mechanical energy is transmitted from the DC motor to the synchronous generator. Figure 5.4 visually explains the connection between them.

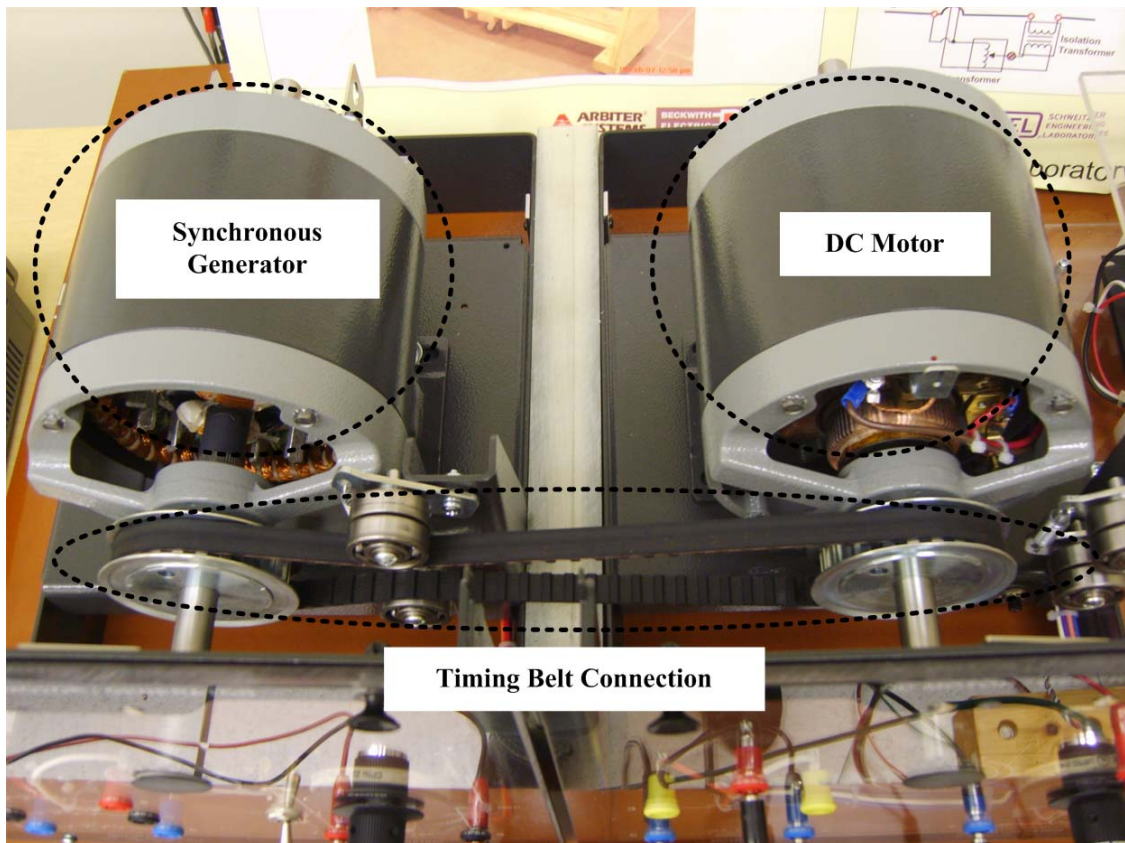


Figure 5.4: Mechanical connection between the synchronous generator and the DC motor.

5.2.2 Data-communication Infrastructure

An Ethernet-based communication infrastructure is installed in the test system for high-speed data communication between the relays and the autonomous state estimator. For this demonstration, IEC61850, an international standard for communication networks and systems in substations, is utilized. The interoperability of IEC61850 is one of the most essential features in situations where multi-vendor IEDs are installed.

Currently, there exists no UMPCU that provides all data sets in real time including connectivity, device models, and measurements. Commercially available relays can be reprogrammed to provide this capability. For the present demonstration, connectivity and device-model data of all devices are provided directly to the autonomous state estimator by pre-computation using the WinIGS [86], a power-system numerical simulator. This program uses the object-oriented-programming method, which indicates that all devices are modeled individually as objects. Therefore, each device has its own device model as well as unique connectivity names. Finally, the autonomous state estimator utilizes these device models and connectivity from the WinIGS to autonomously identify states and to create measurement models, expressed in equation (3.8). In the meantime, the measurement data are continuously streaming from the relays to the autonomous state estimator.

The communication scheme between the relays and the autonomous state estimator is described in Figure 5.5. The SISCO's AX-S4 MMS is implemented as a communication unit, and a grid monitoring system consists of an autonomous state estimator, database, and an OPC client; note that the OPC is a protocol that supports open connectivity for industrial automation. As shown in Figure 5.5, IEC61850 servers (e.g., relays) send data to an IEC61850 client in the communication unit, and then, the data are directly transferred to an OPC server in the same unit, which finally provides them to the OPC client.

It is necessary to point out that the OPC client can be installed in the same machine as the OPC server, or in another machine according to network topology and the customized scheme. In addition, many OPC clients can simultaneously access data stored in the OPC server. In this demonstration, both the grid monitoring system and the communication unit are installed and implemented in one computer.

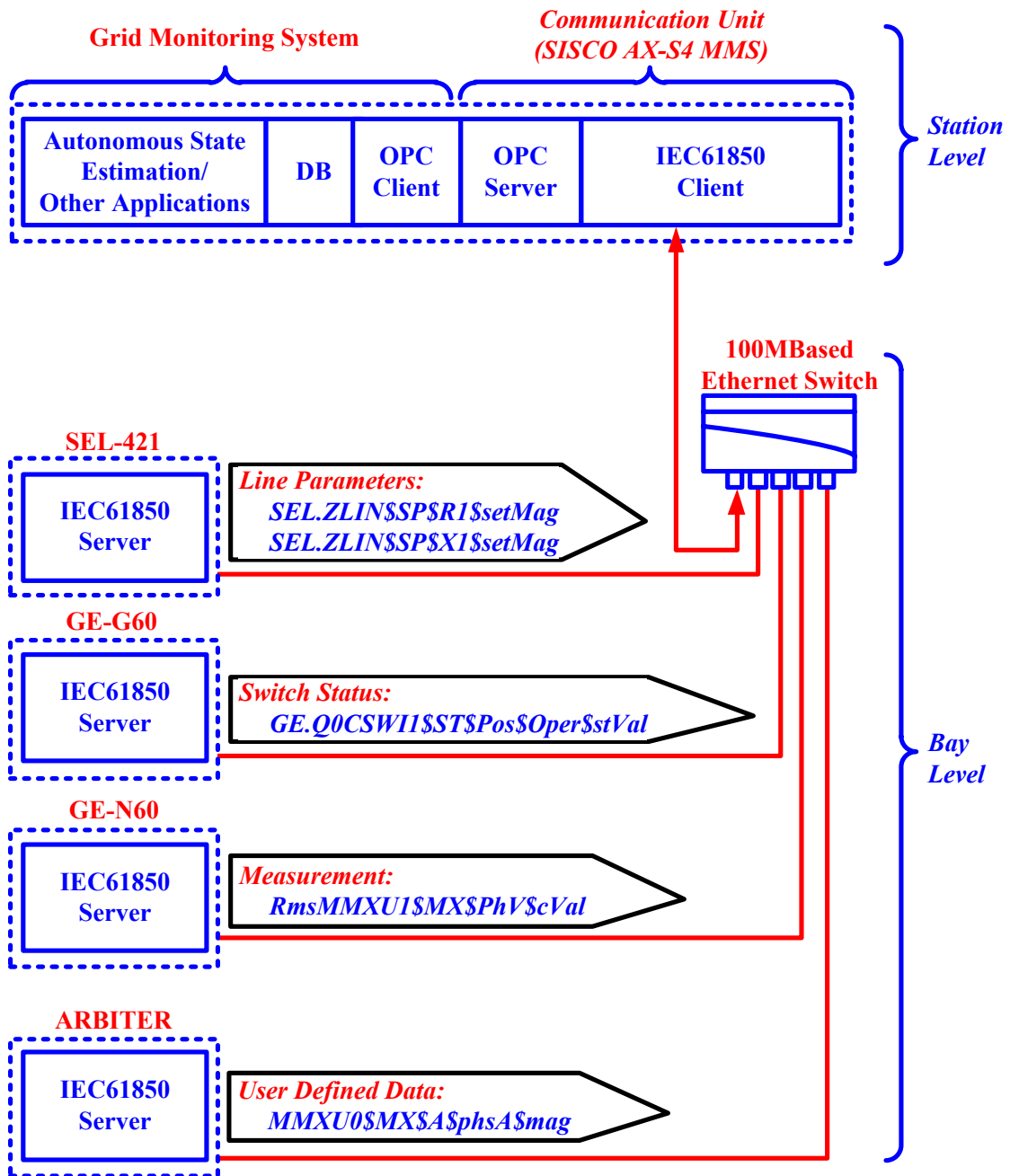


Figure 5.5: Communication scheme between the relays and the autonomous state estimator.

As shown in Figure 5.6, an OPC manager is developed to map LNs into the corresponding measurements for data collection. After this configuration of mapping, the OPC manager can periodically access to the IEC61850 server and retrieve the corresponding data.

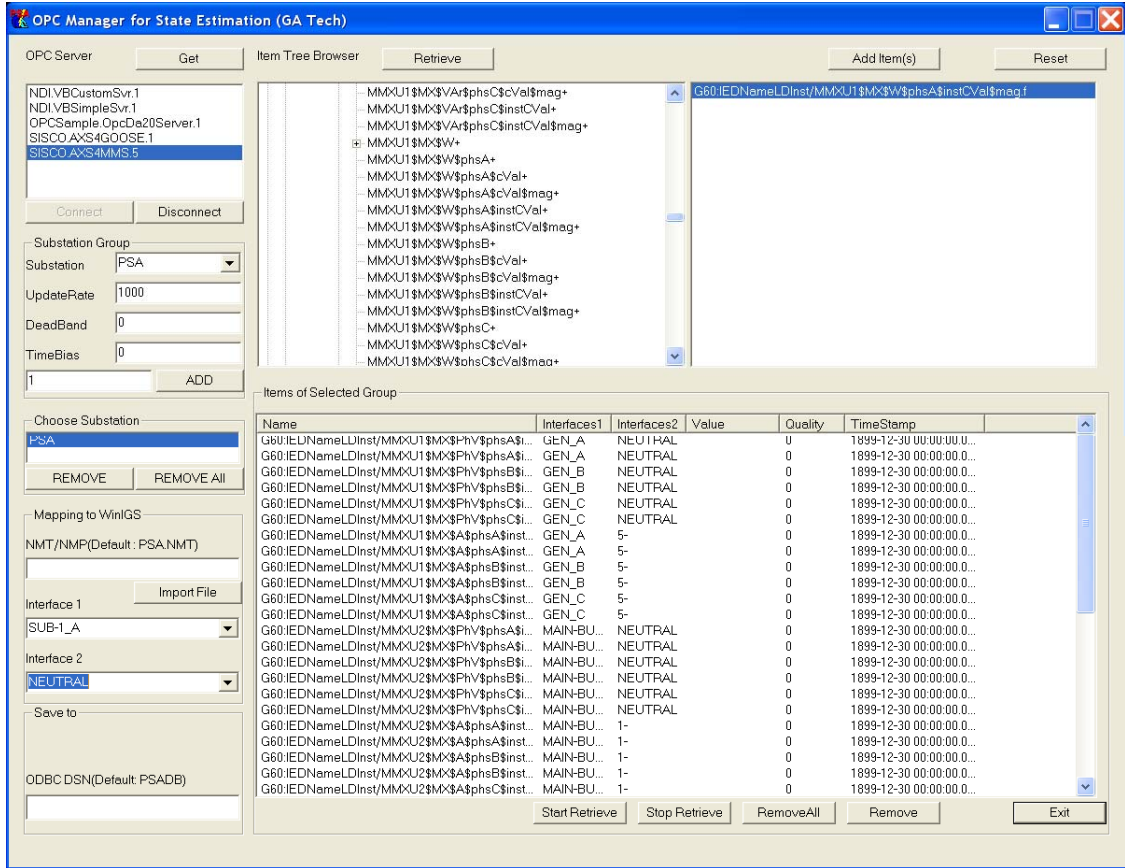


Figure 5.6: OPC manager.

For sharing data, a database system should be set up, so the demonstration uses ODBC, which is a standard database-access method developed by Microsoft Corporation, in order to connect between applications and the DBMS. The ODBC context allows many applications to access to database without understanding the unique interface of database.

5.2.3 Experimental Test

The scaled-down model, described in Figure 5.2, is utilized as a test-bed to perform autonomous state estimation. While the synchronous generator keeps supplying three-phase power to the transmission system, the relays continuously measure analog values through PTs or CTs and send digitized data to the DMS where the autonomous

state estimator is installed. This real-time monitoring system is finally evaluated in terms of time latency, the confidence level, and the errors of estimated state variables.

5.2.3.1 State and Measurement Setup

In Figure 5.2, the symbols V_1 , V_2 , V_3 , I_1 , I_2 , I_3 , and I_4 indicate measurement values that the relays are sampling and sending to the DMS. These particular values are three-phase phasor data. It is assumed that the autonomous state estimator operates in the generation substation only with data from the generation substation. Hence, the measurements V_4 and V_5 are not used as measurement data for this demonstration. Nevertheless, the voltages V_4 and V_5 can be estimated by introducing information (i.e., connectivity, device models, and measurements) of two transmission lines, which are denoted as *XLIN*E-2 and *XLIN*E-3.

For the autonomous state estimation of the test system, a total of 54 states and a total of 75 measurements are defined as listed in Table 5.1 and Table 5.2, respectively. In both the tables, the numbers in parenthesis indicate the number of the corresponding states or measurements. Note that each bus has 8 external states; one bus has four nodes (i.e., A , B , C , and N), and each phase has two states (i.e., the real and imaginary value). Likewise, all across and through measurements are based on three-phase phasor data. A total of 42 meter-based measurements are mapped to the 42 LNs defined in the format of IEC61850, and several relays stream the measurements into the autonomous state estimator at the rate of the x sets of data per second; note that x is user selected. As a result, the autonomous state estimator should be performed x times per second. The performance results will show that the present laboratory setup enables x to be up to three times per second. There was no attempt to optimize the system, but code optimization will eventually allow this system to perform autonomous state estimation as fast as 60 times per second.

Table 5.1: Definition of system states.

Type	Origin	Number
External states	$V_1 (8), V_2 (8), V_3 (8), V_4 (8), V_5 (8)$	40
Internal states	<i>SYNC-GEN</i> (6), <i>XFMR</i> (6)	12
Remote ground	<i>RGROUND</i> (2)	2
Total		54

Table 5.2: Definition of measurement data.

Type		Origin	Number
Meter-based	Across	$V_1 (6), V_2 (6), V_3 (6)$	18
Meter-based	Through	$I_1 (6), I_2 (6), I_3 (6), I_4 (6)$	24
Virtual	Kirchhoff	$-I_1 (6), -I_2 (6), -I_3-I_4 (6)$	18
Virtual	Device models	<i>SYNC-GEN</i> (6), <i>XFMR</i> (7), <i>RGROUND</i> (2)	15
Total			75

5.2.3.2 Performance Test

Time latency in data acquisition, database processing (i.e., recording and retrieving), and autonomous state estimation is measured to evaluate the performance of the overall approach. The results are tabulated in Table 5.3; the data-acquisition time means the elapsed time from when the DMS sends request signal to the relays until when the DMS receives all requested data. The latency time of the data collection is obtained by averaging the 60 trials, and the latency time of autonomous state estimation is a value that averages the 546 trials for about a minute. It is important to note that most of the time latency is due to database manipulations by the third-party software. A lesson learned is that in the next generation of this system, a direct method of streaming data should be implemented to drastically cut down the time latencies.

Table 5.3: Performance test in terms of time latency.

Type		Time (ms)
Data collection	Data-acquisition time	61.50
	Database-recording time	183.18
	Total	244.68
Autonomous state estimation	Database-retrieving time	57.94
	State identification and state estimation	21.03
	Total	78.97

5.2.3.3 State Estimation Results

The results of the performance test indicate that data collection requires at least 244.68ms and that it takes at least 78.97ms to perform autonomous state estimation. Based on these results, the initial settings for the real-time operation of autonomous state estimation are shown in Table 5.4. No attempt was made to optimize the timing performance. This will be the focus of the next generation of the test system.

Table 5.4: Initial settings for the real-time operation of autonomous state estimation.

Type	Setting value
Time interval of data collection	300ms
Time interval of autonomous state estimation	100ms
Weight of across measurement	1.0
Weight of through measurement	1.0
Weight of virtual measurement	0.1
Degrees of freedom	$75 - 54 = 21$

The proposed approach provides typical results from a one-minute test of the autonomous state estimator. During the test period, the state estimator was executed 60

times (i.e., once per second). The results are presented in the following two figures: Figure 5.7 illustrates a voltage measurement with its estimated values, and Figure 5.8 does a current measurement with its estimated values. Note that, in both the figures, the solid lines represent the estimated results, and the dotted lines describe the measured values. The differences between the measured and estimated values are mainly attributable to time latency resulted from serial data measurement and collection, which means that the 75 measurement data are not exactly time-synchronized. Another reason for the differences is that current measurements are not accurate, for the magnitude of currents is too small compared with the sensitivity of the sensors of the relays.

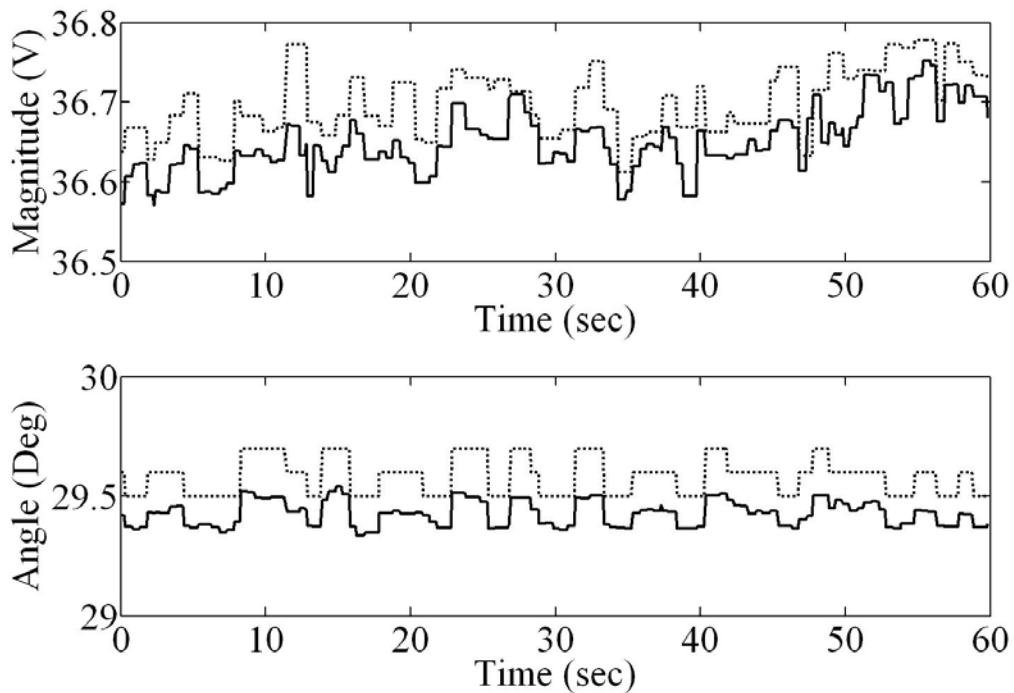


Figure 5.7: Estimated results of V_2 , the phase-A voltage measurement across *Main Bus* and *RGROUND*.

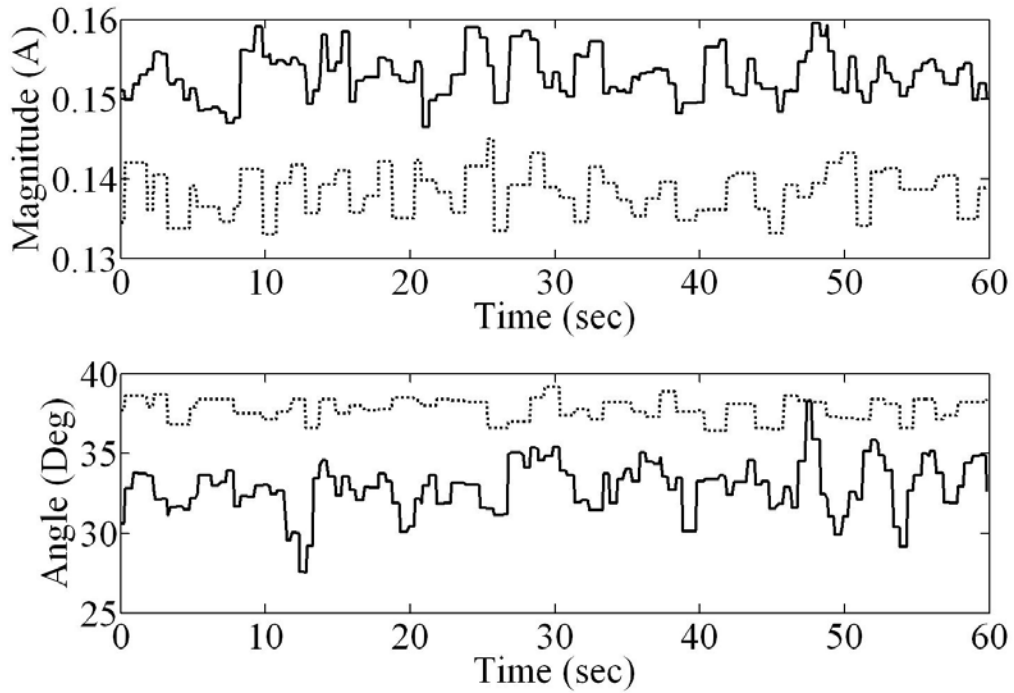


Figure 5.8: Estimated results of I_2 , the phase-A current measurement from *Main Bus* to *XLINe-1*.

Performance metrics of the autonomous state estimator are shown in the following three figures: Figure 5.9 illustrates the chi-square values (i.e., the sum of normalized residuals squared), Figure 5.10 represents the computed confidence level, and Figure 5.11 shows the average standard deviation of the error of the estimated states. It is important to note that the confidence level is almost 100% over the entire testing duration, which verifies that the estimated state variables are highly trustable.

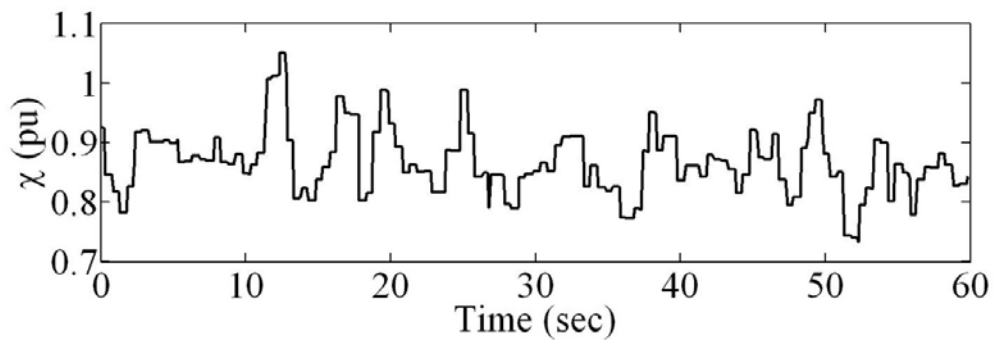


Figure 5.9: Chi-square critical values.

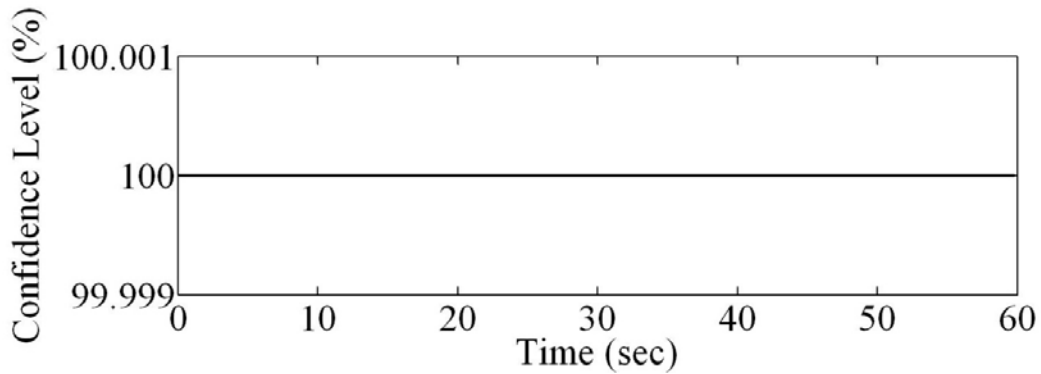


Figure 5.10: Confidence level.

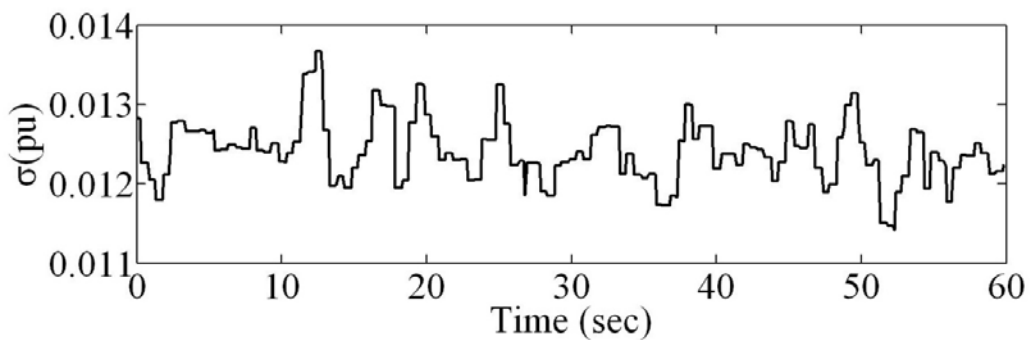


Figure 5.11: Average standard deviation of the error of the estimated states.

5.3 Laboratory Test System 2

The research work also presents the laboratory demonstration of the proposed autonomous state estimation using the smart grid energy system in NEC Laboratories America, Inc., which include a PV system, a programmable load that can emulate daily load profiles, and an energy-storage system that has three operational modes: (1) the standby mode, (2) the inverter mode, and (3) the charger mode. The objective of this demonstration is to verify whether autonomous state estimation can keep tracking of the multi-operational modes of the grid.

5.3.1 System Description

The smart grid energy system is designed to test the IPMS, which operates and controls energy systems that consist of renewable energy resources and energy-storage systems in accordance with various operational objectives (e.g., economic or

environmental dispatch). In this demonstration, autonomous state estimation is also implemented in the IPMS, to provide the accurate operating conditions in real time.

The overall system diagram is described in Figure 5.12. A PV system has a total of 21 PV panels, generating maximum 6kW, and a programmable load can simulate daily load profiles. Meanwhile, an energy-storage system with a maximum output of 10kW provides power to the system according to the optimization algorithms of the IPMS. The test system is connected to the main grid (i.e., the utility), exporting or importing the energy. The power flow can be measured by a grid meter at the point of connection to the main grid. Furthermore, an Arbiter relay, a PV inverter, the energy-storage system, the load, and Tigo Maximizers (i.e., MPPT devices) are streaming measurement data to a database system of the IPMS in real time.

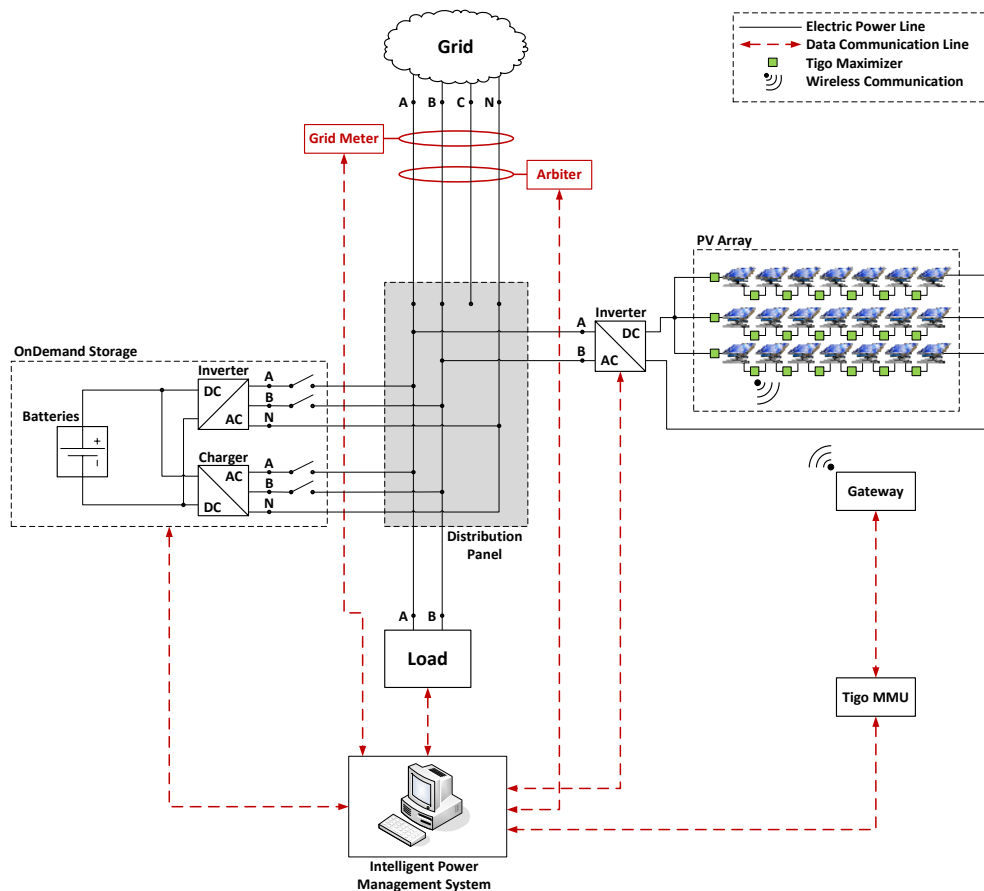


Figure 5.12: Diagram of the smart grid energy system.

The energy-storage system with four battery compartments has three modes: (1) the standby mode, (2) the inverter mode, and (3) the charger mode. In the standby mode, the DC-to-AC inverter and the AC-to-DC charger are disconnected from both the batteries and the grid; the switches at both the sides of the inverter and the charger are open as shown in Figure 5.13. Only small amount of power is consumed by a user display that is represented by the conductance G_B . In the inverter mode, the switches at both sides of the inverter are closed, but in the charger mode, the switches at both the sides of the charger are closed. Note that the autonomous state estimator in the IPMS should be able to automatically change the device model of the storage system according to its operation mode, to generate correct operating conditions. In this model, the conductances G_1 and G_2 are added to take into account the average power loss of the inverter and the charger, respectively.

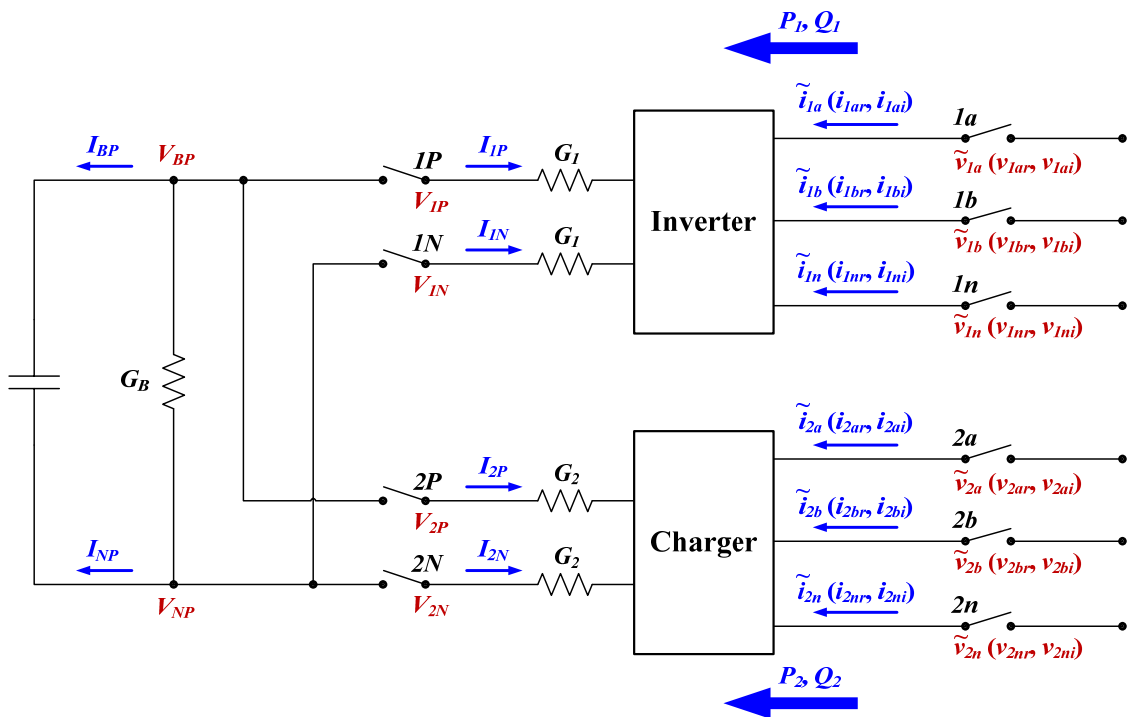


Figure 5.13: Detailed circuit of the storage system.

5.3.2 Test Scenarios

This laboratory demonstration is performed during one and a half days. With the programmable load, a usual daily profile is given during the test as depicted in Figure 5.14. Furthermore, Figure 5.15 represents the on and off status of the inverter and the charger; when the inverter mode or the charger mode is on (i.e., when the switches of both the sides of the inverter or the charger), the value of the inverter or the charger is one, respectively. Otherwise, the value is zero. As described in Figure 5.15, the inverter mode is on around 11am and 10pm on the first day, and then, the mode turns off after a certain time. Right after the inverter mode turns off, the charger mode is on around 11:40am and 23:50pm on the first day. After several hours, the charger mode turns off. It is necessary to point out that if both the charger and inverter mode turns off, the operational mode is standby.

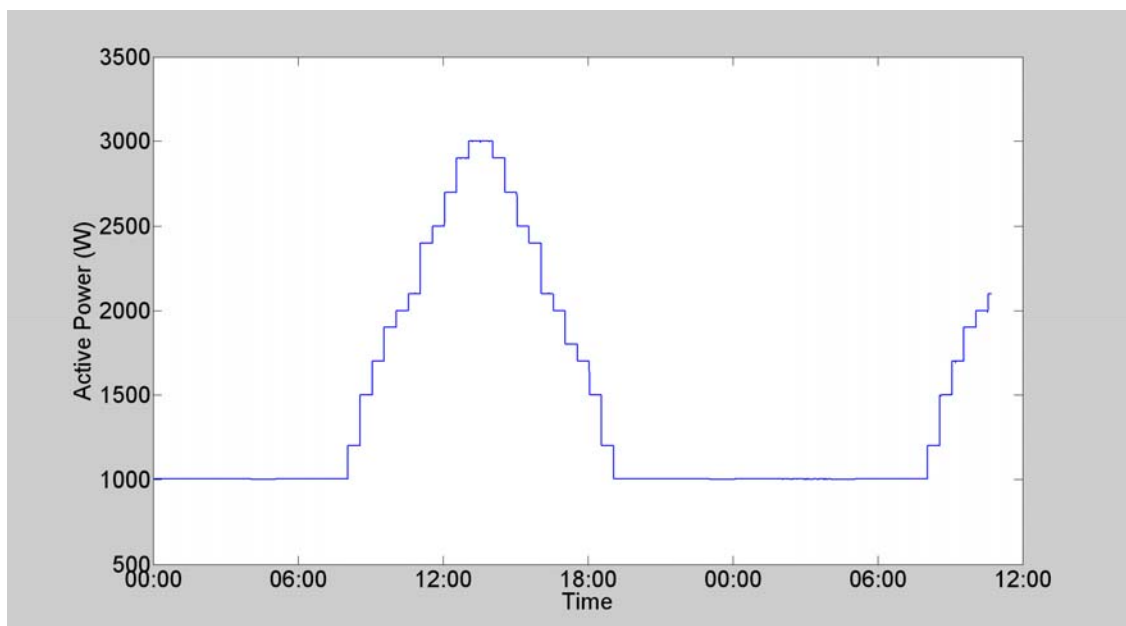


Figure 5.14: Daily load profile.

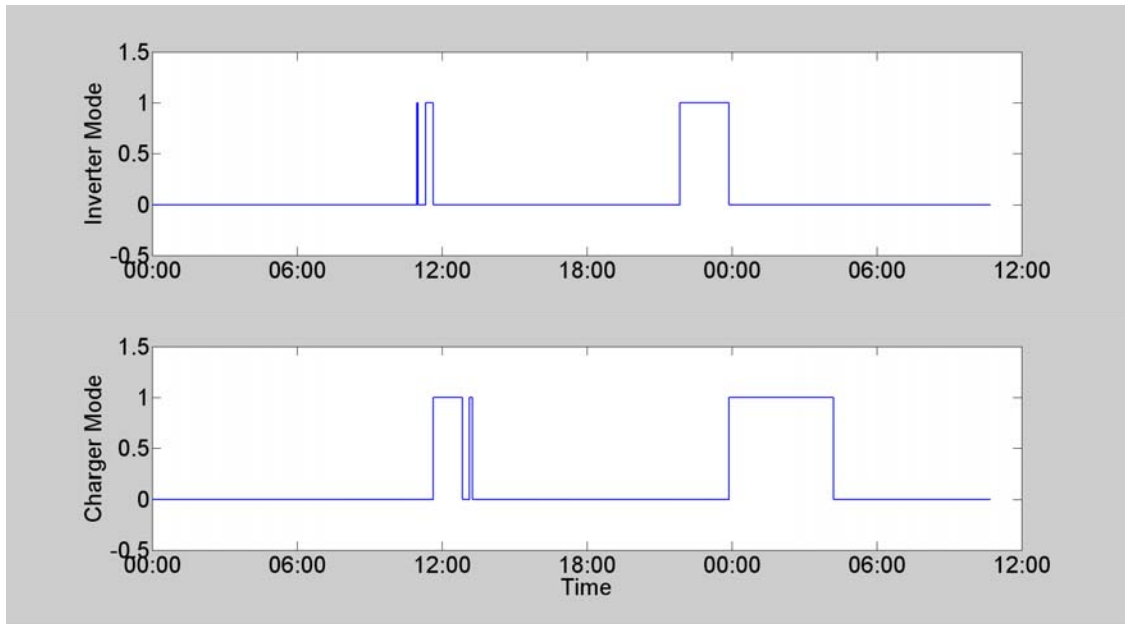


Figure 5.15: On and off status of the inverter and the charger in the energy-storage system.

For autonomous state estimation, the PV inverter, the load, and the energy-storage system are modeled and integrated. In other words, autonomous state estimation is performed with the integrated model of all three devices and the corresponding measurements. Finally, the estimated results can be evaluated from the two points of view: (1) the validation of the measurements and (2) the validation of the operational mode.

5.3.2.1 Validation of Measurements

If there are bad measurements, the statistical evaluation of autonomous state estimation would indicate the existence of bad data by producing the low confidence level. For this test scenario, the individual component is tested with the corresponding measurement data, and then, the integrated model of three devices is tested.

5.3.2.2 Validation of Operational Modes

The statistical evaluation of autonomous state estimation is capable of checking if the system under monitoring operates correctly according to its operational mode. In the test-bed, the energy-storage system has three operational modes, and therefore, the device

model of the system should be able to be changed according to the corresponding mode. Otherwise, the confidence level would be low, and then, it can be concluded that the actual operation of the system do not match the device model. A total of six test scenarios are listed in Table 5.5.

Table 5.5: Test cases.

Test Case	Actual Operation	Device Model
1	Inverter mode	Standby mode
2	Inverter mode	Charger mode
3	Charger mode	Standby mode
4	Charger mode	Inverter mode
5	Standby mode	Inverter mode
6	Standby mode	Charger mode

5.3.3 Experimental Test

The following sub-sections present the test results in terms of (1) the validation of measurements and (2) the validation of the operational mode of the system.

5.3.3.1 Test Results of the Validation of Measurements

For this laboratory demonstration, three devices that include the PV inverter, the load, and the energy-storage system are modeled. Then, each device is individually tested to validate the measurement data, and then, the integrated model of three devices is tested.

5.3.3.1.1 *PV Inverter*

The measured and estimated values of voltages measurements at the phases A and B are presented in Figure 5.16 and Figure 5.17, indicating that the estimated values are almost same as the measured ones. The blue solid line and red dotted line represent measured and estimated values, respectively.

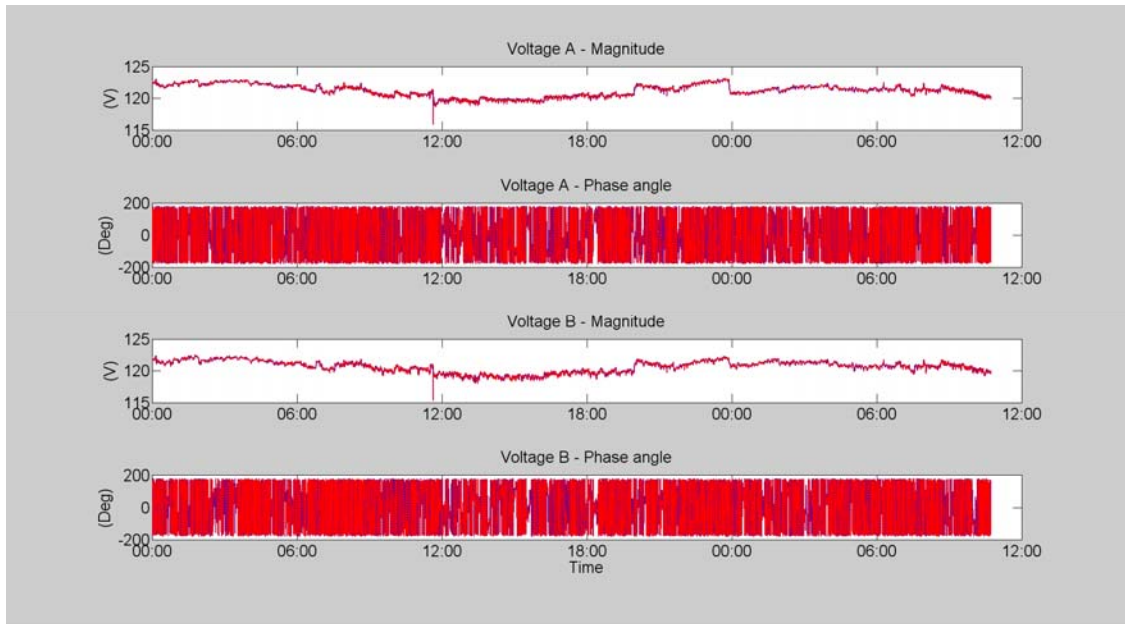


Figure 5.16: Measured and estimated values of voltage measurements at the phases A and B.

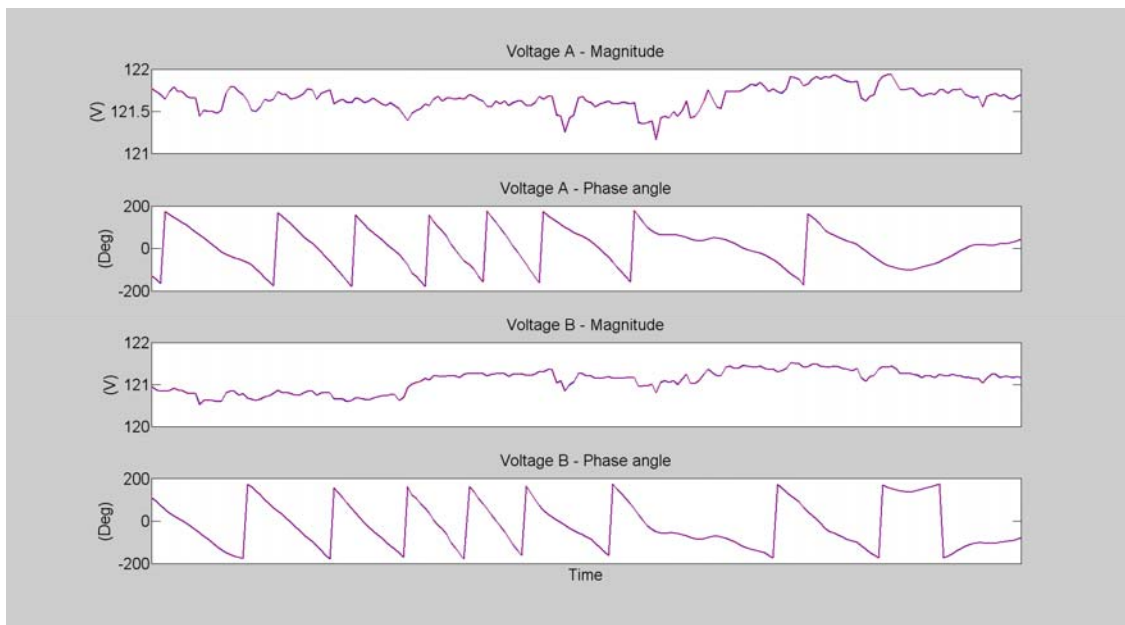


Figure 5.17: Measured and estimated values of voltage measurements at the phases A and B (zoomed in).

The measured and estimated values of the active-power measurement are presented in Figure 5.18 and Figure 5.19, indicating that the estimated values are almost same as the measured ones. The blue solid line and red dotted line represent measured and estimated values, respectively.

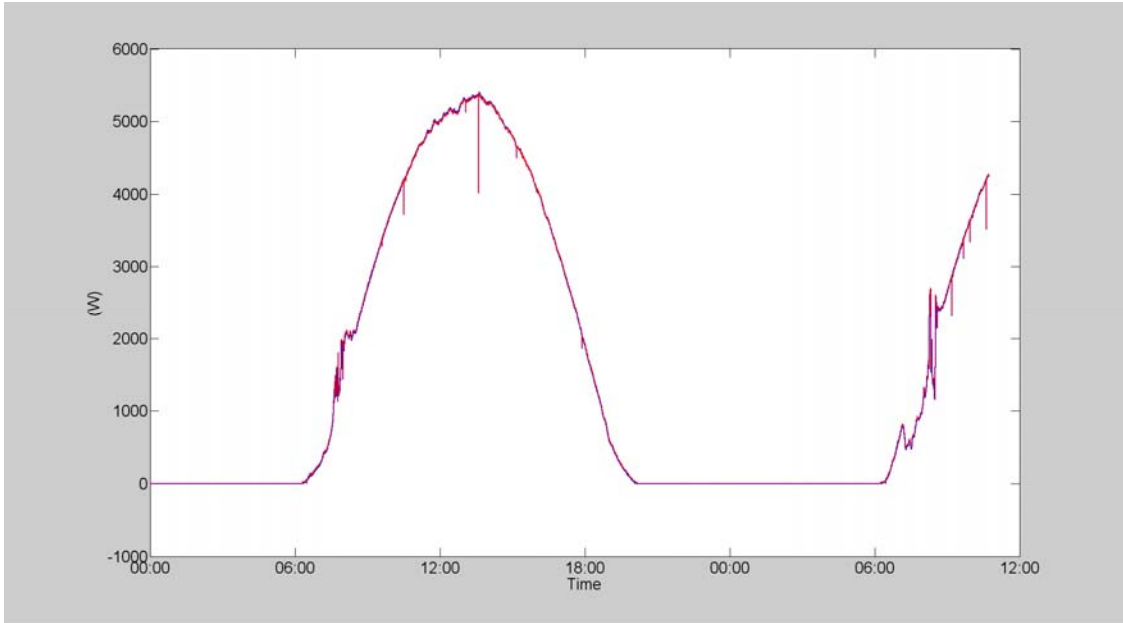


Figure 5.18: Measured and estimated values of the active-power measurement.

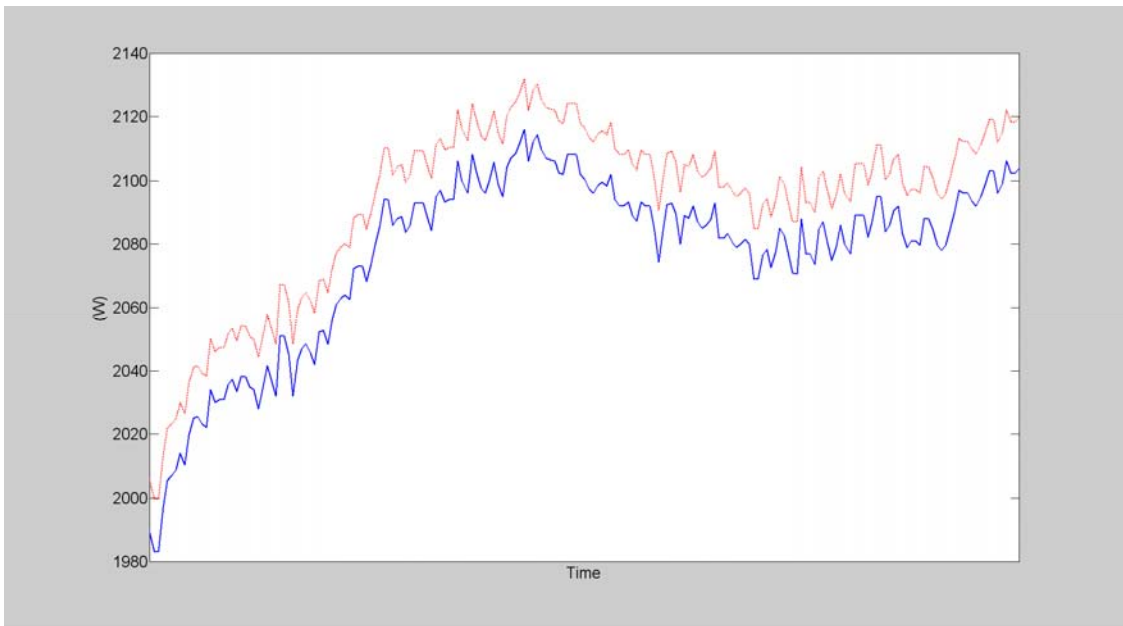


Figure 5.19: Measured and estimated values of the active-power measurement (zoomed in).

Finally, Figure 5.20 represents the confidence level, indicating that the confidence level is 100% over the testing period.

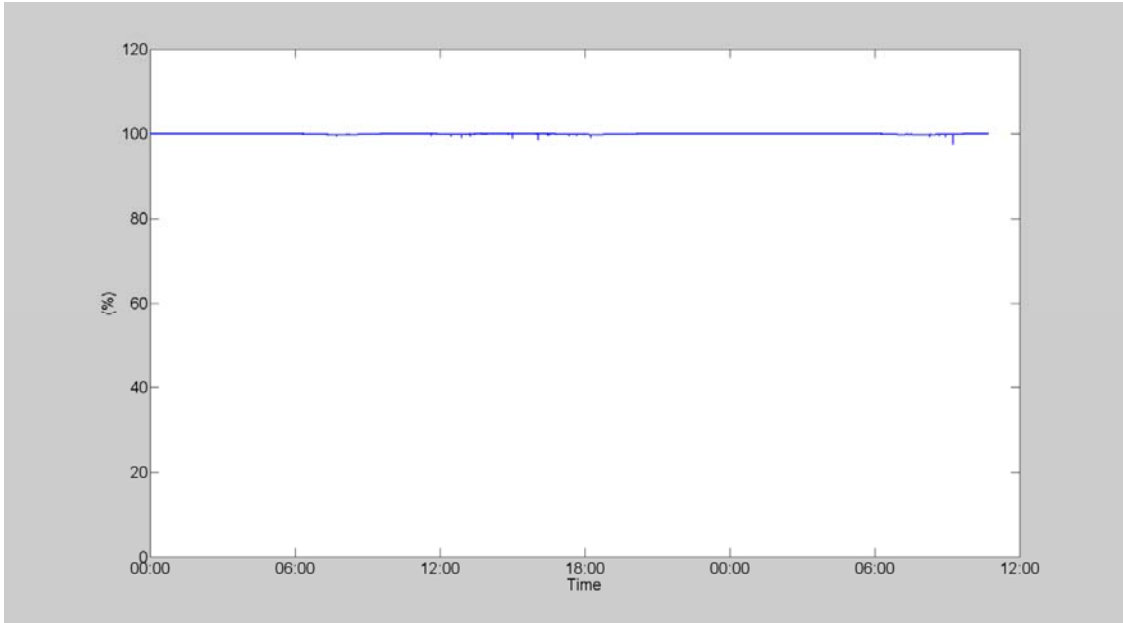


Figure 5.20: Confidence level in the test with the data of the PV inverter.

5.3.3.1.2 Load

The measured and estimated values of voltages measurements at the phases A and B are presented in Figure 5.21 and Figure 5.22, indicating that the estimated values are almost same as the measured ones. The blue solid line and red dotted line represent measured and estimated values, respectively.

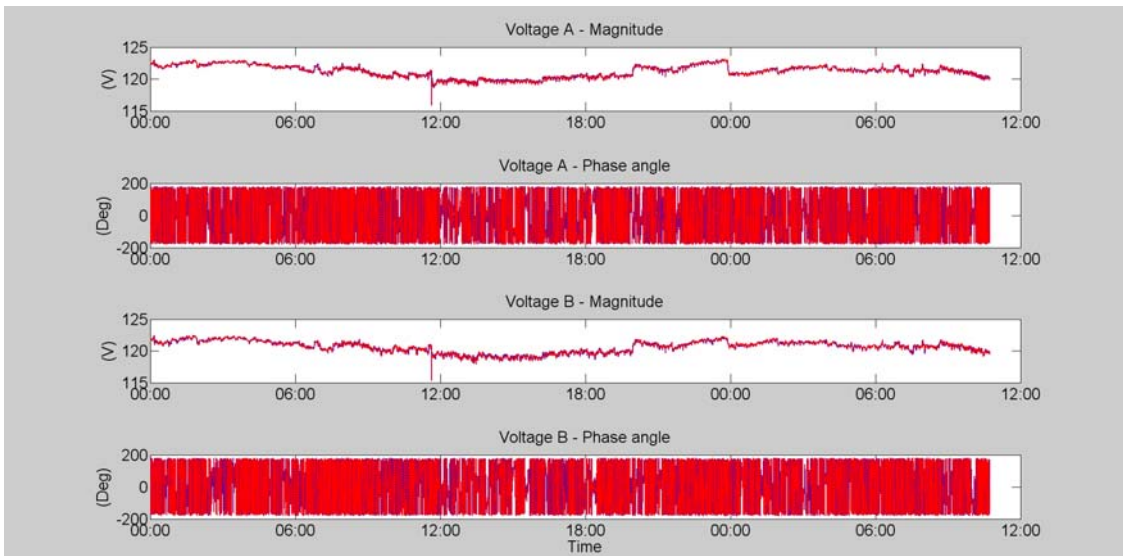


Figure 5.21: Measured and estimated values of voltage measurements at the phases A and B.

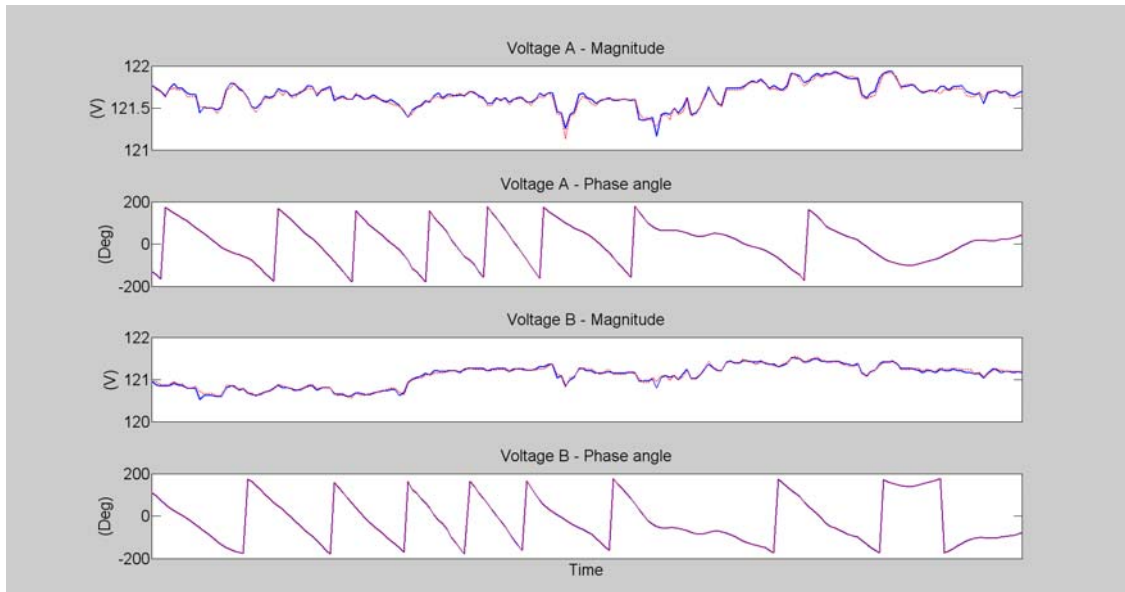


Figure 5.22: Measured and estimated values of voltage measurements at the phases A and B (zoomed in).

The measured and estimated values of the active-power measurement are presented in Figure 5.23 and Figure 5.24, indicating that the estimated values are almost same as the measured ones. The blue solid line and red dotted line represent measured and estimated values, respectively.

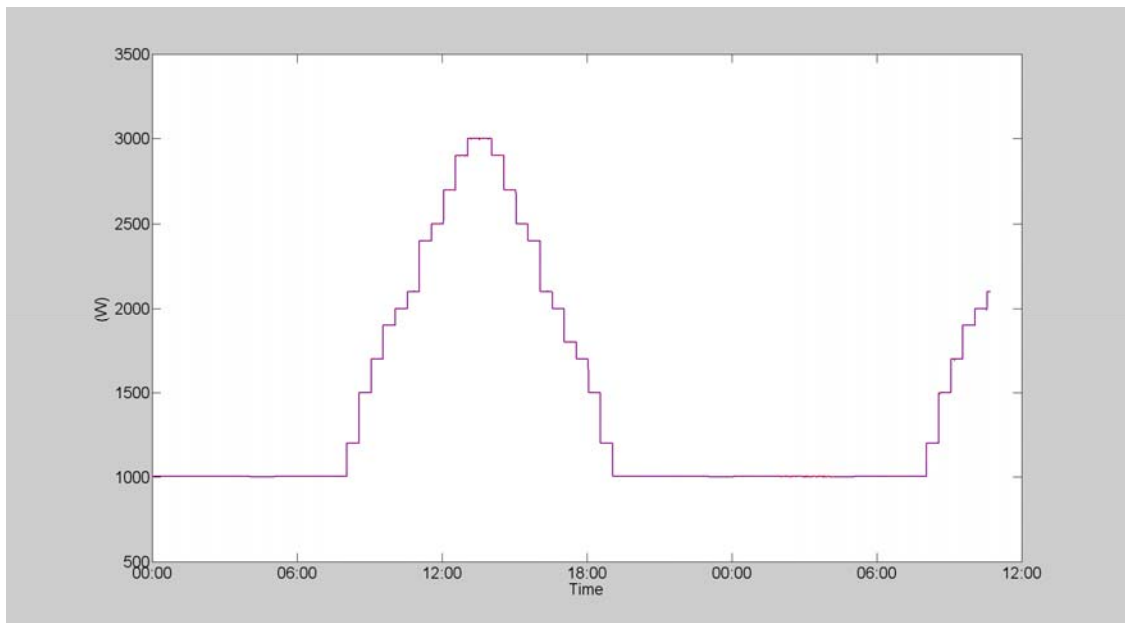


Figure 5.23: Measured and estimated values of the active-power measurement.

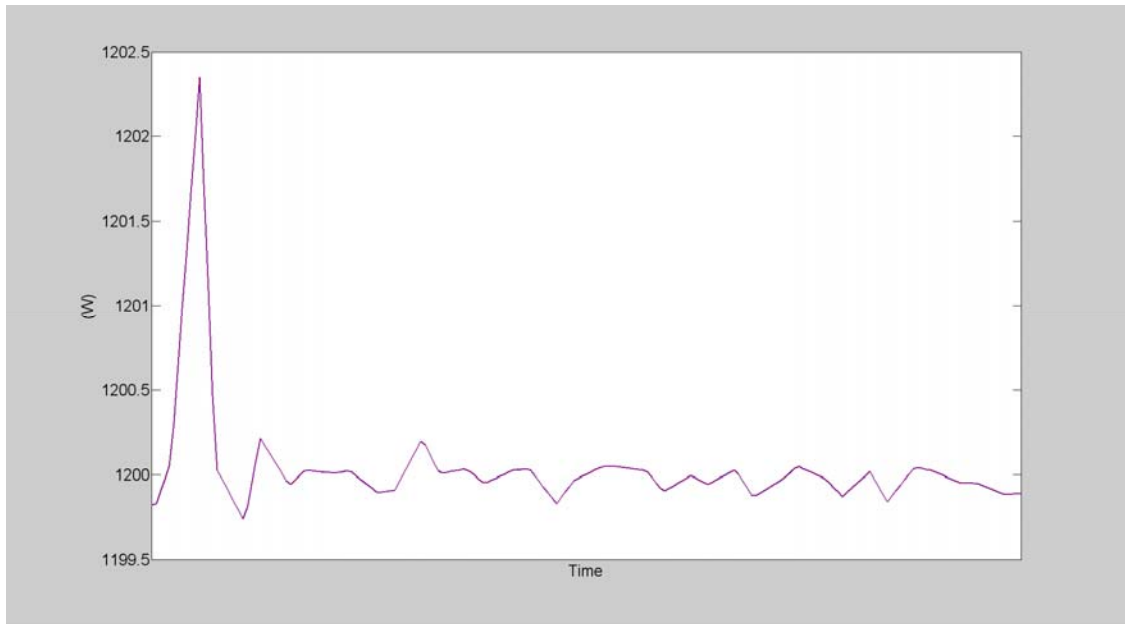


Figure 5.24: Measured and estimated values of the active-power measurement (zoomed in).

Finally, Figure 5.25 represents the confidence level, indicating that the confidence level is 100% over the testing period.

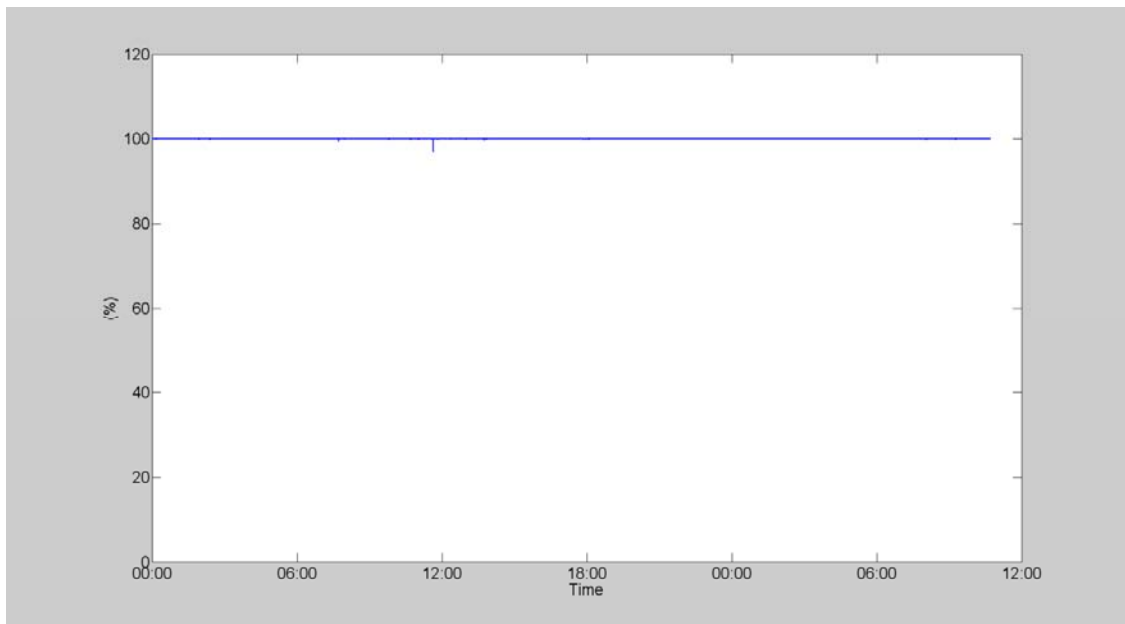


Figure 5.25: Confidence level in the test with the data of the load.

5.3.3.1.3 Energy-storage System

Figure 5.26 represents the confidence level over the testing period, indicating that the transient decrease of the confidence level occurs when the inverter or charger switch operates as marked with red circles. There are two reasons for this transient decrease: the first reason is that device models in use are based on the static model in the frequency domain, and the second one is that the sampling rate is not high enough to capture the transient moments. However, the transient period is very short, and thus, the low confidence level in the transients can be negligible unless fast-response controls are required.

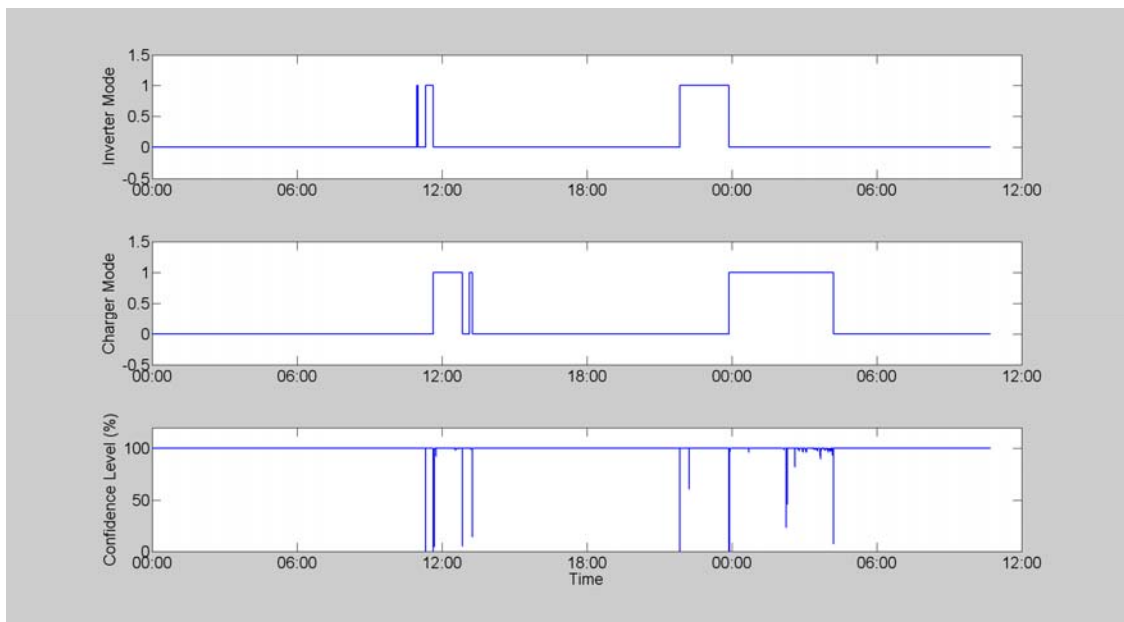


Figure 5.26: Confidence level in the test with the data of the energy-storage system.

Furthermore, it can be pointed out that when the charger mode turns on, the confidence level slightly decreases after a certain period of time. This behavior is marked with red circles in Figure 5.27, which also presents the measured values of the power input to the charger as well as the confidence level. In this figure, the acronyms CC and CV represent the constant-current mode and the constant-voltage mode, respectively.

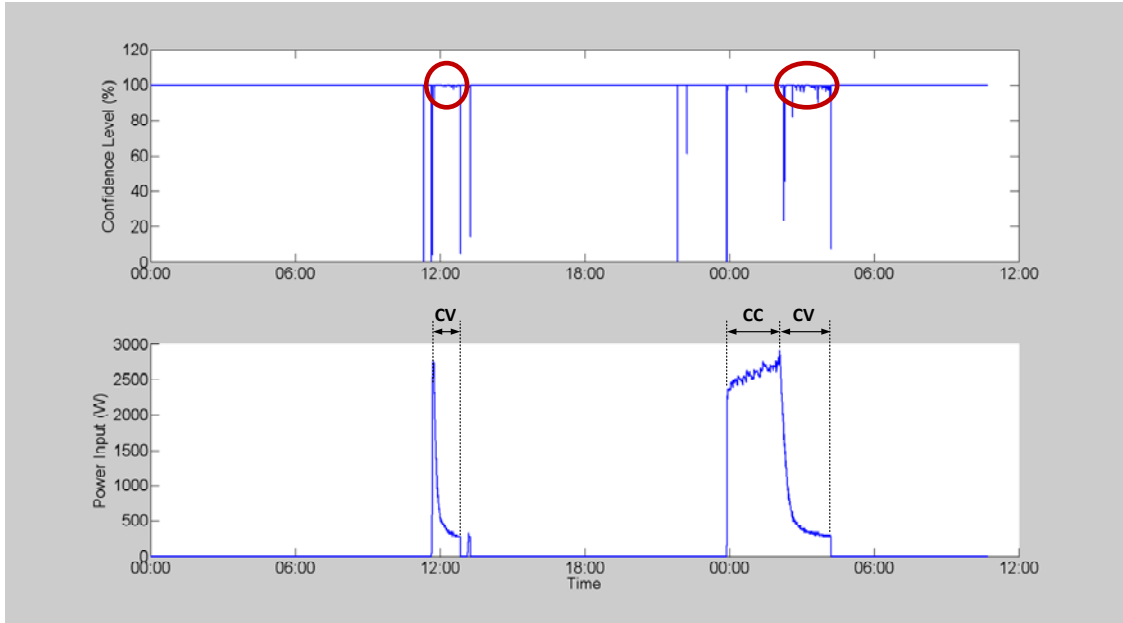


Figure 5.27: Power input to the charger with the confidence level.

Note that the confidence level is low when the storage system are in the constant-voltage charging mode, where the current that flows to batteries decreases significantly while the voltage keeps a constant level. In fact, power-electronics-interfaced devices such as inverters or chargers generate current harmonics, which eventually affect the accuracy of current or power measurements especially when the current magnitude or active power is relatively low. After all, in the constant-voltage mode, where a small amount of active-power flows to the charger, the confidence level could slightly decrease because the device model of the storage system, described in Figure 5.13, has several active-power-related equations including the following two equations:

$$0 = V_{1P}I_{1P} + V_{1N}I_{1N} - \frac{I_{1P}^2}{G_1} - \frac{I_{1N}^2}{G_1} + P_1, \quad (5.1)$$

$$0 = V_{2P}I_{2P} + V_{2N}I_{2N} - \frac{I_{2P}^2}{G_2} - \frac{I_{2N}^2}{G_2} + P_2. \quad (5.2)$$

5.3.3.1.4 Integrated Model

The device models of the PV inverter, the load, and the energy-storage system are integrated into one device model, which is, then, tested for autonomous state estimation. As a result, Figure 5.28 shows the confidence level, which is nearly 100% during the testing period but decrease temporarily at the transient moment of switch operations.

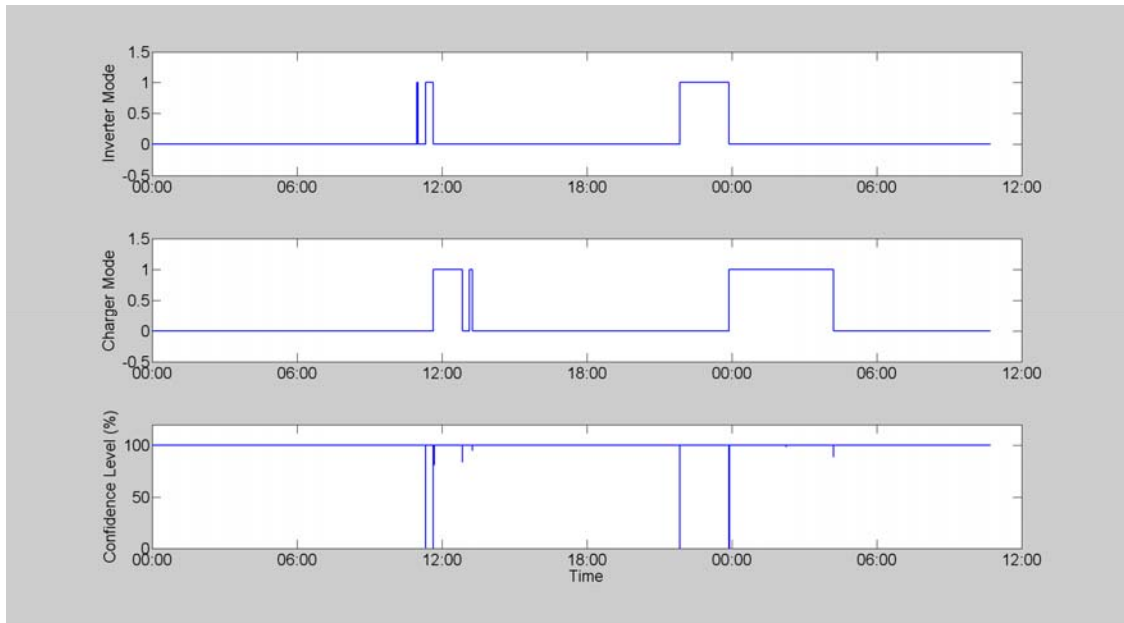


Figure 5.28: Confidence level in the test with the data of the integrated model.

5.3.3.2 Test Results of the Validation of Operational Modes

A total of six test scenarios are performed to verify if autonomous state estimation can keep tracking of the multi-operational modes of the test system. For these tests, the integrated device model of three devices (i.e., the PV inverter, the load, and the energy-storage system) is used.

5.3.3.2.1 *Inverter Operational Mode and Standby Device Model*

The first mismatch case is that the actual storage system operates in the inverter mode, but the device model is based on the standby mode. Figure 5.29 presents the confidence level, pointing out that the confidence level is almost zero during the period of the mismatch

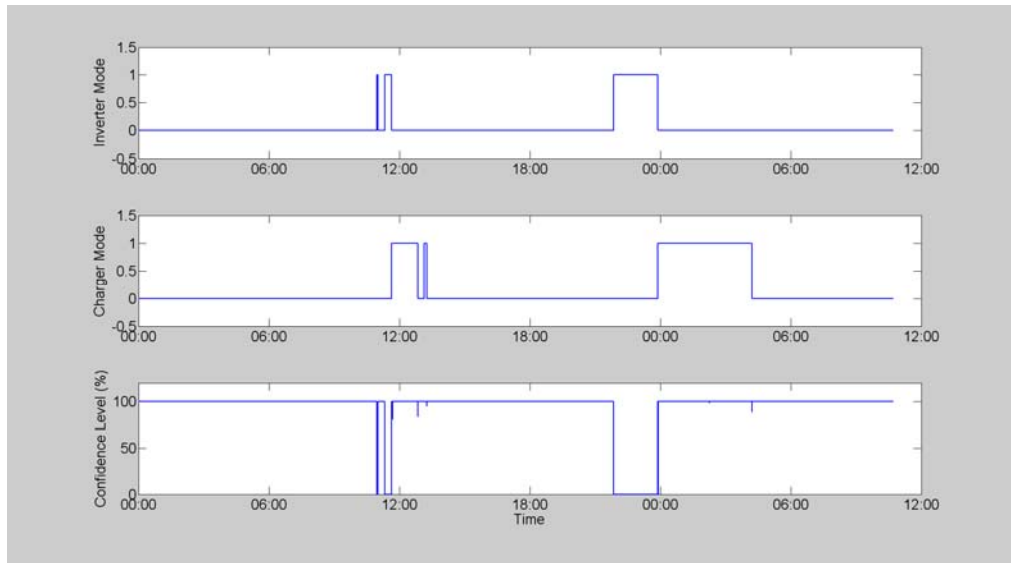


Figure 5.29: Confidence level in the first test case.

5.3.3.2.2 *Inverter Operational Mode and Charger Device Model*

The second mismatch case is that the actual storage system operates in the inverter mode, but the device model is based on the charger mode. In Figure 5.30, the confidence level becomes zero when the device model is inconsistent with the actual operational mode of the storage system.

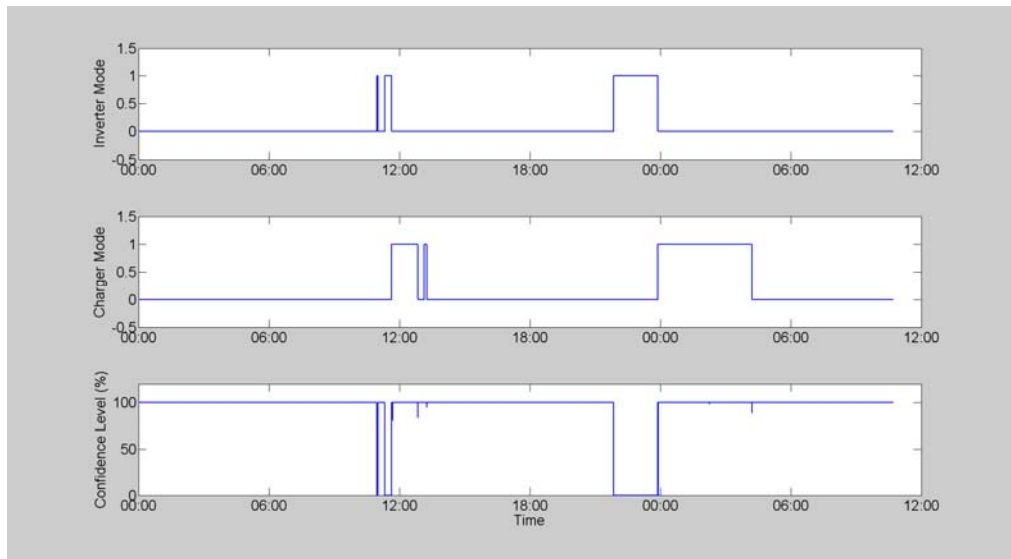


Figure 5.30: Confidence level in the second test case.

5.3.3.2.3 Charger Operational Mode and Standby Device Model

The third mismatch case is that the actual storage system operates in the charger mode, but the device model is based on the standby mode. As described in Figure 5.31, the confidence level is zero at the moment of the mismatch between the actual operational mode and the device model.

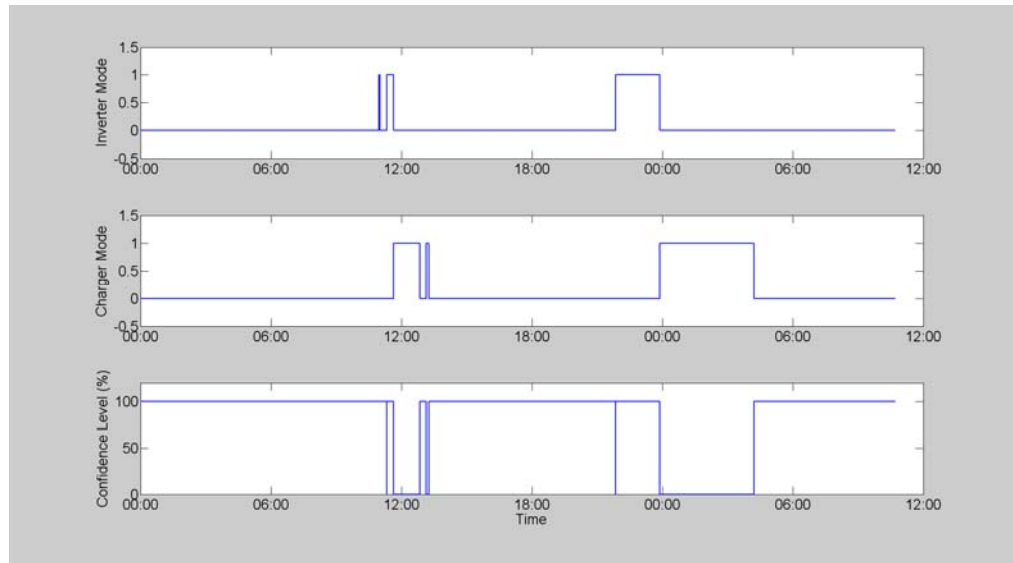


Figure 5.31: Confidence level in the third test case.

5.3.3.2.4 Charger Operational Mode and Inverter Device Model

The fourth mismatch case is that the actual storage system operates in the charger mode, but the device model is based on the inverter mode. The confidence level is presented in Figure 5.32, indicating that the confidence level is zero at the moment of the mismatch between the actual operational mode and the device model.

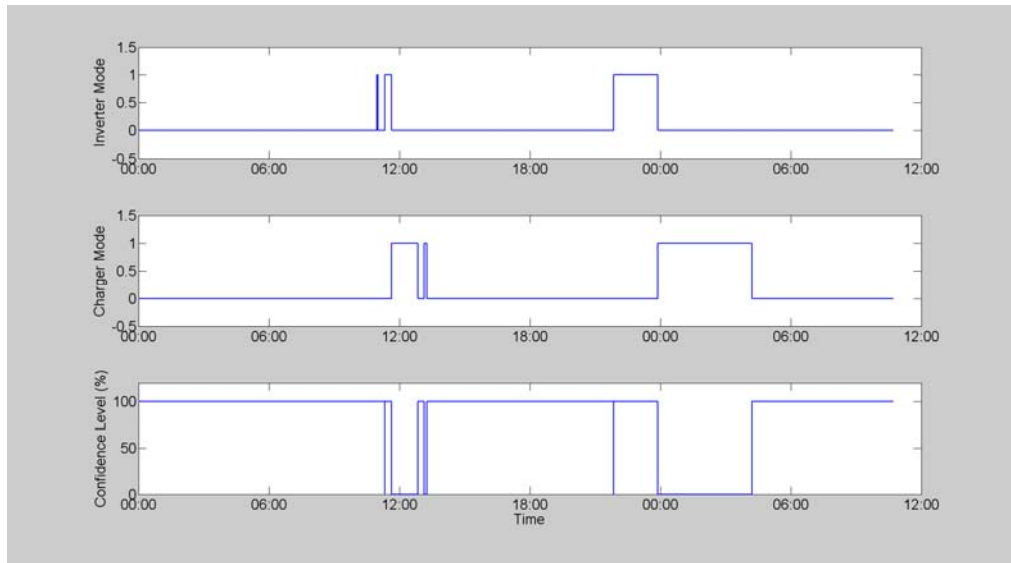


Figure 5.32: Confidence level in the fourth test case.

5.3.3.2.5 Standby Operational Mode and Inverter Device Model

The fifth mismatch case is that the actual storage system operates in the standby mode, but the device model is based on the inverter mode. The confidence level is presented in Figure 5.33, indicating that the confidence level is zero at the moment of the mismatch between the actual operational mode and the device model.

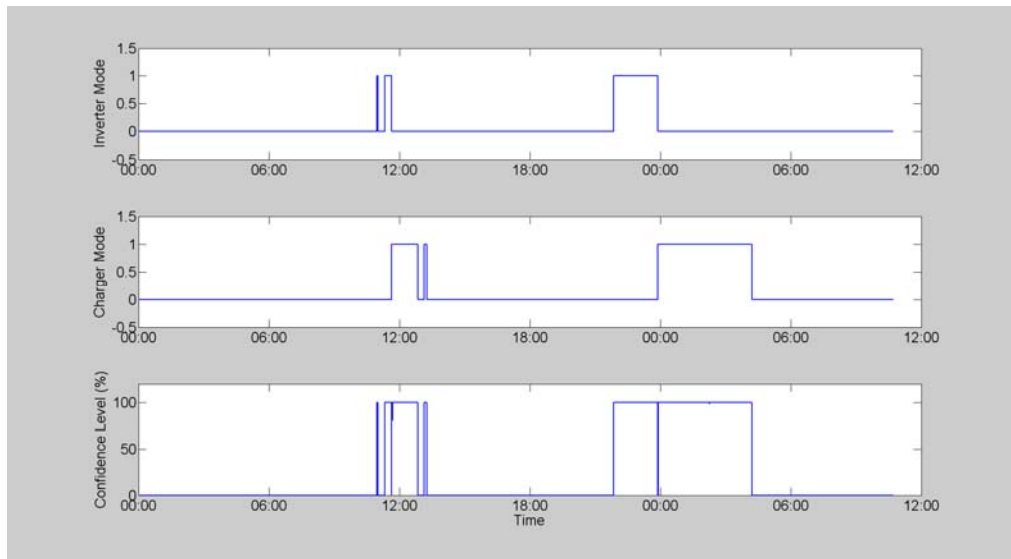


Figure 5.33: Confidence level in the fifth test case.

5.3.3.2.6 Standby Operational Mode and Charger Device Model

The sixth mismatch case is that the actual storage system operates in the standby mode, but the device model is based on the charger mode. The confidence level is presented in Figure 5.34, indicating that the confidence level is zero at the moment of the mismatch between the actual operational mode and the device model.

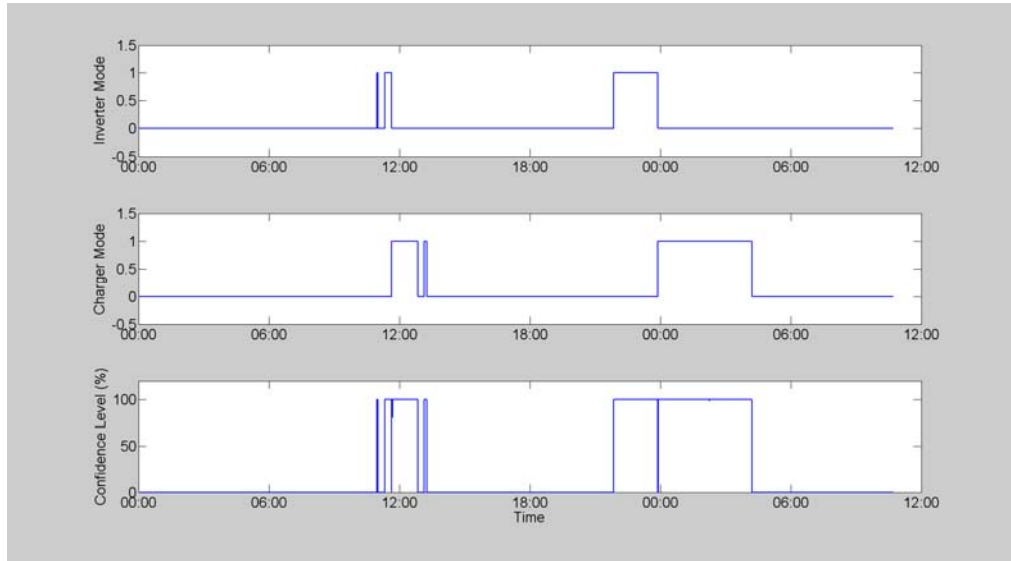


Figure 5.34: Confidence level in the sixth test case.

5.4 Summary

In this chapter, to verify autonomous state estimation at the laboratory level, two test-beds are used: (1) the scaled-down power system in the PSCAL at the Georgia Institute of Technology, and (2) the smart grid energy system in NEC Laboratories America, Inc.

The first laboratory test system consists of a synchronous generator, a DC motor, transmission lines, a step-up transformer, and resistive load, and the data-acquisition system (i.e., PTs, CTs, numerical relays, and merging units) is installed to collect measurement data from the system. For interoperability, the IEC61850 and Ethernet protocol are used for data communication. With connectivity and device models provided by the WinIGS, autonomous state estimation is performed, generating the trustable

operating conditions of the system with a confidence level of 100%. The performance of the autonomous state estimation is evaluated in terms of computational speed, the confidence level, and average standard deviation of the error of estimated values.

The second laboratory test system has PV panels, a PV inverter, a energy-storage system with four battery compartments, and a programmable load that can emulate daily load profiles. The energy-storage system has three operational modes: (1) the standby mode, (2) the inverter mode, and (3) the charger mode. On the concept of autonomous state estimation, the device model of the energy-storage system should be able to be changed in accordance with the modes, and the experimental test results prove that autonomous state estimation provides the correct operating conditions based on the multi-operational modes.

CHAPTER 6

FEASIBILITY STUDY: SETTING-LESS COMPONENT PROTECTION OF THE THREE-PHASE TRANSFORMER

6.1 Overview

This chapter presents the feasibility study of the setting-less component protection scheme with the three-phase, two-winding, variable-tap, and saturable-core transformer. First, hardware requirements and various possibilities for the proposed protection scheme are described, and then, numerical experiments are performed with an example test system and various test scenarios. For the numerical experiments, the WinIGS, a power-system numerical simulator, is used to generate measurement data in the format of COMTRADE, and typical performance results (e.g., the confidence level, the estimated states, the estimated values of measurements, and normalized residuals between estimated and measured values) are also stored in COMTRADE files.

6.2 Hardware Requirements

The best conditions for the proposed protection scheme are as follows: (1) the data-acquisition system is accurate, (2) measurements are time-synchronized, and (3) the data-communication system is as fast as possible so as to support the required throughput, which depends on the sampling rate.

First, the general data-acquisition system is shown in Figure 6.1. The accuracy of the data-acquisition system depends on the accuracy of each individual component in the data-acquisition channel. The most accurate instrument transformers are wound-type PTs for the voltage measurement and magnetic-core CTs for the current measurement. The instrument transformers are recommended to be the highest accuracy class.

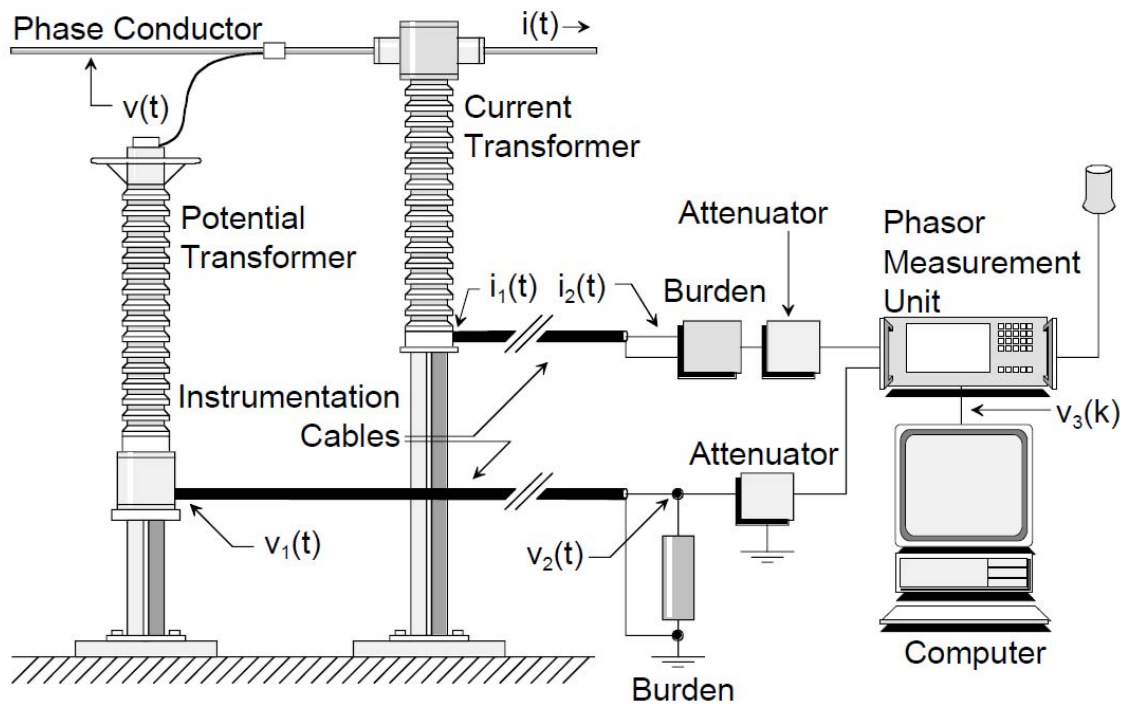


Figure 6.1: Typical data-acquisition system.

Second, the time synchronization of measurements should be satisfied to ensure the accuracy of measurements. Currently, GPS-synchronized measurements can be synchronized to the accuracy of better than one microsecond.

Finally, the communication system should provide fast data transmission to minimize time latency and should be able to meet throughput requirements so that data are continuously streaming into the processing unit.

When taking into account the three conditions aforementioned (i.e., accurate measurements, time synchronism, and fast data communication), two selections can be recommended. The first recommended selection includes a setting-less protection relay (or a UMPCU) with PMU capability, and PTs/CTs with the highest accuracy as described in Figure 6.2. The second recommended selection is related to near-future developments as shown in Figure 6.3. The introduction of merging units provides another alternative for the implementation of the proposed protection method. Indeed, the use of merging units

is advantageous for the proposed method, for measurements based on merging units are highly accurate.

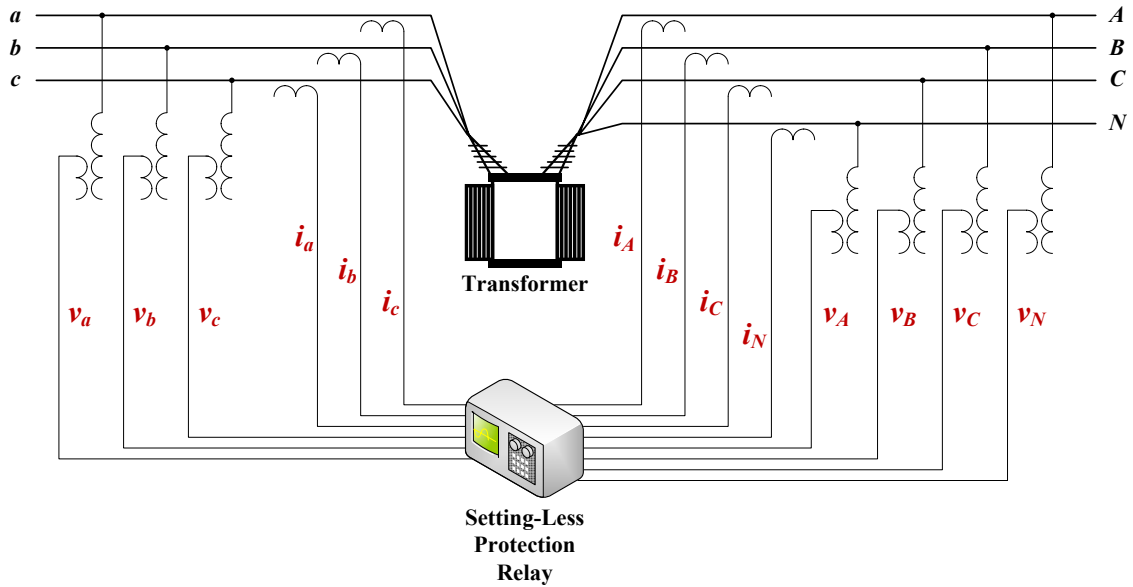


Figure 6.2: Recommended instrumentation and the data-acquisition system with cables.

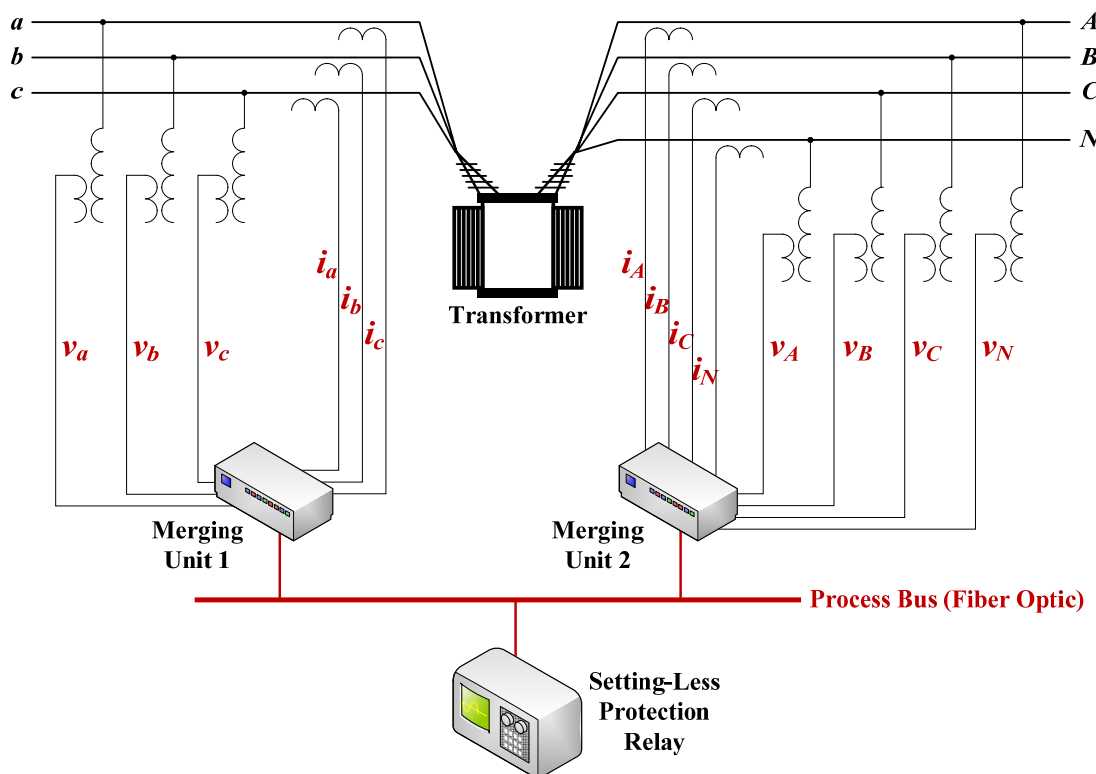


Figure 6.3: Secondary recommended instrumentation and the data-acquisition system with merging units and the process bus.

6.3 Implementation of the Proposed Protection Scheme

This section describes the implementation of the setting-less component protection of the three-phase, two-winding, variable-tap, and saturable-core transformer. The proposed protection algorithm is fundamentally based on dynamic state estimation, thus requiring the definition of the states of the transformer, the definition of measurements, the component dynamic model of the transformer, measurement-model formulation, dynamic state estimation, and finally the protection logic.

Among these, the component dynamic model of the three-phase transformer is presented in equation (C.52), which is developed in APPENDIX C, and the formulation of measurement models, dynamic state estimation, and the protection logic are described in Sections 4.4.3.2, 4.4.2.2, and 4.4.2.3 of CHAPTER 4, respectively.

The following sub-sections deals with the remaining parts of the implementation of the proposed protection method, including the definition of states and measurements.

6.3.1 Definition of States

For a three-phase, delta-wye-connected transformer, a total of 68 states are defined when the exponent n is five: 34 for the present time, t , and 34 for the intermediate time, t_m . The detailed descriptions of the states are listed in Table 6.1.

Table 6.1: All state variables for the three-phase, delta-wye-connected transformer when n is five.

State	Type	Time	Description
$x_1 = v_a(t)$	External	t	Phase-a terminal voltage at the primary side
$x_2 = v_b(t)$	External	t	Phase-b terminal voltage at the primary side
$x_3 = v_c(t)$	External	t	Phase-c terminal voltage at the primary side
$x_4 = v_A(t)$	External	t	Phase-A terminal voltage at the secondary side
$x_5 = v_B(t)$	External	t	Phase-B terminal voltage at the secondary side
$x_6 = v_C(t)$	External	t	Phase-C terminal voltage at the secondary side

$x_7 = v_N(t)$	External	t	Neutral terminal voltage at the secondary side
$x_8 = i_{mA}(t)$	Internal	t	Magnetizing current at the primary-side phase-a coil
$x_9 = e_A(t)$	Internal	t	Phase-a winding voltage at the primary side
$x_{10} = \lambda_A(t)$	Internal	t	Magnetic flux linkage at the phase-a core
$x_{11} = i_{1LA}(t)$	Internal	t	Phase-a terminal current at the primary side
$x_{12} = i_{3LA}(t)$	Internal	t	Phase-A terminal current at the secondary side
$x_{13} = y_{1A}(t)$	Internal	t	Additional state for the nonlinear term at the phase a
$x_{14} = y_{2A}(t)$	Internal	t	Additional state for the nonlinear term at the phase a
$x_{15} = y_{3A}(t)$	Internal	t	Additional state for the nonlinear term at the phase a
$x_{16} = z_A(t)$	Internal	t	Additional state for the nonlinear term at the phase a
$x_{17} = i_{mB}(t)$	Internal	t	Magnetizing current at the primary-side phase-b coil
$x_{18} = e_B(t)$	Internal	t	Phase-b winding voltage at the primary side
$x_{19} = \lambda_B(t)$	Internal	t	Magnetic flux linkage at the phase-b core
$x_{20} = i_{1LB}(t)$	Internal	t	Phase-b terminal current at the primary side
$x_{21} = i_{3LB}(t)$	Internal	t	Phase-B terminal current at the secondary side
$x_{22} = y_{1B}(t)$	Internal	t	Additional state for the nonlinear term at the phase b
$x_{23} = y_{2B}(t)$	Internal	t	Additional state for the nonlinear term at the phase b
$x_{24} = y_{3B}(t)$	Internal	t	Additional state for the nonlinear term at the phase b
$x_{25} = z_B(t)$	Internal	t	Additional state for the nonlinear term at the phase b
$x_{26} = i_{mC}(t)$	Internal	t	Magnetizing current at the primary-side phase-c coil
$x_{27} = e_C(t)$	Internal	t	Phase-c winding voltage at the primary side
$x_{28} = \lambda_C(t)$	Internal	t	Magnetic flux linkage at the phase-c core
$x_{29} = i_{1LC}(t)$	Internal	t	Phase-c terminal current at the primary side
$x_{30} = i_{3LC}(t)$	Internal	t	Phase-C terminal current at the secondary side
$x_{31} = y_{1C}(t)$	Internal	t	Additional state for the nonlinear term at the phase c

$x_{32} = y_{2c}(t)$	Internal	t	Additional state for the nonlinear term at the phase c
$x_{33} = y_{3c}(t)$	Internal	t	Additional state for the nonlinear term at the phase c
$x_{34} = z_c(t)$	Internal	t	Additional state for the nonlinear term at the phase c
$x_{35} = v_a(t_m)$	External	t_m	Phase-a terminal voltage at the primary side
$x_{36} = v_b(t_m)$	External	t_m	Phase-b terminal voltage at the primary side
$x_{37} = v_c(t_m)$	External	t_m	Phase-c terminal voltage at the primary side
$x_{38} = v_A(t_m)$	External	t_m	Phase-A terminal voltage at the secondary side
$x_{39} = v_B(t_m)$	External	t_m	Phase-B terminal voltage at the secondary side
$x_{40} = v_C(t_m)$	External	t_m	Phase-C terminal voltage at the secondary side
$x_{41} = v_N(t_m)$	External	t_m	Neutral terminal voltage at the secondary side
$x_{42} = i_{mA}(t_m)$	Internal	t_m	Magnetizing current at the primary-side phase-a coil
$x_{43} = e_A(t_m)$	Internal	t_m	Phase-a winding voltage at the primary side
$x_{44} = \lambda_A(t_m)$	Internal	t_m	Magnetic flux linkage at the phase-a core
$x_{45} = i_{1LA}(t_m)$	Internal	t_m	Phase-a terminal current at the primary side
$x_{46} = i_{3LA}(t_m)$	Internal	t_m	Phase-A terminal current at the secondary side
$x_{47} = y_{1A}(t_m)$	Internal	t_m	Additional state for the nonlinear term at the phase a
$x_{48} = y_{2A}(t_m)$	Internal	t_m	Additional state for the nonlinear term at the phase a
$x_{49} = y_{3A}(t_m)$	Internal	t_m	Additional state for the nonlinear term at the phase a
$x_{50} = z_A(t_m)$	Internal	t_m	Additional state for the nonlinear term at the phase a
$x_{51} = i_{mB}(t_m)$	Internal	t_m	Magnetizing current at the primary-side phase-b coil
$x_{52} = e_B(t_m)$	Internal	t_m	Phase-b winding voltage at the primary side
$x_{53} = \lambda_B(t_m)$	Internal	t_m	Magnetic flux linkage at the phase-b core
$x_{54} = i_{1LB}(t_m)$	Internal	t_m	Phase-b terminal current at the primary side
$x_{55} = i_{3LB}(t_m)$	Internal	t_m	Phase-B terminal current at the secondary side
$x_{56} = y_{1B}(t_m)$	Internal	t_m	Additional state for the nonlinear term at the phase b

$x_{57} = y_{2B}(t_m)$	Internal	t_m	Additional state for the nonlinear term at the phase b
$x_{58} = y_{3B}(t_m)$	Internal	t_m	Additional state for the nonlinear term at the phase b
$x_{59} = z_B(t_m)$	Internal	t_m	Additional state for the nonlinear term at the phase b
$x_{60} = i_{mC}(t_m)$	Internal	t_m	Magnetizing current at the primary-side phase-c coil
$x_{61} = e_C(t_m)$	Internal	t_m	Phase-c winding voltage at the primary side
$x_{62} = \lambda_C(t_m)$	Internal	t_m	Magnetic flux linkage at the phase-c core
$x_{63} = i_{1LC}(t_m)$	Internal	t_m	Phase-c terminal current at the primary side
$x_{64} = i_{3LC}(t_m)$	Internal	t_m	Phase-C terminal current at the secondary side
$x_{65} = y_{1C}(t_m)$	Internal	t_m	Additional state for the nonlinear term at the phase c
$x_{66} = y_{2C}(t_m)$	Internal	t_m	Additional state for the nonlinear term at the phase c
$x_{67} = y_{3C}(t_m)$	Internal	t_m	Additional state for the nonlinear term at the phase c
$x_{68} = z_C(t_m)$	Internal	t_m	Additional state for the nonlinear term at the phase c

6.3.2 Definition of Measurements

For the proposed transformer protection, the following measurements can be defined:

- Actual measurements: six voltages of phase a-N, phase b-N, phase c-N, phase A-N, phase B-N, and phase C-N at the time t ; seven currents of phase a, phase b, phase c, phase A, phase B, phase C, and phase N at the time t ; six voltages of phase a-N, phase b-N, phase c-N, phase A-N, phase B-N, and phase C-N at the time t_m ; and seven currents of phase a, phase b, phase c, phase A, phase B, phase C, and phase N at the time t_m . Typically, it is assumed that these measurements have measurement errors with standard deviation equal to 0.1pu.
- Virtual measurements: measurements induced from the component dynamic model of the three-phase transformer, which is expressed in equation (C.52). The 8th- to 34th-row and 42nd- to 68th-row equations in equation (C.52) can become

virtual measurements. Typically, it is assumed that these measurements have measurement errors with standard deviation equal to 0.01pu.

- Pseudo measurements: two phase N-g voltages at the times t and t_m . These measurements represent quantities that are not measured generally (e.g., the ground voltage and the neutral current). Typically, it is assumed that these measurements have measurement errors with standard deviation equal to 0.1pu.

Note that for the three-phase transformer, there are 26 actual measurements, 54 virtual measurements, and 2 pseudo measurements; there are a total of 82 measurements. It should be noted that there are 68 states, and therefore, this provides a redundancy of 20.6% [i.e., $(82-68)/68 \times 100$].

It is important to point out that when two consecutive sampling points are captured, the first point becomes a measurement for the intermediate time, t_m , and the second point becomes a measurement for the current time, t .

All across, through, virtual, and pseudo measurements that are used for the proposed setting-less component protection of the three-phase transformer are listed in Table 6.2, Table 6.3, Table 6.4, and Table 6.5, respectively.

Table 6.2: Actual across measurements for the three-phase transformer.

Type	Name	Measurement Model	Standard Deviation
Across	voltage_aN	$z_1 = v_a(t) - v_N(t)$	0.1 (p.u.) * Vscaleh
Across	voltage_bN	$z_2 = v_b(t) - v_N(t)$	0.1 (p.u.) * Vscaleh
Across	voltage_cN	$z_3 = v_c(t) - v_N(t)$	0.1 (p.u.) * Vscaleh
Across	voltage_AN	$z_4 = v_A(t) - v_N(t)$	0.1 (p.u.) * Vscalet
Across	voltage_BN	$z_5 = v_B(t) - v_N(t)$	0.1 (p.u.) * Vscalet
Across	voltage_CN	$z_6 = v_C(t) - v_N(t)$	0.1 (p.u.) * Vscalet
Across	voltage_aNm	$z_7 = v_a(t_m) - v_N(t_m)$	0.1 (p.u.) * Vscaleh
Across	voltage_bNm	$z_8 = v_b(t_m) - v_N(t_m)$	0.1 (p.u.) * Vscaleh

Across	voltage_cNm	$z_9 = v_c(t_m) - v_N(t_m)$	0.1 (p.u.) * Vscaleh
Across	voltage_ANm	$z_{10} = v_A(t_m) - v_N(t_m)$	0.1 (p.u.) * Vscalel
Across	voltage_BNm	$z_{11} = v_B(t_m) - v_N(t_m)$	0.1 (p.u.) * Vscalel
Across	voltage_CNm	$z_{12} = v_C(t_m) - v_N(t_m)$	0.1 (p.u.) * Vscalel

Vscaleh and Vscalel are the scales of the standard deviation of voltage measurements at the primary side and at the secondary side, respectively. These scales are typically determined according to their nominal values.

Table 6.3: Actual through measurements for the three-phase transformer.

Type	Name	Measurement Model	Standard Deviation
Through	current_a	$z_1 = i_a(t) = 1\text{st-row in equation (C.52)}$	0.01 (p.u.) * Iscaleh
Through	current_b	$z_2 = i_b(t) = 2\text{nd-row in equation (C.52)}$	0.01 (p.u.) * Iscaleh
Through	current_c	$z_3 = i_c(t) = 3\text{rd-row in equation (C.52)}$	0.01 (p.u.) * Iscaleh
Through	current_A	$z_4 = i_A(t) = 4\text{th-row in equation (C.52)}$	0.01 (p.u.) * Iscalel
Through	current_B	$z_5 = i_B(t) = 5\text{th-row in equation (C.52)}$	0.01 (p.u.) * Iscalel
Through	current_C	$z_6 = i_C(t) = 6\text{th-row in equation (C.52)}$	0.01 (p.u.) * Iscalel
Through	current_N	$z_7 = i_N(t) = 7\text{th-row in equation (C.52)}$	0.01 (p.u.) * Iscalel
Through	current_am	$z_8 = i_a(t_m) = 35\text{th-row in equation (C.52)}$	0.01 (p.u.) * Iscaleh
Through	current_bm	$z_9 = i_b(t_m) = 36\text{th-row in equation (C.52)}$	0.01 (p.u.) * Iscaleh
Through	current_cm	$z_{10} = i_c(t_m) = 37\text{th-row in equation (C.52)}$	0.01 (p.u.) * Iscaleh
Through	current_Am	$z_{11} = i_A(t_m) = 38\text{th-row in equation (C.52)}$	0.01 (p.u.) * Iscalel
Through	current_Bm	$z_{12} = i_B(t_m) = 39\text{th-row in equation (C.52)}$	0.01 (p.u.) * Iscalel
Through	current_Cm	$z_{13} = i_C(t_m) = 40\text{th-row in equation (C.52)}$	0.01 (p.u.) * Iscalel
Through	current_Nm	$z_{14} = i_N(t_m) = 41\text{st-row in equation (C.52)}$	0.01 (p.u.) * Iscalel

Isacleh and Isaclel are the scales of the standard deviation of current measurements at the primary side and at the secondary side, respectively. These scales are typically determined according to their nominal values.

Table 6.4: Virtual measurements for the three-phase transformer.

Type	Name	Measurement Model	Standard Deviation
Virtual	virtual_t_1	$z_1 = 0 = 8\text{th-row in equation (C.52)}$	0.01 (p.u.)
Virtual	virtual_t_2	$z_2 = 0 = 9\text{th-row in equation (C.52)}$	0.01 (p.u.)
Virtual	virtual_t_3	$z_3 = 0 = 10\text{th-row in equation (C.52)}$	0.01 (p.u.)
Virtual	virtual_t_4	$z_4 = 0 = 11\text{th-row in equation (C.52)}$	0.01 (p.u.)
Virtual	virtual_t_5	$z_5 = 0 = 12\text{th-row in equation (C.52)}$	0.01 (p.u.)
Virtual	virtual_t_6	$z_6 = 0 = 13\text{th-row in equation (C.52)}$	0.01 (p.u.)
Virtual	virtual_t_7	$z_7 = 0 = 14\text{th-row in equation (C.52)}$	0.01 (p.u.)
Virtual	virtual_t_8	$z_8 = 0 = 15\text{th-row in equation (C.52)}$	0.01 (p.u.)
Virtual	virtual_t_9	$z_9 = 0 = 16\text{th-row in equation (C.52)}$	0.01 (p.u.)
Virtual	virtual_t_10	$z_{10} = 0 = 17\text{th-row in equation (C.52)}$	0.01 (p.u.)
Virtual	virtual_t_11	$z_{11} = 0 = 18\text{th-row in equation (C.52)}$	0.01 (p.u.)
Virtual	virtual_t_12	$z_{12} = 0 = 19\text{th-row in equation (C.52)}$	0.01 (p.u.)
Virtual	virtual_t_13	$z_{13} = 0 = 20\text{th-row in equation (C.52)}$	0.01 (p.u.)
Virtual	virtual_t_14	$z_{14} = 0 = 21\text{st-row in equation (C.52)}$	0.01 (p.u.)
Virtual	virtual_t_15	$z_{15} = 0 = 22\text{nd-row in equation (C.52)}$	0.01 (p.u.)
Virtual	virtual_t_16	$z_{16} = 0 = 23\text{rd-row in equation (C.52)}$	0.01 (p.u.)
Virtual	virtual_t_17	$z_{17} = 0 = 24\text{th-row in equation (C.52)}$	0.01 (p.u.)
Virtual	virtual_t_18	$z_{18} = 0 = 25\text{th-row in equation (C.52)}$	0.01 (p.u.)
Virtual	virtual_t_19	$z_{19} = 0 = 26\text{st-row in equation (C.52)}$	0.01 (p.u.)
Virtual	virtual_t_20	$z_{20} = 0 = 27\text{nd-row in equation (C.52)}$	0.01 (p.u.)

Virtual	virtual_t_21	$z_{21} = 0 = 28\text{rd-row in equation (C.52)}$	0.01 (p.u.)
Virtual	virtual_t_22	$z_{22} = 0 = 29\text{th-row in equation (C.52)}$	0.01 (p.u.)
Virtual	virtual_t_23	$z_{23} = 0 = 30\text{th-row in equation (C.52)}$	0.01 (p.u.)
Virtual	virtual_t_24	$z_{24} = 0 = 31\text{st-row in equation (C.52)}$	0.01 (p.u.)
Virtual	virtual_t_25	$z_{25} = 0 = 32\text{nd-row in equation (C.52)}$	0.01 (p.u.)
Virtual	virtual_t_26	$z_{26} = 0 = 33\text{rd-row in equation (C.52)}$	0.01 (p.u.)
Virtual	virtual_t_27	$z_{27} = 0 = 34\text{th-row in equation (C.52)}$	0.01 (p.u.)
Virtual	virtual_tm_1	$z_{28} = 0 = 42\text{nd-row in equation (C.52)}$	0.01 (p.u.)
Virtual	virtual_tm_2	$z_{29} = 0 = 43\text{rd-row in equation (C.52)}$	0.01 (p.u.)
Virtual	virtual_tm_3	$z_{30} = 0 = 44\text{th-row in equation (C.52)}$	0.01 (p.u.)
Virtual	virtual_tm_4	$z_{31} = 0 = 45\text{th-row in equation (C.52)}$	0.01 (p.u.)
Virtual	virtual_tm_5	$z_{32} = 0 = 46\text{th-row in equation (C.52)}$	0.01 (p.u.)
Virtual	virtual_tm_6	$z_{33} = 0 = 47\text{th-row in equation (C.52)}$	0.01 (p.u.)
Virtual	virtual_tm_7	$z_{34} = 0 = 48\text{th-row in equation (C.52)}$	0.01 (p.u.)
Virtual	virtual_tm_8	$z_{35} = 0 = 49\text{th-row in equation (C.52)}$	0.01 (p.u.)
Virtual	virtual_tm_9	$z_{36} = 0 = 50\text{th-row in equation (C.52)}$	0.01 (p.u.)
Virtual	virtual_tm_10	$z_{37} = 0 = 51\text{st-row in equation (C.52)}$	0.01 (p.u.)
Virtual	virtual_tm_11	$z_{38} = 0 = 52\text{nd-row in equation (C.52)}$	0.01 (p.u.)
Virtual	virtual_tm_12	$z_{39} = 0 = 53\text{rd-row in equation (C.52)}$	0.01 (p.u.)
Virtual	virtual_tm_13	$z_{40} = 0 = 54\text{th-row in equation (C.52)}$	0.01 (p.u.)
Virtual	virtual_tm_14	$z_{41} = 0 = 55\text{th-row in equation (C.52)}$	0.01 (p.u.)
Virtual	virtual_tm_15	$z_{42} = 0 = 56\text{th-row in equation (C.52)}$	0.01 (p.u.)
Virtual	virtual_tm_16	$z_{43} = 0 = 57\text{th-row in equation (C.52)}$	0.01 (p.u.)
Virtual	virtual_tm_17	$z_{44} = 0 = 58\text{th-row in equation (C.52)}$	0.01 (p.u.)
Virtual	virtual_tm_18	$z_{45} = 0 = 59\text{th-row in equation (C.52)}$	0.01 (p.u.)

Virtual	virtual_tm_19	$z_{46} = 0 = 60\text{th-row in equation (C.52)}$	0.01 (p.u.)
Virtual	virtual_tm_20	$z_{47} = 0 = 61\text{st-row in equation (C.52)}$	0.01 (p.u.)
Virtual	virtual_tm_21	$z_{48} = 0 = 62\text{nd-row in equation (C.52)}$	0.01 (p.u.)
Virtual	virtual_tm_22	$z_{49} = 0 = 63\text{rd-row in equation (C.52)}$	0.01 (p.u.)
Virtual	virtual_tm_23	$z_{50} = 0 = 64\text{th-row in equation (C.52)}$	0.01 (p.u.)
Virtual	virtual_tm_24	$z_{51} = 0 = 65\text{th-row in equation (C.52)}$	0.01 (p.u.)
Virtual	virtual_tm_25	$z_{52} = 0 = 66\text{th-row in equation (C.52)}$	0.01 (p.u.)
Virtual	virtual_tm_26	$z_{53} = 0 = 67\text{th-row in equation (C.52)}$	0.01 (p.u.)
Virtual	virtual_tm_27	$z_{54} = 0 = 68\text{th-row in equation (C.52)}$	0.01 (p.u.)

Table 6.5: Pseudo measurements for the three-phase transformer.

Type	Name	Measurement Model	Standard Deviation
Pseudo	voltage_N	$z_1 = 0 = v_N(t)$	0.1 (p.u.) * Vscalel
Pseudo	voltage_Nm	$z_2 = 0 = v_N(t_m)$	0.1 (p.u.) * Vscalel

Note that if there is no through measurement for the neutral phase (i.e., the phase N), pseudo measurements for the phase-N current can be added.

6.4 Feasibility Test with Numerical Experiments

The setting-less component protection for the transformer is tested with the simulated data. Specifically, a test system was used to create a number of scenarios. For each scenario, the system was simulated, and measurements were generated and stored in COMTRADE files [87].

As a way to test the feasibility of the proposed setting-less component protection method, the WinIGS is used to create measurements and the component dynamic model of the three-phase transformer; the component dynamic model is provided in the form of matrices and vectors as expressed in equation (C.52) while measurement data are

generated in COMTRADE files. Then, both measurements and the component model become the input data of a setting-less protective relay that performs dynamic state estimation and protection logic. After processing all measurements data from the WinIGS, the protective relay yields test results, which includes the estimated states, the estimated values of the measurements, the raw measurements, the residuals between the estimated and measured values of the measurements, the normalized residuals, the degrees of freedom, the chi-square critical values, the confidence levels, and the processing time; note that these results are also stored in COMTRADE files. Figure 6.4 describes the overall approach for the feasibility test of the setting-less component protection algorithm.

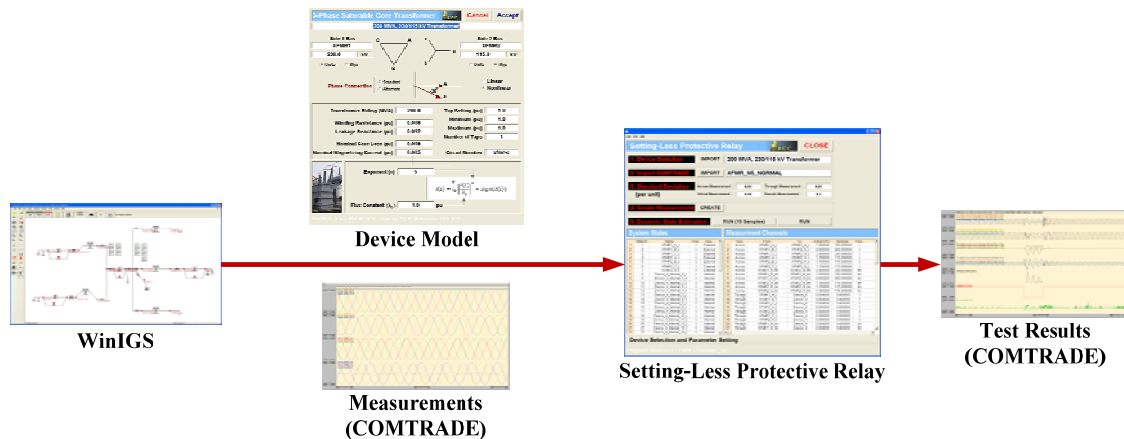


Figure 6.4: Feasibility test scheme for verifying the proposed protection method.

6.4.1 Example Test System and Test Scenarios

To test the feasibility of the proposed protection method, a test system that includes a three-phase transformer under protection and other components around the transformer is created as illustrated in Figure 6.5. The system consists of a 15kV-150MVA-rated generator, an 18kV-350MVA-rated generator, a 15kV-200MVA-rated generator, transformers, and transmission lines, and loads. The three-phase transformer under protection is located at the middle of the entire system, which is marked with a red circle in Figure 6.5; note that the red circle indicates the protection zone of the

transformer. Monitored are six voltages and seven currents at the terminals of the transformer.

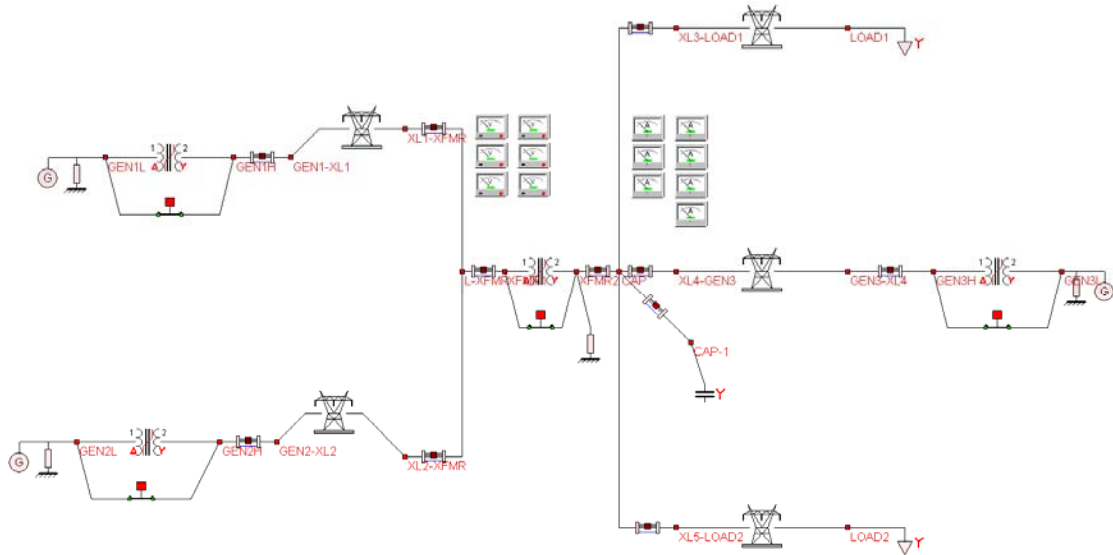


Figure 6.5: Test system for the proposed protection method.

In this test, the exponent n of equation (C.1), which expresses nonlinear characteristics between the magnetizing current and the flux linkage of the transformer core, is five, and the transformer is delta-wye-connected. The settings of the transformer under protection are shown in Figure 6.6.

3-Phase Saturable Core Transformer
AGC
Cancel
Accept

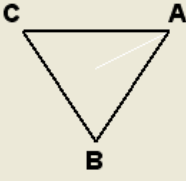
200 MVA, 230/115 kV Transformer

Side 1 Bus

XFMR1

230.0 kV

Delta Wye



Side 2 Bus

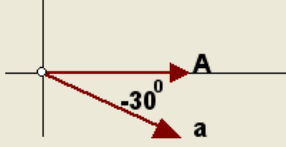
XFMR2

115.0 kV

Delta Wye

Phase Connection

Standard Alternate



Linear Nonlinear

Transformer Rating (MVA)	200.0	Tap Setting (pu)	1.0
Winding Resistance (pu)	0.006	Minimum (pu)	1.0
Leakage Reactance (pu)	0.092	Maximum (pu)	1.0
Nominal Core Loss (pu)	0.005	Number of Taps	1
Nominal Magnetizing Current (pu)	0.005	Circuit Number	xfmr-c



Exponent (n) 5

Flux Constant (λ_0) 1.0 pu

$$i(t) = i_0 \left| \frac{\lambda(t)}{\lambda_0} \right|^n \times \text{sign}(\lambda(t))$$

WinIGS-T - Form: IGS_M173_N - Copyright ?A. P. Meliopoulos 1998-2011

Figure 6.6: Settings of the three-phase transformer under protection.

The actual parameters of the single-phase transformer model in Figure C.1 are given in Table 6.6; these parameters are applicable to every phase of the three-phase transformer.

Table 6.6: Transformer parameters.

Parameter	Value	Parameter	Value
r_1	2.3805 Ω	r_c	158700 Ω
L_1	0.096822 H	L_m	420.964824 H
r_2	0.198375 Ω	i_0	0.002050
L_2	0.008068 H	λ_0	0.862803
N	0.288675		

Note that the scales of the standard deviations of measurements are defined as follows:

$V_{scaleh} = 230$, $V_{scalel} = 115$, $I_{scaleh} = 0.4$, and $I_{scalel} = 0.8$.

Five sets of different test scenarios are tested using the setting-less component protection scheme:

- Test A: the normal operating condition,
- Test B: transformer energization (inrush current),
- Test C: transformer overexcitation,
- Test D: the through-fault condition,
- Test E: the internal-fault condition.

6.4.1.1 Test A: Normal Operating Condition

For the normal operating condition, the test system in Figure 6.5 is used. A set of measurement signals that are monitored during the normal operating condition is shown in Figure 6.7.

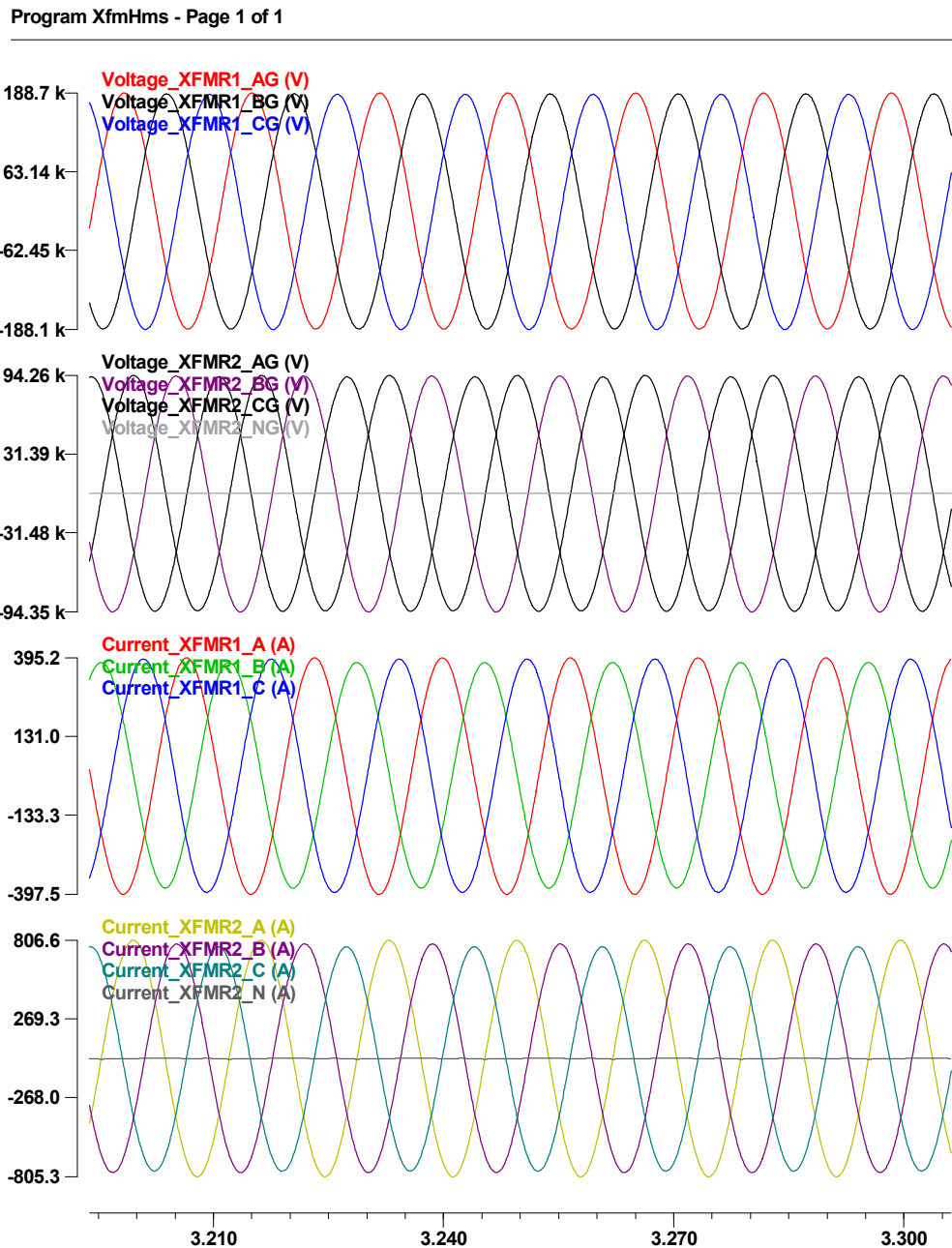


Figure 6.7: Measurements of the transformer (test A: the normal operating condition).

6.4.1.2 Test B: Transformer Energization (Inrush Current)

For transformer energization, the test system in Figure 6.5 is used. A set of measurement signals that are monitored during the energization is shown in Figure 6.8.

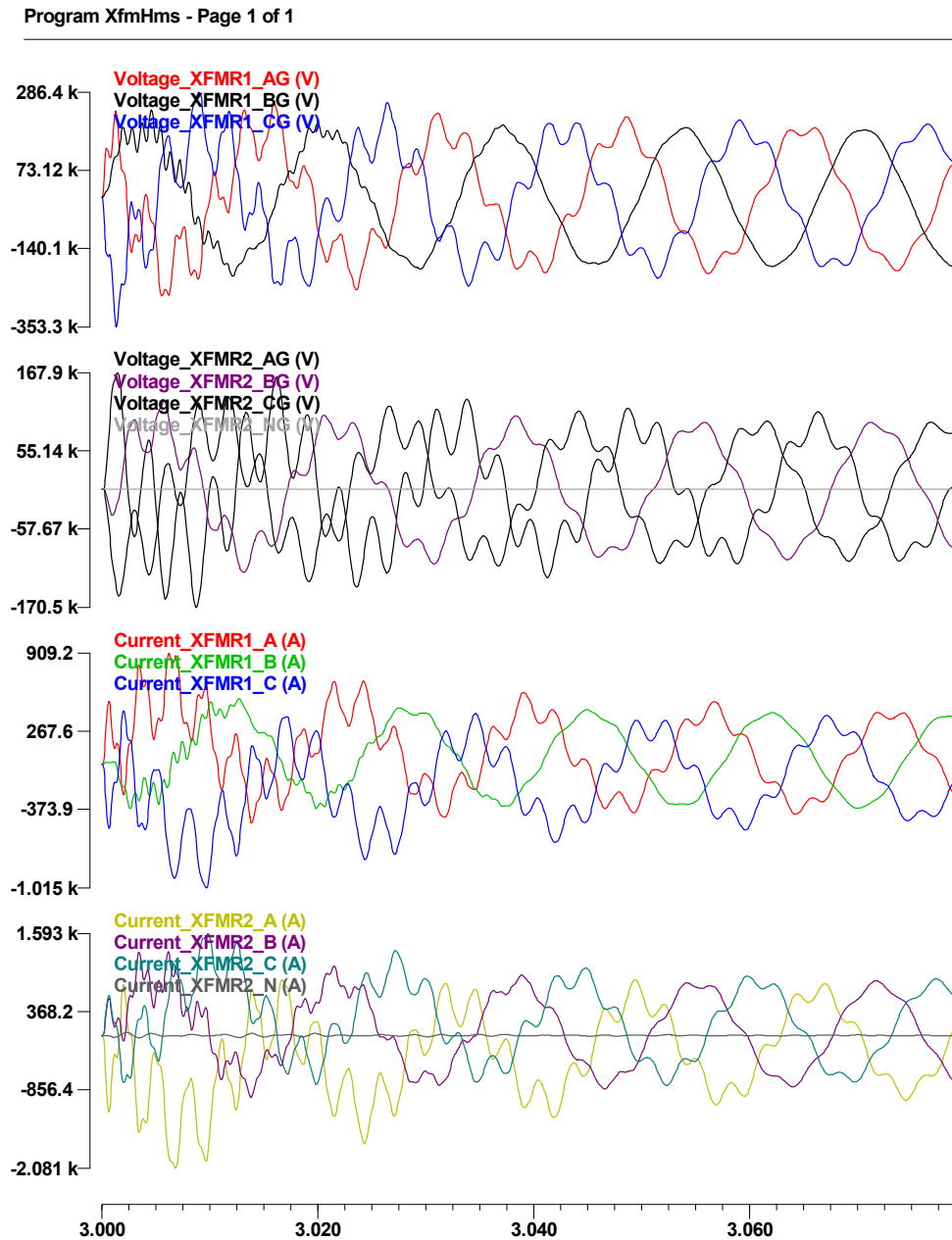


Figure 6.8: Measurements of the transformer [test B: transformer energization (inrush current)].

6.4.1.3 Test C: Transformer Overexcitation

For transformer overexcitation, the test system in Figure 6.5 is used. A set of measurement signals that are monitored during the overexcitation is shown in Figure 6.9.

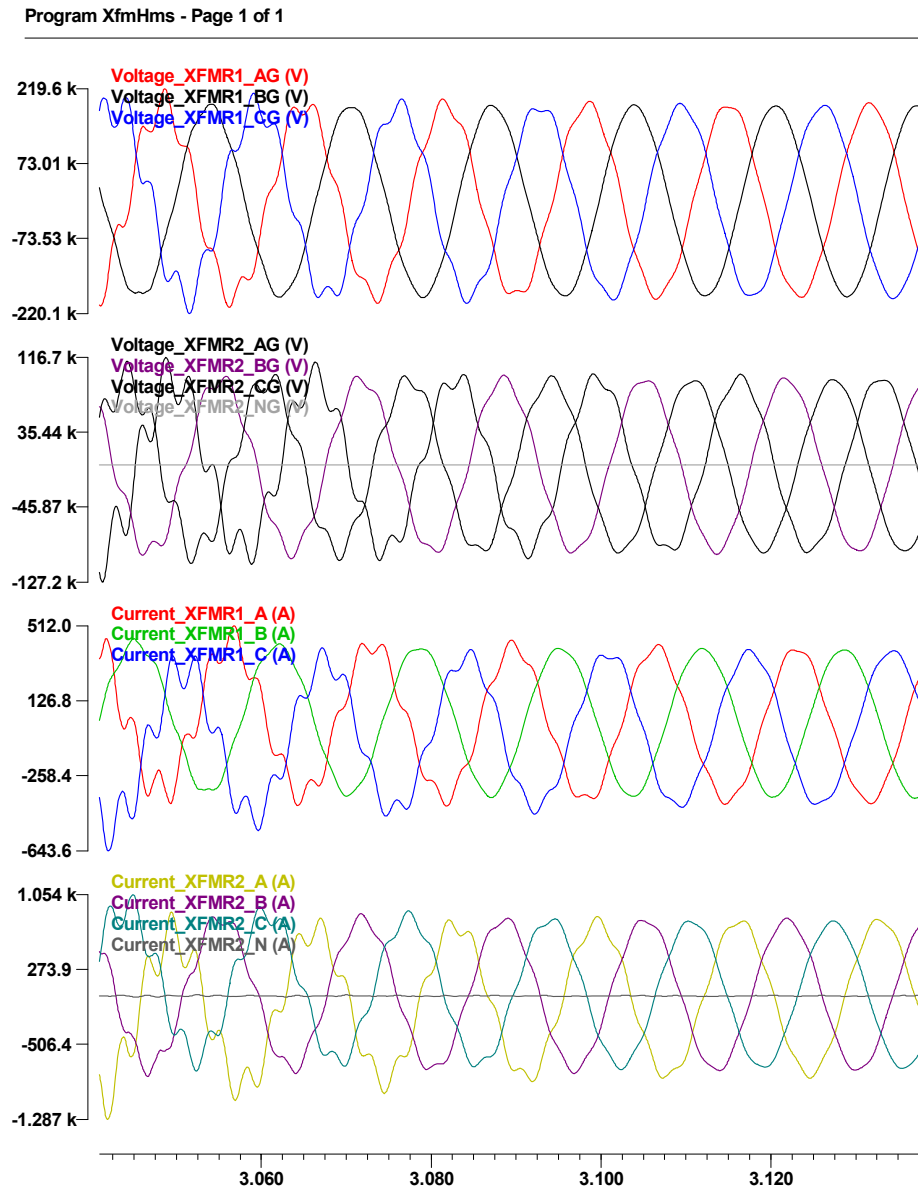


Figure 6.9: Measurements of the transformer (test C: transformer overexcitation).

6.4.1.4 Test D: Through-fault Condition

For the through-fault condition, the test system in Figure 6.5 is used, but single-phase-to-ground fault is given at a certain bus outside the transformer under protection; the faulted location is marked with a red circle in Figure 6.10. The fault lasts for 0.05 seconds, and then, it is cleared.

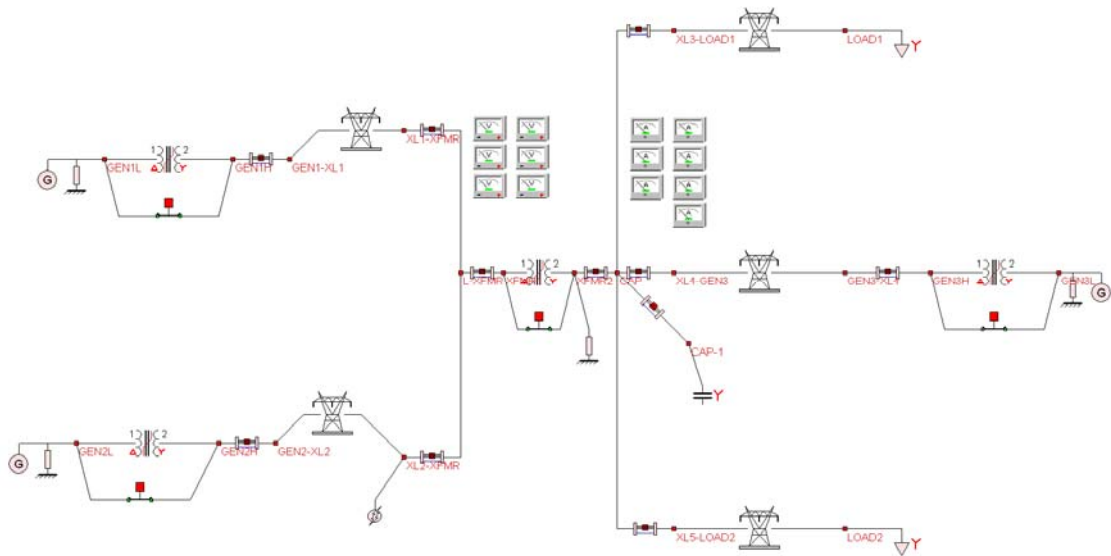


Figure 6.10: Fault location in the test system (test D: the through-fault condition).

A set of measurement signals that are monitored during the through-fault condition is shown in Figure 6.11. The single-phase-to-ground fault is given for 0.05 seconds, starting at 3.20 seconds.

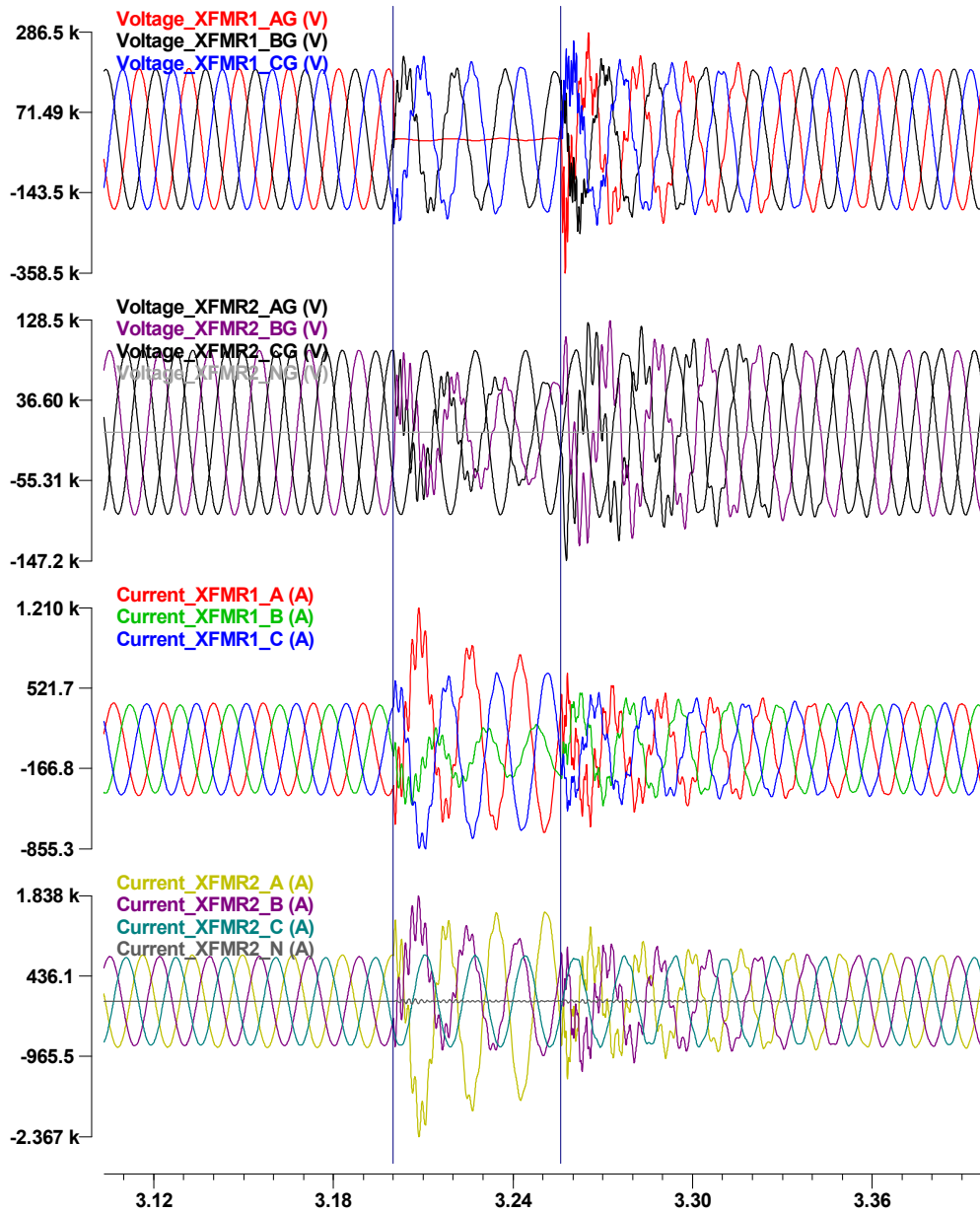


Figure 6.11: Measurements of the transformer (test D: the through-fault condition).

6.4.1.5 Test E: Internal-fault Condition

For the internal-fault condition, the test system in Figure 6.5 is used. The single-phase-to-ground fault occurs at the phase-A terminal on the primary (i.e., left) side of the transformer for 0.05 seconds, and then, the fault is cleared. In Figure 6.12, the faulted location is marked with a red circle.

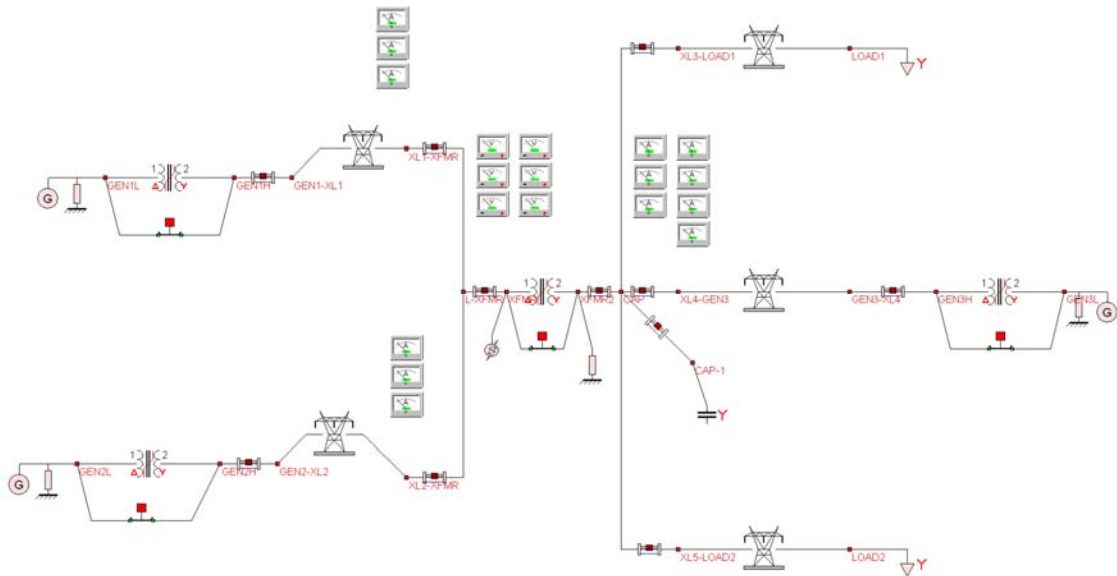


Figure 6.12: Fault location in the test system (test E: the internal-fault condition).

A set of measurement signals that are monitored during the internal-fault condition is shown in Figure 6.13. To simulate the internal-fault condition, the single-phase-to-ground fault is given inside the transformer at the phase A of the primary side for 0.05 seconds, starting at 3.20 seconds.

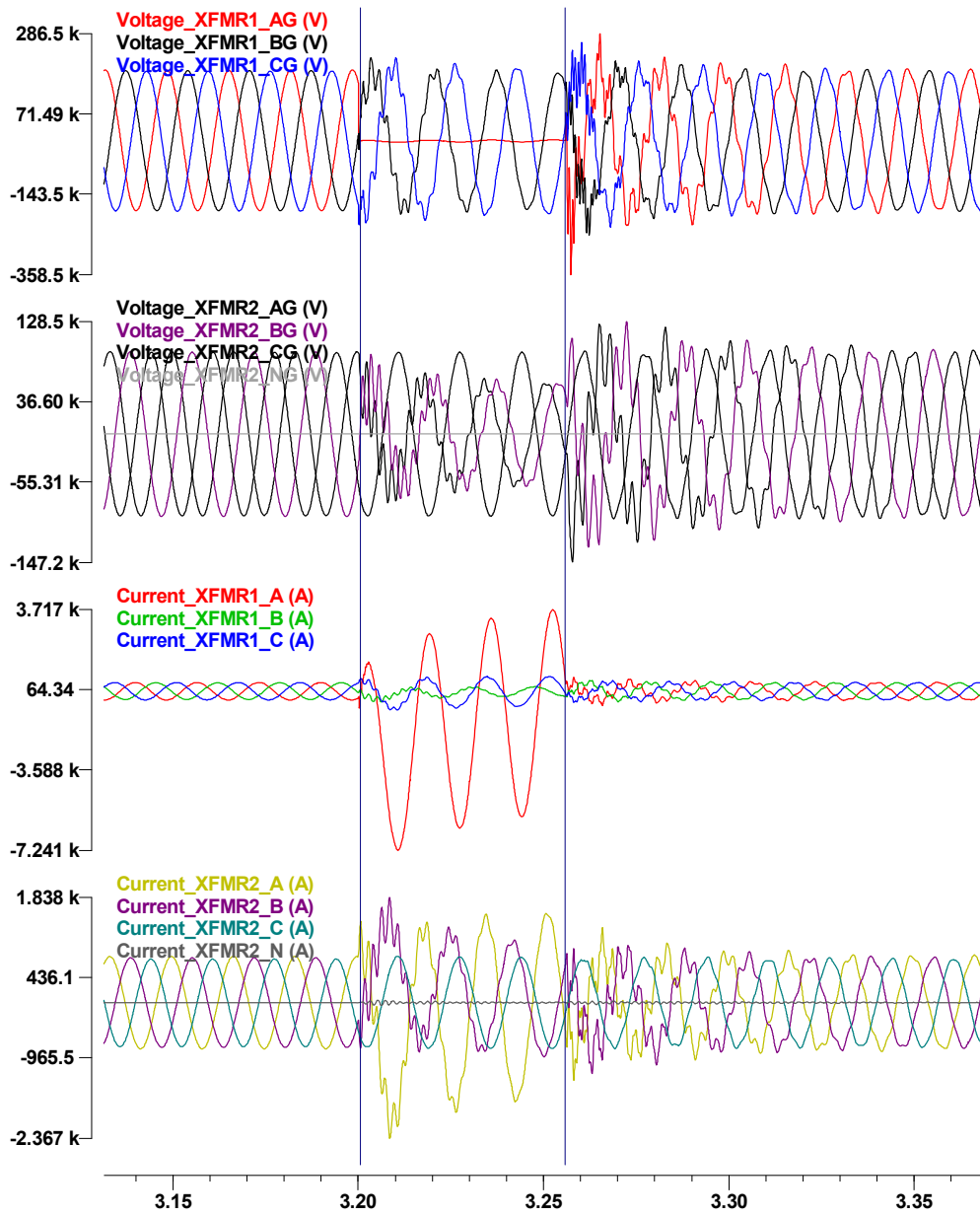


Figure 6.13: Measurements of the transformer (test E: the internal-fault condition).

6.4.2 Test Results

This section presents the test results of the setting-less component protection in the five test scenarios, providing the confidence levels, the estimated and measured values of the across measurements, and the estimated and measured values of the through measurements.

6.4.2.1 Simulation Results for Test A: Normal Operating Condition

For the normal operating condition, the confidence level obtained by the developed dynamic state estimator is shown in Figure 6.14. The result graph shows that the confidence level stays at 100% all the time, which means that the measurements are consistent with the model, and there is no internal fault during the simulation.

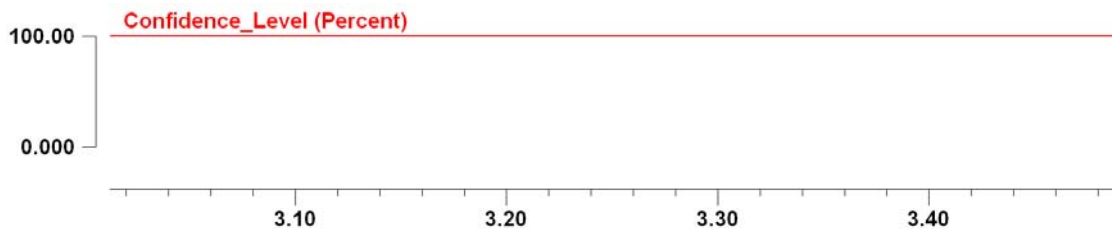


Figure 6.14: Confidence level (test A: the normal operating condition).

The measured and estimated values of the current measurements at the primary and secondary side are compared with different colors as shown in Figure 6.15. Note that the measured and estimated values of all through measurements match very closely; the measured value is z , and the estimated value, $h(x)$, can be computed from the system model, $h()$, and estimated state variables, x . The confidence level of 100% indicates that dynamic state estimation has found the best estimates of x that minimizes the sum of squares of normalized residuals as expressed in equation (3.28). Meanwhile, this figure indicates that the measured values of all through measurements closely match the estimated ones, and thus, it can be concluded that the standard deviation (i.e., σ) of through measurements has a reasonable value (i.e., 0.01).

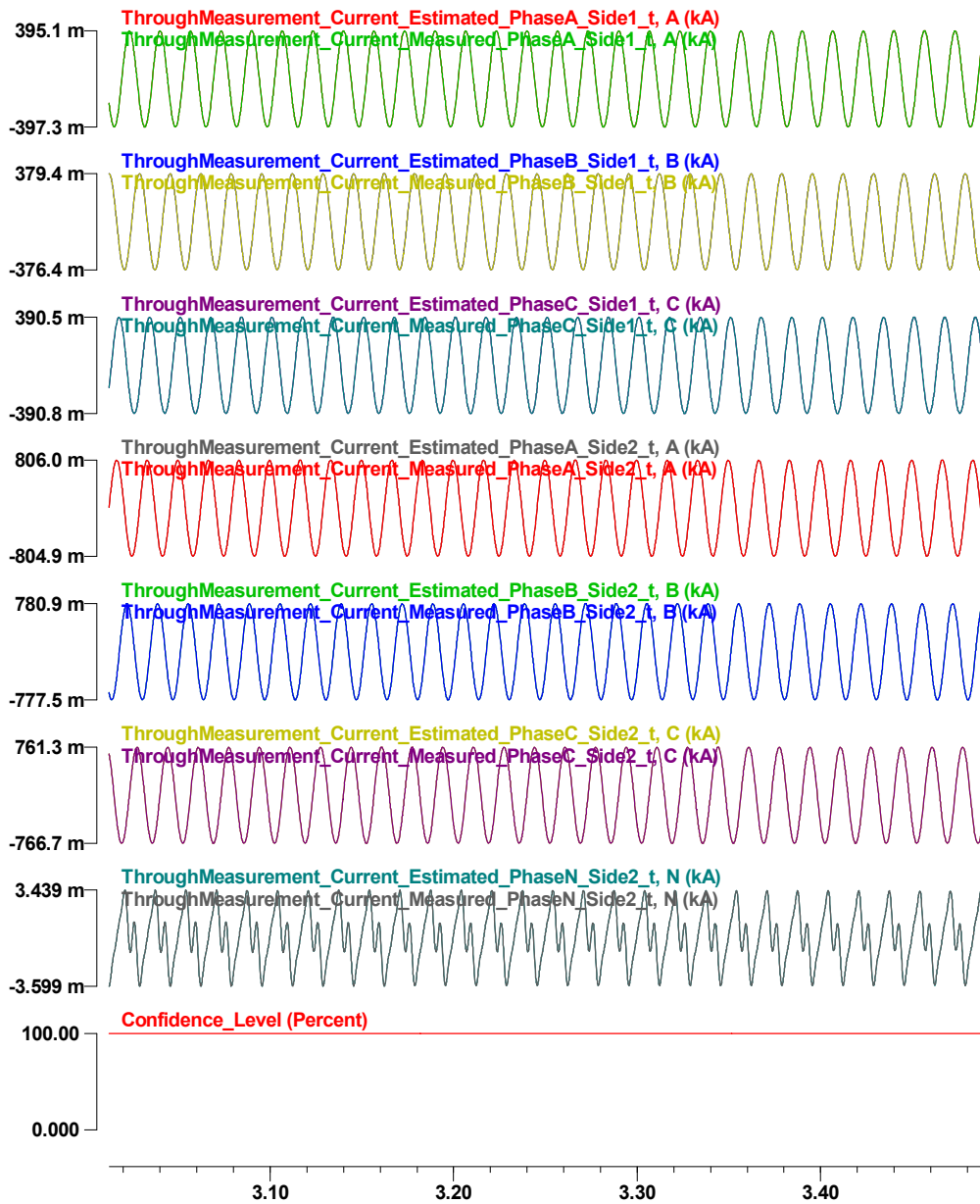


Figure 6.15: Estimated and measured values of the current measurements with the confidence level (test A).

The measured and estimated values of the voltage measurements at the primary and secondary side are also compared in Figure 6.16. Note that the measured and estimated values match very closely. Similar to the through measurements, the standard deviation (i.e., σ) of across measurements has a reasonable value (i.e., 0.1) since the estimated values of all across measurements closely match the measured ones while the confidence level is 100%.

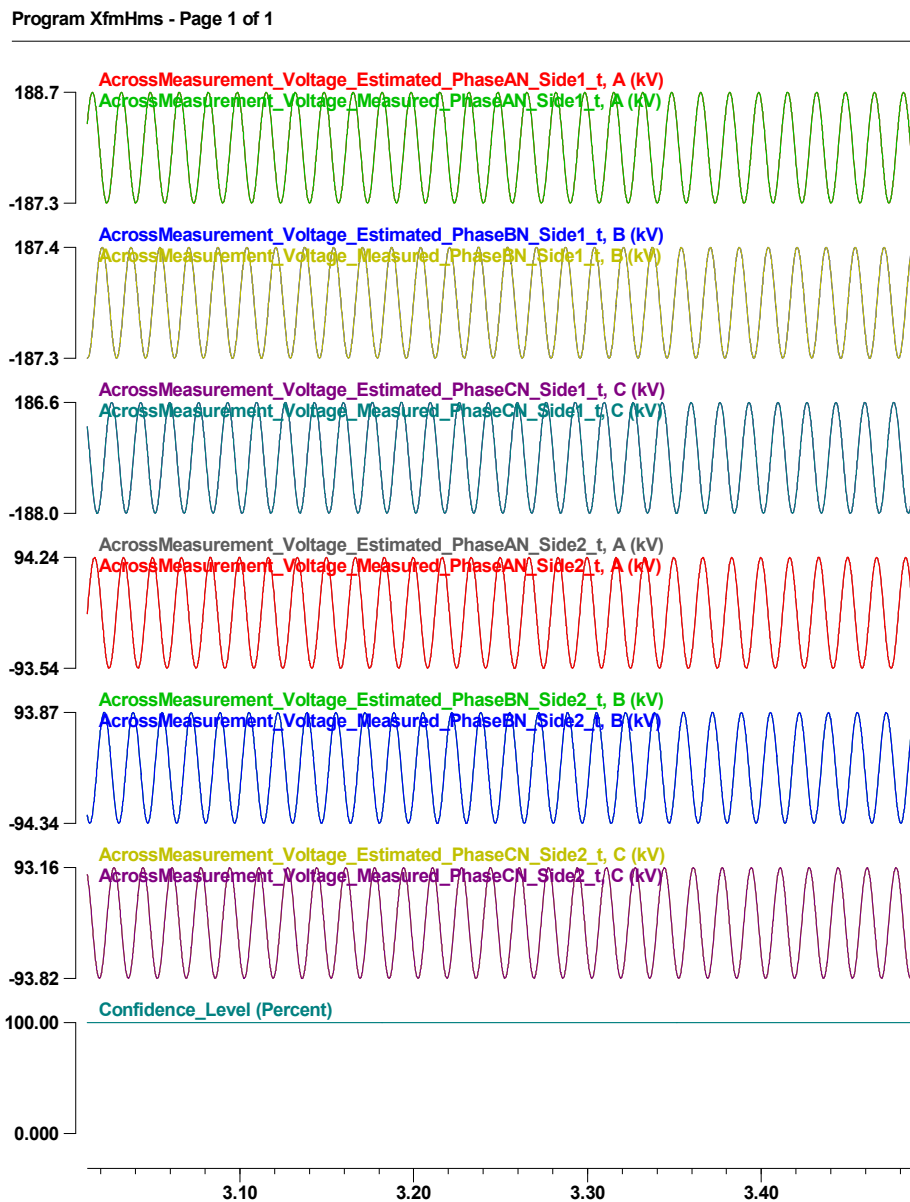


Figure 6.16: Estimated and measured values of the voltage measurements with the confidence level (test A).

From Figure 6.15 and Figure 6.16, it can be concluded that the estimated voltages and currents match closely the measured ones during the normal operation condition.

The estimated value, measured value, residual, and normalized residual of the current measurement at the primary side are presented in the following figure. Note that the residuals are very small. Additionally, the residuals of all measurements in this figure are relatively high at the beginning of the test, and then, they are decreasing as time passes. This is due to the fact that the initial values of the past-history values, $v(t-h)$ and $y(t-h)$, are set to zero because they are unknown when the test begins. However, the actual past-history values at the initial time are not zero, so these inaccurate values eventually increase the residuals. Nevertheless, these relatively large residuals are not significant and decreasing as time passes.

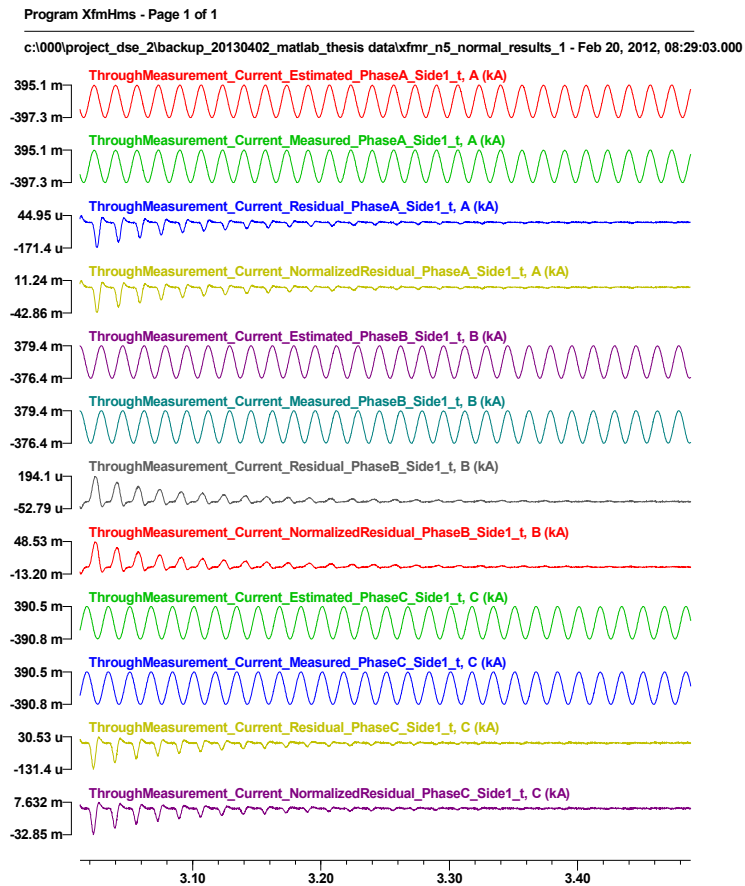


Figure 6.17: Estimated value, measured value, residual, and normalized residual of the current measurement at the primary side (test A).

The estimated value, measured value, residual, and normalized residual of the current measurement at the secondary side are presented in the following figure. Note that the residuals are very small. Additionally, the residuals of all measurements in this figure except the phase-N current measurement are relatively high at the beginning of the test, and then, they are decreasing as time passes. The phase-N current measurement has relatively small values compared to other through measurements, so the initial values of the past-history have little influence on the residuals of the phase-N through measurement.

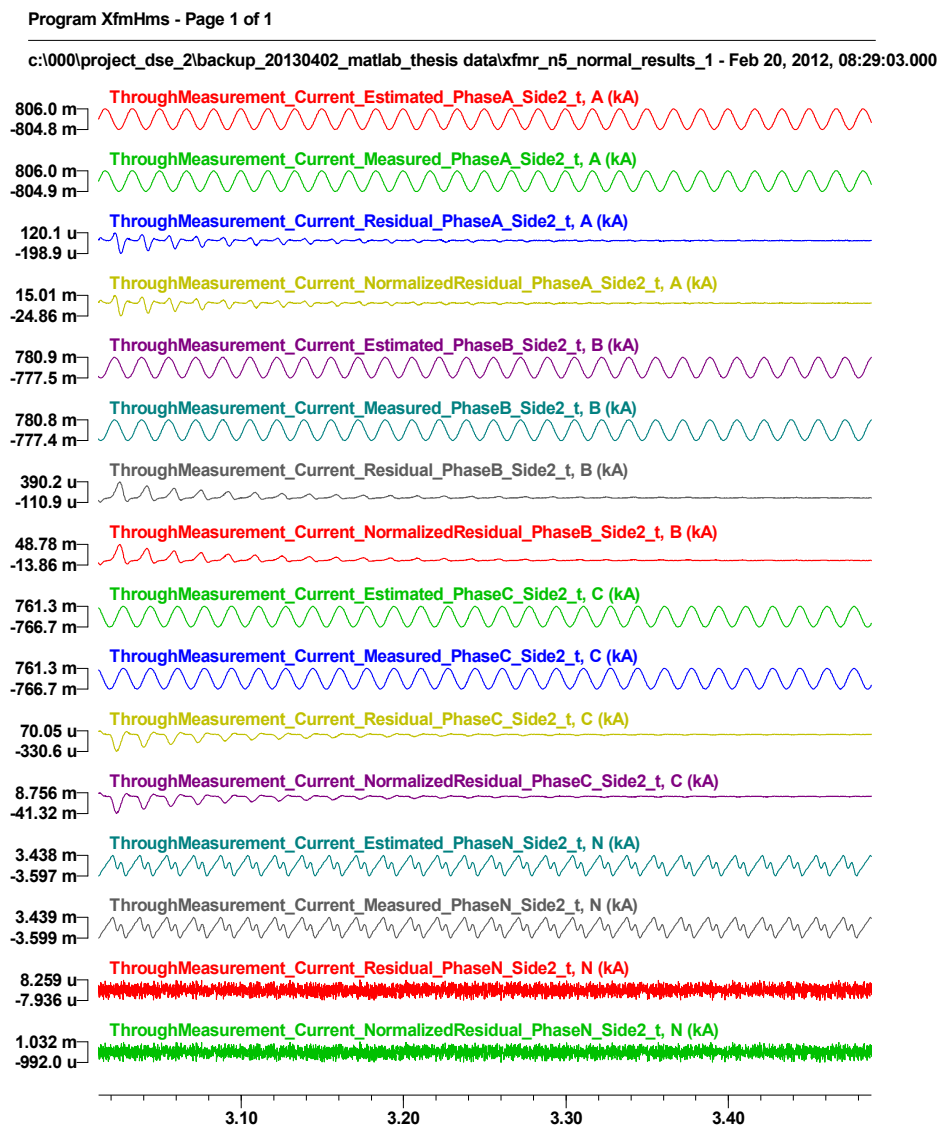


Figure 6.18: Estimated value, measured value, residual, and normalized residual of the current measurement at the secondary side (test A).

The estimated value, measured value, residual, and normalized residual of the voltage measurement at the primary side are presented in the following figure. Note that the residuals are very small. Additionally, the residuals of all measurements in this figure are relatively high at the beginning of the test, and then, they are decreasing as time passes.

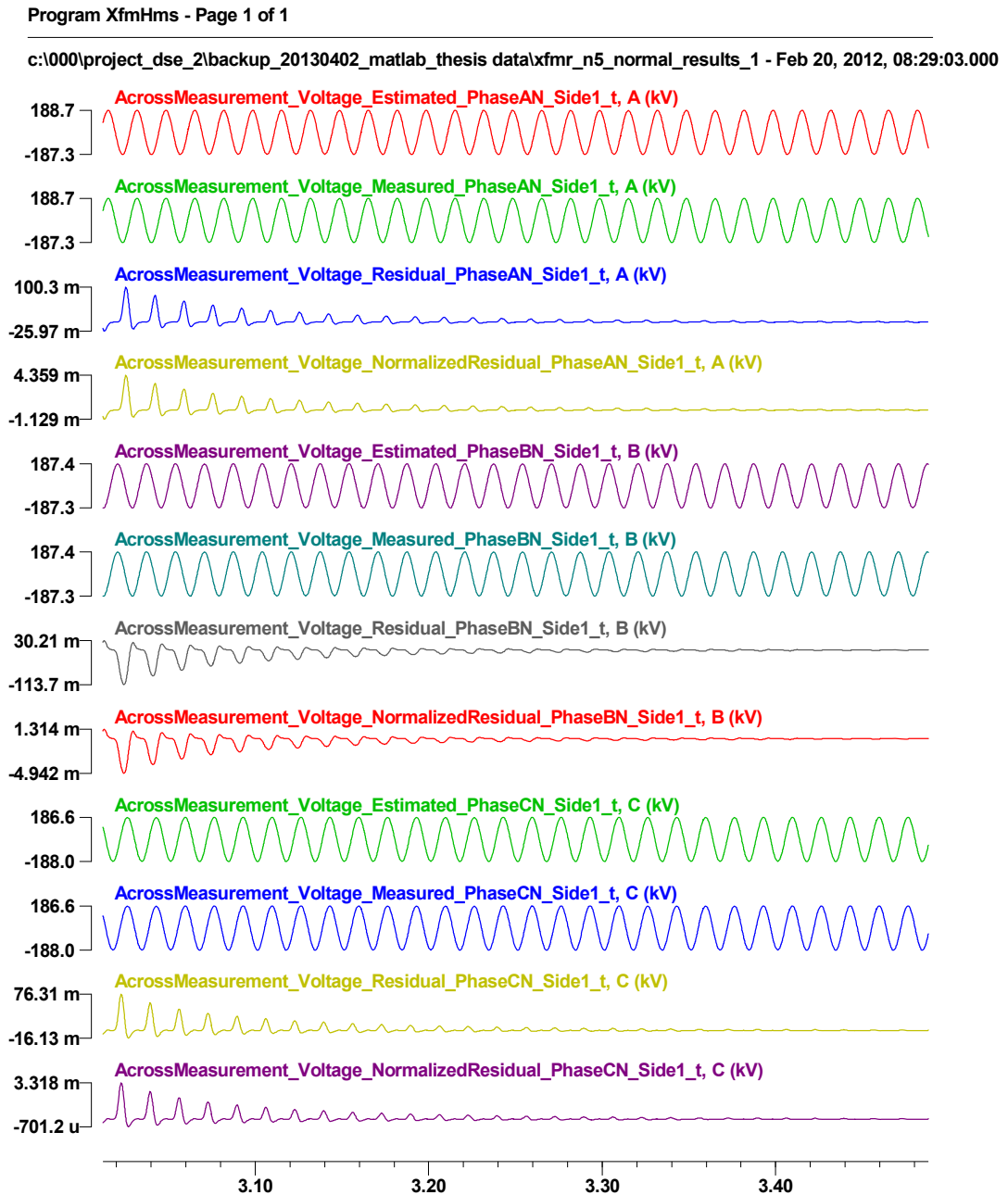


Figure 6.19: Estimated value, measured value, residual, and normalized residual of the voltage measurement at the primary side (test A).

The estimated value, measured value, residual, and normalized residual of the voltage measurement at the secondary side are presented in the following figure. Note that the residuals are very small. Additionally, the residuals of all measurements in this figure are relatively high at the beginning of the test, and then, they are decreasing as time passes.

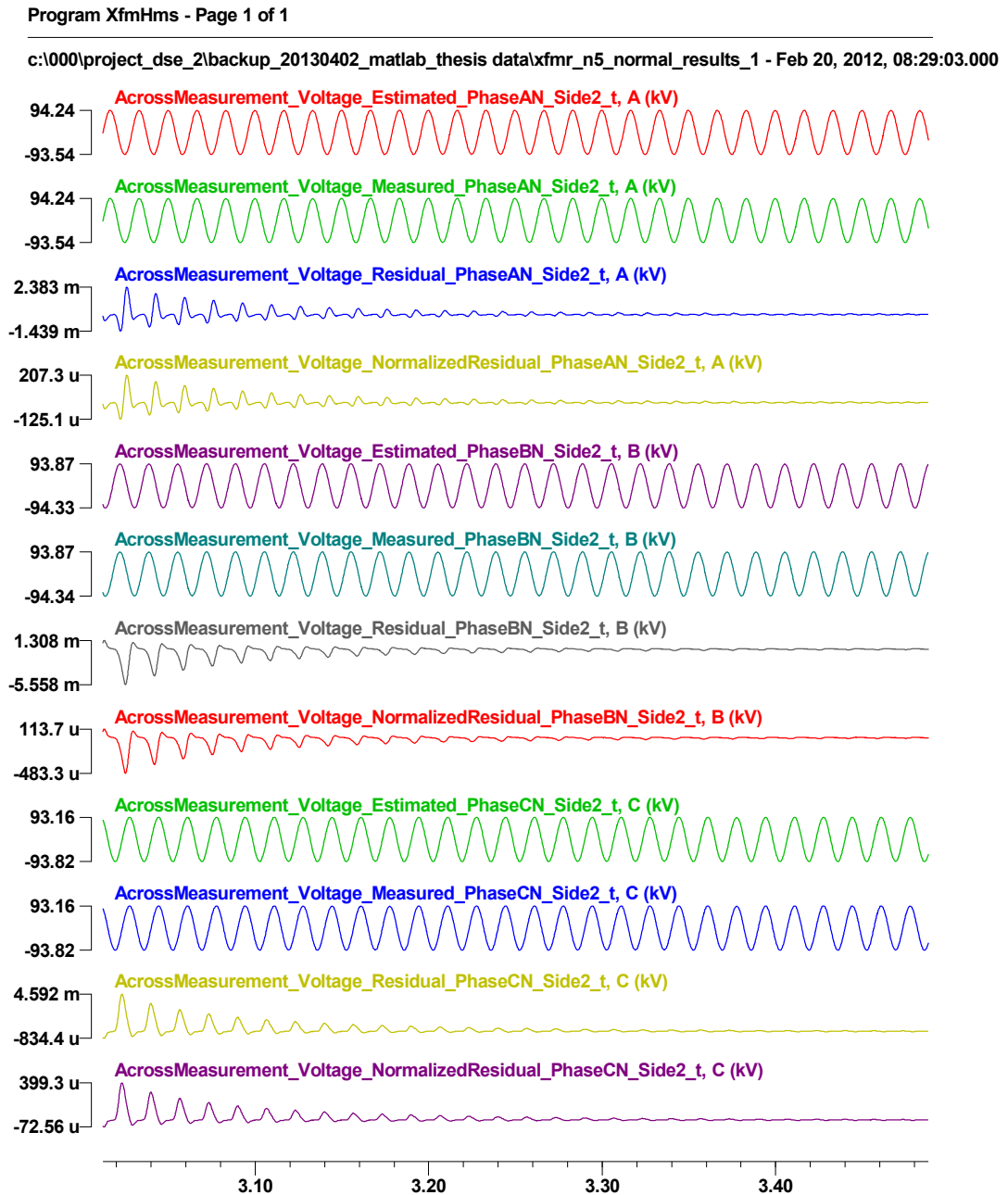


Figure 6.20: Estimated value, measured value, residual, and normalized residual of the voltage measurement at the secondary side (test A).

The simulation results are available for further research and analysis. They are stored in the format of COMTRADE, generating the following files:

- XFMR_N5_NORMAL_results_1.cfg and XFMR_N5_NORMAL_results_1.dat: the estimated values of all state variables, the estimated and measured values of all across measurements, the residuals of all across measurements, the normalized residuals of all across measurements, the estimated and measured values of all through measurements, the residuals of all through measurements, the normalized residuals of all through measurements, the estimated and measured values of all pseudo measurements, the residuals of all pseudo measurements, the normalized residuals of all pseudo measurements, the degrees of freedom, the chi-square critical values, the confidence levels, and the processing time.
- XFMR_N5_NORMAL_results_2.cfg and XFMR_N5_NORMAL_results_2.dat: the estimated and measured values of all virtual measurements, the residuals of all virtual measurements, and the normalized residuals of all virtual measurements, the degrees of freedom, the chi-square critical values, the confidence levels, and the processing time.

6.4.2.2 Simulation Results for Test B: Transformer Energization (Inrush Current)

For the transformer energization, the confidence level obtained by the developed dynamic state estimator is shown in Figure 6.21. The result graph shows that the confidence level stays at 100% all the time, which means that the measurements are consistent with the model, and there is no internal fault during the simulation.

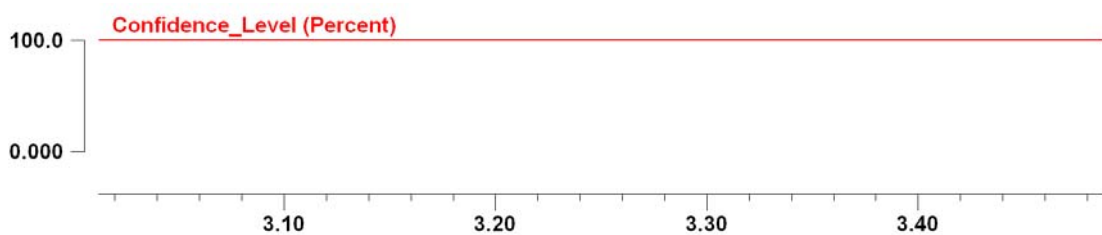


Figure 6.21: Confidence level (test B: transformer energization).

The measured and estimated values of the current measurements at the primary and secondary side are shown with different colors as shown in Figure 6.22. Note that the measured and estimated values match closely even when the transformer is energizing around 3 seconds.

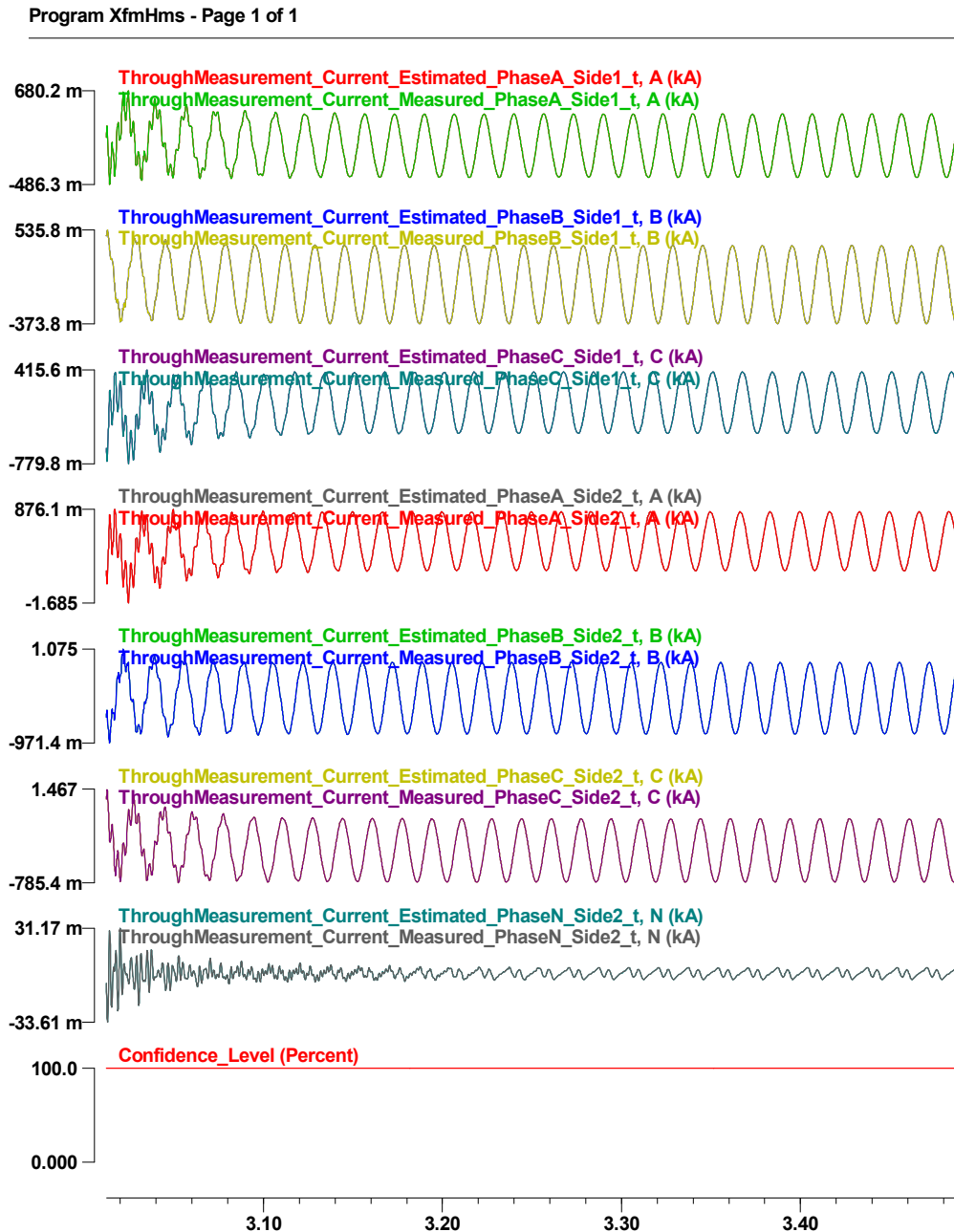


Figure 6.22: Estimated and measured values of the current measurements with the confidence level (test B).

The measured and estimated values of the voltage measurements at the primary and secondary side are also compared in Figure 6.23. Note that the measured and estimated values match closely even when the transformer is energizing around 3 seconds.

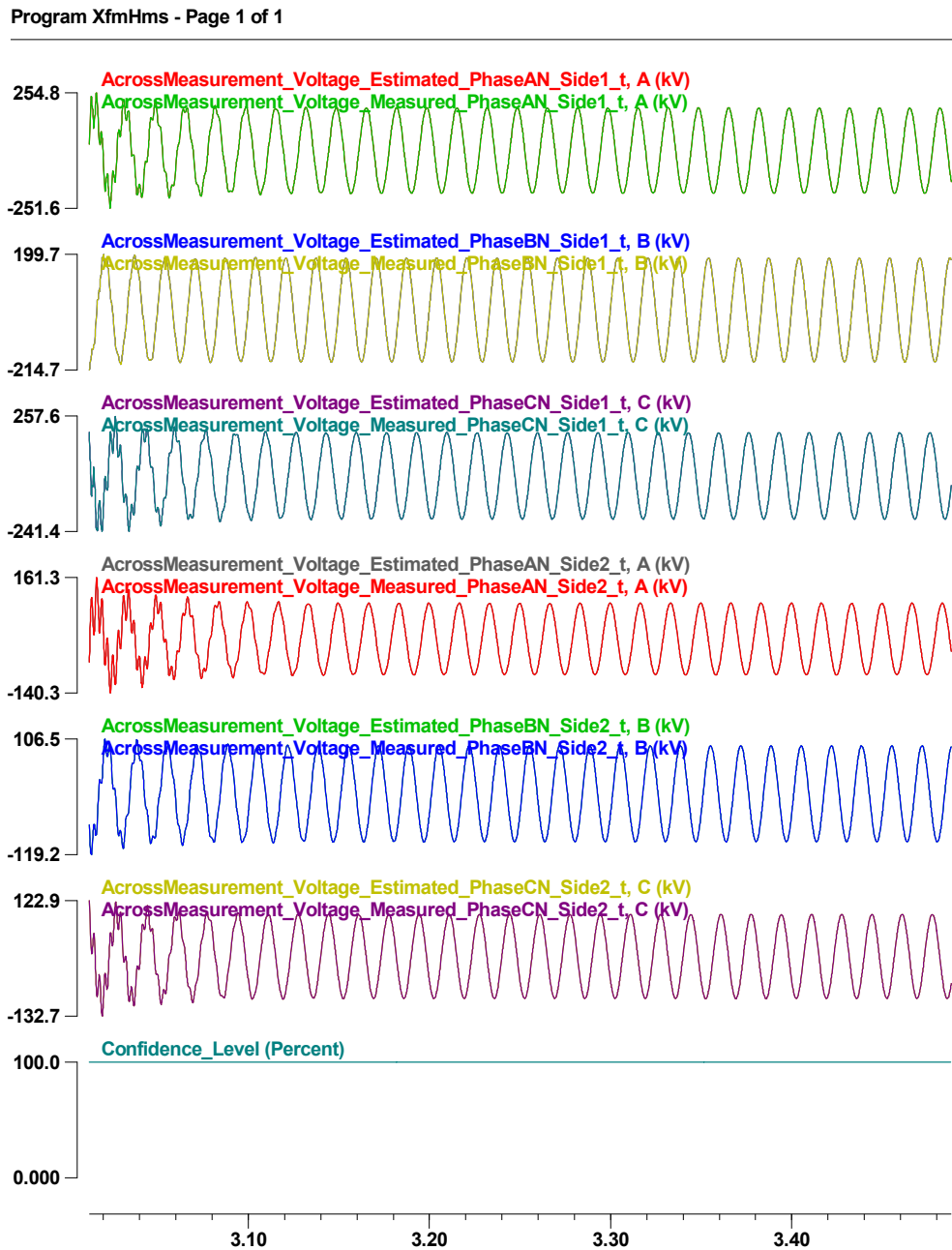


Figure 6.23: Estimated and measured values of the voltage measurements with the confidence level (test B).

From Figure 6.22 and Figure 6.23, it can be concluded that the estimated voltages and currents match closely the measured ones during the transformer energization.

The estimated value, measured value, residual, and normalized residual of the current measurement at the primary side are presented in the following figure. Note that the residuals are very small.

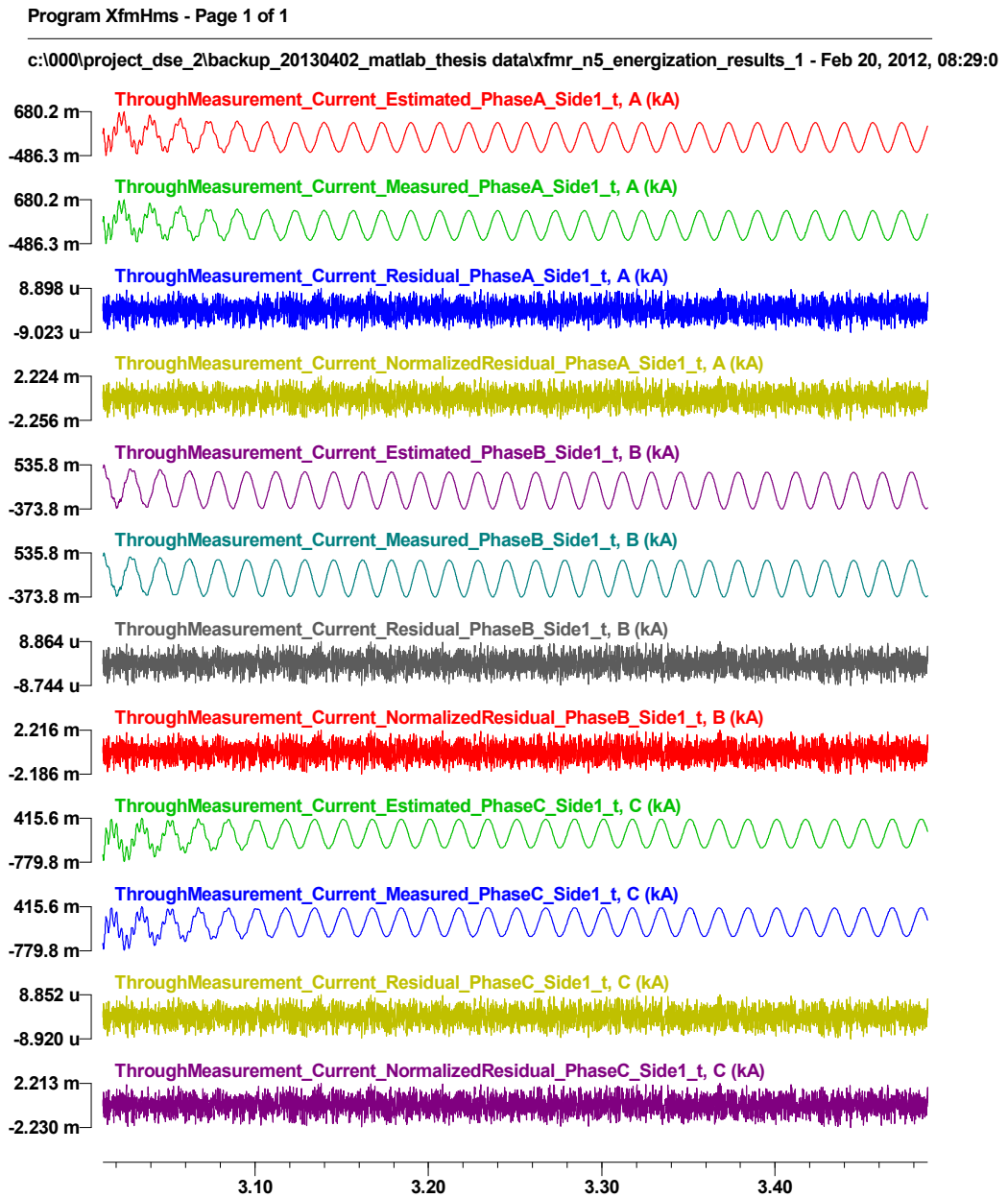


Figure 6.24: Estimated value, measured value, residual, and normalized residual of the current measurement at the primary side (test B).

The estimated value, measured value, residual, and normalized residual of the current measurement at the secondary side are presented in the following figure. Note that residuals are very small.

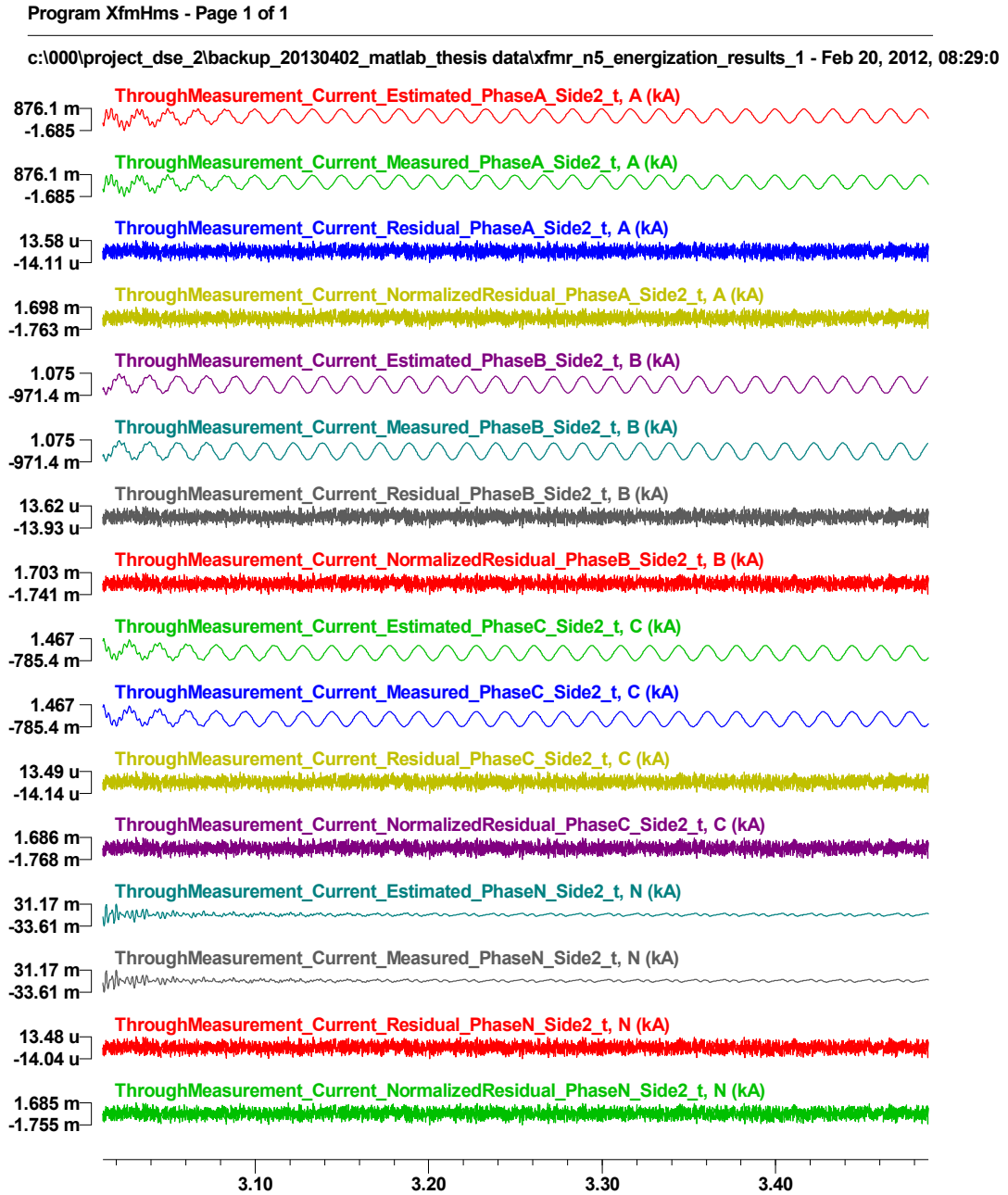


Figure 6.25: Estimated value, measured value, residual, and normalized residual of the current measurement at the secondary side (test B).

The estimated value, measured value, residual, and normalized residual of the voltage measurement at the primary side are presented in the following figure. Note that residuals are very small.

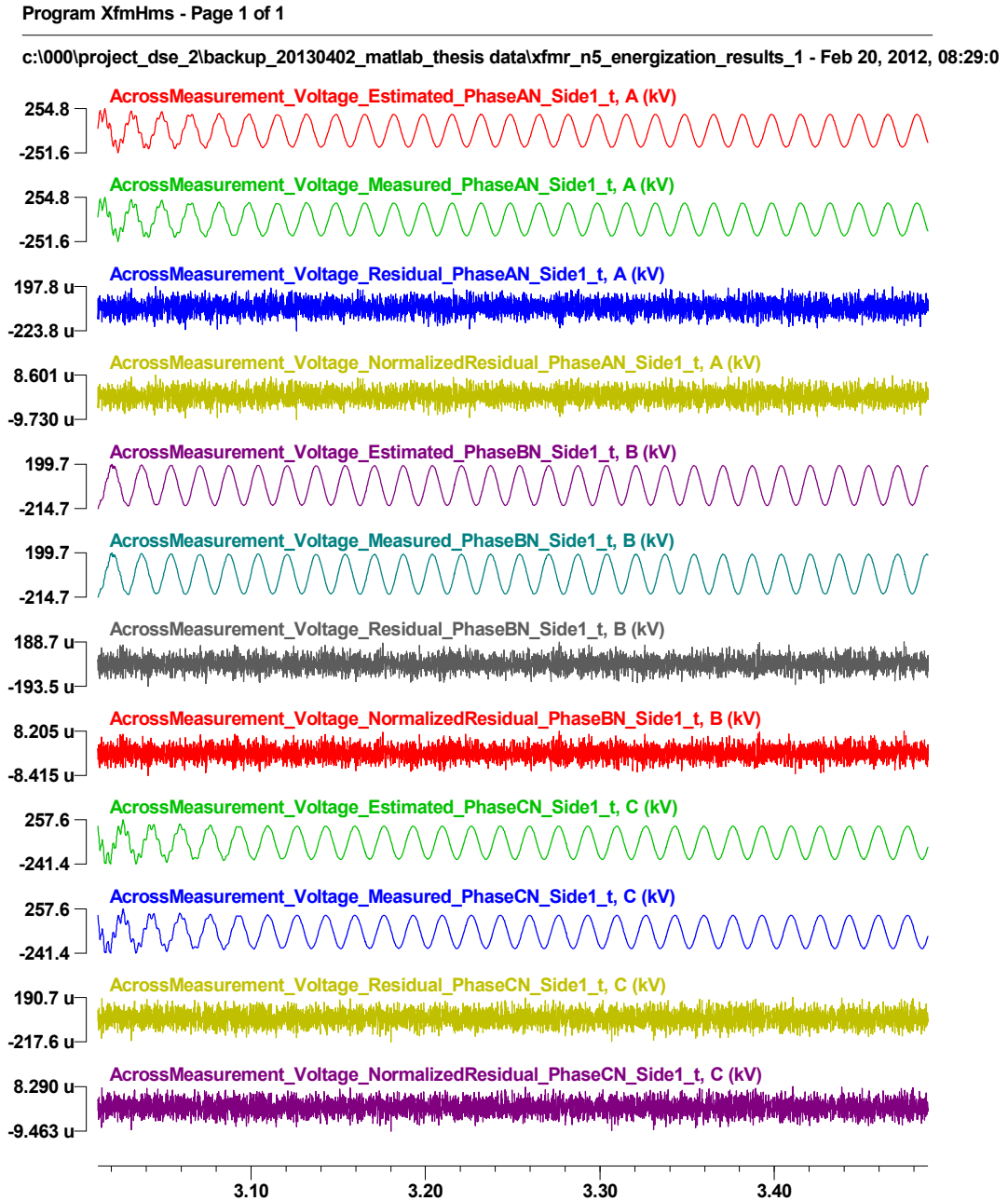


Figure 6.26: Estimated value, measured value, residual, and normalized residual of the voltage measurement at the primary side (test B).

The estimated value, measured value, residual, and normalized residual of the voltage measurement at the secondary side are presented in the following figure. Note that residuals are very small.

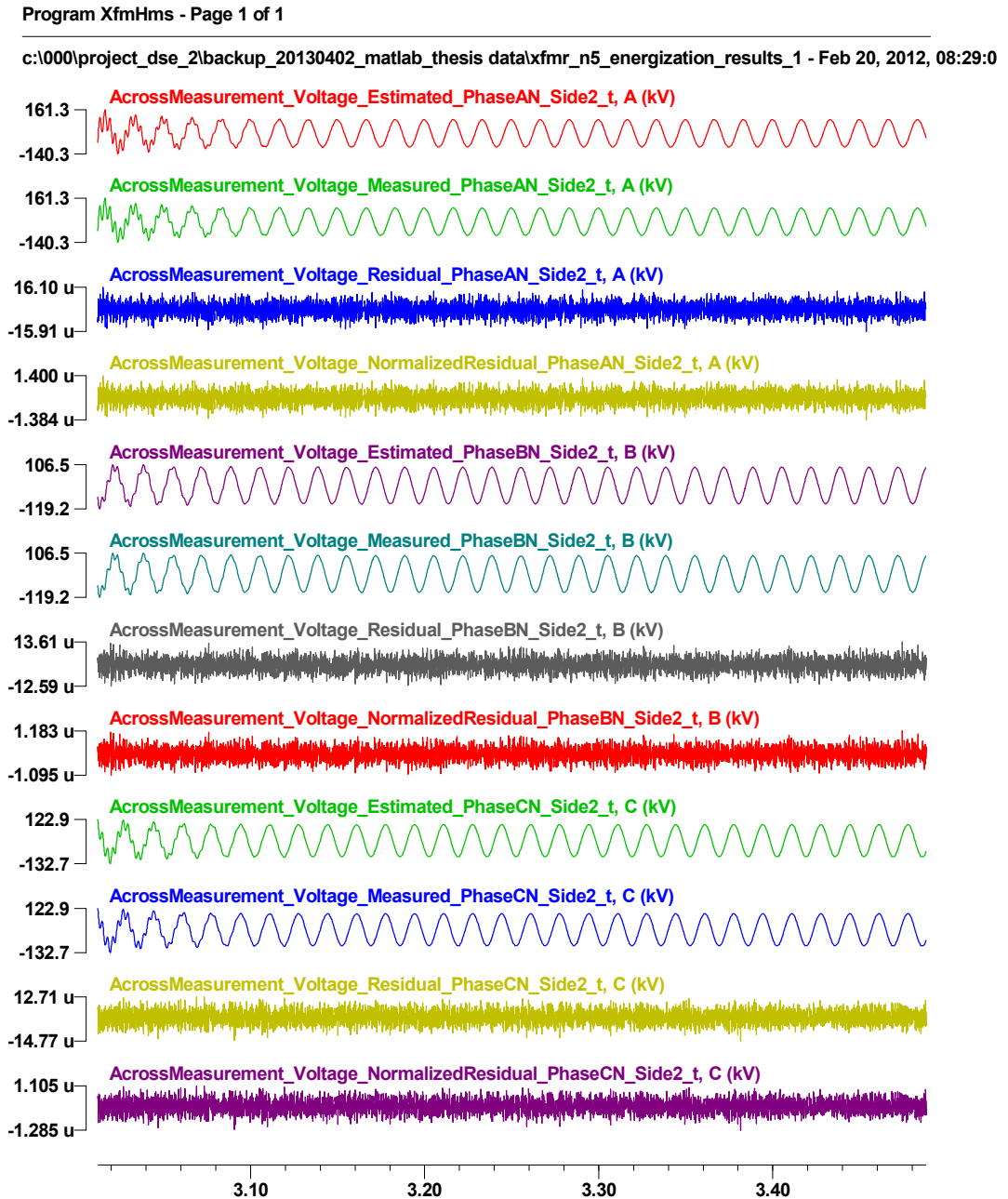


Figure 6.27: Estimated value, measured value, residual, and normalized residual of the voltage measurement at the secondary side (test B).

The simulation results are available for further research and analysis. They are stored in the format of COMTRADE, generating the following files:

- XFMR_N5_ENERGIZATION_results_1.cfg and XFMR_N5_ENERGIZATION_results_1.dat: the estimated values of all state variables, the estimated and measured values of all across measurements, the residuals of all across measurements, the normalized residuals of all across measurements, the estimated and measured values of all through measurements, the residuals of all through measurements, the normalized residuals of all through measurements, the estimated and measured values of all pseudo measurements, the residuals of all pseudo measurements, the normalized residuals of all pseudo measurements, the degrees of freedom, the chi-square critical values, the confidence levels, and the processing time.
- XFMR_N5_ENERGIZATION_results_2.cfg and XFMR_N5_ENERGIZATION_results_2.dat: the estimated and measured values of all virtual measurements, the residuals of all virtual measurements, and the normalized residuals of all virtual measurements, the degrees of freedom, the chi-square critical values, the confidence levels, and the processing time.

6.4.2.3 Simulation Results for Test C: Transformer Overexcitation

For the transformer overexcitation, the confidence level obtained by the developed dynamic state estimator is shown in Figure 6.28. The result graph shows that the confidence level stays at 100% all the time, which means that the measurements are consistent with the model, and there is no internal fault during the simulation.

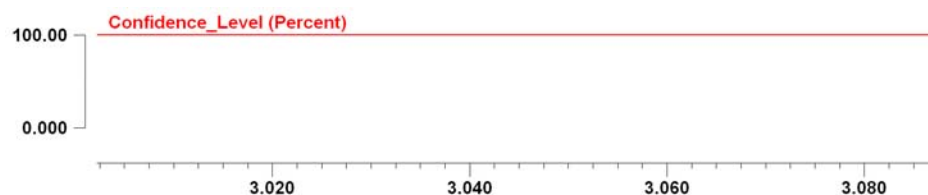


Figure 6.28: Confidence level (test C: transformer overexcitation).

The measured and estimated values of the current measurements at the primary and secondary side are shown with different colors as shown in Figure 6.29. Note that the estimated and measured values match well.

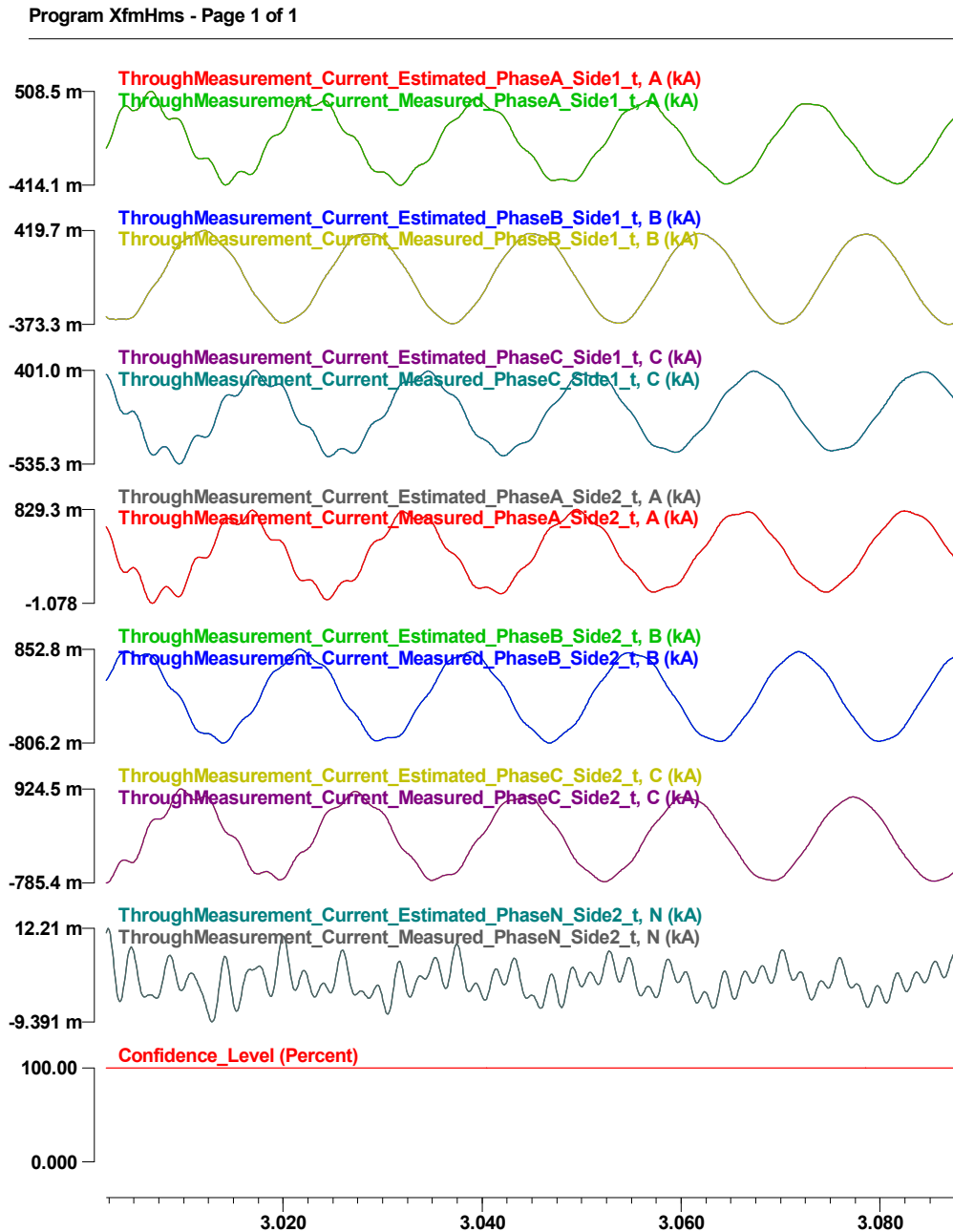


Figure 6.29: Estimated and measured values of the current measurements with the confidence level (test C).

The measured and estimated values of the voltage measurements at the primary and secondary side are also compared in Figure 6.30. Note that the estimated and measured values match well.

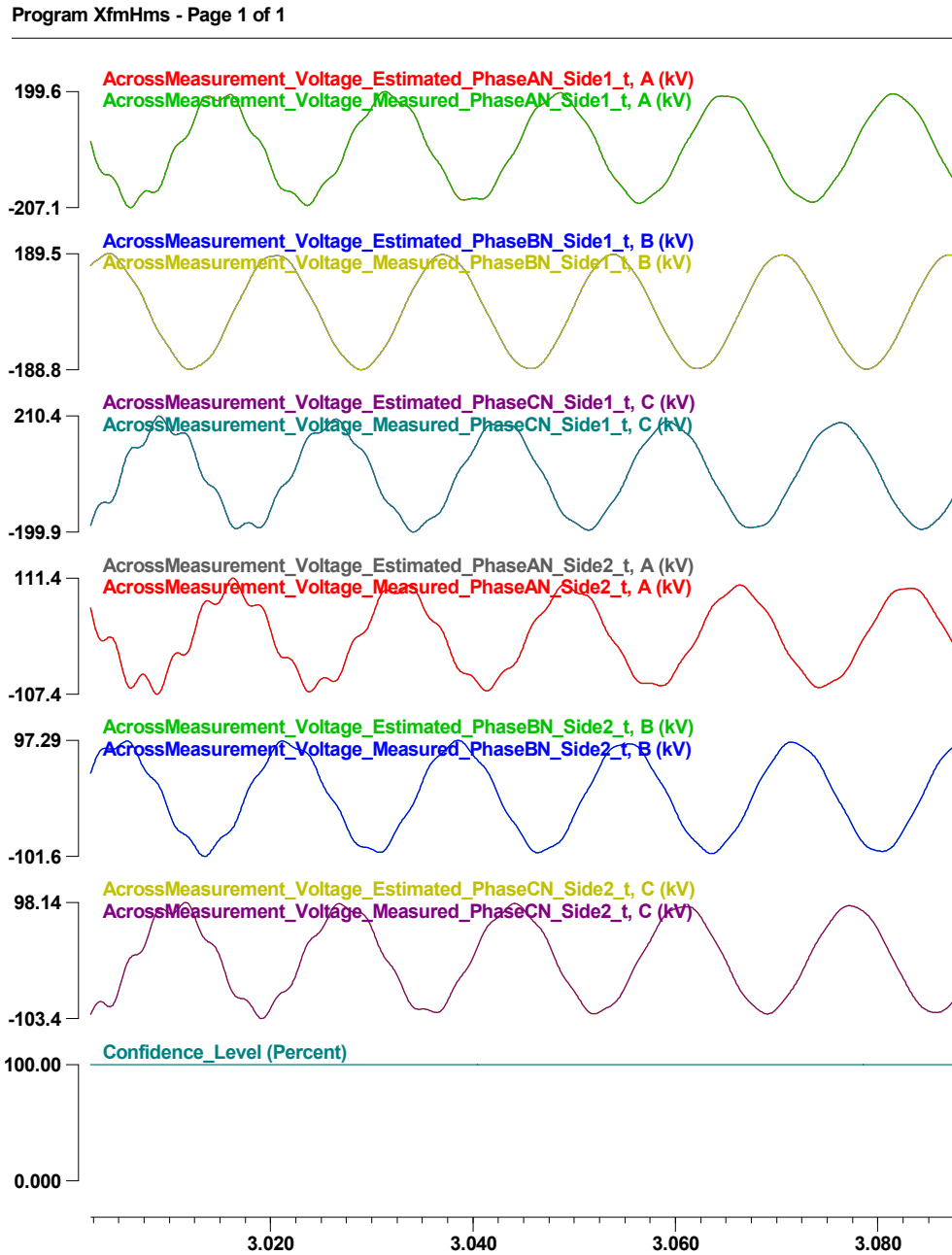


Figure 6.30: Estimated and measured values of the voltage measurements with the confidence level (test C).

From Figure 6.29 and Figure 6.30, it can be concluded that the estimated voltages and currents match well with measured ones during the transformer overexcitation.

The estimated value, measured value, residual, and normalized residual of the current measurement at the primary side are presented in the following figure. Note that the residuals are very small. Additionally, the residuals of all measurements in this figure are relatively high at the beginning of the test, and then, they are decreasing as time passes.

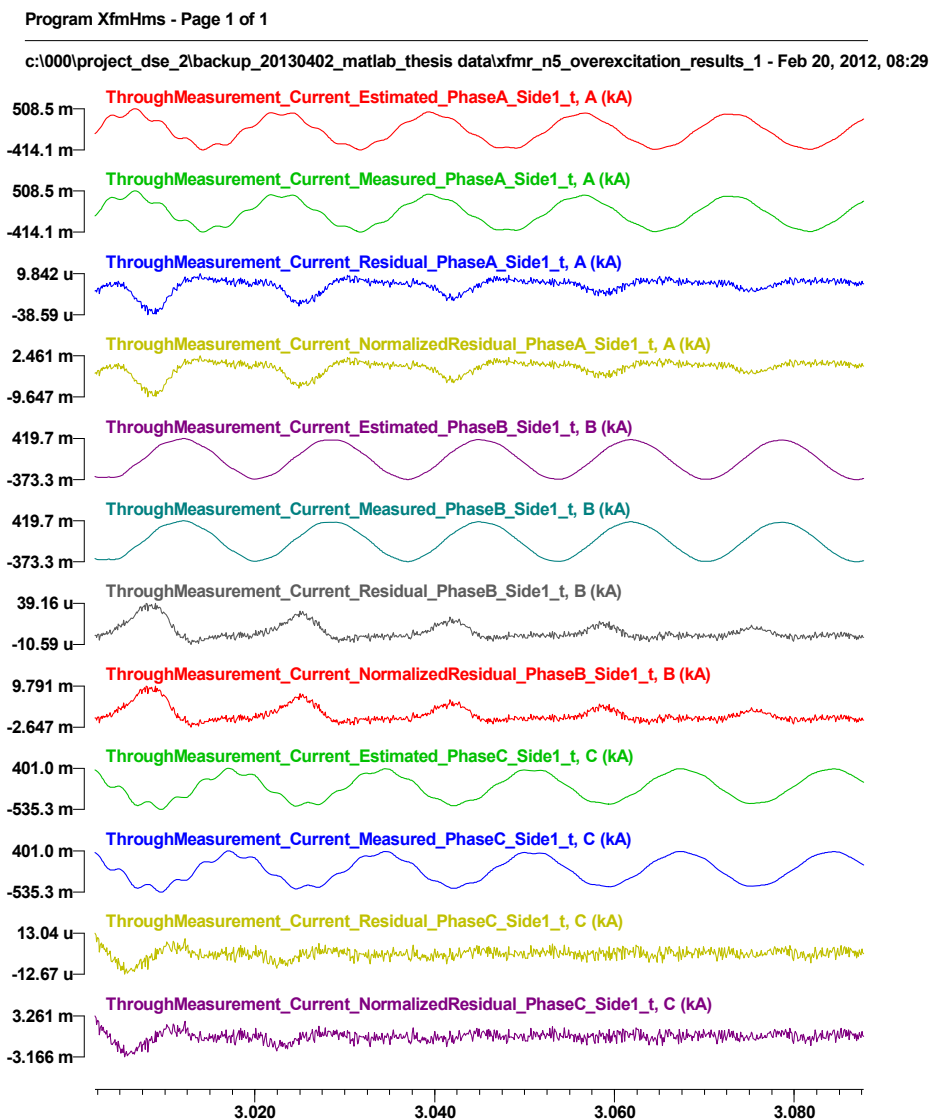


Figure 6.31: Estimated value, measured value, residual, and normalized residual of the current measurement at the primary side (test C).

The estimated value, measured value, residual, and normalized residual of the current measurement at the secondary side are presented in the following figure. Note that residuals are very small. Additionally, the residuals of all measurements in this figure except the phase-N current measurement are relatively high at the beginning of the test, and then, they are decreasing as time passes. The phase-N current measurement has relatively small values compared to other through measurements, so the initial values of the past-history have little influence on the residuals of the phase-N through measurement.

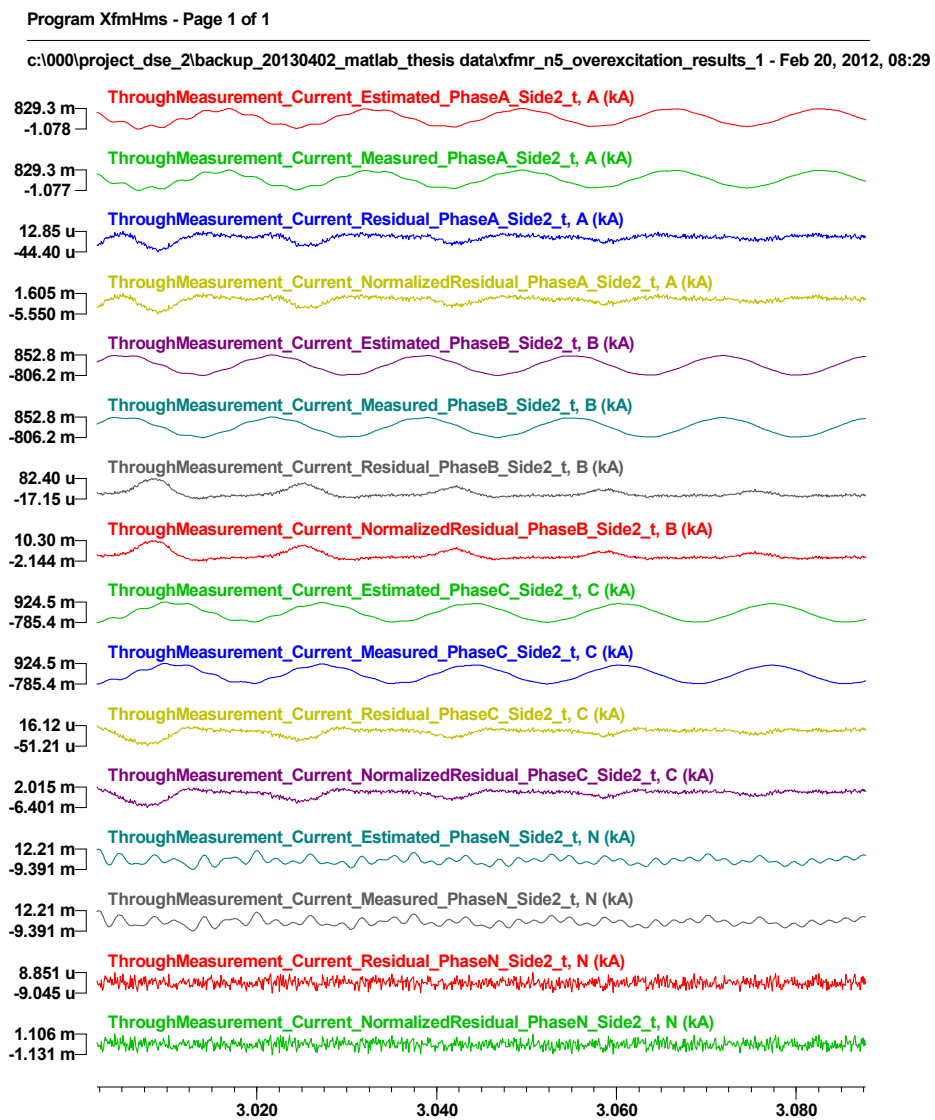


Figure 6.32: Estimated value, measured value, residual, and normalized residual of the current measurement at the secondary side (test C).

The estimated value, measured value, residual, and normalized residual of the voltage measurement at the primary side are presented in the following figure. Note that residuals are very small. Additionally, the residuals of all measurements in this figure are relatively high at the beginning of the test, and then, they are decreasing as time passes.

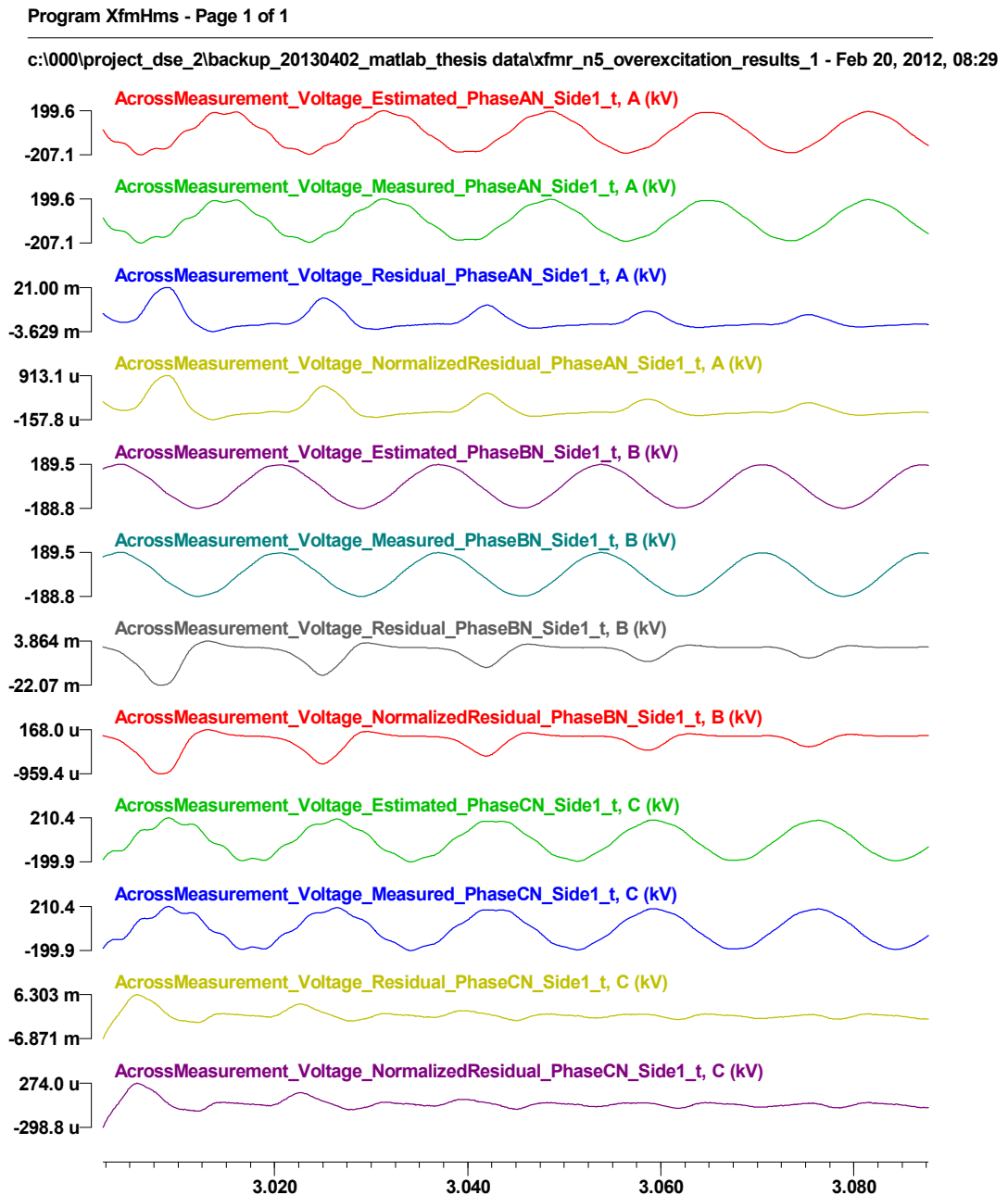


Figure 6.33: Estimated value, measured value, residual, and normalized residual of the voltage measurement at the primary side (test C).

The estimated value, measured value, residual, and normalized residual of the voltage measurement at the secondary side are presented in the following figure. Note that residuals are very small. Additionally, the residuals of all measurements in this figure are relatively high at the beginning of the test, and then, they are decreasing as time passes.

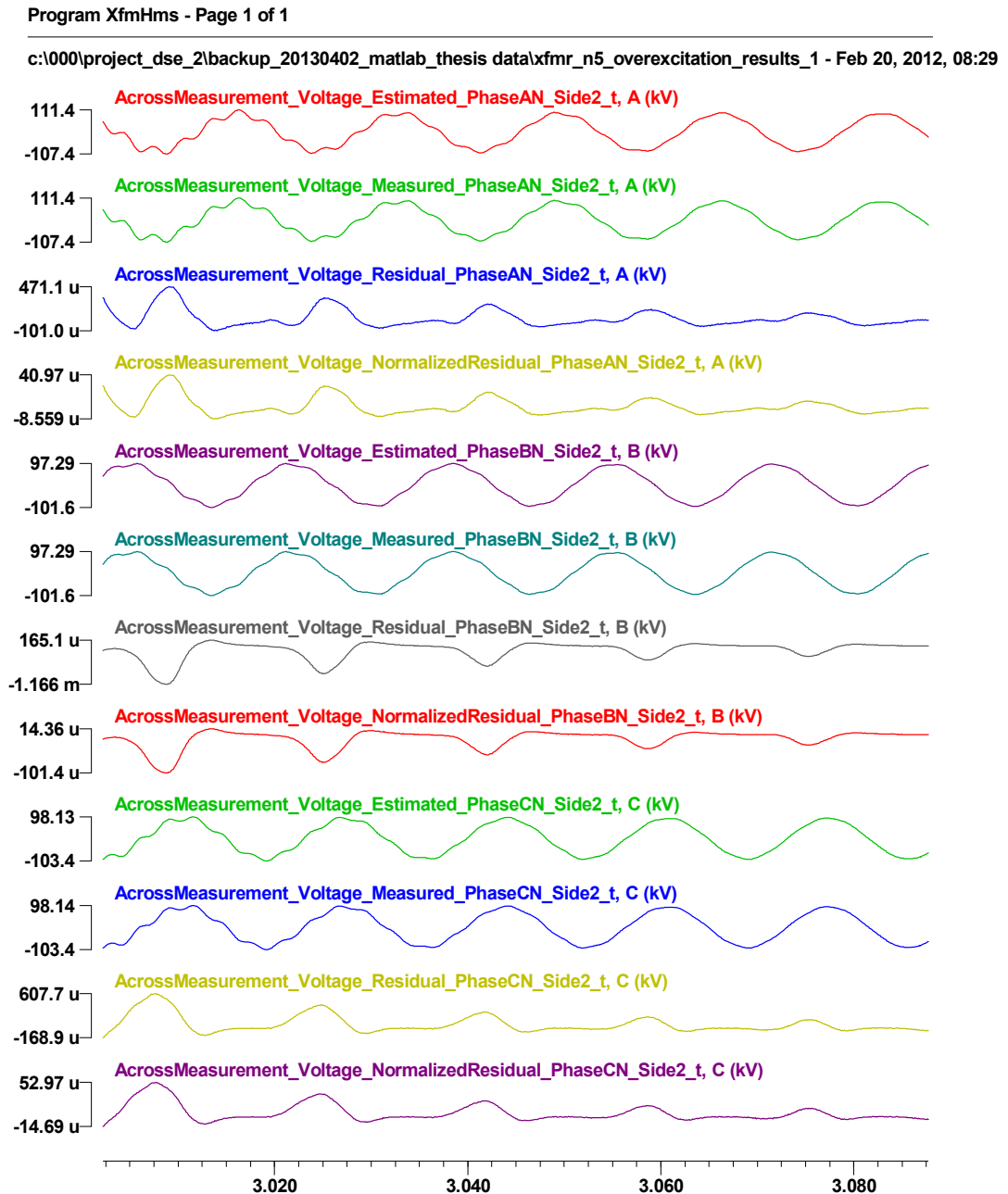


Figure 6.34: Estimated value, measured value, residual, and normalized residual of the voltage measurement at the secondary side (test C).

The simulation results are available for further research and analysis. They are stored in the format of COMTRADE, generating the following files:

- XFMR_N5_OVEREXCITATION_results_1.cfg and XFMR_N5_OVEREXCITATION_results_1.dat: the estimated values of all state variables, the estimated and measured values of all across measurements, the residuals of all across measurements, the normalized residuals of all across measurements, the estimated and measured values of all through measurements, the residuals of all through measurements, the normalized residuals of all through measurements, the estimated and measured values of all pseudo measurements, the residuals of all pseudo measurements, the normalized residuals of all pseudo measurements, the degrees of freedom, the chi-square critical values, the confidence levels, and the processing time.
- XFMR_N5_OVEREXCITATION_results_2.cfg and XFMR_N5_OVEREXCITATION_results_2.dat: the estimated and measured values of all virtual measurements, the residuals of all virtual measurements, and the normalized residuals of all virtual measurements, the degrees of freedom, the chi-square critical values, the confidence levels, and the processing time.

6.4.2.4 Simulation Results for Test D: Through-fault Condition

For the through-fault condition, the confidence level obtained by the developed dynamic state estimator is shown in Figure 6.30. The result graph shows that the confidence level stays at 100% all the time, which means that the measurements are consistent with the model, and there is no internal fault during the simulation.

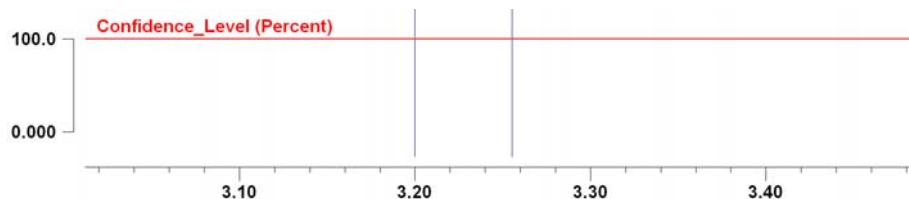


Figure 6.35: Confidence level (test D: the through-fault condition).

The measured and estimated values of the current measurements at the primary and secondary side are shown with different colors as shown in Figure 6.36. The estimated values match well the measured values.

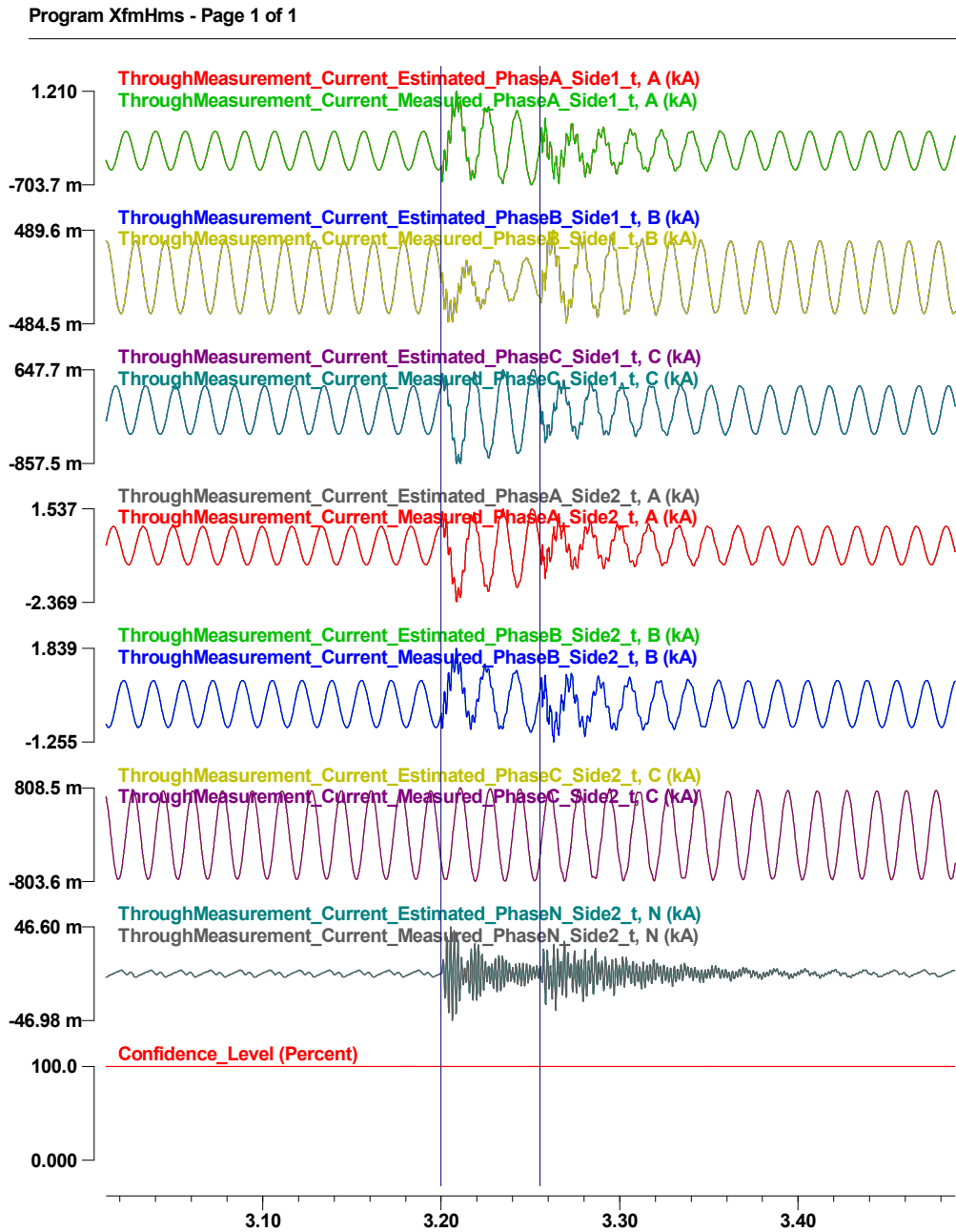


Figure 6.36: Estimated and measured values of the current measurements with the confidence level (test D).

The measured and estimated values of the voltage measurements at the primary and secondary side are also compared in Figure 6.37. The estimated values match well the measured values.

Program XfmHms - Page 1 of 1

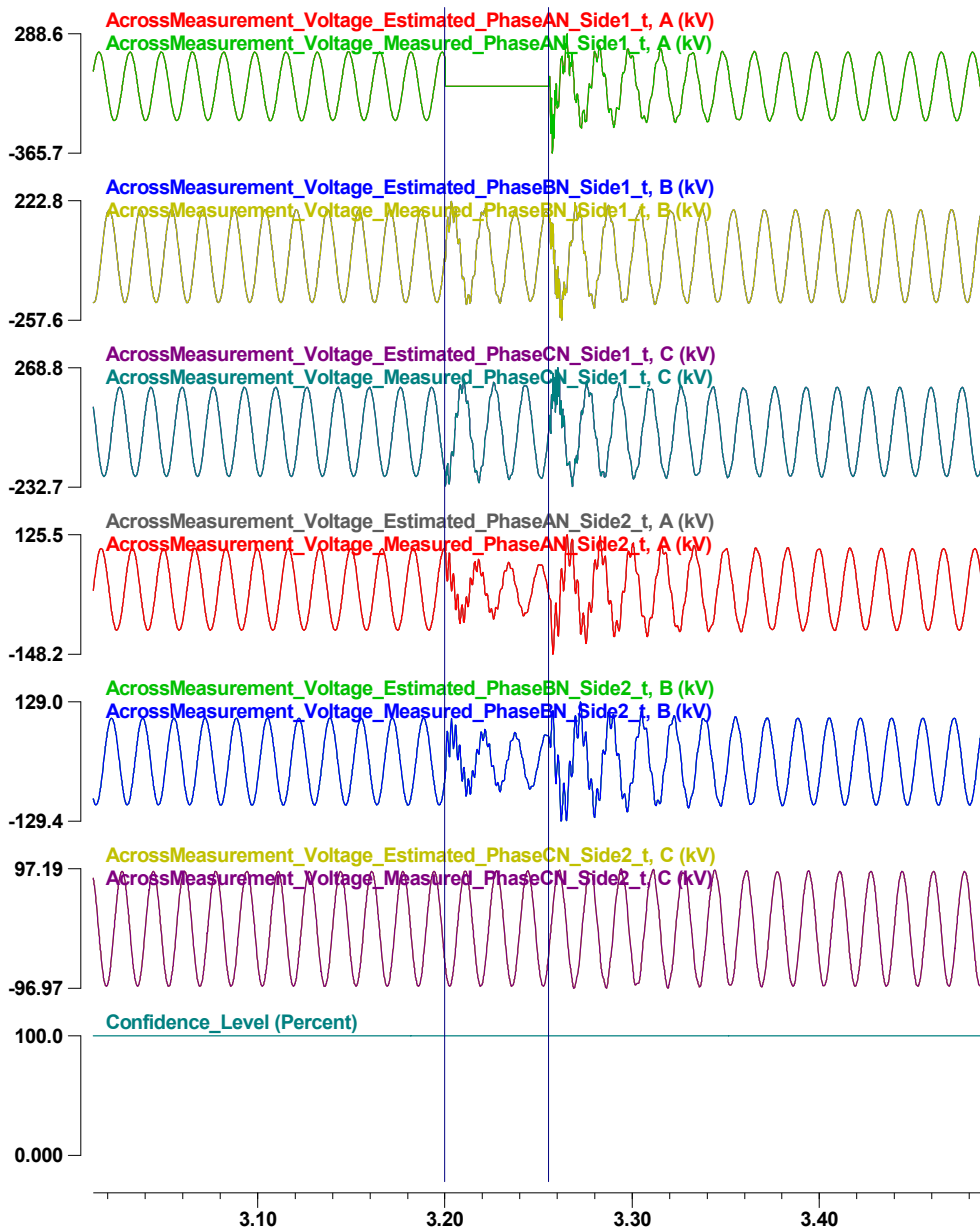


Figure 6.37: Estimated and measured values of the voltage measurements with the confidence level (test D).

From Figure 6.36 and Figure 6.37, it can be concluded that the estimated voltages and currents match well the measured ones during the through-fault condition.

The estimated value, measured value, residual, and normalized residual of the current measurement at the primary side are presented in the following figure. Note that the residuals are very small. Additionally, the residuals of all measurements in this figure are relatively high at the beginning of the test, and then, they are decreasing as time passes.

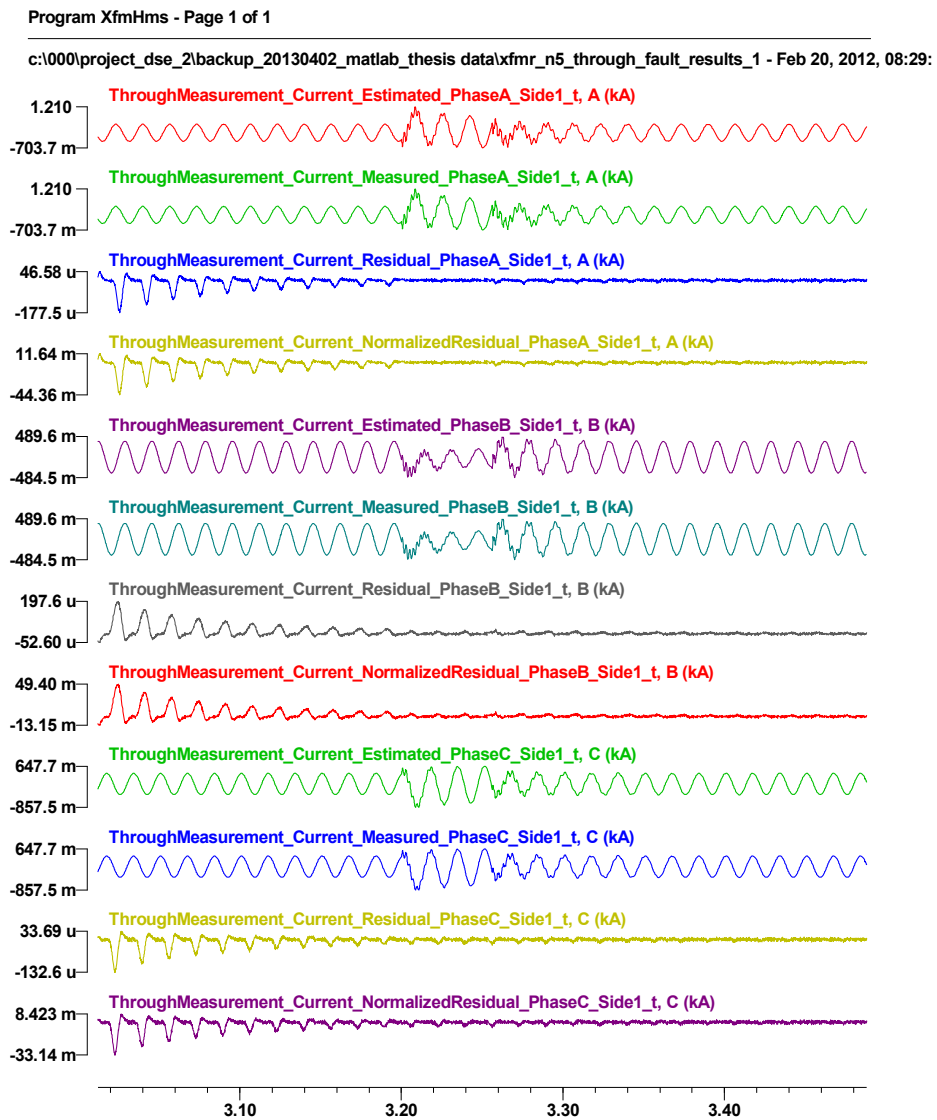


Figure 6.38: Estimated value, measured value, residual, and normalized residual of the current measurement at the primary side (test D).

The estimated value, measured value, residual, and normalized residual of the current measurement at the secondary side are presented in the following figure. Note that residuals are very small. Additionally, the residuals of all measurements in this figure except the phase-N current measurement are relatively high at the beginning of the test, and then, they are decreasing as time passes. The phase-N current measurement has relatively small values compared to other through measurements, so the initial values of the past-history have little influence on the residuals of the phase-N through measurement.

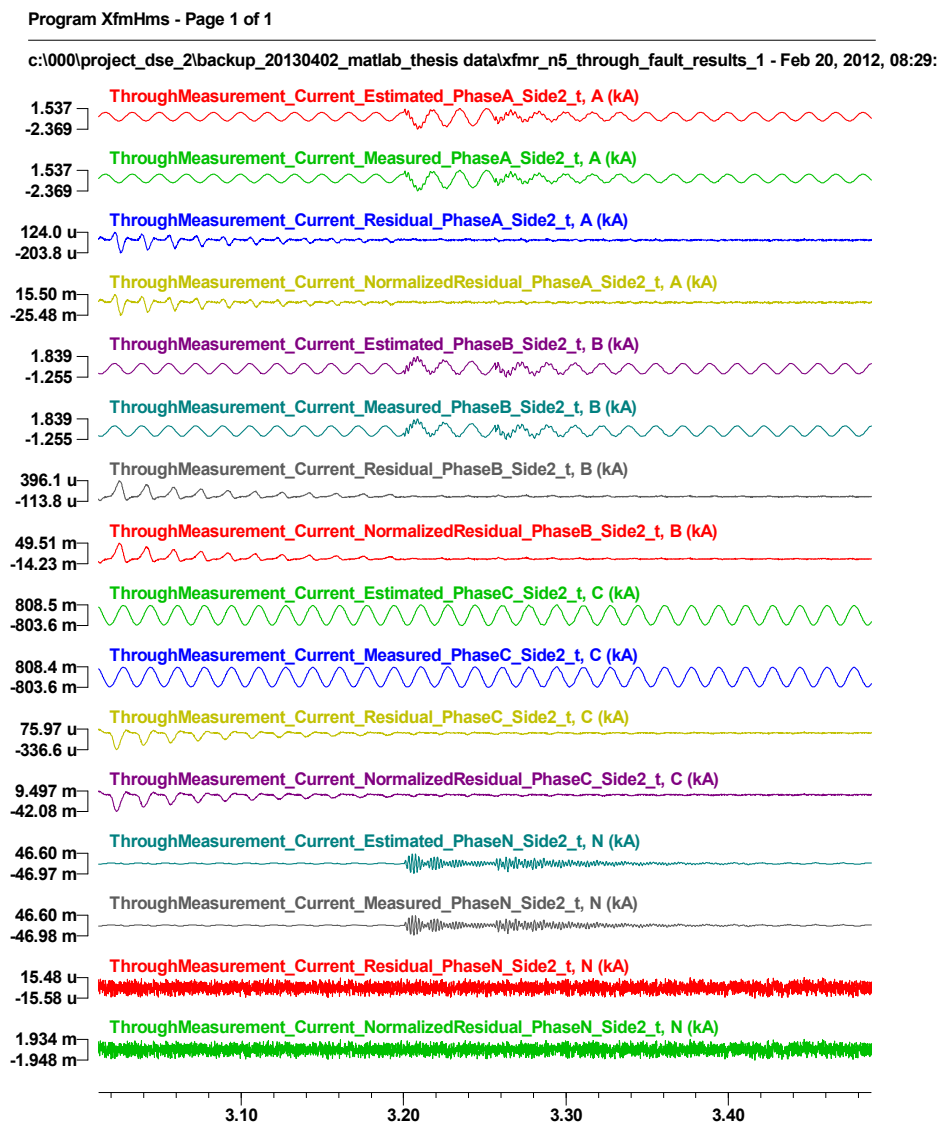


Figure 6.39: Estimated value, measured value, residual, and normalized residual of the current measurement at the secondary side (test D).

The estimated value, measured value, residual, and normalized residual of the voltage measurement at the primary side are presented in the following figure. Note that residuals are very small. Additionally, the residuals of all measurements in this figure are relatively high at the beginning of the test, and then, they are decreasing as time passes.

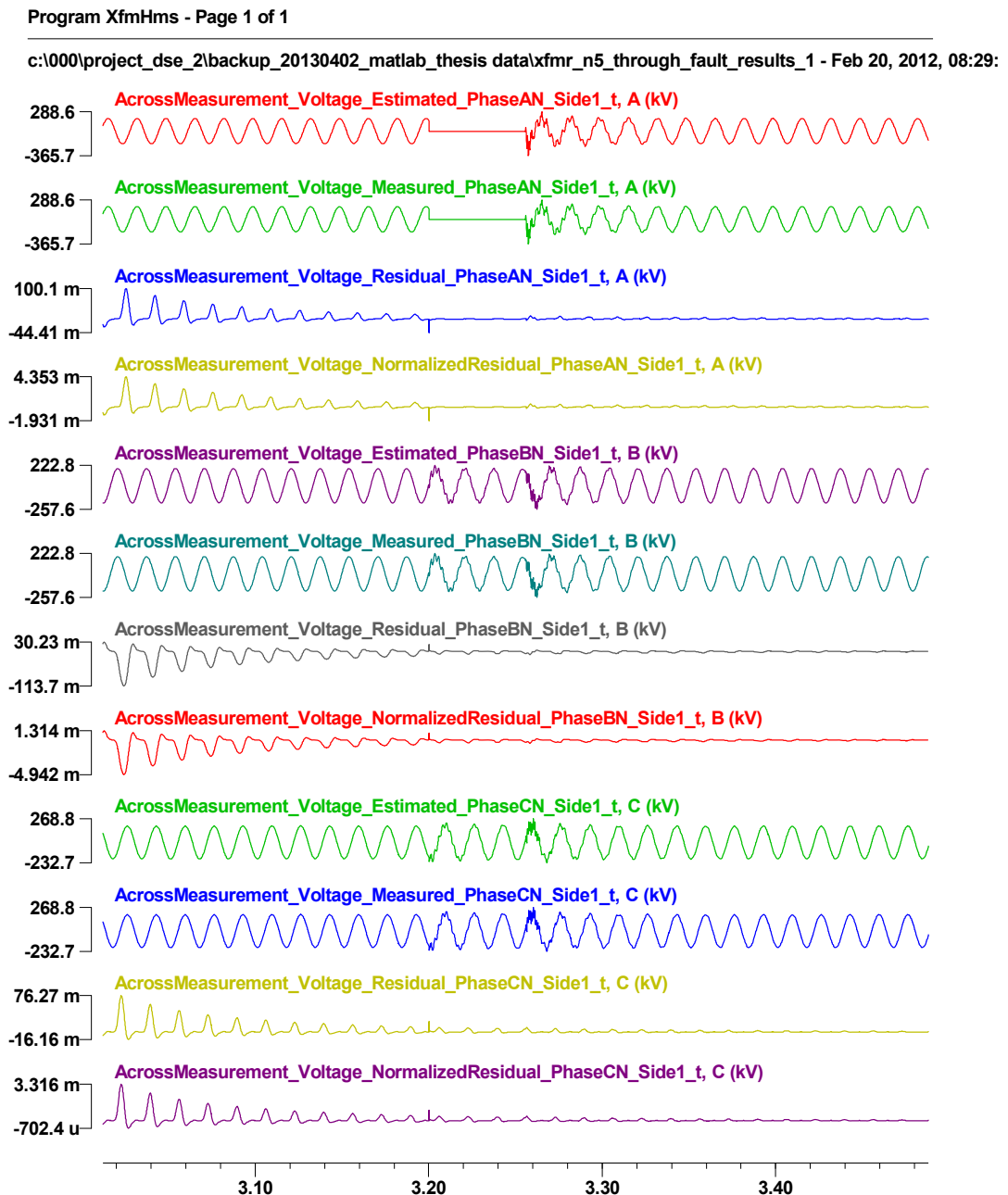


Figure 6.40: Estimated value, measured value, residual, and normalized residual of the voltage measurement at the primary side (test D).

The estimated value, measured value, residual, and normalized residual of the voltage measurement at the secondary side are presented in the following figure. Note that residuals are very small. Additionally, the residuals of all measurements in this figure are relatively high at the beginning of the test, and then, they are decreasing as time passes.

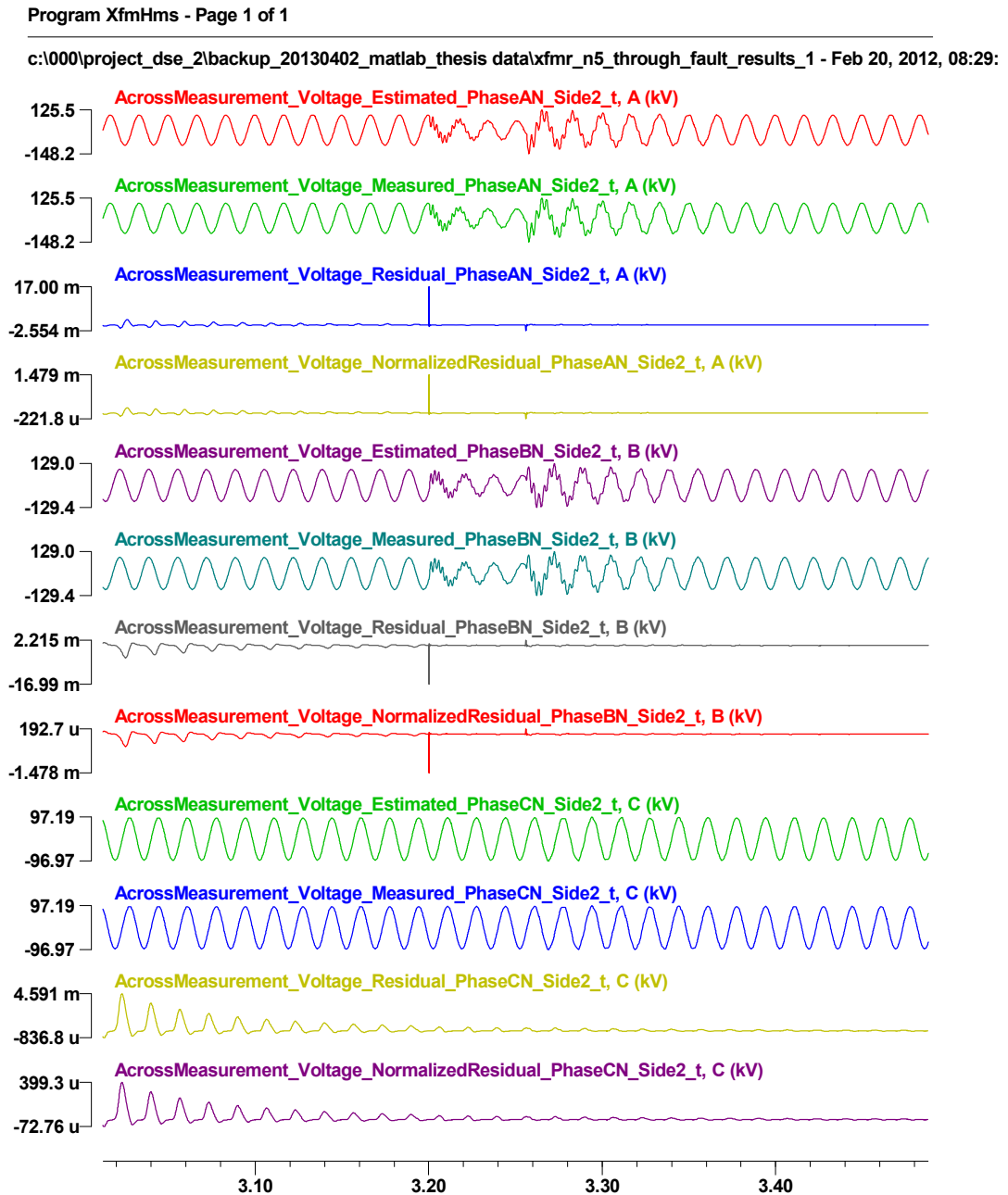


Figure 6.41: Estimated value, measured value, residual, and normalized residual of the voltage measurement at the secondary side (test D).

The simulation results are available for further research and analysis. They are stored in the format of COMTRADE, generating the following files:

- XFMR_N5_THROUGH_FAULT_results_1.cfg and XFMR_N5_THROUGH_FAULT_results_1.dat: the estimated values of all state variables, the estimated and measured values of all across measurements, the residuals of all across measurements, the normalized residuals of all across measurements, the estimated and measured values of all through measurements, the residuals of all through measurements, the normalized residuals of all through measurements, the estimated and measured values of all pseudo measurements, the residuals of all pseudo measurements, the normalized residuals of all pseudo measurements, the degrees of freedom, the chi-square critical values, the confidence levels, and the processing time.
- XFMR_N5_THROUGH_FAULT_results_2.cfg and XFMR_N5_THROUGH_FAULT_results_2.dat: the estimated and measured values of all virtual measurements, the residuals of all virtual measurements, and the normalized residuals of all virtual measurements, the degrees of freedom, the chi-square critical values, the confidence levels, and the processing time.

6.4.2.5 Simulation Results for Test E: Internal-fault Condition

For the internal-fault condition, the confidence level obtained by the dynamic state estimator is shown in Figure 6.42. During most of the time, the confidence level is 100%, which means that the measurements are consistent with the model. However, at 3.2 seconds, the confidence level drops to 0%, which indicates that an internal fault or faults have occurred somewhere in the transformer. Then, the confidence level recovers back to 100% in 0.05 seconds, indicating that the faults are cleared. However, the confidence level is oscillating during 0.05 seconds after the faults are cleared. This is due to the fact that the past-history values, $v(t-h)$ and $y(t-h)$, are inaccurate right after the

faults are cleared (i.e., when the system model is changed). Nevertheless, this oscillation is decreasing as time passes.

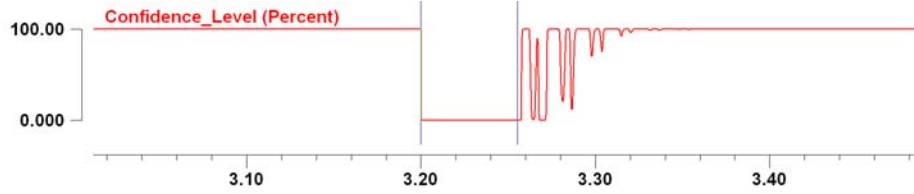


Figure 6.42: Confidence level (test E: the internal-fault condition).

The measured and estimated values of the current measurements at the primary and secondary side are compared with different colors as shown in Figure 6.43. Note the estimated values matches well the measured values for the time intervals outside the fault duration. They do not match well during the internal fault(s).

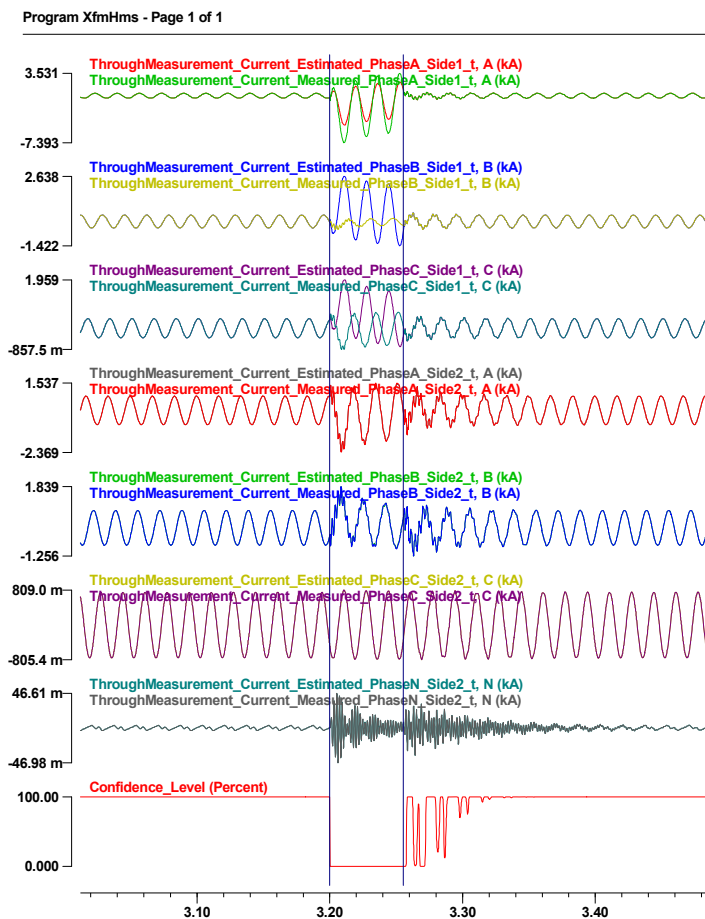


Figure 6.43: Estimated and measured values of the current measurements with the confidence level (test E).

The measured and estimated values of the voltage measurements at the primary and secondary side are also compared in Figure 6.44.

Program XfmHms - Page 1 of 1

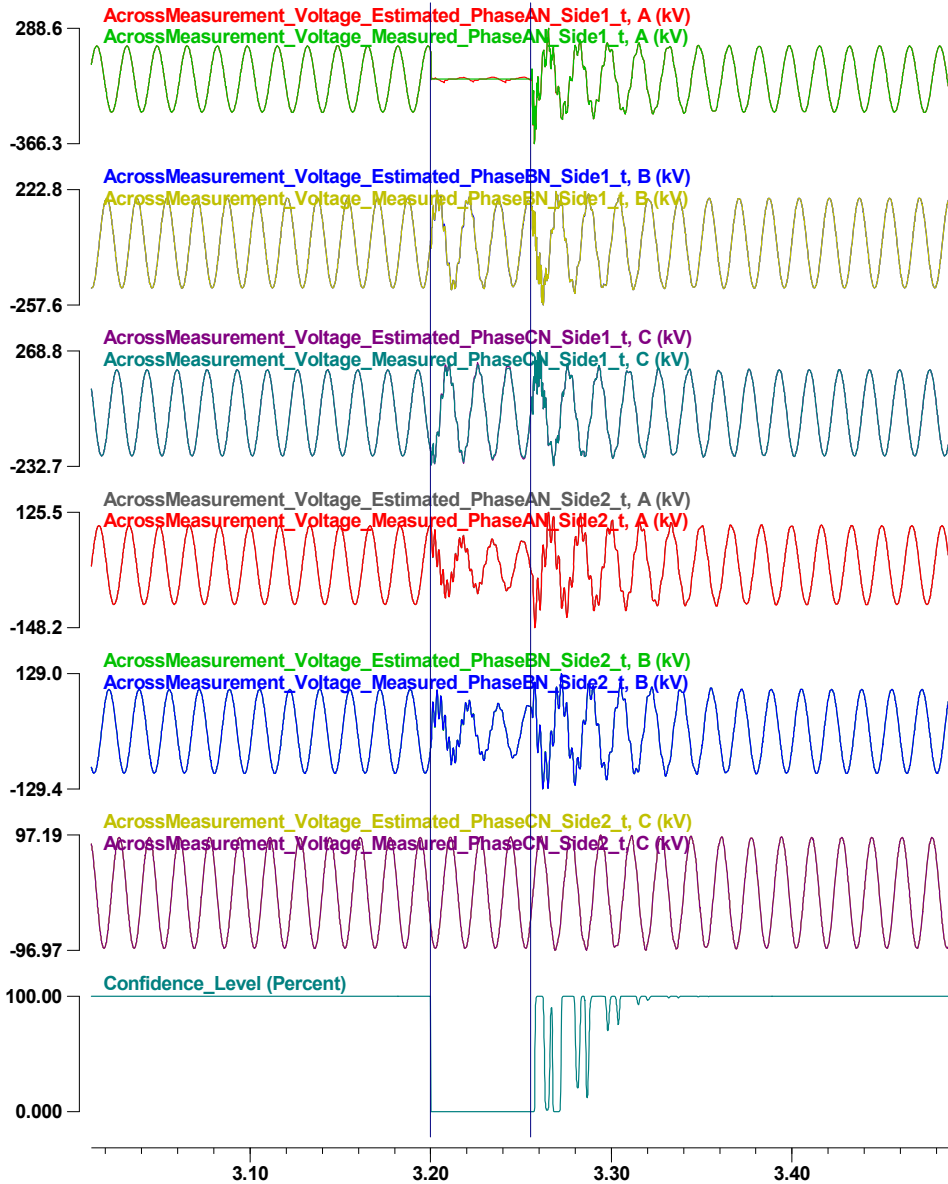


Figure 6.44: Estimated and measured values of the voltage measurements with the confidence level (test E).

Note that there is a specific duration in which the confidence level is zero, and therefore, it can be concluded that any internal faults have occurred in the transformer under protection during this period.

The estimated value, measured value, residual, and normalized residual of the current measurement at the primary side are presented in the following figure. Note that the residuals are high during the internal fault condition and small outside the fault time interval.

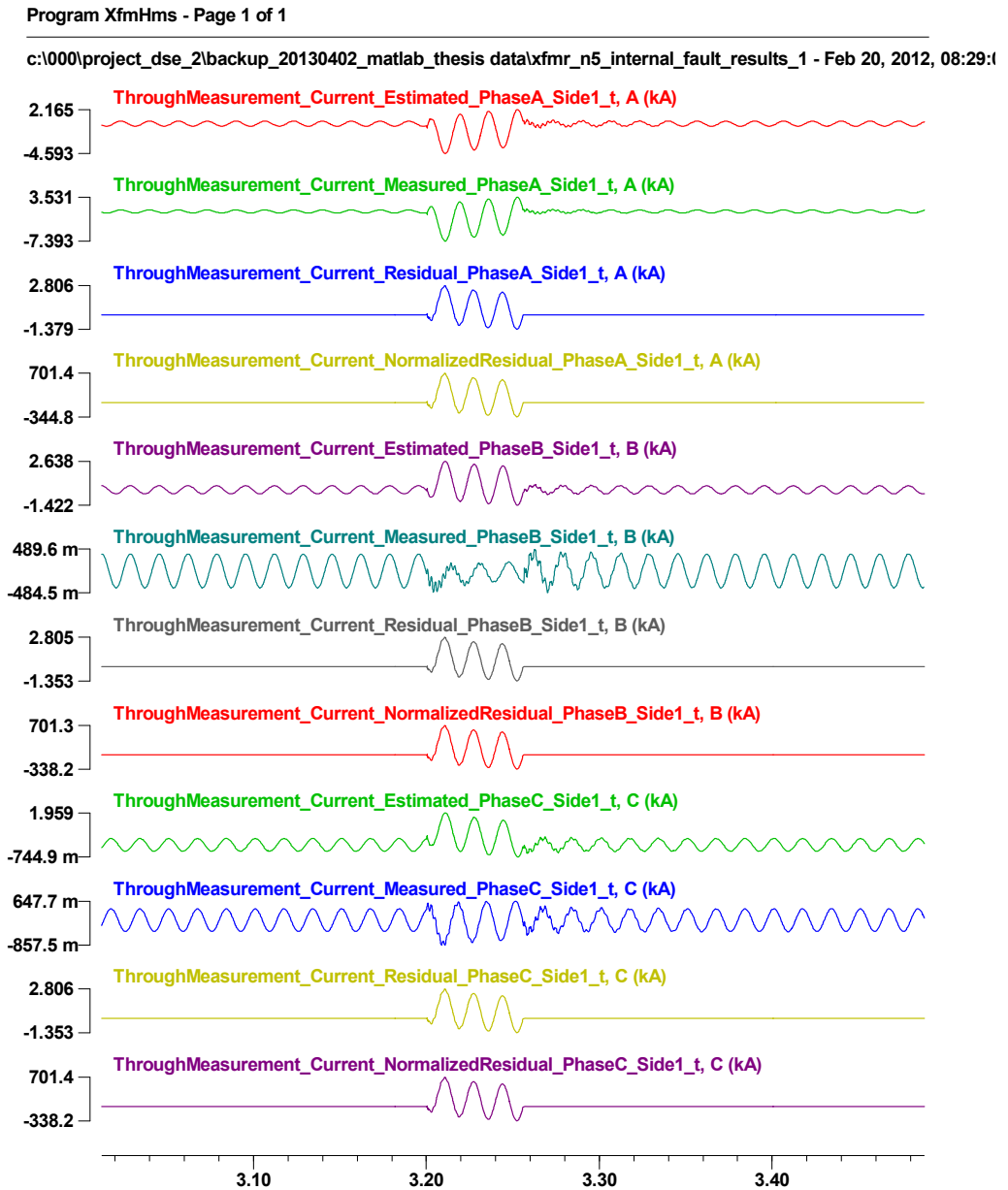


Figure 6.45: Estimated value, measured value, residual, and normalized residual of the current measurement at the primary side (test E).

The estimated value, measured value, residual, and normalized residual of the current measurement at the secondary side are presented in the following figure. Note that the residuals are high during the internal fault condition and small outside the fault time interval.

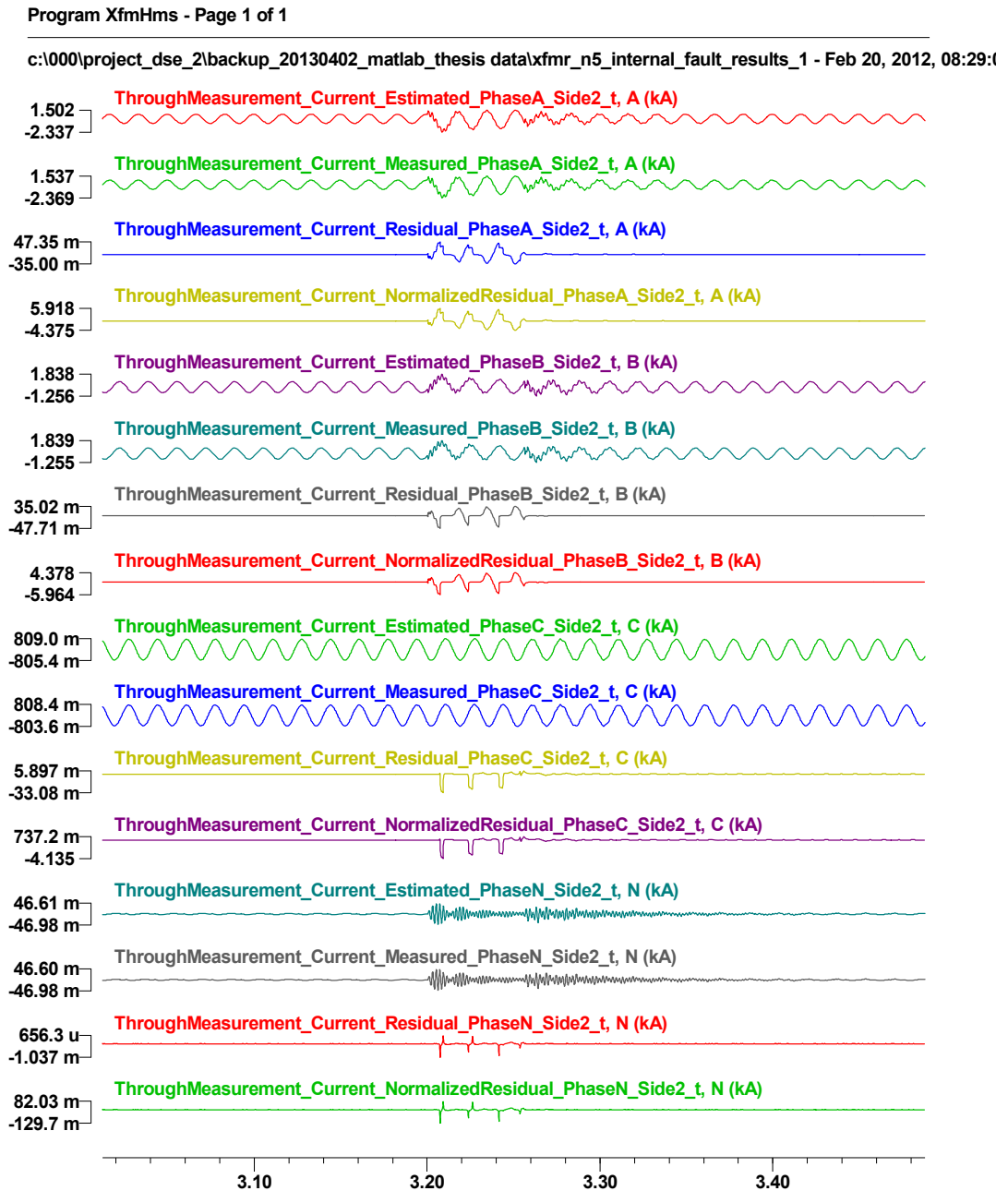


Figure 6.46: Estimated value, measured value, residual, and normalized residual of the current measurement at the secondary side (test E).

The estimated value, measured value, residual, and normalized residual of the voltage measurement at the primary side are presented in the following figure. Note that the residuals are high during the internal fault condition and small outside the fault time interval.

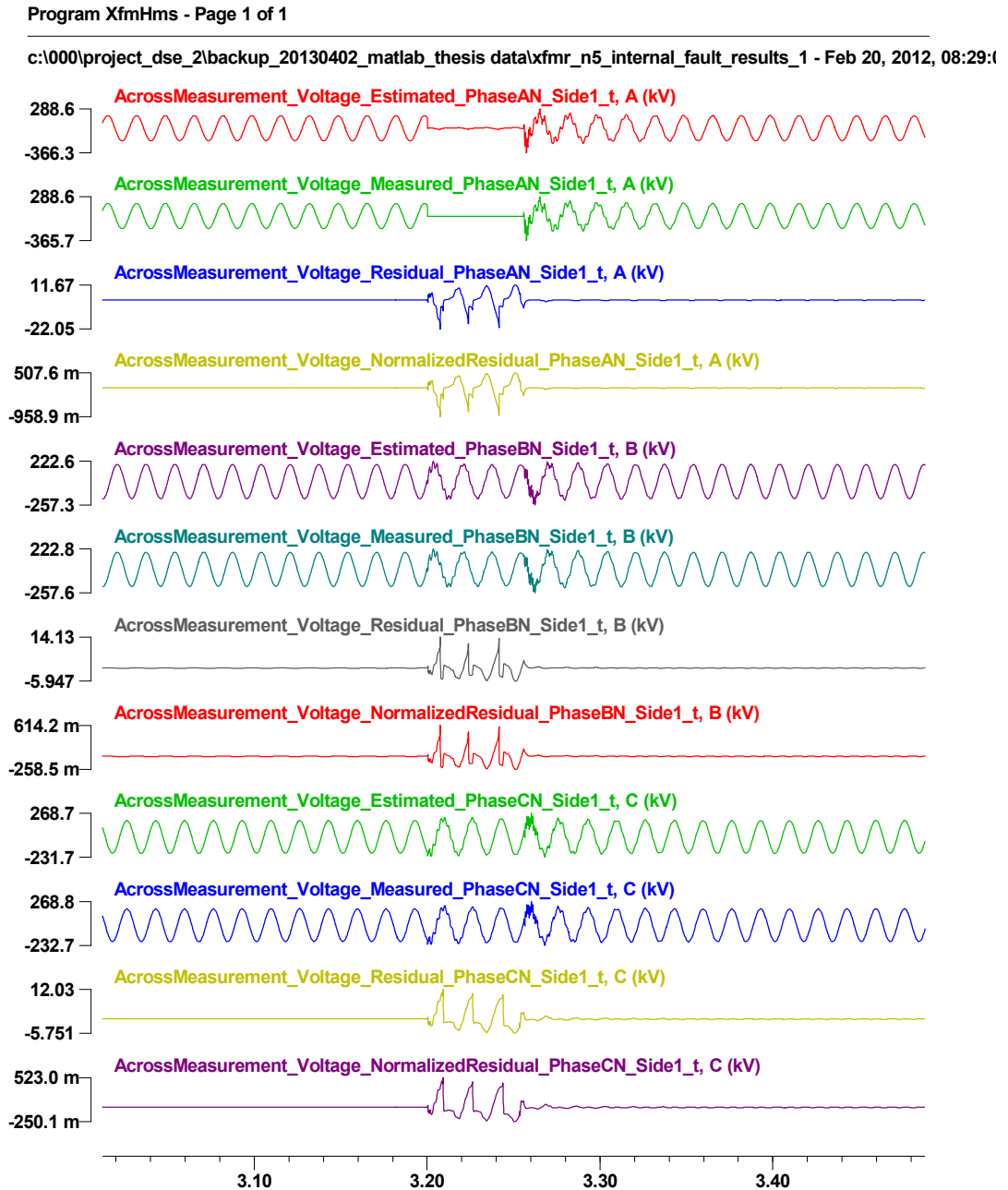


Figure 6.47: Estimated value, measured value, residual, and normalized residual of the voltage measurement at the primary side (test E).

The estimated value, measured value, residual, and normalized residual of the voltage measurement at the secondary side are presented in the following figure. Note that the residuals are high during the internal fault condition and small outside the fault time interval.

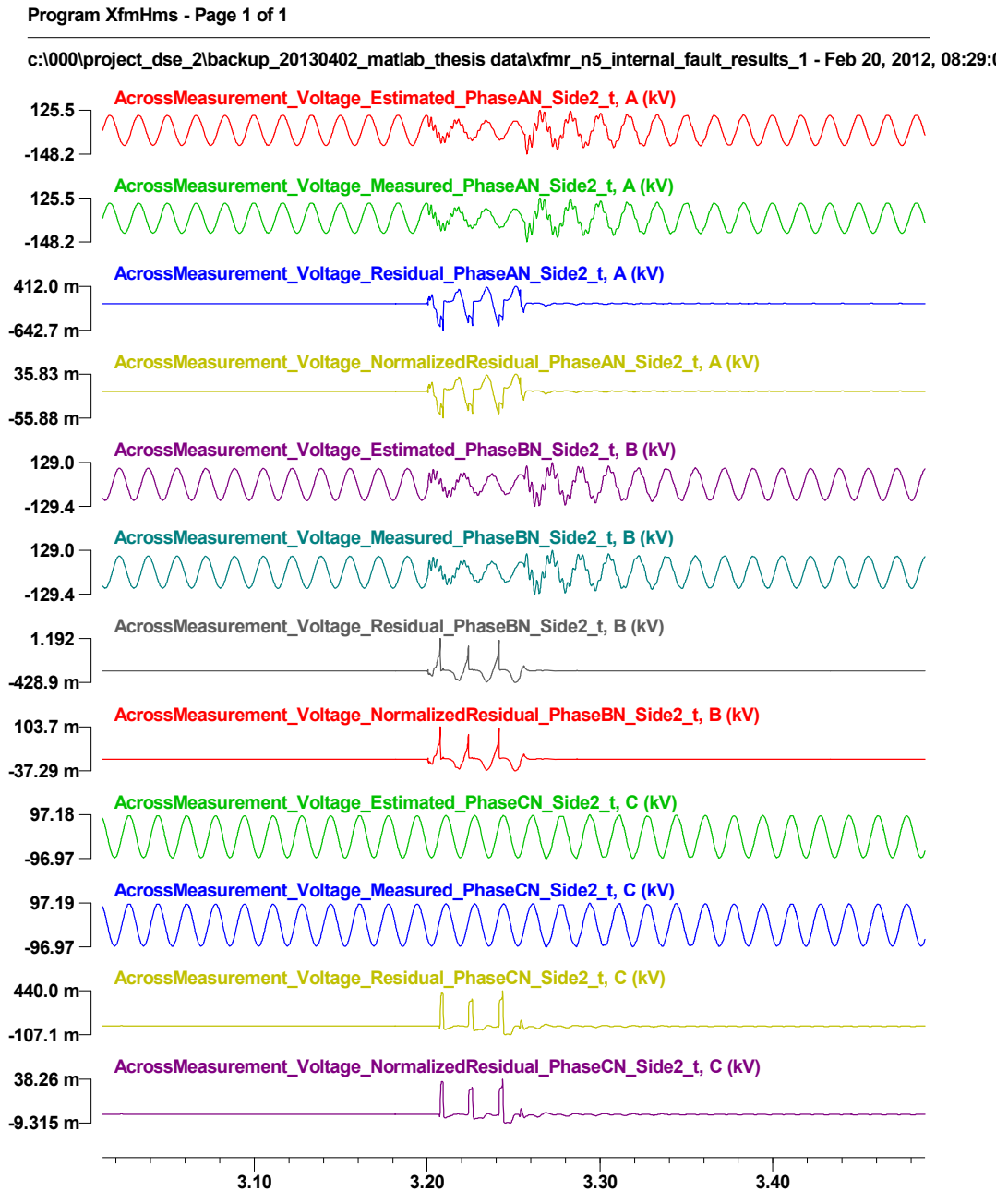


Figure 6.48: Estimated value, measured value, residual, and normalized residual of the voltage measurement at the secondary side (test E).

The simulation results are available for further research and analysis. They are stored in the format of COMTRADE, generating the following files:

- XFMR_N5_INTERNAL_FAULT_results_1.cfg and XFMR_N5_INTERNAL_FAULT_results_1.dat: the estimated values of all state variables, the estimated and measured values of all across measurements, the residuals of all across measurements, the normalized residuals of all across measurements, the estimated and measured values of all through measurements, the residuals of all through measurements, the normalized residuals of all through measurements, the estimated and measured values of all pseudo measurements, the residuals of all pseudo measurements, the normalized residuals of all pseudo measurements, the degrees of freedom, the chi-square critical values, the confidence levels, and the processing time.
- XFMR_N5_INTERNAL_FAULT_results_2.cfg and XFMR_N5_INTERNAL_FAULT_results_2.dat: the estimated and measured values of all virtual measurements, the residuals of all virtual measurements, and the normalized residuals of all virtual measurements, the degrees of freedom, the chi-square critical values, the confidence levels, and the processing time.

6.5 Summary

In this chapter, the setting-less component protection scheme is applied to the three-phase, two-winding, variable-tap, and saturable-core transformer. First, hardware requirements are discussed in terms of the accuracy of measurements, time synchronism, and fast data communications. Based on the requirements, there are two recommended selections: the first selection consists of a setting-less protection relay, PTs, CTs, and cables, and the second one includes a setting-less protection relay, PTs, CTs, cables, merging units, and the process bus equipped with fiber optic cables.

To verify the proposed protection scheme, numerical experiments are performed with the following five test scenarios: (1) the normal operating condition, (2) transformer energization, (3) transformer overexcitation, (4) the through-fault condition, and (5) the internal-fault condition. For the numerical experiments, the WinIGS software and the COMTRADE format are used. The results of the numerical experiments indicates that the confidence level becomes zero only when the internal faults occur inside the transformer under protection, finally verifying that the proposed setting-less component protection can reliably differentiate transformer internal faults from other conditions that indicate normal transformer operation.

CHAPTER 7

CONCLUSIONS AND FUTURE RESEARCH DIRECTION

7.1 Conclusions

This research work focuses on new operation, control, and protection schemes for the restructured distribution system, which is characterized by the high penetration of DGs and power-electronics-interfaced devices. These new schemes are aiming to solve newly emerging grid problems in the distribution system from the three points of view: (1) protection gaps, (2) the operation and control of DGs, and (3) the need for short-term operational planning. First, the small fault currents of inverter-based DGs and dynamically changing system topology have been reasons for protection gaps that may lead traditional protection methods to false operations, so new philosophy of protection should be introduced and developed. Next, the characteristics of DGs based on renewable energy resources are continuously varying with environmental conditions, thereby requiring instant-by-instant management to maximize the utilization of the DGs. Finally, short-term operational planning is recommended in the restructured distribution system because it is difficult to schedule the long-term planning of non-dispatchable DGs, which is, in general, unpredictable in the long term. Moreover, the unintentional changes of operational modes (e.g., switching to the islanded mode in emergency conditions) are occurring in microgrids, so operational purposes and constraints must switch and adapt in real time.

7.1.1 Design of Autonomous State Estimation

In an attempt to solve the newly emerging grid problems, this research work proposes the autonomous and decentralized operation, providing architecture and functionality as guidelines. The most fundamental tool for the autonomous operation is

the ability to autonomously extract the model of the system in real time. This research work introduces the concept of autonomous state estimation, which integrates all information from all available devices in the local distribution system for extracting accurate operating conditions in real time. For autonomous state estimation, the three types of essential data are defined: (1) connectivity, (2) device models, and (3) measurements. The connectivity refers to externally connecting points, and the device model represents mathematical equations that describe the characteristic of a component. The measurement data are numeric quantities measured by sensors in the field. For the integration of these data, this research work proposes to deploy UMPCUs or data-acquisition units (e.g., meters, relays, or recorders) over a wide area; the UMPCU can not only monitor a device under management but protect or control the device autonomously.

Based on connectivity and device models, autonomous state estimation autonomously identifies state variables and integrates all device models, forming the entire system model. Along with measurement data that streaming into the autonomous state estimator, general state estimation, the well-known weighted-least-squares method, is performed. This procedure is repeated in real time, which eventually produces the real-time operating conditions of the local distribution system, making it possible to detect the reconfiguration of system topology, which occurs when devices are plugged-in or unplugged or when switches are operating.

The results of state estimation can be evaluated by the goodness of fit of models to measurement data. Indeed, the goodness of fit can be quantified by the confidence level, which is the probability that the distribution of measurement errors are within expected bounds. In general, the high confidence level indicates that the system model is consistent with measurement data. On the other hand, if there are any bad data, then the confidence level is definitely low.

7.1.2 Autonomous Operation of the Distribution System with DGs

This research work applies autonomous state estimation to the autonomous operation of the distribution system from the three points of view: (1) setting-less component protection, (2) instant-by-instant management, and (3) short-term operational planning. These autonomous operations have different operational time frames; the setting-less component protection operates every few cycles, the instant-by-instant management does every few seconds, and the short-term operational planning does every few minutes. Taking into consideration the time frames and operational purposes, both the setting-less component protection and the instant-by-instant management need to be implemented in a decentralized way, but the short-term operational planning is more suited to centralized operation by the local DMS.

First, an innovative component protection scheme that is autonomous, setting-less, and adaptive is proposed in this research work. The key concept is to use dynamic state estimation, which produces the dynamic model of a component under protection using real-time measurements and component dynamic models. Then, the results of dynamic state estimation are evaluated using the well-known chi-square test, providing the confidence level, which becomes an indicator that determines if any internal faults occur or not. Meanwhile, the dynamic states estimated can be converted to quasi-static states using GPS-synchronized measurement and phasor computation and then provided to the local DMS.

Second, this research work proposes how to use the three sets of essential data (i.e., connectivity, device models, and measurements) for determining the maximum power points of a DG. Then, a generation controller uses the maximum power points for regulating the DG to pull out maximum available power from renewable energy resources. This research work deals with the MPPT of the PV panels and DFIG-based wind turbines.

Finally, this research work proposes short-term operational planning based on autonomous state estimation, which computes the real-time operating conditions of non-dispatchable DGs that utilize renewable energy resources. Then, for the remaining generation units dispatchable, operating points that achieve multiple operational objectives (e.g., economic or environmental dispatch) can be optimized. Furthermore, this research work defines objective functions and constraints based on the three operational modes (i.e., the grid-connected mode, the islanded mode, and the assistant mode).

7.1.3 Laboratory Demonstration of Autonomous State Estimation

The autonomous state estimation has been experimentally tested in two laboratory setups: (1) the scaled-down power system in the PSCAL at the Georgia Institute of Technology, and (2) the smart grid energy system in NEC Laboratories America, Inc. The purpose of these experimental demonstrations is to prove the feasibility of the proposed autonomous state estimation.

The scaled-down power system at the Georgia Institute of Technology has a generation system (e.g., a three-phase synchronous generator and a DC motor), a transmission system (e.g., transmission lines, a step-up transformer, and switches), loads, and a data-acquisition system (e.g., PTs, CTs, numerical relays, and merging units). For data communication, IEC61850 and Ethernet protocols are implemented, ensuring interoperability between multi-vendor devices. In this demonstration, while the WinIGS provides the connectivity and device model data, the numerical relays are streaming measurement data to the local DMS through data-communication lines. Then, based on these data, an autonomous state estimator in the DMS extracts accurate operating conditions in real time. Several performance metrics (e.g., the confidence level, computational speed, and average standard deviation of estimated states) are also presented.

The autonomous state estimation has been also implemented in the smart grid energy system in NEC Laboratories America, Inc., which consists of PV panels, a PV inverter, a storage system with four battery compartments, and a programmable load that can emulate daily load profiles. In particular, the storage system operates in three operational modes: (1) the standby mode, (2) the inverter mode, and (3) the charger mode. The main purpose of testing with this laboratory setup is to verify the capability of autonomous state estimation to adapt to dynamic grid situations such as multi-operational modes. The test results verify that an autonomous state estimator in this demonstration can track of the multi-operational modes of the storage system, providing real-time operating conditions.

7.1.4 Feasibility Test of Setting-less Component Protection of the Transformer

This research work finally performs numerical simulation for the feasibility study of the setting-less component protection method. In specific, the three-phase, two-winding, variable-tap, and saturable-core transformer is tested, for transformers often lead relays to false trips in case of energization and excessive inrush currents or overexcitation that generates distorted currents. Numerical experiments with five test scenarios are performed: (1) the normal operating condition, (2) transformer energization, (3) transformer overexcitation, (4) the through-fault condition, and (5) the internal-fault condition. For this test, this research work uses the WinIGS to build a test system, to emulate the given test scenarios, and to generate measurement data. The results of these numerical experiments prove that the proposed setting-less component protection for the transformer is capable of successfully distinguish internal faults from other conditions (e.g., normal operating conditions, energization, overexcitation, and through-fault conditions).

7.1.5 Component Modeling

In appendices, two modeling techniques are presented (i.e., the quadratic integration method and model quadratization) and several device models such as the PV array and the three-phase transformer.

7.2 Contributions

This thesis describes two major contributions, which are fundamental for the protection, control and operation of the smart power grid. These are: (1) the autonomous state estimation that provides the real-time model of the system in an autonomous manner and at very high speeds – the real-time model is fundamental for the model-based control and operation of an electric power grid, and (2) the setting-less protection approach with an application to the protection of transformers.

The autonomous state estimation is an automated state estimation for the restructured distribution system. In other words, the autonomous state estimation utilizes three types of essential data (i.e., connectivity, device models, and measurements) from all available devices in the distribution system to automate the process of general state estimation (e.g., the formulation of measurement models), eventually computing the accurate real-time operating conditions of the distribution system. As a result, this automated process of the autonomous state estimation enables capturing the dynamic changes of system topology. Any changes in the system topology or newly plugged-in devices are automatically included in the autonomous state estimation without human intervention. Previously, various researches on the state estimation for the distribution system have been conducted [64], [88-93], but they do not deal with defining data types and standard format for the purpose of automating the state-estimation process. Consequently, the previous methods of distribution-system state estimation lack of adaptability to the dynamic conditions of the distribution system as well as plug-and-play capability.

The setting-less component protection scheme is based on dynamic state estimation and the confidence level (i.e., the goodness of fit of measurements to the component model). This new protection method is autonomous, setting-less, and adaptive; in other words, the method can securely differentiate any internal faults of the component from other normal conditions without manual settings or coordination with other protective functions. For validation, this research work applies the proposed method to transformer protection because secure relay operations have been a crucial issue in transformer protection (i.e., the inrush currents or overexcitation currents of transformers causing false relay operations). Naturally, various protection algorithms (e.g., time-delay settings, the desensitization of relays, voltage consideration, the harmonic-restraint method, waveform-shape identification, and the dwell-time method) have been developed [25-27], but these methods are not perfect for identifying inrush currents or sometimes compromise dependability or speed because of relay settings. In contrast, the proposed new protection scheme can securely distinguish internal-fault conditions from other normal conditions (e.g., transformer energization, transformer overexcitation, or through-fault conditions) as verified in numerical simulations and tests.

7.3 Future Work Direction

This research work introduces autonomous state estimation and its application to design the architecture and functionality of the autonomous operation of the distribution system with DGs. The feasibility has been assessed with laboratory demonstrations and numerical experiments. The extension of this research work focuses on two issues: (1) the upgrade of the existing laboratory test system with more generation systems and autonomous controllers and (2) the actual development and implementation of the proposed autonomous operation in terms of setting-less component protection, instant-by-instant management, and short operational planning.

The first extension of this research work is to integrate more generation systems, which include renewable energy resources such as the solar or wind energy, to the existing laboratory system. This multi-generation system could be a test-bed for implementing autonomous state estimation and its applications to the autonomous operations. Furthermore, the extended demonstration may include the plug-and-play test of various loads, DGs or energy-storage systems, eventually developing autonomous controllers to the point where reliable, stable, efficient, and secure operation can be demonstrated.

The next remaining work is to actually develop and implement the autonomous operation of the distribution system in three areas: (1) setting-less component protection, (2) instant-by-instant management, and (3) short-term operational planning. The feasibility test of the setting-less component protection needs to be extended to inverter-interfaced DGs, which contain semiconductor-based active devices such as diodes, thyristors, and other switching electronics. This extended test is significant because of the increasing penetration of inverter-interfaced DGs, which generate relatively small fault currents. Next, for implementing the instant-by-instant management, the explicit and accurate models of generation resources including the PV array and the wind turbine are required first, and then, the MPPT algorithm and the control schemes should be developed according to the type of DGs. In fact, the control of the PV system or the wind-turbine system is based on the inverter, and thus, inverter-control schemes should be designed. Last but not least, for the short-term operational planning, more detailed objective functions and constraints should be defined, taking into account various grid conditions such as multi-operational modes, spinning reserve, and battery size.

APPENDIX A

DEVICE MODELING TECHNIQUE

A.1 Overview

In this appendix, two innovative methods for deriving the device model are presented: (1) the quadratic integration method and (2) model quadratization. The quadratic integration method converts the differential equations to the standard form of device models as expressed in equation (3.3), and the model quadratization reduces the nonlinearity.

A.2 Quadratic Integration Method

In an attempt to implement differential equations in device modeling, the quadratic integration method can simplify the differential equations [66], [94], generating the standard form of device models, equation (3.3). This integration method is a fourth-order-accurate method, thereby being more accurate than the traditional trapezoidal integration method and free from artificial numerical oscillations. The basic concept of quadratic integration method is that functions vary quadratically over the time period of one integration step, h , as described in Figure A.1.

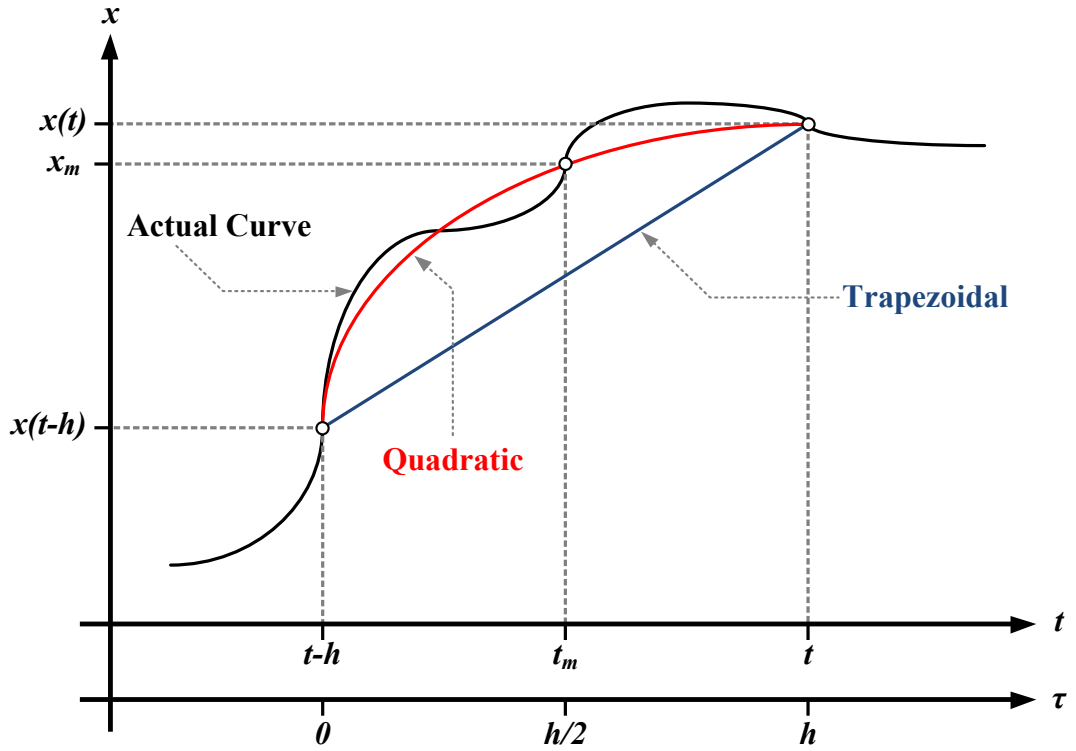


Figure A.1: Quadratic integration method.

The quadratic function $x(\tau)$ in one integration time step, from $t-h$ to t , can be expressed as follows:

$$x(\tau) = a + b\tau + c\tau^2, \quad (\text{A.1})$$

where

$$a = x(t-\tau), \quad (\text{A.2})$$

$$b = \frac{1}{h}(-3x(t-h) + 4x_m - x(t)), \quad (\text{A.3})$$

$$c = \frac{2}{h^2}(x(t-h) - 2x_m + x(t)). \quad (\text{A.4})$$

For example, a dynamic system is represented as follows:

$$\frac{dx(t)}{dt} = Ax(t), \quad (\text{A.5})$$

where A is the coefficient matrix. If this equation is integrated from $t-h$ to t and from $t-h$ to $t-h/2$, then the following matrix equation is obtained:

$$\begin{bmatrix} \frac{h}{24}A & I - \frac{h}{3}A \\ I - \frac{h}{6}A & \frac{2h}{3}A \end{bmatrix} \begin{bmatrix} x(t) \\ x_m \end{bmatrix} = \begin{bmatrix} I + \frac{5h}{24}A \\ I + \frac{h}{6}A \end{bmatrix} x(t-h), \quad (\text{A.6})$$

where I is the identity matrix.

A.3 Model Quadratization

The model nonlinearity can be quadratized with additional states and equations in such a way that the order is no greater than two [67], [95], and then, the model can be expressed as the standard form of device models, equation (3.3). For example, the nonlinearity of the transformer saturable core can be characterized with the nonlinear function of the magnetizing current and the magnetic flux linkage as follows:

$$i_m(t) = i_0 \left| \frac{\lambda(t)}{\lambda_0} \right|^n \text{sign}(\lambda(t)) = 0, \quad (\text{A.7})$$

where $i_m(t)$ is the magnetizing current, $\lambda(t)$ is the magnetic flux linkage, i_0 and λ_0 are the equation constants, $\text{sign}()$ is the sign function, and n is the exponent.

The number of additional internal states is determined by the following rule:

$$m = m_1 + m_2, \quad (\text{A.8})$$

where

$$m_1 = \text{int}(\log_2(n)), \quad (\text{A.9})$$

$$m_2 = (\# \text{ of ones in the binary representation of } n) - 1. \quad (\text{A.10})$$

Accordingly, the nonlinear function of the transformer can be quadratized as follows:

$$y_1(t) = (\lambda(t) / \lambda_0)^2, \quad (\text{A.11})$$

$$y_2(t) = y_1(t)^2, \quad (\text{A.12})$$

⋮

$$y_{m_1(t)} = y_{m_1-1}(t)^2, \quad (\text{A.13})$$

$$y_{m_1+1}(t) = y_{m_1}(t) \cdot y_{j_1}(t), \quad (\text{A.14})$$

$$y_{m_1+2}(t) = y_{m_1+1}(t) \cdot y_{j_2}(t), \quad (\text{A.15})$$

⋮

$$\begin{cases} y_m(t) = y_{m-1}(t) \cdot y_{j_{m_2}}(t), & \text{if } n \text{ even,} \\ y_m(t) = y_{m-1}(t) \cdot \lambda(t) / \lambda_0, & \text{if } n \text{ odd,} \end{cases} \quad (\text{A.16})$$

$$i_m(t) = i_0 \cdot \text{sign}(\lambda(t)) \cdot y_m(t), \quad (\text{A.17})$$

where j_1 to j_{m_2} are the internal state variables corresponding to the ones in the binary representation of n except the most significant bit.

One of advantages of model quadratization is that model nonlinearity can be reduced even though the quadratized model is same as the high-degree polynomial equation with no approximation. Therefore, the iterative computation of state estimation becomes more efficient. Another advantage is that model quadratization can reformulate the nonlinear model into the standard form of device models as represented in equation (3.3).

A.4 Summary

The main purpose of this appendix is to introduce two innovative methods to facilitate to derive the device model from mathematical equations of the component model: (1) the quadratic integration method and (2) model quadratization. By means of these two methods, any component can be formulated in the standard form of device models, which is expressed as equation (3.3).

APPENDIX B

PV-ARRAY MODEL

B.1 Overview

This appendix describes how to model the PV array in the standard form of device models, equation (3.3), which plays a pivotal role in integrating device models for the purpose of autonomous state estimation. First, the ideal PV cell is modeled, followed by modeling the practical PV array. To express the PV array model in the standard form, the exponential term should be implemented using Taylor series and then quadratized using the model quadratization method, finally generating the device model in the ACF. Once the device model is obtained, state variables for the PV array model can be defined.

B.2 Component Model Description

To obtain the PV model, the single-diode model is used [33], [96]. The ideal equivalent circuit is depicted in Figure B.1, representing the terminal current and voltage of a PV cell as I and V , respectively. It is necessary to point out that the equivalent circuit in Figure B.1 represents the model of an ideal PV cell as described in the following basic equations:

$$I = I_{pv,cell} - I_d, \quad (\text{B.1})$$

$$I_d = I_{0,cell} \left[\exp\left(\frac{qV}{akT}\right) - 1 \right], \quad (\text{B.2})$$

where $I_{pv,cell}$ is the current generated by the incident light, I_d is the Shockley diode current, $I_{0,cell}$ is the reverse saturation current of the diode, q is the electron charge (i.e., $1.60217646 \times 10^{-19} \text{C}$), k is the Boltzmann constant (i.e., $1.3806503 \times 10^{-23} \text{J/K}$), T is the temperature of the p - n junction (K), and a is the diode ideality constant.

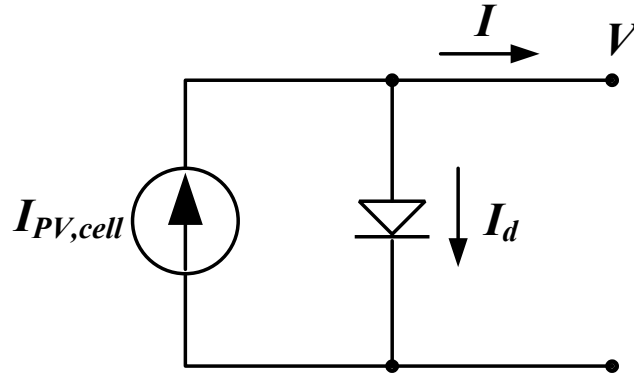


Figure B.1: Equivalent circuit of the ideal PV cell.

In general, no PV system consists of only one PV cell, but a set of PV cells are connected in series or parallel to increase the output terminal voltage or current, respectively. These connected PV cells become a PV panel, and a set of PV panels can also be connected in series or parallel to obtain a large PV system (i.e., a PV array). Furthermore, the practical PV array contains the equivalent series resistance, R_s , and the equivalent parallel resistance, R_p , as shown in Figure B.2. Finally, the practical PV array is expressed as follows:

$$I = I_{pv} - I_0 \left[\exp\left(\frac{V + R_s I}{V_t a}\right) - 1 \right] - \frac{V + R_s I}{R_p}, \quad (\text{B.3})$$

where

$$I_{pv} = I_{pv,cell} N_p, \quad (\text{B.4})$$

$$I_0 = I_{0,cell} N_p, \quad (\text{B.5})$$

$$V_t = N_s k T / q, \quad (\text{B.6})$$

I_{pv} is the light-generated current of the PV array with N_p cells connected in parallel, I_0 is the saturation current, and V_t is the thermal voltage of the PV array with N_s cells connected in series.

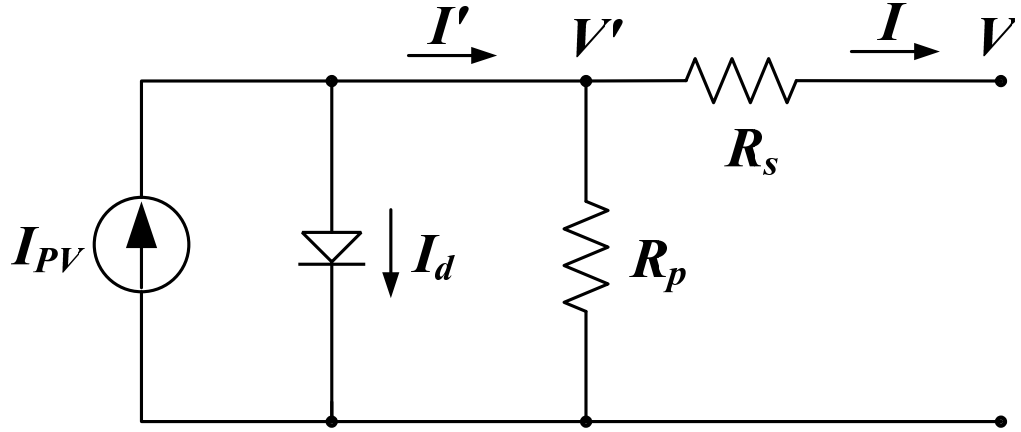


Figure B.2: Equivalent circuit of the practical PV array.

Most of parameters, which define the nonlinear I-V equation, can be determined using experimental data specified in the datasheets of the PV manufacturer. Among the parameters of the I-V equation, however, two parameters, I_{pv} and I_0 , randomly vary with the temperature of the PV cell, T , and the solar irradiation, G , as expressed in two subsequent equations:

$$I_{pv} = (I_{pv,n} + K_I \Delta T) \frac{G}{G_n}, \quad (\text{B.7})$$

$$I_0 = I_{0,n} \left(\frac{T_n}{T} \right)^3 \exp \left[\frac{qE_g}{ak} \left(\frac{1}{T_n} - \frac{1}{T} \right) \right], \quad (\text{B.8})$$

where

$$\Delta T = T - T_n, \quad (\text{B.9})$$

$I_{pv,n}$ is the light-generated current at the nominal condition (i.e., 25°C and 1000W/m²); K_I is the coefficient of the current temperature; T and T_n are the actual and nominal temperature, respectively (K); G and G_n are the actual and nominal irradiation on the device surface, respectively (W/m²); $I_{0,n}$ is the diode saturation current at the nominal condition; and E_g is the bandgap energy of the semiconductor.

In conclusion, the PV model can be described in equations (B.3), (B.7), and (B.8) with the two parameters, the PV current (i.e., I_{pv}) and the saturation current (i.e., I_0).

These two parameters, which define the I-V characteristics of the PV array, are the functions of the temperature of solar cells, T , and the solar irradiation, G , which are changing at every moment.

B.3 ACF Model Description

To express the PV-array model in the standard form of device models as expressed in equation (3.3), external and internal state variables are defined in Figure B.3. The external states include the terminal voltages (i.e., v_1 , v_2 , v_3 , and v_4), and the internal states are the two voltages (i.e., v_x and v_a) and the diode current (i.e., I_d). It should be pointed out that whereas v_1 and v_3 denote the real parts of the terminal voltages, v_2 and v_4 are the imaginary parts of the terminal voltages, which are always zero because the terminal voltages are direct voltage. Likewise, the real parts of the terminal currents are defined as i_1 and i_3 , and the imaginary parts of the terminal currents are i_2 and i_4 , which are also zero because the terminal currents are also DC.

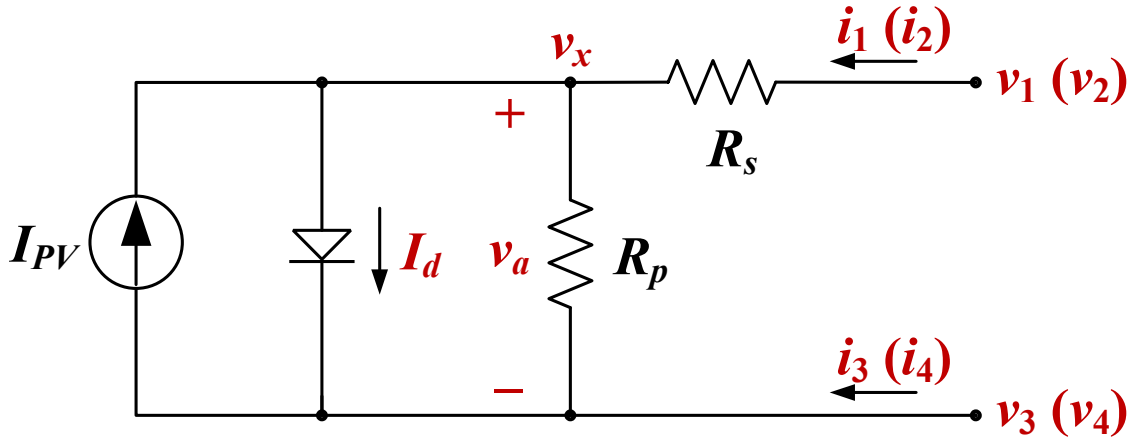


Figure B.3: Definition of the external and internal states of the PV-array model.

Based on the external and internal state variables defined, the PV-array model can be represented by the following equations:

$$i_1 = \frac{1}{R_s}(v_1 - v_x), \quad (\text{B.10})$$

$$i_2 = 0, \quad (\text{B.11})$$

$$i_3 = -\frac{1}{R_s}(v_1 - v_x), \quad (\text{B.12})$$

$$i_4 = 0, \quad (\text{B.13})$$

$$v_2 = 0, \quad (\text{B.14})$$

$$v_4 = 0, \quad (\text{B.15})$$

$$v_a = v_x - v_3, \quad (\text{B.16})$$

$$I_d = I_0 \left\{ \exp\left(\frac{v_a}{V_t a}\right) - 1 \right\}, \quad (\text{B.17})$$

$$I_{pv} - I_d - \frac{v_x}{R_p} + \frac{1}{R_1}(v_1 - v_x) = 0. \quad (\text{B.18})$$

In equation (B.17), the exponential function can be expanded with the following Taylor series:

$$\exp\left(\frac{v_a}{V_t a}\right) = 1 + \frac{v_a}{V_t a} + \frac{1}{2}\left(\frac{v_a}{V_t a}\right)^2 + \frac{1}{6}\left(\frac{v_a}{V_t a}\right)^3 + H.O.T, \quad (\text{B.19})$$

where *H.O.T* indicates the higher order terms. Note that the terms higher than three order are very small, and therefore, they can be omitted. In addition, as presented in equation (3.3), the order of nonlinear terms should be no more than two, thus introducing additional state variables, y_1 . Finally, equations (B.10) to (B.18) can be rearranged as follows:

$$i_1 = \frac{1}{R_s}v_1 - \frac{1}{R_s}v_x, \quad (\text{B.20})$$

$$i_2 = 0, \quad (\text{B.21})$$

$$i_3 = -\frac{1}{R_s}v_1 + \frac{1}{R_s}v_x, \quad (\text{B.22})$$

$$i_4 = 0, \quad (\text{B.23})$$

$$0 = v_3, \quad (\text{B.24})$$

$$0 = v_4, \quad (\text{B.25})$$

$$0 = v_3 - v_x + v_a, \quad (\text{B.26})$$

$$0 = \frac{I_0}{V_t a} v_a - I_d + \frac{I_0}{2(V_t a)^2} y_1 + \frac{I_0}{6(V_t a)^3} y_1 \cdot v_a, \quad (\text{B.27})$$

$$0 = I_{pv} + \frac{1}{R_1} v_1 - \left(\frac{1}{R_p} + \frac{1}{R_1} \right) v_x - I_d, \quad (\text{B.28})$$

$$0 = -y_1 + v_a^2. \quad (\text{B.29})$$

The aforementioned equations can be defined with the following state vectors:

$$\tilde{V} = [v_1, v_2, v_3, v_4]^T, \quad (\text{B.30})$$

$$y(t) = [v_x, v_a, I_d, y_1]^T, \quad (\text{B.31})$$

where \tilde{V} is the external voltages in phasor form, and $y(t)$ is the internal states. Finally, equations (B.20) to (B.29) can be expressed as the following ACF, becoming the standard form of the device model, equation (3.3):

$$\begin{bmatrix} \tilde{I} \\ 0 \\ 0 \end{bmatrix} = \begin{bmatrix} K_1 \\ K_2 \\ K_3 \end{bmatrix} + \begin{bmatrix} L_{11} & L_{12} & L_{13} \\ L_{21} & L_{22} & L_{23} \\ L_{31} & L_{32} & L_{33} \end{bmatrix} \begin{bmatrix} \tilde{V} \\ y(t) \\ y(t_m) \end{bmatrix} - \begin{bmatrix} N_{11} & N_{12} \\ N_{21} & N_{22} \\ N_{31} & N_{32} \end{bmatrix} \begin{bmatrix} 0 \\ y(t-h) \end{bmatrix} + \begin{bmatrix} f_1(t) \\ f_2(t) \\ f_3(t) \end{bmatrix}, \quad (\text{B.32})$$

where

$$\tilde{I} = [i_1, i_2, i_3, i_4]^T, \quad (\text{B.33})$$

B.4 State Variables

Finally, state variables for a PV array can be defined as follows:

$$\begin{bmatrix} \tilde{V} \\ y(t) \\ y(t_m) \end{bmatrix}, \quad (\text{B.34})$$

indicating there are a total of 12 state variables.

B.5 Summary

This appendix presents how to model the PV-array model. The device model developed can be utilized to define state variables for the device and to generate the three types of data (i.e., connectivity, device models, and measurements), which are essential to implement autonomous state estimation as well as the MPPT algorithm for the PV generation system.

APPENDIX C

THREE-PHASE-TRANSFORMER MODEL

C.1 Overview

This appendix presents the component dynamic model of the three-phase, two-winding, variable-tap, and saturable-core transformer, which is used for the setting-less component protection scheme. The development proceeds as follows: first, a single-phase transformer is described with mathematical equations, which are then quadratized and integrated, finally generating the component dynamic model of the single-phase transformer in the AQCF as expressed in equation (4.4). Subsequently, the models of each phase are interconnected to provide the overall three-phase model.

C.2 Component Model Description of the Single-phase Transformer

The three-phase saturable-core transformer contains nonlinear characteristic between the magnetizing current and the flux linkage of the transformer core, which is described by the following polynomial function with high degrees:

$$i_m(t) = i_0 \left| \frac{\lambda(t)}{\lambda_0} \right|^n \text{sign}(\lambda(t)), \quad (\text{C.1})$$

where $i_m(t)$ is the magnetizing current, $\lambda(t)$ is the magnetic flux linkage, i_0 and λ_0 are the equation constants, $\text{sign}()$ is the sign function, and n is the exponent.

To derive the device model of the three-phase transformer, at first, it is required to derive state-space equations for the single-phase model. For this purpose, the equivalent circuit for the practical single-phase transformer is described in Figure C.1. The loss in the primary winding occurs at the resistance r_1 in series with the primary winding. Similarly, the resistance r_2 accounts for the loss in the secondary winding. Two

inductances L_1 and L_2 represent the magnetic flux leakage of the primary and secondary winding, respectively. The shunt core resistance, r_c , characterizes the core loss, and both the shunt inductance, L_m , and the magnetizing current, $i_m(t)$, take into consideration the reactive power loss in the magnetizing core.

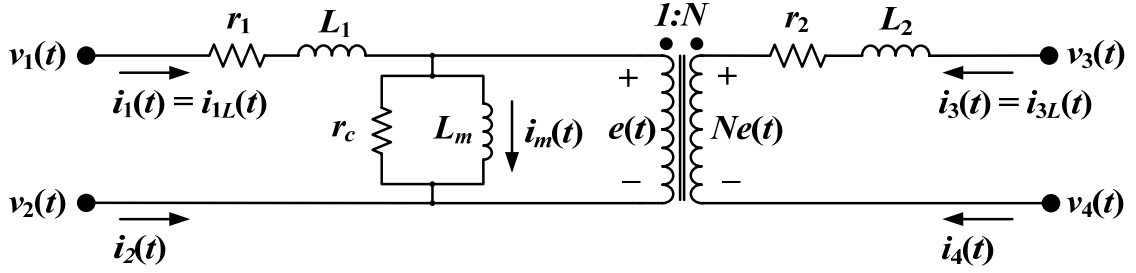


Figure C.1: Single-phase-transformer model.

Circuit analysis can describe the single-phase transformer model, yielding the following equations:

$$i_1(t) = i_{1L}(t), \quad (\text{C.2})$$

$$i_1(t) + i_2(t) = 0, \quad (\text{C.3})$$

$$i_3(t) = i_{3L}(t), \quad (\text{C.4})$$

$$i_3(t) + i_4(t) = 0, \quad (\text{C.5})$$

$$r_c i_1(t) + r_c N i_3(t) = r_c i_m(t) + e(t), \quad (\text{C.6})$$

$$i_m(t) = i_0 \left(\frac{\lambda(t)}{\lambda_0} \right)^5, \quad (\text{C.7})$$

$$v_1(t) - v_2(t) = r_1 i_{1L}(t) + L_1 \frac{d}{dt} i_{1L}(t) + e(t), \quad (\text{C.8})$$

$$v_3(t) - v_4(t) = r_2 i_{3L}(t) + L_2 \frac{d}{dt} i_{3L}(t) + Ne(t), \quad (\text{C.9})$$

$$e(t) = \frac{d}{dt} \lambda(t). \quad (\text{C.10})$$

Above equations can be rearranged as follows:

$$i_1(t) = i_{1L}(t), \quad (\text{C.11})$$

$$i_1(t) + i_2(t) = 0, \quad (\text{C.12})$$

$$i_3(t) = i_{3L}(t), \quad (\text{C.13})$$

$$i_3(t) + i_4(t) = 0, \quad (\text{C.14})$$

$$r_c i_1(t) + r_c N i_3(t) = r_c i_m(t) + e(t), \quad (\text{C.15})$$

$$0 = i_m(t) - i_0 \left(\frac{\lambda(t)}{\lambda_0} \right)^5, \quad (\text{C.16})$$

$$v_1(t) - v_2(t) = r_1 i_{1L}(t) + L_1 \frac{d}{dt} i_{1L}(t) + e(t), \quad (\text{C.17})$$

$$v_3(t) - v_4(t) = r_2 i_{3L}(t) + L_2 \frac{d}{dt} i_{3L}(t) + Ne(t), \quad (\text{C.18})$$

$$0 = e(t) - \frac{d}{dt} \lambda(t). \quad (\text{C.19})$$

Based on the above equations, state variables can be determined as follows:

$$s_{1\phi}(t) = [v_1(t), v_2(t), v_3(t), v_4(t), i_m(t), e(t), \lambda(t), i_{1L}(t), i_{3L}(t)]^T, \quad (\text{C.20})$$

where $s_{1\phi}(t)$ is the vector of state variables without introducing additional state variables for nonlinear terms. However, the high-order nonlinear term in equation (C.16) needs to be quadratized into several nonlinear terms whose order is at most two, thereby introducing additional state variables and equations.

C.3 Quadratized Model Description of the Single-phase Transformer

The single-phase-transformer model has a nonlinear term, so the model should be quadratized by introducing additional state variables and equations. When the exponent n is five, the quadratized model is provided below. Note that equations (C.30), (C.31), and (C.32) have quadratic terms.

$$i_1(t) = i_{1L}(t), \quad (\text{C.21})$$

$$i_1(t) + i_2(t) = 0, \quad (\text{C.22})$$

$$i_3(t) = i_{3L}(t), \quad (\text{C.23})$$

$$i_3(t) + i_4(t) = 0, \quad (\text{C.24})$$

$$r_c i_1(t) + r_c N i_3(t) = r_c i_m(t) + e(t), \quad (\text{C.25})$$

$$0 = i_m(t) - z(t), \quad (\text{C.26})$$

$$0 = v_1(t) - v_2(t) - e(t) - r_1 i_{1L}(t) - L_1 \frac{d}{dt} i_{1L}(t), \quad (\text{C.27})$$

$$0 = v_3(t) - v_4(t) - N \cdot e(t) - r_2 i_{3L}(t) - L_2 \frac{d}{dt} i_{3L}(t), \quad (\text{C.28})$$

$$0 = e(t) - \frac{d}{dt} \lambda(t), \quad (\text{C.29})$$

$$0 = y_1(t) - \left(\frac{\lambda(t)}{\lambda_0} \right)^2, \quad (\text{C.30})$$

$$0 = y_2(t) - y_1(t)^2, \quad (\text{C.31})$$

$$0 = y_3(t) - y_2(t) \cdot \frac{\lambda(t)}{\lambda_0}, \quad (\text{C.32})$$

$$0 = -i_0 y_3(t) + z(t). \quad (\text{C.33})$$

The state variables of the single-phase transformer are defined as follows:

$$\begin{aligned} x_{1\phi}(t) = [v_1(t), v_2(t), v_3(t), v_4(t), i_m(t), e(t), \lambda(t), i_{1L}(t), i_{3L}(t), \\ y_1(t), y_2(t), y_3(t), z(t)]^T, \end{aligned} \quad (\text{C.34})$$

where $x_{1\phi}(t)$ is the vector of the state variables of the quadratized single-phase transformer.

C.4 AQCF Model Description of the Single-phase Transformer

The equations that describe the single-phase transformer can be written simply as follows:

$$X_1 \cdot i_{1\phi}(t) = X_2 \cdot x_{1\phi}(t) + X_3 \frac{d}{dt} x_{1\phi}(t) + f(t), \quad (\text{C.35})$$

$$f(t) = \begin{bmatrix} x_{1\phi}(t)^T \cdot Q_1 \cdot x_{1\phi}(t) \\ x_{1\phi}(t)^T \cdot Q_2 \cdot x_{1\phi}(t) \\ \vdots \\ x_{1\phi}(t)^T \cdot Q_{13} \cdot x_{1\phi}(t) \end{bmatrix}, \quad (\text{C.36})$$

where

$$i_{1\phi}(t) = [i_1(t), i_2(t), i_3(t), i_4(t), 0, 0, 0, 0, 0, 0, 0, 0]^T, \quad (\text{C.37})$$

$$X_1 = \begin{bmatrix} 1 & 0 & 0 & 0 & 0 & 0 & 0 & 0 & 0 & 0 & 0 & 0 & 0 \\ 1 & 1 & 0 & 0 & 0 & 0 & 0 & 0 & 0 & 0 & 0 & 0 & 0 \\ 0 & 0 & 1 & 0 & 0 & 0 & 0 & 0 & 0 & 0 & 0 & 0 & 0 \\ 0 & 0 & 1 & 1 & 0 & 0 & 0 & 0 & 0 & 0 & 0 & 0 & 0 \\ r_c & 0 & r_c N & 0 & 0 & 0 & 0 & 0 & 0 & 0 & 0 & 0 & 0 \\ 0 & 0 & 0 & 0 & 0 & 0 & 0 & 0 & 0 & 0 & 0 & 0 & 0 \\ 0 & 0 & 0 & 0 & 0 & 0 & 0 & 0 & 0 & 0 & 0 & 0 & 0 \\ 0 & 0 & 0 & 0 & 0 & 0 & 0 & 0 & 0 & 0 & 0 & 0 & 0 \\ 0 & 0 & 0 & 0 & 0 & 0 & 0 & 0 & 0 & 0 & 0 & 0 & 0 \\ 0 & 0 & 0 & 0 & 0 & 0 & 0 & 0 & 0 & 0 & 0 & 0 & 0 \\ 0 & 0 & 0 & 0 & 0 & 0 & 0 & 0 & 0 & 0 & 0 & 0 & 0 \\ 0 & 0 & 0 & 0 & 0 & 0 & 0 & 0 & 0 & 0 & 0 & 0 & 0 \\ 0 & 0 & 0 & 0 & 0 & 0 & 0 & 0 & 0 & 0 & 0 & 0 & 0 \end{bmatrix}, \quad (\text{C.38})$$

$$X_2 = \begin{bmatrix} 0 & 0 & 0 & 0 & 0 & 0 & 0 & 1 & 0 & 0 & 0 & 0 & 0 \\ 0 & 0 & 0 & 0 & 0 & 0 & 0 & 0 & 0 & 0 & 0 & 0 & 0 \\ 0 & 0 & 0 & 0 & 0 & 0 & 0 & 0 & 1 & 0 & 0 & 0 & 0 \\ 0 & 0 & 0 & 0 & 0 & 0 & 0 & 0 & 0 & 0 & 0 & 0 & 0 \\ 0 & 0 & 0 & 0 & r_c & 1 & 0 & 0 & 0 & 0 & 0 & 0 & 0 \\ 0 & 0 & 0 & 0 & 1 & 0 & 0 & 0 & 0 & 0 & 0 & 0 & -1 \\ 1 & -1 & 0 & 0 & 0 & -1 & 0 & -r_1 & 0 & 0 & 0 & 0 & 0 \\ 0 & 0 & 1 & -1 & 0 & -N & 0 & 0 & -r_2 & 0 & 0 & 0 & 0 \\ 0 & 0 & 0 & 0 & 0 & 1 & 0 & 0 & 0 & 0 & 0 & 0 & 0 \\ 0 & 0 & 0 & 0 & 0 & 0 & 0 & 0 & 0 & 1 & 0 & 0 & 0 \\ 0 & 0 & 0 & 0 & 0 & 0 & 0 & 0 & 0 & 0 & 1 & 0 & 0 \\ 0 & 0 & 0 & 0 & 0 & 0 & 0 & 0 & 0 & 0 & 0 & 1 & 0 \\ 0 & 0 & 0 & 0 & 0 & 0 & 0 & 0 & 0 & 0 & 0 & -i_0 & 1 \end{bmatrix}, \quad (\text{C.39})$$

$$X_3 = \begin{bmatrix} 0 & 0 & 0 & 0 & 0 & 0 & 0 & 0 & 0 & 0 & 0 & 0 & 0 & 0 \\ 0 & 0 & 0 & 0 & 0 & 0 & 0 & 0 & 0 & 0 & 0 & 0 & 0 & 0 \\ 0 & 0 & 0 & 0 & 0 & 0 & 0 & 0 & 0 & 0 & 0 & 0 & 0 & 0 \\ 0 & 0 & 0 & 0 & 0 & 0 & 0 & 0 & 0 & 0 & 0 & 0 & 0 & 0 \\ 0 & 0 & 0 & 0 & 0 & 0 & 0 & 0 & 0 & 0 & 0 & 0 & 0 & 0 \\ 0 & 0 & 0 & 0 & 0 & 0 & 0 & 0 & 0 & 0 & 0 & 0 & 0 & 0 \\ 0 & 0 & 0 & 0 & 0 & 0 & 0 & -L_1 & 0 & 0 & 0 & 0 & 0 & 0 \\ 0 & 0 & 0 & 0 & 0 & 0 & 0 & 0 & -L_2 & 0 & 0 & 0 & 0 & 0 \\ 0 & 0 & 0 & 0 & 0 & 0 & -1 & 0 & 0 & 0 & 0 & 0 & 0 & 0 \\ 0 & 0 & 0 & 0 & 0 & 0 & 0 & 0 & 0 & 0 & 0 & 0 & 0 & 0 \\ 0 & 0 & 0 & 0 & 0 & 0 & 0 & 0 & 0 & 0 & 0 & 0 & 0 & 0 \\ 0 & 0 & 0 & 0 & 0 & 0 & 0 & 0 & 0 & 0 & 0 & 0 & 0 & 0 \\ 0 & 0 & 0 & 0 & 0 & 0 & 0 & 0 & 0 & 0 & 0 & 0 & 0 & 0 \end{bmatrix}, \quad (\text{C.40})$$

$$Q_1 = Q_2 = \dots = Q_9 = Q_{13} = \text{diag}([0, 0, 0, 0, 0, 0, 0, 0, 0, 0, 0, 0, 0, 0]), \quad (\text{C.41})$$

$$Q_{10} = \text{diag}([0, 0, 0, 0, 0, 0, 0, -(1/\lambda_0)^2, 0, 0, 0, 0, 0, 0]), \quad (\text{C.42})$$

$$Q_{11} = \text{diag}([0, 0, 0, 0, 0, 0, 0, 0, 0, -1, 0, 0, 0, 0]), \quad (\text{C.43})$$

$$Q_{12} = \begin{bmatrix} 0 & 0 & 0 & 0 & 0 & 0 & 0 & 0 & 0 & 0 & 0 & 0 & 0 & 0 \\ 0 & 0 & 0 & 0 & 0 & 0 & 0 & 0 & 0 & 0 & 0 & 0 & 0 & 0 \\ 0 & 0 & 0 & 0 & 0 & 0 & 0 & 0 & 0 & 0 & 0 & 0 & 0 & 0 \\ 0 & 0 & 0 & 0 & 0 & 0 & 0 & 0 & 0 & 0 & 0 & 0 & 0 & 0 \\ 0 & 0 & 0 & 0 & 0 & 0 & 0 & 0 & 0 & 0 & 0 & 0 & 0 & 0 \\ 0 & 0 & 0 & 0 & 0 & 0 & 0 & 0 & 0 & 0 & 0 & 0 & 0 & 0 \\ 0 & 0 & 0 & 0 & 0 & 0 & 0 & 0 & 0 & 0 & -1/\lambda_0 & 0 & 0 & 0 \\ 0 & 0 & 0 & 0 & 0 & 0 & 0 & 0 & 0 & 0 & 0 & 0 & 0 & 0 \\ 0 & 0 & 0 & 0 & 0 & 0 & 0 & 0 & 0 & 0 & 0 & 0 & 0 & 0 \\ 0 & 0 & 0 & 0 & 0 & 0 & 0 & 0 & 0 & 0 & 0 & 0 & 0 & 0 \\ 0 & 0 & 0 & 0 & 0 & 0 & 0 & 0 & 0 & 0 & 0 & 0 & 0 & 0 \\ 0 & 0 & 0 & 0 & 0 & 0 & 0 & 0 & 0 & 0 & 0 & 0 & 0 & 0 \\ 0 & 0 & 0 & 0 & 0 & 0 & 0 & 0 & 0 & 0 & 0 & 0 & 0 & 0 \end{bmatrix}. \quad (\text{C.44})$$

Equation (C.35) can be solved for $i_{1\phi}(t)$ using row operations, eventually being rearranged as follows:

$$i_{1\phi}(t) = A \cdot x_{1\phi}(t) + B \frac{d}{dt} x_{1\phi}(t) + f(t), \quad (\text{C.45})$$

where

$$A = Y \cdot X_2, \quad (\text{C.46})$$

$$B = Y \cdot X_3, \quad (\text{C.47})$$

$$Y = \begin{bmatrix} 1 & 0 & 0 & 0 & 0 & 0 & 0 & 0 & 0 & 0 & 0 & 0 & 0 & 0 \\ -1 & 1 & 0 & 0 & 0 & 0 & 0 & 0 & 0 & 0 & 0 & 0 & 0 & 0 \\ 0 & 0 & 1 & 0 & 0 & 0 & 0 & 0 & 0 & 0 & 0 & 0 & 0 & 0 \\ 0 & 0 & -1 & 1 & 0 & 0 & 0 & 0 & 0 & 0 & 0 & 0 & 0 & 0 \\ -r_c & 0 & -r_c N & 0 & 1 & 0 & 0 & 0 & 0 & 0 & 0 & 0 & 0 & 0 \\ 0 & 0 & 0 & 0 & 0 & 1 & 0 & 0 & 0 & 0 & 0 & 0 & 0 & 0 \\ 0 & 0 & 0 & 0 & 0 & 0 & 1 & 0 & 0 & 0 & 0 & 0 & 0 & 0 \\ 0 & 0 & 0 & 0 & 0 & 0 & 0 & 1 & 0 & 0 & 0 & 0 & 0 & 0 \\ 0 & 0 & 0 & 0 & 0 & 0 & 0 & 0 & 1 & 0 & 0 & 0 & 0 & 0 \\ 0 & 0 & 0 & 0 & 0 & 0 & 0 & 0 & 0 & 1 & 0 & 0 & 0 & 0 \\ 0 & 0 & 0 & 0 & 0 & 0 & 0 & 0 & 0 & 0 & 1 & 0 & 0 & 0 \\ 0 & 0 & 0 & 0 & 0 & 0 & 0 & 0 & 0 & 0 & 0 & 1 & 0 & 0 \\ 0 & 0 & 0 & 0 & 0 & 0 & 0 & 0 & 0 & 0 & 0 & 0 & 1 & 0 \\ 0 & 0 & 0 & 0 & 0 & 0 & 0 & 0 & 0 & 0 & 0 & 0 & 0 & 1 \end{bmatrix}. \quad (\text{C.48})$$

To derive the AQCF of the single-phase transformer model, the differential equations in equation (C.45) should be integrated using the quadratic integration method with the integration time step, h . Note that in equation (C.45), only the seventh-, eighth-, and ninth-row equations, which are induced from the differential equations [i.e., equations (C.27), (C.28), and (C.29)] have differential terms, so they should be integrated quadratically. The integration results are as follows:

$$\begin{bmatrix} i_{1\phi}(t) \\ i_{1\phi}(t_m) \end{bmatrix} = L \begin{bmatrix} x_{1\phi}(t) \\ x_{1\phi}(t_m) \end{bmatrix} - N \cdot x_{1\phi}(t-h) + \begin{bmatrix} f(t) \\ f(t_m) \end{bmatrix}, \quad (\text{C.49})$$

where

$$L = \begin{bmatrix} A_1 & 0 \\ \frac{h}{6}A_2 + B_2 & \frac{2h}{3}A_2 \\ A_3 & 0 \\ 0 & A_1 \\ -\frac{h}{24}A_2 & \frac{h}{3}A_2 + B_2 \\ 0 & A_3 \end{bmatrix}, \quad (\text{C.50})$$

$$N = \begin{bmatrix} 0 \\ -\frac{h}{6}A_2 + B_2 \\ 0 \\ 0 \\ -\frac{5h}{24}A_2 + B_2 \\ 0 \end{bmatrix}, \quad (\text{C.51})$$

A_1 is the first six rows of the matrix A , A_2 is the 7th to 9th rows of the matrix A , A_3 is the 10th to 13th rows of the matrix A , and B_2 is the 7th to 9th rows of matrix B .

C.5 AQCF Model Description of the Three-phase Transformer

The AQCF model of the three-phase delta-wye-connected transformer can be derived by integrating the three sets of the AQCF of the single-phase transformer as described in Figure C.2.

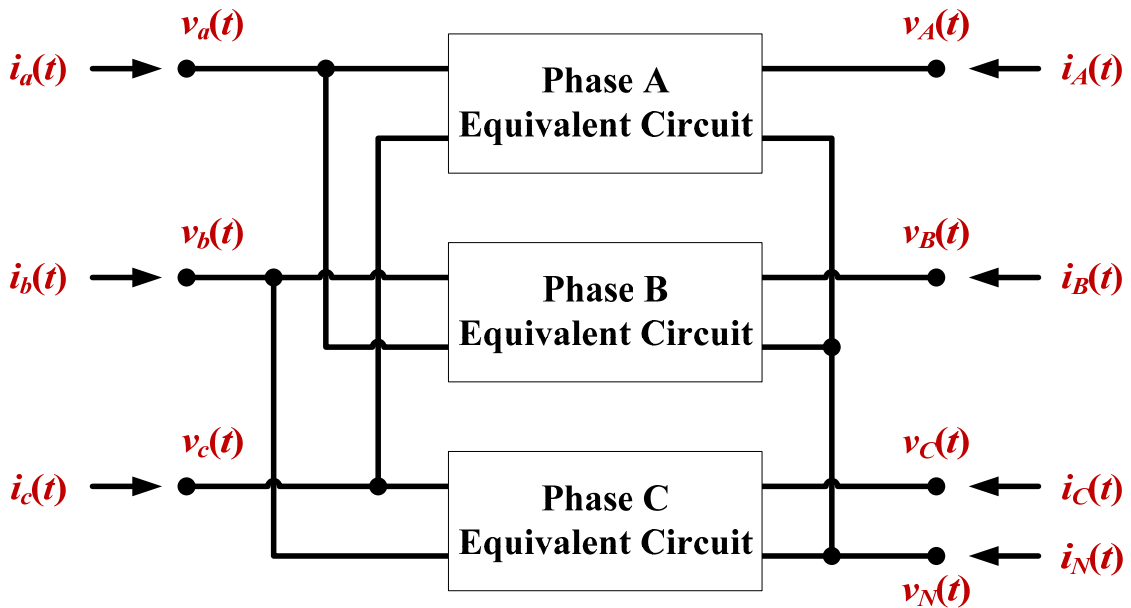


Figure C.2: Delta-wye connection of three single-phase transformers.

In order to integrate the three sets of the AQCF of the single-phase transformer, the pointers of the AQCF of the single-phase transformer need to be re-assigned to those of the AQCF of the three-phase transformer. Figure C.3 represents the indices of the

AQCFs of the single-phase transformer and the three-phase delta-wye-connected transformer.

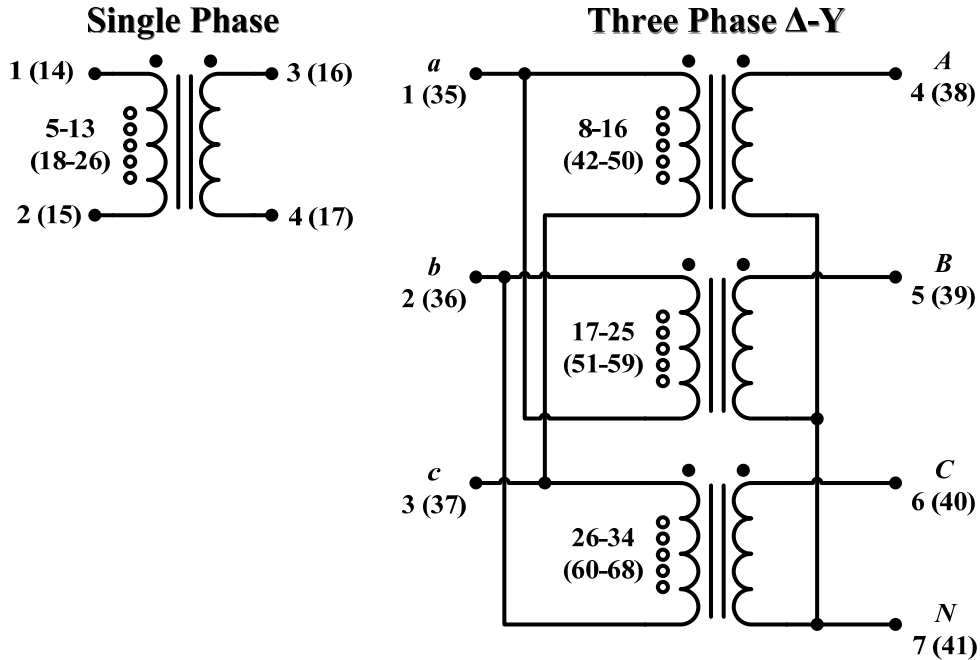


Figure C.3: Indices of the AQCFs of the single-phase transformer and the three-phase delta-wye-connected transformer.

The pointer mapping of external and internal states between the AQCF of the single-phase transformer and that of the three-phase delta-wye-connected transformer are shown in Table C.1.

Table C.1: Pointer mapping between the AQCF of the single-phase transformer and that of the AQCF of the three-phase transformer.

Phase	Indices of the AQCF of the three-phase transformer that correspond to the sequential indices of the AQCF of the single-phase transformer
1	1, 3, 4, 7, 8, 9, 10, 11, 12, 13, 14, 15, 16, 35, 37, 38, 41, 42, 43, 44, 45, 46, 47, 48, 49, 50
2	2, 1, 5, 7, 17, 18, 19, 20, 21, 22, 23, 24, 25, 36, 35, 39, 41, 51, 52, 53, 54, 55, 56, 57, 58, 59
3	3, 2, 6, 7, 26, 27, 28, 29, 30, 31, 32, 33, 34, 37, 36, 40, 41, 60, 61, 62, 63, 64, 65, 66, 67, 68

The device matrices, L and N , which are described in the AQCF of the single-phase transformer, equation (C.49), are integrated into the AQCF of the three-phase transformer based on the following algorithm, thereby providing the integrated matrices, $L_{3\phi}$ and $N_{3\phi}$:

```

For   PHASE = 1:3
      For   I = 1:26
            K1 = POINTERPHASE(I)
            For   J = 1:26
                  K2 = POINTERPHASE(J)
                  L3φ(K1, K2) = L3φ(K1, K2) + L(I,J)
            End
            For   J = 1:13
                  K2 = POINTERPHASE(J)
                  N3φ(K1, K2) = N3φ(K1, K2) + N(I,J)
            End
      End
End
End
End

```

where $PHASE$ is the phase index of the single-phase transformer, and $POINTER_{PHASE}()$ is the function that converts the index of the single-phase transformer to that of the three-phase transformer. For instance, $POINTER_1(3)$ is 4.

As a result of integrating three sets of the AQCF of the single-phase transformer, the component device model of the three-phase transformer can be obtained as follows:

$$\begin{bmatrix} i_{3\phi}(t) \\ 0 \\ i_{3\phi}(t_m) \\ 0 \end{bmatrix} = \begin{bmatrix} L_{11} & L_{12} & L_{13} & L_{14} \\ L_{21} & L_{22} & L_{23} & L_{24} \\ L_{31} & L_{32} & L_{33} & L_{34} \\ L_{41} & L_{42} & L_{43} & L_{44} \end{bmatrix} \begin{bmatrix} v_{3\phi}(t) \\ y_{3\phi}(t) \\ v_{3\phi}(t_m) \\ y_{3\phi}(t_m) \end{bmatrix} + \begin{bmatrix} f_{3\phi,1}(t) \\ f_{3\phi,2}(t) \\ f_{3\phi,1}(t_m) \\ f_{3\phi,2}(t_m) \end{bmatrix} - \begin{bmatrix} b_1(t-h) \\ b_2(t-h) \\ b_3(t-h) \\ b_4(t-h) \end{bmatrix}, \quad (C.52)$$

where

$$b(t-h) = \begin{bmatrix} b_1(t-h) \\ b_2(t-h) \\ b_3(t-h) \\ b_4(t-h) \end{bmatrix} = \begin{bmatrix} N_{11} & N_{12} \\ N_{21} & N_{22} \\ N_{31} & N_{32} \\ N_{41} & N_{42} \end{bmatrix} \begin{bmatrix} v_{3\phi}(t-h) \\ y_{3\phi}(t-h) \end{bmatrix}, \quad (\text{C.53})$$

$$i_{3\phi}(t) = [i_a(t), i_b(t), i_c(t), i_A(t), i_B(t), i_C(t), i_N(t)]^T, \quad (\text{C.54})$$

$$v_{3\phi}(t) = [v_a(t), v_b(t), v_c(t), v_A(t), v_B(t), v_C(t), v_N(t)]^T, \quad (\text{C.55})$$

$$y_{3\phi}(t) = [i_{mA}(t), e_A(t), \lambda_A(t), i_{1LA}(t), i_{3LA}(t), y_{1A}(t), y_{2A}(t), y_{3A}(t), z_A(t), \\ i_{mB}(t), e_B(t), \lambda_B(t), i_{1LB}(t), i_{3LB}(t), y_{1B}(t), y_{2B}(t), y_{3B}(t), z_B(t), \\ i_{mC}(t), e_C(t), \lambda_C(t), i_{1LC}(t), i_{3LC}(t), y_{1C}(t), y_{2C}(t), y_{3C}(t), z_C(t)]^T, \quad (\text{C.56})$$

$$f_{3\phi}(t) = \begin{bmatrix} f_{3\phi,1}(t) \\ f_{3\phi,2}(t) \end{bmatrix}, \quad (\text{C.57})$$

$$f_{3\phi,1}(t) = \begin{bmatrix} \begin{bmatrix} v_{3\phi}(t) \\ y_{3\phi}(t) \\ v_{3\phi}(t_m) \\ y_{3\phi}(t_m) \end{bmatrix} \\ \begin{bmatrix} v_{3\phi}(t) \\ y_{3\phi}(t) \\ v_{3\phi}(t_m) \\ y_{3\phi}(t_m) \end{bmatrix} \\ \vdots \\ \begin{bmatrix} v_{3\phi}(t) \\ y_{3\phi}(t) \\ v_{3\phi}(t_m) \\ y_{3\phi}(t_m) \end{bmatrix} \end{bmatrix}, \quad (\text{C.58})$$

$$f_{3\phi,2}(t) = \begin{bmatrix} [v_{3\phi}(t)^T \quad y_{3\phi}(t)^T \quad v_{3\phi}(t_m)^T \quad y_{3\phi}(t_m)^T] Q_8 \begin{bmatrix} v_{3\phi}(t) \\ y_{3\phi}(t) \\ v_{3\phi}(t_m) \\ y_{3\phi}(t_m) \end{bmatrix} \\ [v_{3\phi}(t)^T \quad y_{3\phi}(t)^T \quad v_{3\phi}(t_m)^T \quad y_{3\phi}(t_m)^T] Q_9 \begin{bmatrix} v_{3\phi}(t) \\ y_{3\phi}(t) \\ v_{3\phi}(t_m) \\ y_{3\phi}(t_m) \end{bmatrix} \\ \vdots \\ [v_{3\phi}(t)^T \quad y_{3\phi}(t)^T \quad v_{3\phi}(t_m)^T \quad y_{3\phi}(t_m)^T] Q_{34} \begin{bmatrix} v_{3\phi}(t) \\ y_{3\phi}(t) \\ v_{3\phi}(t_m) \\ y_{3\phi}(t_m) \end{bmatrix} \end{bmatrix}, \quad (\text{C.59})$$

$$L_{3\phi} = \begin{bmatrix} L_{11} & L_{12} & L_{13} & L_{14} \\ L_{21} & L_{22} & L_{23} & L_{24} \\ L_{31} & L_{32} & L_{33} & L_{34} \\ L_{41} & L_{42} & L_{43} & L_{44} \end{bmatrix}, \quad (\text{C.60})$$

$$N_{3\phi} = \begin{bmatrix} N_{11} & N_{12} \\ N_{21} & N_{22} \\ N_{31} & N_{32} \\ N_{41} & N_{42} \end{bmatrix}. \quad (\text{C.61})$$

C.6 State Variables

Finally, state variables for the delta-wye-connected three-phase transformer are defined as follows:

$$\begin{bmatrix} v_{3\phi}(t) \\ y_{3\phi}(t) \\ v_{3\phi}(t_m) \\ y_{3\phi}(t_m) \end{bmatrix}, \quad (\text{C.62})$$

indicating there are a total of 68 state variables.

C.7 Summary

This appendix presents how to develop the component dynamic model of the three-phase, two-winding, variable-tap, and saturable-core transformer, which is used for the setting-less component protection scheme. Finally, the component dynamic model is expressed in the AQCF, as presented in equation (C.52).

REFERENCES

- [1] C. Roe, J. Meisel, A. P. S. Meliopoulos, F. Evangelos, and T. Overbye, "Power system level impacts of PHEVs," in *Proc. the 42nd Annual Hawaii International Conference on System Sciences*, 2009, pp. 1-10.
- [2] J. D. Glover and M. S. Sarma, "Chapter 1: Introduction" in *Power system analysis and design*, 3rd ed.: Brooks/Cole, 2002, pp. 1-24.
- [3] A. v. Meier, "Chapter 6: Transmission and distribution" in *Electric power systems: A conceptual introduction*: A Wiley-Interscience, 2006, pp. 144-159.
- [4] EPRI, "Intelligrid." [Online]. Available: <http://intelligrid.epri.com>
- [5] R. Pool, "Electric dreams [global electrification]," *Power Engineer*, vol. 19, no. 1, pp. 12-15, 2005.
- [6] J. Hughes, "Intelligrid architecture concepts and IEC61850," in *Proc. IEEE PES Transmission and Distribution Conference and Exhibition*, May 2006, pp. 401-404.
- [7] M. Samotyj and B. Howe, "Creating tomorrow's intelligent electric power delivery system," in *Proc. the 18th International Conference and Exhibition on Electricity Distribution*, Jun. 2005.
- [8] M. McGranaghan and G. Gilchrist, "Telecommunications assessment for a consumer portal," in *Proc. IEEE PES General Meeting*, 2006.
- [9] A. Didierjean, "What is a consumer portal?," in *Proc. IEEE PES Transmission and Distribution Conference and Exhibition*, May 2006, pp. 471-473.
- [10] R. H. Lasseter and P. Piagi, "Extended microgrid using (DER) distributed energy resources," in *Proc. IEEE PES General Meeting*, Jun. 2007.
- [11] R. H. Lasseter, "Microgrids," in *Proc. IEEE PES Winter Meeting*, vol. 1, 2002, pp. 305-308.
- [12] R. H. Lasseter and P. Paigi, "Microgrid: A conceptual solution," in *Proc. the 35th Annual IEEE Power Electronics Specialists Conference*, vol. 6, Jun. 2004, pp. 4285-4290.

- [13] B. Kroposki, R. Lasseter, T. Ise, S. Morozumi, S. Papatlianassiou, and N. Hatziargyriou, "Making microgrids work," *IEEE Power and Energy Magazine*, vol. 6, no. 3, pp. 40-53, 2008.
- [14] M. Barnes, J. Kondoh, H. Asano, J. Oyarzabal, G. Ventakaramanan, R. Lasseter, N. Hatziargyriou, and T. Green, "Real-world microgrids-an overview," in *Proc. IEEE International Conference on System of Systems Engineering*, Apr. 2007.
- [15] P. Basak, A. K. Saha, S. Chowdhury, and S. P. Chowdhury, "Microgrid: Control techniques and modeling," in *Proc. the 44th International Universities Power Engineering Conference*, Sep. 2009.
- [16] A. A. Zaidi and F. Kupzog, "Microgrid automation - a self-configuring approach," in *Proc. IEEE International Multitopic Conference*, Dec. 2008, pp. 565-570.
- [17] P. Mazza, "Powering up the smart grid: A northwest initiative for job creation, energy security, and clean, affordable electricity," *Climate Solutions*, 2005.
- [18] E. Santacana, G. Rackliffe, L. Tang, and X. Feng, "Getting smart," *IEEE Power and Energy Magazine*, vol. 8, no. 2, pp. 41-48, Mar. 2010.
- [19] U.S. Department of Energy (DoE), "The smart grid: An introduction."
- [20] S. Massoud Amin and B. F. Wollenberg, "Toward a smart grid: Power delivery for the 21st century," *IEEE Power and Energy Magazine*, vol. 3, no. 5, pp. 34-41, 2005.
- [21] X. Chen, S. Yongmei, and L. Yuewu, "A preliminary study on the business model for electric vehicle charging stations," in *Proc. China International Conference on Electricity Distribution*, Sep. 2010.
- [22] C. Guille and G. Gross, "Design of a conceptual framework for the V2G implementation," in *Proc. IEEE Energy 2030 Conference*, Nov. 2008.
- [23] T. Markel, M. Kuss, and M. Simpson, "Value of plug-in vehicle grid support operation," in *Proc. IEEE Innovative Technologies for an Efficient and Reliable Electricity Supply*, Sep. 2010, pp. 325-332.
- [24] G. Andersson, P. Donalek, R. Farmer, N. Hatziargyriou, I. Kamwa, P. Kundur, N. Martins, J. Paserba, P. Pourbeik, J. Sanchez-Gasca, R. Schulz, A. Stankovic, C. Taylor, and V. Vittal, "Causes of the 2003 major grid blackouts in north america and europe, and recommended means to improve system dynamic performance," *IEEE Trans. Power Systems*, vol. 20, no. 4, pp. 1922-1928, 2005.

- [25] S. Patel, "Fundamentals of transformer inrush," in *Proc. the 65th Annual Georgia Tech Protective Relaying Conference*, May 2011.
- [26] J. H. Harlow, *Electric power transformer engineering*, 2nd ed.: CRC Press, 2007.
- [27] R. Hunt, J. Schaefer, and B. Bentert, "Practical experience in setting transformer differential inrush restraint," in *Proc. the 61st Annual Conference for Protective Relay Engineers*, Apr. 2008, pp. 118-141.
- [28] E. Sortomme, G. J. Mapes, B. A. Foster, and S. S. Venkata, "Fault analysis and protection of a microgrid," in *Proc. the 40th North American Power Symposium*, Sep. 2008.
- [29] S. A. Gopalan, V. Sreeram, H. H. C. Iu, Z. Xu, Z. Y. Dong, and K. P. Wong, "Fault analysis of an islanded multi-microgrid," in *Proc. IEEE PES General Meeting*, Jul. 2012.
- [30] H. Nikkhajoei and R. H. Lasseter, "Microgrid protection," in *Proc. IEEE PES General Meeting*, Tampa, Florida, Jun. 2007.
- [31] N. Jayawarna, N. Jenkins, M. Barnes, M. Lorentzou, S. Papathanassiou, and N. Hatziagyriou, "Safety analysis of a microgrid," in *Proc. International Conference on Future Power Systems*, Nov. 2005.
- [32] Y. Han, X. Hu, and D. Zhang, "Study of adaptive fault current algorithm for microgrid dominated by inverter based distributed generators," in *Proc. the 2nd IEEE International Symposium on Power Electronics for Distributed Generation Systems*, Jun. 2010, pp. 852-854.
- [33] M. G. Villalva, J. R. Gazoli, and E. R. Filho, "Comprehensive approach to modeling and simulation of photovoltaic arrays," *IEEE Trans. Power Electronics*, vol. 24, no. 5, pp. 1198-1208, May 2009.
- [34] C. Feltes and I. Erlich, "Variable frequency operation of DFIG based wind farms connected to the grid through VSC-HVDC link," in *Proc. IEEE PES General Meeting*, Jun. 2007.
- [35] A. P. Meliopoulos, G. J. Cokkinides, R. Huang, and E. Farantatos, "Integrated smart grid hierarchical control," in *Proc. the 45th Annual Hawaii International Conference on System Sciences*, Jan. 2012, pp. 1967-1976.

- [36] A. Milo, H. Gaztanaga, I. Etxeberria-Otadui, E. Bilbao, and P. Rodriguez, "Optimization of an experimental hybrid microgrid operation: Reliability and economic issues," in *Proc. IEEE Bucharest PowerTech Conference*, Bucharest, Romania, Jun. 2009.
- [37] V. Skendzic and A. Guzma, "Enhancing power system automation through the use of real-time ethernet," in *Proc. Power Systems Conference: Advanced Metering, Protection, Control, Communication, and Distributed Resources*, Mar. 2006, pp. 480-495.
- [38] J. Belagur and R. Schmidt, "IP communication for substation automation, distribution automation, and other utility applications - a business case," in *Proc. IEEE PES Transmission and Distribution Conference and Exposition*, Apr. 2008.
- [39] *Communication Networks and Systems in Substations - Part 4: System and Project Management*, IEC 61850-4 ed 2.0, Apr. 2011.
- [40] *IEEE Standard for Synchrophasors for Power Systems*, IEEE Std C37.118-2005, Mar. 2006.
- [41] H. W. Beaty and D. G. Fink, "Section 25: Computer applications in the electric power industry" in *Standard handbook for electrical engineers*, 15th ed.: McGraw-Hill, 2007, pp. 15-16.
- [42] A. A. Sallam and O. P. Malik, "Chapter 13: SCADA systems and smart grid vision" in *Electric distribution systems*, 1st ed.: John Wiley & Sons, Inc., 2011, pp. 469-493.
- [43] D. J. Gaushell and W. R. Block, "SCADA communication techniques and standards," *IEEE Computer Applications in Power*, vol. 6, no. 3, pp. 45-50, Jul. 1993.
- [44] J. Y. Cai, H. Zhenyu, J. Hauer, and K. Martin, "Current status and experience of wams implementation in north america," in *Proc. IEEE PES Transmission and Distribution Conference and Exhibition: Asia and Pacific*, Dalian, China, 2005.
- [45] T. Babnik, U. Gabrijel, B. Mahkovec, M. Perko, and G. Sitar, "Wide area measurement system in action," in *Proc. IEEE Power Tech*, Lausanne, Jul. 2007, pp. 1646-1651.
- [46] R. E. Brown, "Impact of smart grid on distribution system design," in *Proc. IEEE PES General Meeting*, Jul. 2008.

- [47] J. Fan and S. Borlase, "The evolution of distribution," *IEEE Power and Energy Magazine*, vol. 7, no. 2, pp. 63-68, 2009.
- [48] A. Abur and A. G. Exposito, "Chapter 1: Introduction" in *Power system state estimation: Theory and implementation*: Marcel Dekker, Inc., 2004.
- [49] F. C. Schweppe, "Power system static-state estimation, part III: Implementation," *IEEE Trans. Power App. Syst.*, vol. PAS-89, no. 1, pp. 130-135, Jan. 1970.
- [50] F. C. Schweppe and D. B. Rom, "Power system static-state estimation, part II: Approximate model," *IEEE Trans. Power App. Syst.*, vol. PAS-89, no. 1, pp. 125-130, Jan. 1970.
- [51] F. C. Schweppe and J. Wildes, "Power system static-state estimation, part I: Exact model," *IEEE Trans. Power App. Syst.*, vol. PAS-89, no. 1, pp. 120-125, Jan. 1970.
- [52] A. Abur and A. G. Exposito, "Chapter 2: Weighted least squares state estimation" in *Power system state estimation: Theory and implementation*: Marcel Dekker, Inc., 2004.
- [53] A. P. S. Meliopoulos and G. K. Stefopoulos, "Characterization of state estimation biases," in *Proc. International Conference on Probabilistic Methods Applied to Power Systems*, Sep, 2004, pp. 600-607.
- [54] Z. Shan and A. Abur, "Effects of nontransposed lines and unbalanced loads on state estimation," in *Proc. IEEE PES Winter Meeting*, vol. 2, 2002, pp. 975-979.
- [55] A. P. S. Meliopoulos, B. Fardanesh, and S. Zelingher, "Power system state estimation: Modeling error effects and impact on system operation," in *Proc. the 34th Annual Hawaii International Conference on System Sciences*, Jan. 2001.
- [56] A. P. S. Meliopoulos, G. J. Cokkinides, and G. K. Stefopoulos, "Numerical experiments for three-phase state estimation performance and evaluation," in *Proc. IEEE Power Tech*, Russia, Jun. 2005.
- [57] C. W. Hansen and A. S. Debs, "Power system state estimation using three-phase models," *IEEE Trans. Power Syst.*, vol. 10, no. 2, pp. 818-824, 1995.
- [58] A. P. S. Meliopoulos, "State estimation for mega RTOs," in *Proc. IEEE PES Summer Meeting*, vol. 3, Jul. 2002, pp. 1698-1703.

- [59] A. V. Jaen, P. C. Romero, and A. G. Exposito, "Substation data validation by a local three-phase generalized state estimator," *IEEE Trans. Power Syst.*, vol. 20, no. 1, pp. 264-271, 2005.
- [60] A. P. S. Meliopoulos and G. J. Cokkinides, "Advanced synchrophasor applications," in *Proc. IEEE PES General Meeting*, Jul. 2010.
- [61] A. P. S. Meliopoulos, G. J. Cokkinides, F. Galvan, B. Fardanesh, and P. Myrda, "Advances in the supercalibrator concept - practical implementations," in *Proc. the 40th Annual Hawaii International Conference on System Sciences*, Jan. 2007.
- [62] A. P. S. Meliopoulos, G. J. Cokkinides, O. Wasynczuk, E. Coyle, M. Bell, C. Hoffmann, C. Nita-Rotaru, T. Downar, L. Tsoukalas, and R. Gao, "PMU data characterization and application to stability monitoring," in *Proc. IEEE PES General Meeting*, 2006.
- [63] M. C. Janssen and A. Apostolov, "IEC 61850 impact on substation design," in *Proc. IEEE PES Transmission and Distribution Conference and Exposition*, Apr. 2008.
- [64] C. N. Lu, J. H. Teng, and W. H. E. Liu, "Distribution system state estimation," *IEEE Trans. Power Syst.*, vol. 10, no. 1, pp. 229-240, 1995.
- [65] S. Choi, B. Kim, G. J. Cokkinides, and A. P. S. Meliopoulos, "Autonomous state estimation for the smart grid - laboratory implementation," in *Proc. IEEE PES Transmission and Distribution Conference and Exposition*, New Orleans, Apr. 2010.
- [66] A. P. S. Meliopoulos, G. J. Cokkinides, and G. Stefopoulos, "Quadratic integration method," in *Proc. International Power System Transients Conference*, Montreal, Jun. 2005.
- [67] G. K. Stefopoulos, G. J. Cokkinides, and A. P. S. Meliopoulos, "Quadratized model of nonlinear saturable-core inductor for time-domain simulation," in *Proc. IEEE PES General Meeting*, Jul. 2009.
- [68] A. P. S. Meliopoulos, G. J. Cokkinides, and G. K. Stefopoulos, "Symbolic integration of dynamical systems by collocation methods," in *Proc. IEEE PES Power Systems Conference and Exposition*, Oct. 2006, pp. 362-367.
- [69] A. P. S. Meliopoulos, G. J. Cokkinides, F. Galvan, and B. Fardanesh, "Distributed state estimator advances and demonstration," in *Proc. the 41st Annual Hawaii International Conference on System Sciences*, Jan. 2008.

- [70] A. P. S. Meliopoulos, G. J. Cokkinides, C. Hedrington, and T. L. Conrad, "The supercalibrator - a fully distributed state estimator," in *Proc. IEEE PES General Meeting*, Jul. 2010.
- [71] A. P. S. Meliopoulos, G. J. Cokkinides, F. Galvan, B. Fardeanesh, and P. Myrda, "Delivering accurate and timely data to all," *IEEE Power and Energy Magazine*, vol. 5, no. 3, pp. 74-86, May 2007.
- [72] A. P. S. Meliopoulos, G. J. Cokkinides, Z. Tan, S. Choi, Y. Lee, and P. Myrda, "Setting-less protection: Feasibility study," in *Proc. the 46th Annual Hawaii International Conference on System Sciences*, Jan. 2013.
- [73] S. Choi, Y. Lee, G. J. Cokkinides, and A. P. S. Meliopoulos, "Dynamically adaptive transformer protection using dynamic state estimation," in *Proc. the Protection, Automation & Control World*, Dublin, Ireland, Jun. 2011.
- [74] E. Farantatos, G. K. Stefopoulos, G. J. Cokkinides, and A. P. S. Meliopoulos, "PMU-based dynamic state estimation for electric power systems," in *Proc. IEEE PES General Meeting*, Jul. 2009.
- [75] R. Huang, E. Farantatos, G. J. Cokkinides, and A. P. S. Meliopoulos, "Substation based dynamic state estimator - numerical experiment," in *Proc. IEEE PES Transmission and Distribution Conference and Exposition*, New Orleans, Apr. 2010.
- [76] T. Esrasm and P. L. Chapman, "Comparison of photovoltaic array maximum power point tracking techniques," *IEEE Trans. Energy Conversion*, vol. 22, no. 2, pp. 439-449, Jun. 2007.
- [77] M. A. S. Masoum, H. Dehbonei, and E. F. Fuchs, "Theoretical and experimental analyses of photovoltaic systems with voltage and current-based maximum power-point tracking," *IEEE Trans. Energy Conversion*, vol. 17, no. 4, pp. 514-522, Dec. 2002.
- [78] A. Soetedjo, A. Lomi, and W. P. Mulayanto, "Modeling of wind energy system with MPPT control," in *Proc. 2011 International Conference on Electrical Engineering and Informatics (ICEEI)*, Jul. 2011.
- [79] P. Ledesma and J. Usaola, "Doubly fed induction generator model for transient stability analysis," *IEEE Trans. Energy Conversion*, vol. 20, no. 2, pp. 388-397, 2005.

- [80] P. Li, S. Zhang, Y. Wang, G. Sun, L. Zhou, and X. Wang, "Research on economic optimal operation of microgrid," in *Proc. IEEE International Conference on Power System Technology*, Oct. 2012.
- [81] M. Meiqin, J. Meihong, D. Wei, and L. Chang, "Multi-objective economic dispatch model for a microgrid considering reliability," in *Proc. the 2nd IEEE International Symposium on Power Electronics for Distributed Generation Systems*, Jun. 2010, pp. 993-998.
- [82] S. Mohagheghi, R. H. Alaileh, G. Cokkinides, and A. P. S. Meliopoulos, "Distributed state estimation based on the supercalibrator concept - laboratory implementation," in *Proc. iREP Symposium*, Aug. 2007.
- [83] S. Mohagheghi, R. H. Alaileh, G. J. Cokkinides, and A. P. S. Meliopoulos, "A laboratory setup for a substation scaled model," in *Proc. IEEE Power Tech*, Lausanne, Jul. 2007, pp. 1203-1208.
- [84] Q. B. Dam, S. Mohagheghi, R. H. Alaileh, G. K. Stefopoulos, G. J. Cokkinides, and A. P. S. Meliopoulos, "A laboratory setup for relay and GPS-synchronized equipment transient testing," in *Proc. IEEE PES General Meeting*, Jul. 2008.
- [85] A. P. S. Meliopoulos, G. J. Cokkinides, S. Mohagheghi, Q. B. Dam, R. H. Alaileh, and G. K. Stefopoulos, "A laboratory setup of a power system scaled model for testing and validation of EMS applications," in *IEEE Power Tech*, Bucharest, Jun. 2009.
- [86] *Integrated grounding system for windows (WinIGS)*, Advanced Grounding Concepts, Atlanta, GA. [Online]. Available: <http://www.ap-concepts.com>
- [87] *IEEE Standard Common Format for Transient Data Exchange (COMTRADE) for Power Systems*, IEEE Std C37.111-1999, Mar. 1999.
- [88] M. Karimi, H. Mokhlis, A. H. A. Bakar, A. Shahriari, M. A. Faradonbeh, and H. M. Rosli, "Impact of load modeling in distribution state estimation," in *Proc. IEEE International Power Engineering and Optimization Conference (PEOCO)*, Melaka, Malaysia, Jun. 2012, pp. 67-71.
- [89] A. A. Yaghoti, M. Parsa, and V. J. Majd, "Electrical distribution networks state estimation," in *Proc. the 18th International Conference and Exhibition on Electricity Distribution*, Turin, Jun. 2005.

- [90] X. Feng, F. Yang, and W. Peterson, "A practical multi-phase distribution state estimation solution incorporating smart meter and sensor data," in *Proc. IEEE PES General Meeting*, Jul. 2012.
- [91] N. Katic, L. Fei, G. Svenda, and Z. Yongji, "Distribution state estimation field testing," in *Proc. China International Conference on Electricity Distribution (CICED)*, Sep. 2012.
- [92] D. A. Haughton and G. T. Heydt, "A linear state estimation formulation for smart distribution systems," *IEEE Trans. Power Syst.*, vol. 28, no. 2, pp. 1187-1195, May 2013.
- [93] M. E. Baran and A. W. Kelley, "State estimation for real-time monitoring of distribution systems," *IEEE Trans. Power Syst.*, vol. 9, no. 3, pp. 1601-1609, Aug. 1994.
- [94] A. P. Meliopoulos, G. J. Cokkinides, and G. K. Stefopoulos, "Improved numerical integration method for power/power electronic systems based on three-point collocation," in *Proc. the 44th IEEE Conference on Decision and Control, and European Control Conference*, Dec. 2005, pp. 6780-6787.
- [95] G. Stefopoulos, G. J. Cokkinides, and A. P. S. Meliopoulos, "Expert symbolic transient simulator based on quadratic integration method," in *Proc. the 13th International Conference on Intelligent Systems Application to Power Systems*, Nov. 2005, pp. 347-353.
- [96] M. G. Villalva, J. R. Gazoli, and E. R. Filho, "Modeling and circuit-based simulation of photovoltaic arrays," in *Proc. Brazilian Power Electronics Conference*, Sep. 2009, pp. 1244-1254.

VITA

SUNGYUN CHOI

Sungyun Choi (Korean: 최승연) was born in Seoul, South Korea in October 1979. After he earned his high-school diploma in February 1998, he joined the School of Electrical Engineering at Korea University in Seoul, South Korea in March 1998, where he received his B.E. diploma in 2002. Then, he worked as a network and systems engineer at Incube Tech Co., Ltd. in Seoul, South Korea since 2002. Then, he started graduate studies at the Georgia Institute of Technology in Atlanta, Georgia since 2007, receiving an M.S. degree in the School of Electrical and Computer Engineering in 2009.

Since 2007, under the supervision of Professor A. P. Sakis Meliopoulos, Sungyun conducted research in the PSCAL at the Georgia Institute of Technology as a graduate research assistant. His research interest lies in state estimation, modeling and simulation, protection, and laboratory demonstrations in the area of electric power. In September 2011, he earned an award for winning the 2011 GE Smart Grid Challenge, which was supported by GE Energy. He has been a member of the Institute of Electrical and Electronics Engineers and the IEEE Power and Energy Society.